Dissertation
submitted to the
Combined Faculties for the Natural Sciences and for Mathematics
of the Ruperto-Carola University of Heidelberg, Germany
for the degree of
Doctor of Natural Sciences

put forward by
Dipl.-Phys. Bodo Werner
born in Heidelberg

Oral examination: 28.10.2015

Spectroscopic UV/vis limb measurements from aboard the NASA Global Hawk: Implications for the photochemistry and budget of bromine in the tropical tropopause layer

Referees: Prof. Dr. Klaus Pfeilsticker
Prof. Dr. Thomas Leisner

Abstract:

The present thesis reports on the world's first measurements of the second most important ozone-depleting halogen bromine at the entrance to the stratosphere (14 - 18.5 km, $\theta \approx$ 330 - 400 K) over the East and Central Pacific in late winter 2013. The measurements were performed within the NASA-ATTREX project from aboard the unmanned aerial vehicle Global Hawk. For the interpretation of the remote-sensing DOAS measurements of O_3, NO_2 and BrO, use of complementary measurements of brominated source gases (SGs) and dynamical tracers (e.g. CH_3Br, halons, very short-lived species (VSLS), CH_4) and model simulations of the chemical transport model (CTM) SLIMCAT/TOMCAT, is made.
The agreement of measured and modelled CH_4, O_3, and NO_2 shows that the major dynamical and photochemical processes are represented well in the CTM. Considering surface concentrations of the brominated organic SGs of in total 20.5 ppt, the measured BrO mixing ratios (0.5 - 9.0 ppt) are well explained. An exception are regions where the contribution of the short-lived CH_2Br_2 or the partitioning of $BrONO_2$ plays an important role. The present observations confirm previous findings on the formation of $BrONO_2$ of our workgroup.
Depending on the flight, a total bromine budget (Br_y) in the tropical tropopause layer (TTL) of 20.3 ppt to 22.3 ppt is inferred. For each fligh the contribution to total bromine of the long-lived brominated SGs stays constant (CH_3Br + halons = 14.6 ppt), while the amount of VSLS and inorganic bromine varies between 5.7 ppt and 7.7 ppt. Thus, the present observations set a tighter constraint on the role of bromine for ozone depletion in the TTL than previous studies.

Zusammenfassung:

Die vorliegende Arbeit berichtet über die weltweit ersten Messungen des zweitwichtigsten Ozon-zerstörenden Halogens Brom an der Eingangstür zur Stratosphäre (14 - 18.5 km, $\theta \approx$ 330 - 400 K) über dem tropischen Ost-/Zentralpazifik im Spätwinter 2013. Die Messungen fanden im Rahmen des NASA-ATTREX-Projekts an Bord des unbemannten Forschungsflugzeugs Global Hawk statt. Zur Interpretation der Fernerkundungs-Messungen von O_3, NO_2 und BrO mittels der DOAS-Methode, werden weitere Messungen (CH_4 und organische bromierte Quellgase wie CH_3Br, Halone und VSLS (engl. very short-lived species)), sowie Modellrechnungen des chemischen Transportmodells (CTM) SLIMCAT/TOMCAT herangezogen.
Der Vergleich des gemessenen CH_4, O_3 und NO_2 und dem Modell zeigt, dass das CTM die hauptsächlichen dynamischen und photochemischen Prozesse gut abbildet. Werden im CTM die Bodenkonzentrationen der organischen Quellgase von in Summe 20.5 ppt berücksichtigt, so werden die gessenen BrO-Konzentrationen (0.5 - 9.0 ppt) im allgemeinen von dem CTM gut erklärt. Eine Ausnahme bilden Regionen in denen die Konzentrationen des kurzlebigen Quellgases CH_2Br_2 oder die Photochemie von $BrONO_2$ eine wesentliche Rolle spielt. Der letzte Befund zur Bildung von $BrONO_2$ bestätigt frühere Ergebnisse unserer Arbeitsgruppe.
Aus den Beobachtungen lässt sich auf eine Gesamtmenge von Brom (Br_y) in der tropischen Tropopausen-Schicht (engl. TTL) im Bereich zwischen 20.3 ppt und 22.3 ppt, je nach Flug, schließen. Während für jeden Flug der Zufluss der langlebigen Quellgase (CH_3Br + Halone = 14.6 ppt) konstant bleibt, schwankt der Zufluss der VSLS und des anorganischen Broms zwischen 5.7 ppt und 7.7 ppt. Diese Messungen schränken somit die Rolle des Broms für den stratosphärischen Ozonabbau stärker als bisher bekannt ein.

Contents

1 Introduction

Today the stratosphere is perceived as an important part of the global environment (Seinfeld and Pandis, 2006). Compared to the turbulence-driven troposphere, vertical energy transport in the stratosphere is largely dominated by transfer of electromagnetic radiation. Near the equator, the stratosphere reaches from about 18 km, at mid-latitudes from about 10 - 12 km, and in polar regions from about 8 km to about 50 km altitude. Its importance for the global environment is threefold: (a) It shields the biosphere from harmful UV radiation by absorption of electromagnetic radiation due to ozone (O_3) below the threshold of the carbon to carbon dissociation energy ($E_\lambda \geq 3.6$ eV), i.e. wavelengths $\lambda \leq 330$ nm (Brasseur and Solomon, 1986), (b) for imposing a radiative forcing onto the climate system which largely depends on its ozone, water vapor, and CO_2 concentrations (IPCC, 2013), and (c) for its potential to downward control some dynamical processes acting in the troposphere (Baldwin and Dunkerton, 2001).

The first manned balloon probe of the stratosphere occurred on July 31, 1901, when Reinhard Süring and Arthur Berson risked the ascent, in an open gondola, to an altitude of 10550 m over Potsdam/Germany (Berson, A. and Süring, R., 1901). Their instrumentation consisted of a Mercury barometer, an aneriod-barograph (a canister barometer), a so-called aspiration-psychrometer, and a blackbody thermometer. With the help of those instruments they monitored the temperature, pressure, and water vapor concentration during balloon ascent. Earlier unmanned atmospheric soundings by Léon Teisserenc de Bort over France (Teisserenc de Bort, 1902) and the data collected by Reinhard Süring and Arthur Berson suggested increasing temperatures above the tropopause. This led the befriended Léon Teisserenc de Bort and Richard Aßmann to announce the discovery of the stratosphere in 1902 (Aßmann, 1902).

My thesis is devoted to the amount and photochemistry of bromine in the stratosphere. Therefore, in the following some landmark developments and discoveries in photochemistry, rather than of the dynamical or radiative processes, relevant for the stratosphere are briefly summarised.

Stratospheric ozone was discovered by the French physicists Charles Fabry and Henri Buisson in 1913, when they performed the first spectroscopic measurements of atmospheric scattered light in the UV spectral range (Fabry and Buisson, 1913). By 1924, the British meteorologist G. M. B. Dobson had developed a simple spectrophotometer (the Dobsonmeter). With the aid of the Dobsonmeter F. W. P. Götz performed the first quantitative profile measurements of stratospheric ozone

at Arosa/Switzerland in 1926. Today these so-called 'Umkehr' measurements form the world's longest record of the amount and profile of stratospheric ozone (Dobson et al., 1926).

In 1930 Sidney Chapman developed a theory, based on the photochemistry of a pure oxygen atmosphere and UV radiation, to explain the existence of ozone (Chapman, 1930). Over the next few decades Dobsonmeters were used to measure the total column amount of ozone at an increasing number of locations. The obtained ozone climatology showed that the amount of ozone were at a minimum at the equator and increased towards the poles. Additionally they began exhibiting a strong seasonal variation with a maximum in the spring and a minimum in the late fall or early winter. This distribution of ozone was in direct conflict with the predictions of the Chapman theory that predicted ozone to be a maximum at the equator and decreasing towards the pole.

An answer to this puzzle was put forward in 1949 by A. W. Brewer and G. M. B. Dobson (Brewer, 1949), when they suggested that there was a basic circulation through the stratosphere that moved ozone around and modified the concentrations that would be predicted by the purely photochemical Chapman theory. This circulation consisted of slow upward motion into the stratosphere in the tropics; a slow downward and poleward motion at middle latitudes, and return of air to the troposphere at middle and high latitudes.

Even when considering the so-called HO_x catalytic ozone loss cycle, which was proposed by Nicolet and Bates in 1950 to explain mesospheric ozone (Bates and Nicolet, 1950), chemical evidence was accumulated by the middle 1960s that the production-loss balance in the Chapman theory of photochemistry of ozone was quantitatively incorrect. This finding led P. Crutzen to propose the so-called NO_x catalytic ozone loss cycle (Crutzen, 1971). This was followed by a study of H. S. Johnston (Johnston, 1971), who quantitatively calculated the change in stratospheric ozone due to a fleet of super-sonic aircraft that eventually would emit large amounts of ozone destroying nitrogen monoxide (NO) into the lower stratosphere.

In 1974 Molina and Rowland proposed that man-made fluorochlorocarbons, even though long-lived in the atmosphere, would release reactive chlorine that could ultimately destroy stratospheric ozone (Molina and Rowland, 1974). The idea that the halogen chlorine may catalytically destroy stratospheric ozone was later complemented by the suggestion that two other halogens, i.e. bromine and iodine may also contribute to the global decline in stratospheric ozone (Wofsy et al. (1975) and Solomon et al. (1994)). An ultimate proof of the theory that halogens may cause a dramatic loss in stratospheric ozone became evident in 1985 when the ozone hole over Antarctica was discovered. After its possible causes were intensively investigated and unambiguous evidences on the role the halogens chlorine and bromine play in its formation were found (Farman et al., 1985), a phase-out of many man-made halogen bearing molecules was agreed to in the protocol of Montreal in 1989 and its various amendments (see http://ozone.unep.org/en/montreal_protocol.php).

Mostly due to various time-scales involved in decreasing the stratospheric burden of man-made halogens, in the 1990s global ozone was still declining and the ozone hole continued to widen. By the mid-2000s a turning point was reached leading to a reversal in the decline of global ozone, and a small but noticeable recovery of the ozone hole. In effect, for the present composition of the stratosphere both phenomenon are assessed to be caused 2/3 by chlorine and 1/3 by bromine mediated ozone loss, while a prominent role of iodine in stratospheric ozone destruction could be ruled-out, primarily due to its low concentration in the stratosphere (WMO, 2014).

Past research revealed that total stratospheric bromine (Br_y) was comprised of 4 major sources, or contributions: (1) CH_3Br emitted mostly by natural and anthropogenic sources with a contribution of presently 7 ppt to Br_y, (2) the 4 major halons ($CClBrF_2$, or halon-1211; $CBrF_3$, or halon-1301; CBr_2F_2, or halon-1202, and $CBrF_2CBrF_2$, or halon-2402) all emitted from anthropogenic sources with a contribution of presently 8 ppt to Br_y, (3) so-called very short-lived species (VSLS) and (4) inorganic bromine of the upper troposphere. Contributions (3) and (4) together are assessed to account for 5 (2-8) ppt of stratospheric bromine (WMO, 2014). The agreed emission phase-out of chlorine and bromine bearing molecules in the Montreal protocol and its amendments brought about an effect. Total stratospheric Br_y was assessed to be 20 (16–23) ppt in 2011, and had decreased at $\sim 0.6 \pm 0.1\%$ per year between peak levels observed in 2000–2001 and 2012. This decline was found to be consistent with the decrease in total tropospheric organic Br based on measurements of CH_3Br, and the halons (WMO, 2014).

Estimates of Br_y essentially rely on two methods: First, the so-called organic (Br_y^{org}) method, where all bromine from organic source gases (SG) found at stratospheric entry level is added (Wamsley et al. (1998), Pfeilsticker et al. (2000), Brinckmann et al. (2012), and others). Second total inorganic bromine (Br_y^{inorg}) which is inferred from atmospheric measurements (e.g., from the ground, high-flying balloons or satellites of the most abundant bromine species BrO, assisted by a suitable correction for the Br_y^{inorg} partitioning inferred from photochemical modelling) (e.g., Pfeilsticker et al. (2000), Richter et al. (2002), Van Roozendael et al. (2002), Sioris et al. (2005), Dorf et al. (2006), Hendrick et al. (2007), Dorf et al. (2008), Theys et al. (2009), Theys et al. (2011), Rozanov et al. (2011), Parrella et al. (2013), Stachnik et al. (2013), and others). While the organic method is rather precise for the measured species (accuracies are several 0.1 ppt), it suffers from the short-coming of not accounting for any inorganic bromine (contribution 4) directly entering the stratosphere. However, uncertainties in the inorganic method come from uncertainties in the measuring BrO as well as in the modelling Br_y^{inorg} partitioning. The combined error amounts to $\pm(2.5 - 4)$ ppt, depending on the type of observation and probed photochemical regime.

Further only few simultaneous measurements of Br_y^{org} and Br_y^{inorg} have yet been performed at stratospheric entry level, in particular in the critical region, i.e., the

tropics, where a tighter constraint of contributions 3 and 4 for Br_y could be expected. These few simultaneous measurements included the stratospheric balloon measurements performed over tropical Brazil (e.g., from Teresina) in 2005, and 2008 from Brinckmann et al. (2012), where a contribution of VSLS bromine to Br_y^{org} (contribution 3) of 1.25 ± 0.16 ppt, and 2.25 ± 0.24 ppt were found, and the study of Dorf et al. (2008), who inferred that contributions 3 and 4 to Br_y were 4.0 ± 2.5 ppt, and 2.5 ± 2.6 ppt, respectively. Salawitch et al. (2005) assessed the impact of VSLS bromine to the trend of global ozone. This additional Br_y (assumed constant over time) causes more ozone depletion because associated BrO provides a reaction partner for ClO, which increases due to anthropogenic sources.

Past in-situ measurements of Br_y^{org} within the tropical tropopause layer (TTL) over the Western Pacific, where most of the stratospheric air is predicted to originate (e.g., Fueglistaler et al. (2009), Aschmann et al. (2009), Hossaini et al. (2012b), Ashfold et al. (2012), and others), indicated typical VSLS concentrations of 2.7 ppt (range 1.4 - 4.6 ppt) at the level of zero radiative heating (LZRH) and 1.4 ppt (range 0.7 - 3.4 ppt) at the tropical tropopause ($\theta = 380$K) (e.g., Schauffler et al. (1998), Schauffler et al. (1999), Laube et al. (2008), Brinckmann et al. (2012), Tegtmeier et al. (2012), Wisher et al. (2014), and WMO (2014)). Even though all these VSLS measurements (contributions 3) agreed (within the error bars) with Br_y assessed from a larger suite of ground-based, balloon-borne and satellite studies (contributions 3 and 4) ranging between 3 - 8 ppt with a mean 6 ppt (e.g., Pfeilsticker et al. (2000), Richter et al. (2002), Van Roozendael et al. (2002), Sioris et al. (2005), Dorf et al. (2006), Hendrick et al. (2007), Dorf et al. (2008), Theys et al. (2009), Theys et al. (2011), Rozanov et al. (2011), Parrella et al. (2013), Stachnik et al. (2013), and others), they tend to be somehow lower, possibly indicating that some inorganic bromine (presumably 1 - 2 ppt, contribution 4) is also directly transported from the troposphere into stratosphere.

In a recent study, Hossaini et al. (2015) provided evidence for the efficiency of short-lived halogens (i.e., by contribution 3) to influence climate through depletion of stratospheric ozone. Without explicitly considering the contribution from inorganic bromine readily transported across the tropical tropopause (contribution 4), they concluded that natural short-lived bromine substances, when normalised by halogen content, exert a 3.6 times larger ozone radiative effect than long-lived halo-carbons.

The present PhD thesis addresses first measurements of BrO (and of NO_2, O_3, and of some source gases by collaborating research groups) made during the NASA ATTREX deployments of the NASA Global Hawk into the TTL and subtropical lowermost stratosphere of the Eastern and Western Pacific in 2013 and 2014. From collected NASA ATTREX data, novel and exciting information in the atmospheric composition, in particular of the bromine bearing source (contribution 1 2 and 3) and product gases (contribution 4) at stratospheric entry level, i.e. the TTL, and the extra tropical lowermost stratosphere can be inferred. The focus of the present PhD thesis is to assess and to test the amount and photochemistry of brominated

source gases, i.e. BrO, and Br_y^{inorg} (= Br + BrO + HBr + $BrONO_2$ + HOBr + BrCl) which is inferred from photochemical modelling.

Chapter 2 provides scientific background information on the relevant aspects of physics and chemistry of the TTL, including a basic overview of the photochemical processes of the different trace gases that were measured in the scope of this thesis. Chapter 3 presents the physical fundamentals of radiative transfer processes in the atmosphere and a derivation of the radiative transfer equation which needs to be resolved in our technique to measure trace gases. Chapter 4 introduces the NASA ATTREX project and gives an overview of the collected data. Chapter 5 describes the major features of the mini-DOAS instrument used during the NASA ATTREX mission to measure O_3, NO_2, BrO, O_4 and H_2O. Chapter 6 deals with methods used in the course of the data analysis: the DOAS method, radiative transfer modelling and chemical transport modelling. Chapter 7 discusses extensively the used inversion methods. Chapter 8 presents and discusses comprehensively the major results. Chapter 9 summarises the findings and gives an outlook on open scientific issues.

2 The Tropical Tropopause Layer (TTL)

The measurements and their consequences on which the present thesis reports are performed in the so-called *tropical tropopause layer* (TTL). The first section of this chapter gives a very short introduction of the vertical structure of the atmosphere, then second a definition of the TTL is given. The TTL acts as a gate to the stratosphere for ozone-depleting substances (ODS), like bromine (Fueglistaler et al. (2009)). Therefore the TTL has a unique meaning in terms of determining the amount of stratospheric ODS, which have a direct impact on stratospheric ozone and global climate. Despite its relevance it is one of the least understood regions in the atmosphere. In the last section of this chapter the major photochemical reactions regarding nitrogen, ozone and halogens are listed.

2.1 Vertical structure of the atmosphere

The section about atmospheric structure is only a very brief summary. A comprehensive overview can be found in various textbooks, e.g. Brasseur and Solomon (1986), Roedel (2000), Finlayson-Pitts and Pitts Jr. (2000).

The total mass of the atmosphere is $5.148 \cdot 10^{18}$ kg. Atmospheric pressure is a direct result of the weight of the air. Under standard conditions (e.g. the *U.S. Standard Atmosphere*) with a temperature at sea level of 288.15 K, the pressure is p_0=1013 hPa := 1 atm. Subsequently the air number density at sea level is $2.5 \cdot 10^{19}$ cm^{-3}. The barometric height formula describes the pressure as a function of altitude:

$$p(z) = p_0 \exp(-\frac{z}{z_0}) \tag{2.1}$$

with the scale height

$$z_0 = \frac{k \cdot T}{m \cdot g} \tag{2.2}$$

To give a rough estimate of the pressure gradient in the atmosphere, the scale height $z_0 \approx 8$ km is a good choice.

The atmosphere can be divided in different layers by several characteristics. Most common is to separate the layers by the behaviour of the temperature gradient. The altitude regions where the temperature gradient changes its sign are called pauses

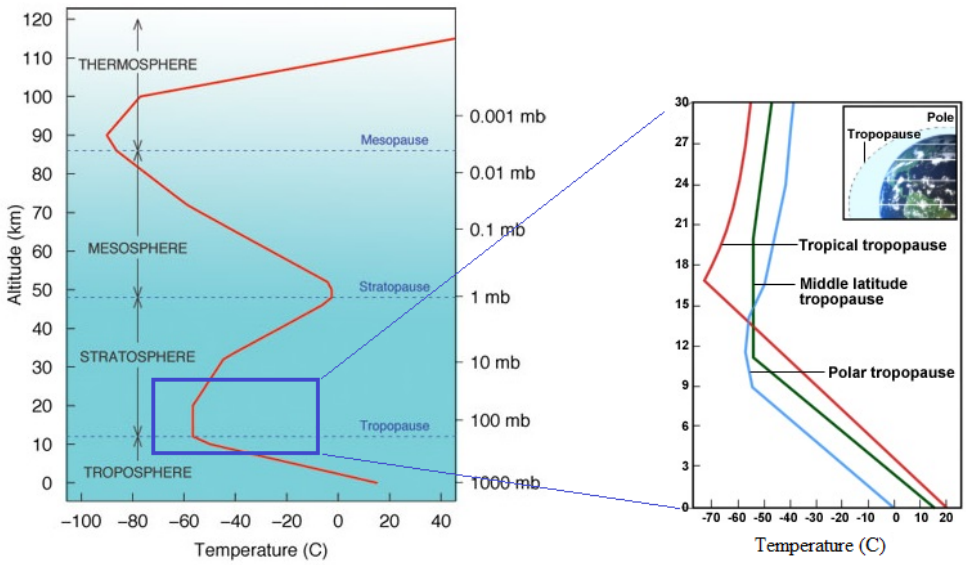

Figure 2.1: Vertical structure of the atmosphere and temperature profile according to the U.S. Standard Atmosphere. (Left panel adapted from Steven C. Wofsy, 2006, Abbott Lawrence Rotch Professor of Atmospheric and Environmental Science, lecture notes. Right panel adapted from COMET® Website at http://meted.ucar.edu/.)

while the layers in between are called spheres (see Figure 2.1). The right panel shows that the tropopause height changes strongly with latitude.

2.2 Definition and dynamics of the TTL

In contrast to mid- and higher latitudes where the transition from troposphere to stratosphere (related to e.g. temperature gradient, ozone, etc...) is represented by a rather sharp defined tropopause, in the tropical region this transition occurs in an extended vertical layer. Therefore it is commonly called tropical tropopause layer. This layer of several kilometres vertical extent shows both tropospheric and stratospheric characteristics.

The upper and lower bound is commonly defined by terms of the potential temperature. Fueglistaler et al. (2009) suggests a vertical boundary of the TTL with a bottom of 150 hPa, 355 K, 14 km (pressure, potential temperature, and altitude) and a top of 70 hPa, 425 K, 18.5 km. Depending on the cloud cover, the LZRH often lies at slightly larger altitudes than this lower bound (Fueglistaler et al., 2009). Gettelman and Forster (2002) defines the lower bound of the TTL as the LZRH for clear sky conditions which often corresponds to a minimum in ozone, and the upper bound by the cold point tropopause (CPT) at ∼17 km.

Transport of air masses in the atmosphere is generally constrained by conservation of energy and of angular momentum (quantified by the potential vorticity PV). Regarding the conservation of energy one has to distinguish between adiabatic and diabatic transport. Adiabatic transport of air parcels happens without energy exchange with the environment. From the Poisson equation for adiabatic processes one obtains the definition of the potential temperature Θ:

$$\frac{T^{\kappa}}{p^{\kappa-1}} = const. \tag{2.3}$$

$$\Rightarrow \Theta = T \cdot \left(\frac{p_0}{p}\right)^{\frac{\kappa-1}{\kappa}} \tag{2.4}$$

with p_0 being surface pressure, $\frac{\kappa-1}{\kappa} \approx 0.286$ (for air). The potential temperature is the temperature that the parcel would acquire if adiabatically brought to a reference pressure p_0. Diabatic transport allows exchange of energy by radiation, both heating or cooling of the air parcel. Air parcels can move along (adiabatic) and perpendicular (diabatic) to isentropes of potential temperature. Meridional horizontal transport is mainly limited by PV conservation.

Figure 2.2 shows a schematic of the tropical upper troposphere, lower stratosphere and the TTL (Fueglistaler et al., 2009). The left panels shows convection and cloud processes, the right panel illustrates the zonal mean circulation and the net radiation budgets. Arrows indicate circulation, black dashed line is clear sky LZRH, black solid lines show isentropes (in Kelvin; based on ERA-40[1]). Tropical deep convection (circle (a)-(g)-(b)) reaches altitudes of 10-15 km, with the main outflow at around 200 hPa. Outflow rapidly decays with height in TTL, and there are rare penetrations of the tropopause and direct injection of air into the lowermost stratosphere. Tropical deep convenction allows fast vertical transport of tracers from boundary layer into the TTL. In some cases convection reaches higher and may even penetrate the stratosphere by overshooting its level of neutral buoyancy (h). Convective transport of air parcels is dominated by adiabatic processes.

In the upper TTL radiation processes become relatively more important and thus the transport processes are mainly diabatic. Air masses not reaching the level of zero heating (LZRH) are radiatively cooled and consecutively subside (b). Above the LZRH air is net heated (Figure 2.2 (d)) and ascends further via diabatic heating. Air that enters the stratosphere undergoes a freeze-drying process near the CPT (Brewer (1949)) and therefore the CPT temperature is a key feature in determining the stratospheric water content. (Holton et al. (1995)).

Large gradients in potential vorticity associated with the subtropical jets (Figure 2.2 (c), 2.3 black contour lines) limit meridional transport in the lower part of the TTL, while in the upper part of the TTL transport to higher latitudes and mixing

[1] http://www.ecmwf.int/en/forecasts/datasets/era-40-dataset-sep-1957-aug-2002

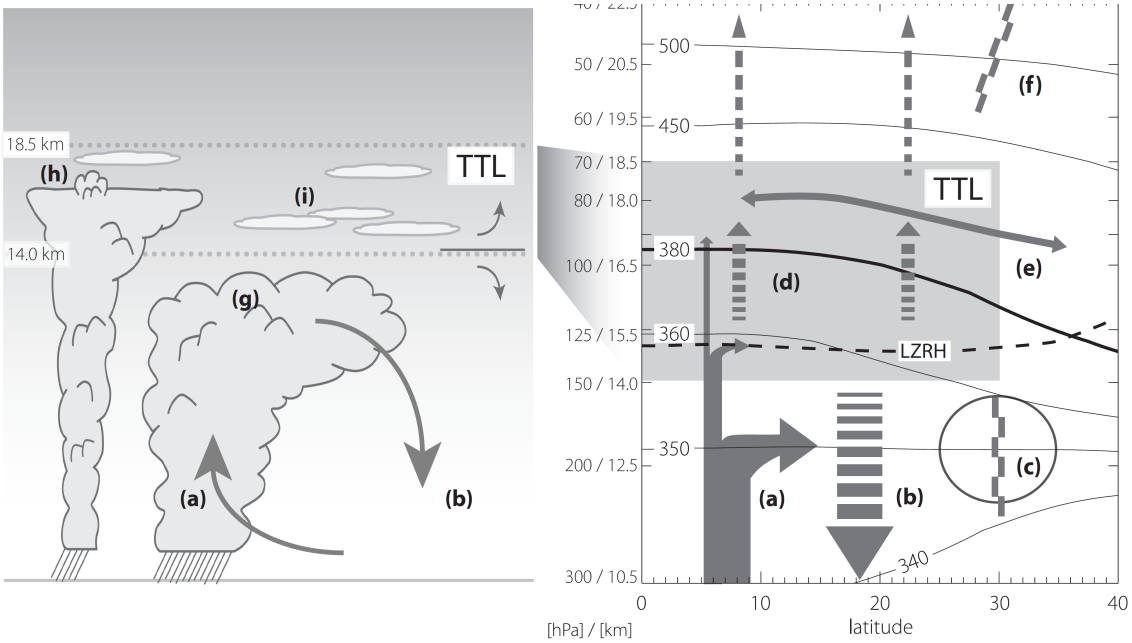

Figure 2.2: Schematic of cloud processes and transport (left) and of zonal mean circulation (right). Adopted from Fueglistaler et al. (2009)

of air into the tropics from higher latitudes (Volk et al. (1996), Minschwaner et al. (1996)) is observed (Figure 2.2 (e)).

In the upper TTL and LS, air is transported to the mid-latitudes in a quasi-horizontal two-way meridional exchange above the subtropical jets in both hemispheres (Randel and Jensen, 2013) This is the lower branch of the so-called Brewer Dobson circulation (BDC). The details of the two-way transport at higher altitudes can be found in e.g. Bönisch et al. (2011), and will not be further discussed here.

The constraints on vertical and horizontal transport lead to basically three different regimes of air masses in the subtropical region (Figure 2.3). These were partially probed during during the 2013 NASA-ATTREX deployment (details in chapter 4). The 2013 NASA-ATTREX measurements (details in chapter 4) probed air masses in the region between -10°S to 35°N, and up to 18.5 km altitude (red box in Figure 2.3):

(I) Air from the extratropical upper troposphere / lower stratosphere (Ex-UTLS)

(II) Mixed air of the Ex-UTLS and the TTL

(III) Pure TTL air

The labelling I, II, III for the different regimes is kept throughout this thesis. Depending on whether type I or III is dominant in the mixed layer regime it is further

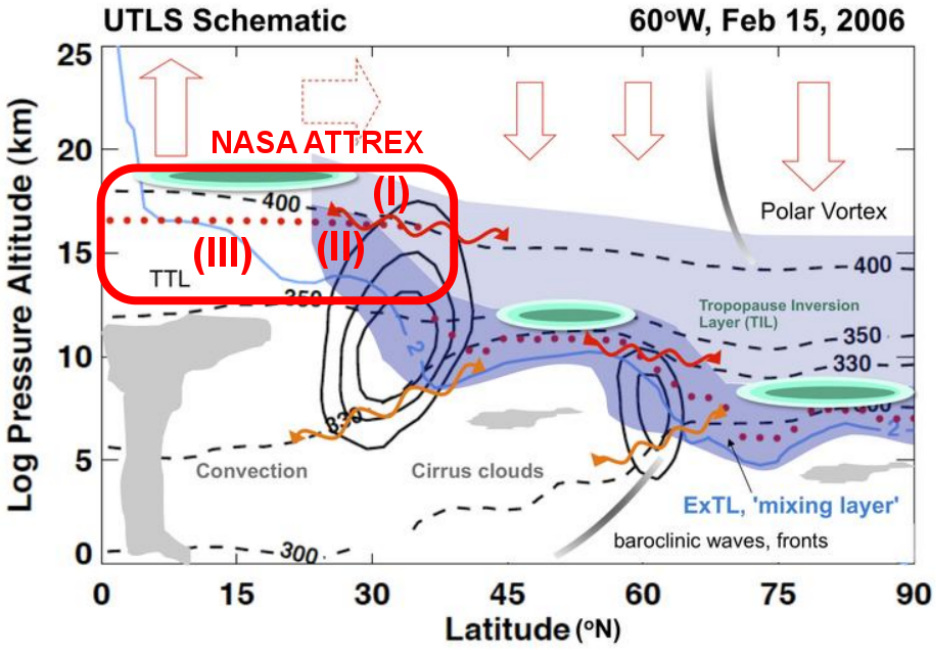

Figure 2.3: Illustrated schematically are the Ex-UTLS (dark and light blue shading), extratropical transition layer (ExTL) and TTL. Important marks: Wind contours (solid black lines 10 m/s interval), potential temperature surfaces (dashed black lines), thermal tropopause (red dots), potential vorticity surface (2 PVU: light blue solid line). Adopted from Gettelman et al. (2011).

on labelled as IIa or IIb. Besides other proxys, the different regimes can be identified by their CH_4 content (indicating age of air with respect to the last surface contact).

2.3 Stratospheric photochemistry

The chemistry in the TTL and stratosphere is not only influenced by dynamics and transport processes, it is also mainly driven by solar radiation, which is called photochemistry. As mentioned in the introduction, this thesis focusses on the measurements and interpretation of the trace gases ozone (O_3), bromine monoxide (BrO), nitrogen dioxide (NO_2) within the tropical UT, TTL and extratropical lowermost stratosphere. The following section provides an overview of the chemical processes of these species with a focus on the TTL and stratosphere.

2.3.1 Ozone

Ozone is one of the central trace gases in the Earth's atmosphere. Due to its absorption in the UV-A (315-400 nm) and UV-B (280-315 nm) wavelength range it protects life on Earth from a major part of dangerous short-wave radiation. But it also plays an important role in the troposphere, where it influences the oxidative capacity of the troposphere.

Reaction cycles involving oxygen, hydrogen, nitrogen and halogen containing species govern the formation and destruction of stratospheric ozone. In 1930 Sidney Chapman (Chapman, 1930) published the first simple theory on stratospheric ozone, involving only oxygen species. Molecular oxygen (O_2) is photolysed by ultraviolet radiation with wavelengths below 242 nm. The oxygen atoms react with molecular oxygen to ozone via a three-body reaction:

$$O_2 + h\nu \longrightarrow 2\,O \tag{2.5}$$
$$O + O_2 + M \longrightarrow O_3 + M \tag{2.6}$$

Ozone loss happens through photolysis by UV radiation with wavelength below 310 nm followed by the reaction with another oxygen atom or ozone:

$$O_3 + h\nu \longrightarrow O_2 + O(^3P) \tag{2.7}$$
$$O_3 + h\nu \longrightarrow O_2 + O(^1D) \tag{2.8}$$
$$O(^1D) + M \longrightarrow O(^3P) + M \tag{2.9}$$
$$O + O + M \longrightarrow O_2 + M \tag{2.10}$$
$$O(^3P) + O_3 \longrightarrow 2\,O_2. \tag{2.11}$$

Due to the strong attenuation of solar UV radiation, photolysis of molecular oxygen and thus O_3 production occurs mainly in the upper stratosphere. Together with photo-dissociation of O_3 (reaction 2.7 and 2.8) an equilibrium between O_3 and O builds up. Within this equilibrium, forward and backward reactions of atomic oxygen to O_3 happens in the order of seconds (2.5 and 2.6). The rapid transformation of one species to the other allows the definition of families, where the lifetime of the

whole family is rather long. The O_x family is defined as the sum of odd-oxygen like O_3, $O(^3P)$ and $O(^1D)$.

Total ozone loss is further increased via catalytic cycles:

$$\begin{aligned} X + O_3 &\longrightarrow XO + O_2 && (2.12)\\ O + XO &\longrightarrow X + O_2 && (2.13)\\ \text{net}: O + O_3 &\longrightarrow 2\,O_2\,. && (2.14) \end{aligned}$$

where odd-oxygen is transformed into its reservoir XO by a catalyst X, which can be substituted by the radicals OH (Bates and Nicolet, 1950), NO (Crutzen, 1970; Johnston, 1971), Cl (Molina and Rowland, 1974), Br (Wofsy et al., 1975) and possibly I (Solomon et al., 1994). These catalytic cycles are much more efficient than the O_x cycle. A single Cl or Br atom can destroy hundreds of ozone molecules before it reacts into an ozone inert reservoir gas, breaking the catalytic cycle. It can destroy up to a tens of thousands of ozone molecules during the total time of its stay in the stratosphere (WMO (2011)). Reactions with Br are discussed in detail in 2.3.3.

There are additional cycles involving the $HO_x = H + OH + HO_2$ catalyst, e.g. the following, where O_3 is destroyed without involving atomic oxygen:

$$\begin{aligned} OH + O_3 &\longrightarrow HO_2 + O_2 && (2.15)\\ HO_2 + O_3 &\longrightarrow OH + 2\,O_2 && (2.16)\\ \text{net}: 2\,O_3 &\longrightarrow 3\,O_2\,. && (2.17) \end{aligned}$$

The combination of different families of catalysts leads to further catalytic cycles of O_3 destruction:

$$\begin{aligned} X + O_3 &\longrightarrow XO + O_2 && (2.18)\\ Y + O_3 &\longrightarrow YO + O_2 && (2.19)\\ XO + YO &\longrightarrow X + Y + O_2 && (2.20)\\ \text{net}: 2\,O_3 &\longrightarrow 3\,O_2\,, && (2.21) \end{aligned}$$

where possible candidates are: X = OH and Y = Cl, X = OH and Y = Br, X = Br and Y = Cl. The efficiency of the different cycles depend on the reaction speed and the number of cycle the catalyst can undergo before it is lost in a chain termination reaction. From 12 to 25 km altitude the HO_x and BrO_x ($= Br + BrO$) catalytic cycles are most important, while between 25 km and 40 km the O_3 destruction is dominated by NO_x. The relative importance also depends on tropospheric loading of inorganic bromine, BrO_y^{inorg} (Figure 2.4). Since O_3 loss due to the coupled ClO-BrO cycle is completely assigned to BrO_x, the importance of BrO_x compared to ClO_x ($= Cl + ClO + 2\,Cl_2O_2$) in the lower stratosphere is somewhat disproportionate. In this calculation IO_x ($= I + IO$) is only of minor importance.

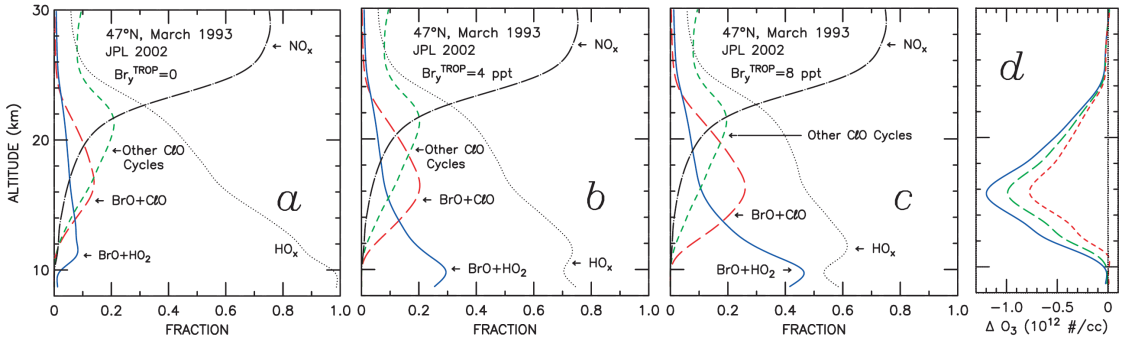

Figure 2.4: Fraction of odd oxygen loss by various catalytic cycles within the AER model at 47°N, March 1993, for model runs with tropospheric BrO_y^{inorg} (here called Br_y^{TROP}) of 0, 4, and 8 ppt (panels a-c, as indicated). Panel d. Difference between the ozone profile at 47°N, March 1993 and the profile at 47°N, March 1980 for runs with BrO_y^{inorg} of 0, 4, and 8 ppt. Adopted from Salawitch et al. (2005).

2.3.2 The nitrogen cycle

The dominant source of the $NO_x (= NO + NO_2)$ catalyst is the greenhouse gas N_2O. The importance of N_2O for the future evolution of ozone will increase as halo-carbons return more and more towards pre-industrial levels (Portmann et al., 2012). N_2O is produced at the surface and is relatively inert in the troposphere. It is transported to the stratosphere where it is broken down via photolysis:

$$N_2O + h\nu \longrightarrow N_2 + O(^1D) \tag{2.22}$$
$$N_2O + O(^1D) \longrightarrow 2\,NO \tag{2.23}$$
$$\longrightarrow N_2 + O_2\,. \tag{2.24}$$

The global lifetime of N_2O is approximately 114 years (WMO (2014) and Ko et al. (2013)). Removal of reactive nitrogen occurs in the middle and upper stratosphere effectively through the reaction

$$NO + N \longrightarrow N_2 + O. \tag{2.25}$$
$$\tag{2.26}$$

Due to the lack of nitrogen atoms this reaction is negligible in the lower stratosphere. According to reactions 2.13 to 2.12 odd oxygen loss via the NO_x catalytic cycle goes along with interconversion of NO and NO_2

$$NO + O_3 \longrightarrow NO_2 + O_2 \tag{2.27}$$
$$NO_2 + O \longrightarrow NO + O_2 \tag{2.28}$$
$$\tag{2.29}$$

Below ∼30 km odd oxygen is reproduced again via photolysis ($\lambda \leq$405 nm) of NO_2 which balances the O_x loss caused by reactions 2.27 and 2.28.

$$NO_2 + h\nu \longrightarrow NO + O \tag{2.30}$$

Conversion of NO to NO_2 can also be driven by BrO, ClO and other oxidants instead of O_3. Subsequent photolysis of NO_2 even represent net formation, processes of odd oxygen:

$$NO + ClO \longrightarrow NO_2 + Cl \tag{2.31}$$
$$NO + BrO \longrightarrow NO_2 + BrO \tag{2.32}$$
$$\tag{2.33}$$

With absence of sunlight photolysis of NO_2 fades out and NO is rapidly converted to NO_2 which forms NO_3 through reaction with O_3

$$NO_2 + O_3 \longrightarrow NO_3 + O_2. \tag{2.34}$$

During daytime NO_3 concentration are negligible since it is instantaneously broken down by photolysis yielding NO_2 or NO. However, during the night, NO_3 reacts with NO_2 and forms the reservoir species N_2O_5:

$$NO_2 + NO_3 + M \longrightarrow N_2O_5 + M \tag{2.35}$$

During the day N_2O_5 is photolysed again at moderate rate:

$$N_2O_5 + h\nu \longrightarrow +NO_2 + NO_3 \tag{2.36}$$

Of special interest for the present study are the additional nitrogen reservoirs $ClONO_2$ and $BrONO_2$ which act as the same time as reservoirs for ClO_x and BrO_x radicals:

$$NO_2 + ClO + M \longrightarrow ClONO_2 + M \tag{2.37}$$
$$NO_2 + BrO + M \longrightarrow BrONO_2 + M. \tag{2.38}$$

Release of the catalysts BrO and ClO from their reservoirs can occur again through photolysis:

$$ClONO_2 + h\nu \longrightarrow ClO + NO_2 \tag{2.39}$$
$$BrONO_2 + h\nu \longrightarrow BrO + NO_2 \tag{2.40}$$

The photolysis rate coefficient of reaction 2.40 is listed with a 1σ-uncertainty of 1.465 at 220 K (Sander et al., 2011). The efficiency of the $BrONO_2$ photolysis has a major impact on the Br_y^{inorg} partitioning in the Ex-UTLS. Section 8.3 presents a sensitivity study on the photochemical equilibrium of the reactions 2.38 and 2.40. In this context most notably is that this study supports the findings of a larger J_{BrONO_2}/k ratio as in (Sander et al., 2011). This is in agreement with Kreycy (2012).

2.3.3 The bromine cycle

This section contains a short compilation of chemical reactions regarding ozone-related bromine photochemistry.

BrO_x constituents undergo rapid interconversion according the catalytic cycle in equations 2.12-2.14

$$\begin{aligned} Br + O_3 &\longrightarrow BrO + O_2 && (2.41)\\ BrO + O &\longrightarrow Br + O_2 && (2.42) \end{aligned}$$

and

$$\begin{aligned} BrO + h\nu &\longrightarrow Br + O && (2.43)\\ BrO + NO &\longrightarrow Br + NO_2 && (2.44)\\ BrO + ClO &\longrightarrow Br + OClO \quad 60\% && (2.45)\\ &\longrightarrow Br + ClO_2 \quad 32\% && (2.46)\\ &\longrightarrow BrCl + O_2 \quad 8\%\,. && (2.47) \end{aligned}$$

The reaction rate of equation 2.41 is very important for the inorganic Br_y partitioning within in the TTL where Br atoms and BrO have the lion's share of Br_y^{inorg}. Section 8.3 presents a sensitivity study on the rate coefficient within the uncertainty range as in Sander et al. (2011). The branching ratios of equations 1 are given for T=200 K according to Sander et al. (2011).

BrO_x radicals are scavenged by NO_2 (equation 2.38), H_2O and CH_2O forming the main reservoir species:

$$\begin{aligned} BrO + HO_2 &\longrightarrow HOBr + O_2 && (2.48)\\ Br + HO_2 &\longrightarrow HBr + O_2 && (2.49)\\ Br + CH_2O &\longrightarrow HBr + CHO\,. && (2.50) \end{aligned}$$

Release of BrO_x occurs through photolysis of $BrONO_2$ (equation 2.40) or in the case of HBr through reaction with OH:

$$\begin{aligned} BrONO_2 + h\nu &\longrightarrow Br + NO_3 && (2.51)\\ &\longrightarrow BrO + NO_2 && (2.52)\\ HOBr + h\nu &\longrightarrow OH + Br && (2.53)\\ HBr + OH &\longrightarrow Br + H_2O\,. && (2.54) \end{aligned}$$

The importance of some of those reactions and the uncertainties of their rate coefficients are discussed in chapter 8.

2.3.4 Heterogeneous chemistry

Besides gas-phase reactions discussed in the preceding sections, heterogeneous reactions on the surface of particles play an important role in stratospheric chemistry (e.g. Douglass and Stolarski (1989), Brasseur et al. (1990), Hanson et al. (1994),...). Mostly all stratospheric aerosols consist of H_2SO_4, other solutes (e.g. meteoric dust), and H_2O, either in the liquid or in the solid phase. The halogen reservoir gases HCl or HBr may be dissolved in liquid droplets or adsorbed on aerosol surfaces. Heterogeneous reactions typically require much lower activation energy and proceed much faster than gas phase reactions between the same species, which makes them very efficient. The following heterogeneous reactions involving bromine species convert reservoirs to more reactive species,

$$\mathrm{BrONO_2(g) + HCl(s) \longrightarrow BrCl(s) + HNO_3(s)} \tag{2.55}$$

$$\mathrm{BrONO_2(g) + H_2O(s) \longrightarrow HOBr(g) + HNO_3(s)} \tag{2.56}$$

$$\mathrm{HOBr(g) + HCl(s) \longrightarrow BrCl(g) + H_2O(s)} \tag{2.57}$$

where (g) and (s) indicate gas phase and condensed phase, respectively. These reactions convert relatively long-lived inorganic halogen species from the gas phase and condensed phase to shorter-lived halogen species in the gas phase, while the NO_x, or HO_x components stay in the condensed phase. Since the halogen containing products are less stable with respect to photo-dissociation than the educts, the above reactions are often referred to as bromine activation. Another important heterogeneous reaction converts the nighttime NO_x reservoir N_2O_5 from the gas phase to nitric acid in the solid phase:

$$\mathrm{N_2O_5(g) + H_2O(s) \longrightarrow 2HNO_3(s)} \tag{2.58}$$

The relative importance of the heterogeneous reactions depends on temperature, composition and phase of the aerosol. Figure 2.5 illustrates the reaction probability of some heterogeneous reactions on stratospheric sulfate aerosol. Hydrolysis of N_2O_5 and $BrONO_2$ are the most important reactions under typical conditions in the stratosphere. By that reaction inorganic bromine can be washed out and therefore the total bromine budget can be decreased when making its way through the TTL and lower stratosphere. This provides a possible reason for the findings in chapter 8. For further studies see also Aschmann et al. (2009), Aschmann et al. (2011), and Aschmann and Sinnhuber (2013))).

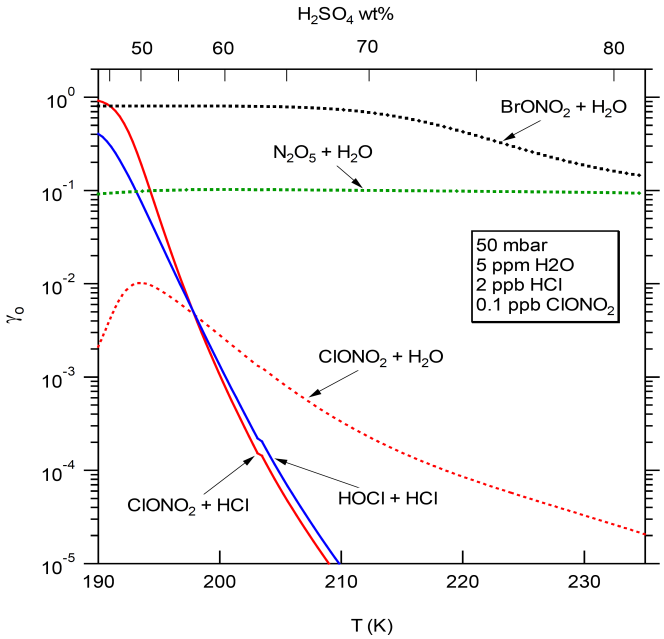

Figure 2.5: Recommended reactive uptake coefficients as a function of temperature for key stratospheric heterogeneous processes on sulfuric acid aerosols. The uptake coefficient γ_0 can be regarded as a measure of the reaction probability. For $ClONO_2$ and HOCl species, the aerosol radius used in the calculation is 10–5 cm, a typical value in the stratosphere. Because the current uptake models for N_2O_5 and $BrONO_2$ hydrolysis do not provide the information about the reacto-diffusive length l, the aerosol radius used in the calculation is assumed to be much larger than their reacto-diffusive length (i.e. l for N_2O_5 and $BrONO_2$ are set to zero.). Adopted from Sander et al. (2011).

2.4 Stratospheric bromine budget

Halogen species play an important role in stratospheric ozone destruction (equation 2.18 and following). Due to their strong bonding, fluorine species are photochemically very stable and are therefore negligible for stratospheric ozone depletion. Though less abundant than chlorine in the stratosphere bromine plays a major role in ozone depletion due to the 64 times higher chemical efficiency on an annual average (Sinnhuber et al., 2009). The contribution of iodine species is still not fully clear. Upper limits of IO and OIO and the implications for total gaseous iodine and stratospheric ozone have been inferred by Bösch et al. (2003). Recent measurements of Volkamer et al. (2015) report concentrations of IO of 0.2-0.55 ppt in the MBL but decreasing to less than 0.1 ppt in the free troposphere.

The main focus of this thesis is to assess the total amount of bromine entering the stratosphere through the TTL gateway. Bromine reaching the TTL (Figure 2.7)

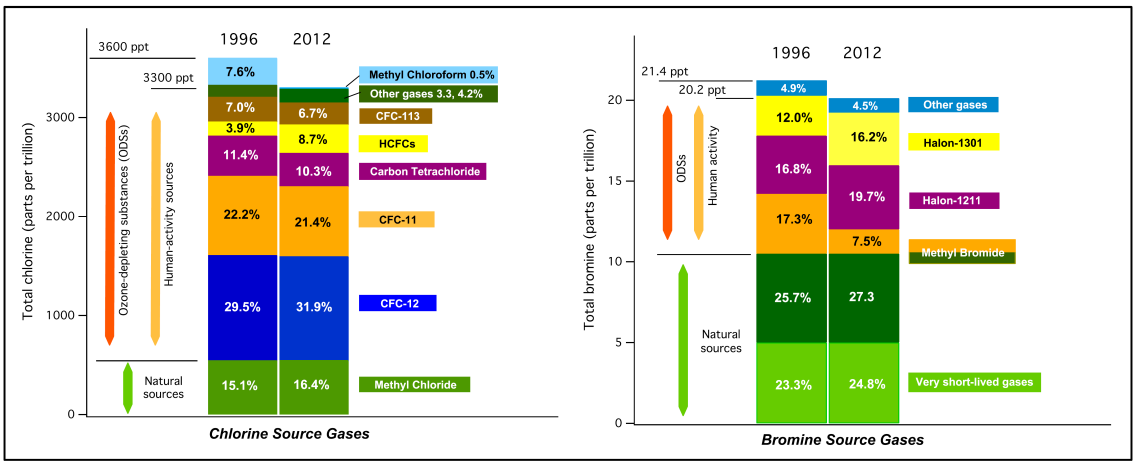

Figure 2.6: Relative contribution of source gases for chlorine and bromine in 1996 and 2012. Natural and anthropogenic sources are distinguished. The amounts are derived from tropospheric observations. The sum of very-short species CH_2Cl_2,$CHCl_3$,C_2Cl_4,$COCL_2$ is shown as "other gases" for chlorine, while halon-1202 and halon-2402 are included as "other gases" for bromine. Adopted from WMO (2014).

has potentially four major contributions (Figure 2.6, right panel):

1. Methyl bromide: CH_3Br
2. Four major halons: H-1202, H-1211, H-1301, H-2404
3. Very short lived species (VSLS): CH_2BrCl, CH_2Br_2, $CHBrCL_2$, $CHBr_2Cl$ and $CHBr_3$
4. Direct injection of inorganic bromine Br_y^{inorg}: Br, BrO, HBr, HOBr and $BrONO_2$

CH_3Br mole fractions continued to decline during 2008–2012, and by 2012 had decreased to 7.0 ± 0.1 ppt, a reduction of 2.2 ppt from peak levels measured during 1996–1998. This atmospheric decline is primarily driven by continued decrease in total reported consumption of CH_3Br from fumigation. As of 2009, reported consumption for quarantine and pre-shipment (QPS) uses, which are exempted uses (not controlled) under the Montreal Protocol, surpassed consumption for controlled uses. As a result of the decrease in atmospheric CH_3Br, the natural oceanic source is now comparable to the oceanic sink (WMO, 2014).

Halon-1211 ($CBrClF_2$), halon-2402 ($CBrF_2CBrF_2$), and halon-1202 (CBr_2F_2) mole fractions continued to decline from peak values observed in the early and mid-2000s. Recent trends in halon-1211, halon-1301, and halon-2402 agree with those anticipated in the A1-2010 scenario (Velders et al., 2009). The A1-2010 scenario is later on used in the initialisation of the chemical transport model SLIMCAT (Section

8.2). Since 2008 there is a significant decrease of total bromine originating from halons with an average rate of decline of -0.06 ppt/yr between 2008 and 2012 WMO (2014).

Halogens from long-lived anthropogenic substances are the principal cause of recent ozone depletion. As many of those species are controlled by the Montreal Protocol and its amendments and their emissions are phased out, halogenated very-short lived species with life-times generally below six months gain more and more importance for stratospheric ozone depletion (e.g. Laube et al. (2008)). Short-lived

Table 2.1: Lifetime and marine boundary layer abundances of brominated VSLS. The lifetime is given for the free troposphere (WMO, 2014).

Substance	**Lifetime (days)**	**WMO (2011)**		**WMO (2014)**	
		Mean (ppt)	Range (ppt)	Mean (ppt)	Range (ppt)
CH_2BrCl	137	0.5	0.4-0.6	0.1	0.07-0.12
CH_2Br_2	123	1.1	0.7-1.5	0.9	0.6-1.7
$CHBrCl_2$	78	0.3	0.1-0.9	0.3	0.1-0.9
$CHBr_2Cl$	59	0.3	0.1-0.8	0.3	0.1-0.8
$CHBr_3$	24	1.6	0.5-2.4	1.2	0.4-4.0

bromine substances (Table 2.1) are mainly produced naturally by seaweed and phytoplankton (Law and Sturges, 2007). In recent research many attempts are made to better quantify the impact of VSLS to ozone and the therefore changing radiation balance in the stratosphere. Hossaini et al. (2015) concludes that potential further significant increase in the atmospheric abundance of short-lived halogen species, through changing natural processes (Dessens et al. (2009), Hossaini et al. (2012a), Hepach et al. (2014)) or continued anthropogenic emissions (Leedham et al., 2013), could be important for future climate. An exact quantification of brominated VSLS is difficult due to the relatively short local lifetimes, combined with spatially and temporally varying sources (e.g. Carpenter et al. (1999)). This implies a complication when determining global budgets for these gases because extensive global-scale observations are required. For example, Ashfold et al. (2014) found that around two thirds of the measured $CHBr_3$ concentration at a site in Borneo may be due to emissions in a region covering less than 1% of the tropics.

The lifetimes of CH_3Br and the halons are sufficiently long that spatial gradients in the troposphere are small. Rapid convective transport within the tropics also support a fraction of the short-lived source gases (SG) to escape oxidation in the troposphere and to detrain into the TTL or LMS (Figure 2.7). In the course of the ascent a part of the VSL SG is photolysed and converted to their inorganic product gases (PG). A part of the brominated PGs is washed during the ascent. The other part, presumably 1-2 ppt (contribution 4), enters directly the TTL.

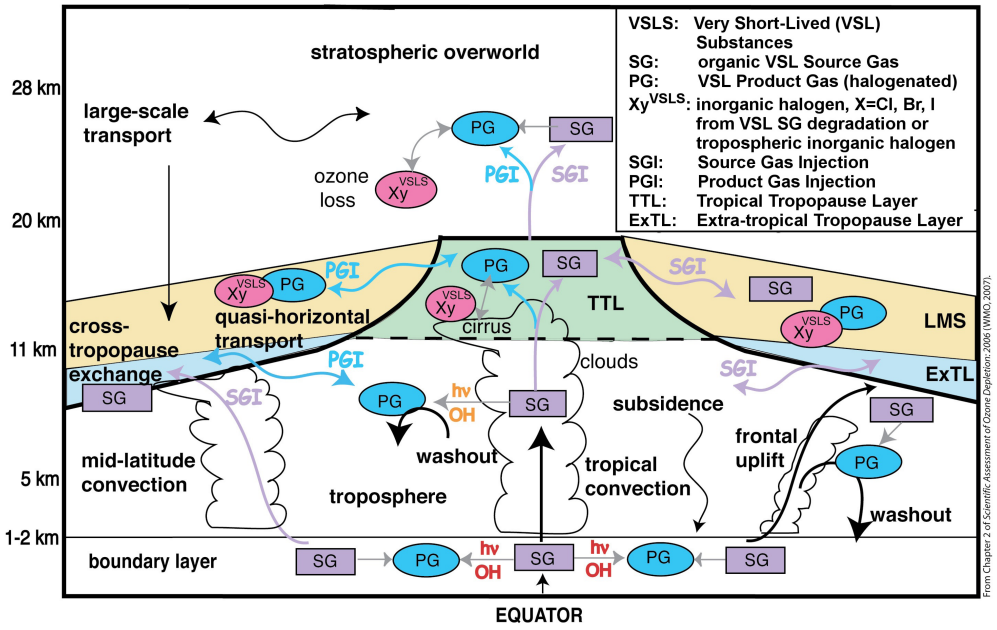

Figure 2.7: Schematic drawing of principal chemical and dynamical pathways transporting VSL source gases (SG) and organic/inorganic product gases (PG). Stratospheric halogen loading is maintained by transport of source gases followed by their degradation in the stratosphere (the SGI pathway), and transport of intermediate products and inorganic halogens produced in the troposphere (the PGI pathway). Tropospheric inorganic halogens can derive from degradation of VSL SGs, or from inorganic halogen sources. This figure is an update to Figure 2-2 in WMO (2003); courtesy of K.S. Law (Service d'Aéronomie/CNRS, France) and P.H. Haynes and R.A. Cox (University of Cambridge, U.K.)

For long lived and thus well-mixed halogenated source gases, the details of their troposphere-to-stratosphere transport are of minor importance. However, for very short-lived substances (VSLS), whose lifetimes may be comparable to tropospheric transport timescales, transport processes — along with physical and chemical processes that occur in the TTL — may strongly impact their stratospheric source gas (SGI) and product gas injections (PGI).

To date the best estimates of VSLS bromine are direct observations of SGs around the tropical tropopause (e.g. Sala et al. (2014b)), two BrO profile measurements in the TTL (Dorf et al., 2008), satellite measurements of BrO (e.g. Sinnhuber et al. (2005), Sihler et al. (2012)), and an estimated PGI contribution from recent global modelling. A range is derived by summing the lower limits of SGI and PGI estimates as well as the upper limits (Table 1-9). This leads to a total estimated range of 2–8 ppt Br_y^{VSLS} VSLS (WMO, 2014).

For 2011 air, total stratospheric Br_y was assessed to be 20 (16–23) ppt, and previ-

ous observations indicated a decrease of ∼0.6 ± 0.1% per year between peak levels observed in 2000–2001 (Figure 2.8) and 2012. This observed decline is consistent with the decrease in total tropospheric organic bromine based on measurements of CH_3Br and the halons.

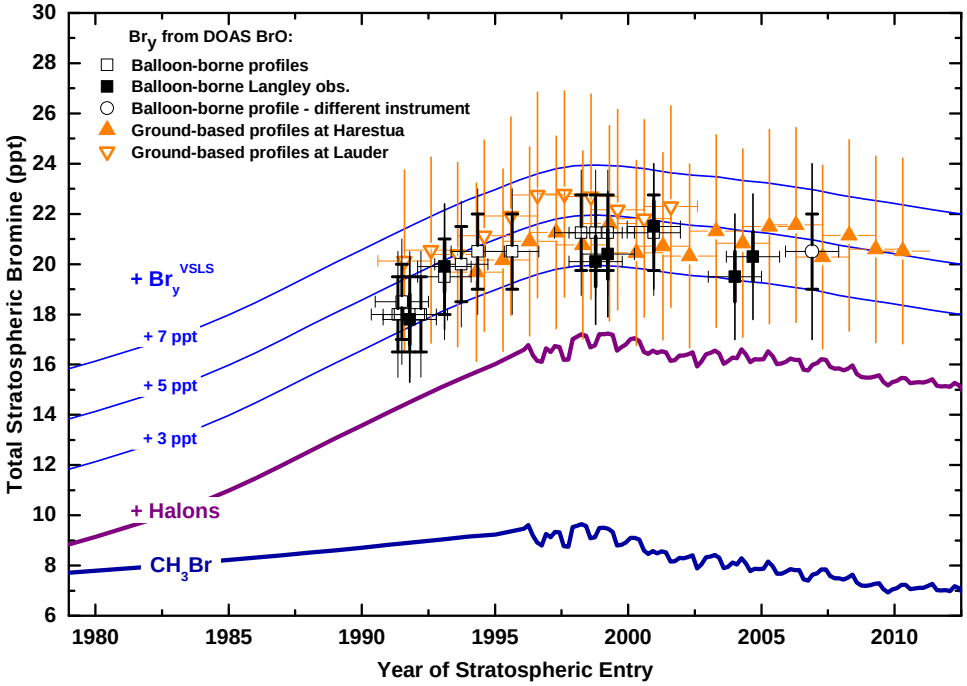

Figure 2.8: Changes in total stratospheric Br_y (ppt) derived from balloon-borne BrO observations (squares) (update of Dorf et al. (2006)) and annual mean mixing ratios calculated from ground-based UV/vis measurements of stratospheric BrO made at Harestua (60°N) and Lauder (45°S) (filled and open orange triangles, respectively). Stratospheric trends are compared to trends in measured surface bromine (ppt) with additional constant amounts of Br_y added (thin lines). Dark blue line shows global tropospheric bromine from CH_3Br as measured in firn air (pre-1995, including consideration of a changing interhemispheric gradient; Butler et al. (1999)) and ambient air (after 1995, Montzka et al. (2003)) with no correction for tropospheric CH_3Br loss. Purple line shows the sum of methyl bromide plus halons (Butler et al., 1999)) and Fraser et al. (1999) through 1995; Montzka et al. (2003) thereafter). Thin blue lines show bromine from CH_3Br, halons, plus additional constant amounts of 3, 5, and 7 ppt Br. Total inorganic bromine is derived from (i) stratospheric measurements of BrO and photochemical modeling that accounts for BrO/Bry partitioning from slopes of Langley BrO observations above balloon float altitude (filled squares); and (ii) lowermost stratospheric BrO measurements (open squares and circles). Adopted from WMO (2014).

3 Radiative transfer in the atmosphere

This chapter focuses on radiative transfer (RT) processes in the atmosphere. Section 3.1 starts with some basics about solar radiation. Section 3.2.2 and 3.2.1 deals with the interaction, scattering and absorption, of the incoming solar radiation with molecules and particles. Section 3.3 introduces the radiative transfer equation (RTE) which describes mathematically the transfer of energy as photons propagate through a medium, considering all interaction processes.

3.1 Solar radiation

The extraterrestrial solar irradiance is nearly that of a black body with a temperature of 5800K. Figure 3.1 shows the solar irradiance (for definition see next paragraph) $F_0(\lambda)$ measured with the SOLSPEC instrument and published by Thuillier et al. (2003). Superimposed on the broadband black body spectrum there are characteristic absorption lines caused by light elements in the photosphere of the Sun. These lines were discovered by the German physicist Joseph von Fraunhofer (Fraunhofer (1817), Kirchhoff (1860)) and are therefore Fraunhofer lines. In the lower panel of Figure 3.1 one can nicely see two of the strongest Fraunhofer lines, the calcium lines at 393 nm and 396 nm.

For the deduction of photochemical parameters in section 8.3 some definitions have to be made. The *spectral radiance* $I(\lambda)$ is defined as the incident radiant energy per time and wavelength, called spectral flux Φ, on the area element A and the solid angle Ω:

$$I(\lambda) = \frac{\Phi(\lambda)}{\Omega \cdot A} \; [\mathrm{Wnm^{-1}m^{-2}sr^{-1}}] \tag{3.1}$$

The amount of radiant energy within a cone of solid angle Ω is called *spectral irradiance* $E(\lambda)$:

$$E(\lambda) = \int_{\Omega} I(\lambda, \phi, \theta) \cdot \cos\theta d\Omega \; [\mathrm{Wnm^{-1}m^{-2}}] \tag{3.2}$$

The integration of the radiance (equation 3.1) over the whole sphere (4π) lead to the *actinic flux* $F(\lambda)$ which represents the radiant energy flux out of all directions

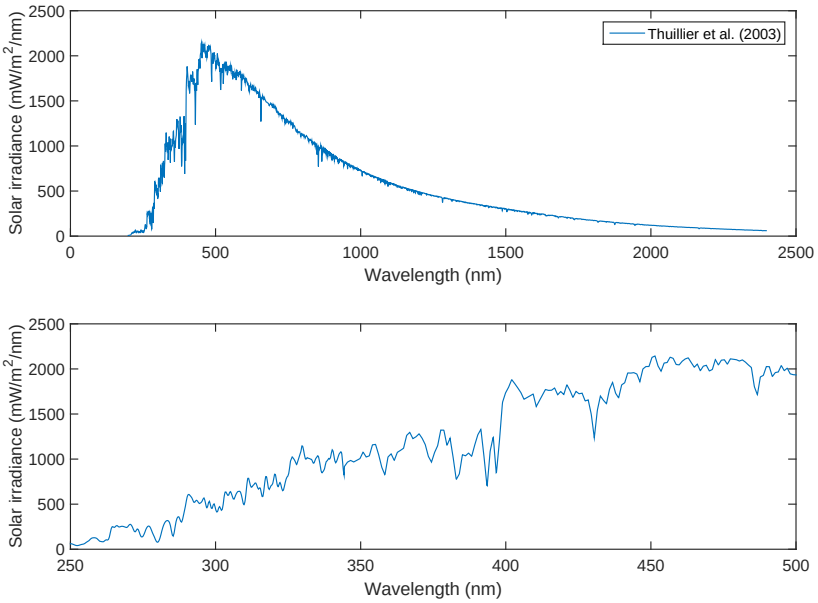

Figure 3.1: Solar irradiance from Thuillier et al. (2003). Top panel: 200 nm - 2400 nm, bottom panel: upper UV and visible wavelength range, 250 nm - 500 nm. This is the relevant wavelength range for the spectroscopic measurements in this work.

through a spherical surface:

$$F(\lambda) = \int_{4\pi} I(\lambda) d\Omega \ [\mathrm{Wm^{-2}nm^{-1}}] \tag{3.3}$$

The actinic flux is the relevant quantity in determining the photolysis rate J of molecules. J is the product of the actinic flux, the absorption cross section (see section 3.2.1) and the quantum yield q (molecules photon^{-1}), integrated over all wavelengths (Brasseur and Solomon (2005)):

$$J = \int_{\lambda} F(\lambda) \cdot \sigma(\lambda) \cdot q(\lambda) d\lambda \tag{3.4}$$

3.2 Interaction of radiation with particles and molecules

Radiation traversing the atmosphere interacts in a variety of processes with air molecules or aerosol and cloud particles. Absorption results in a removal of the radiation from the radiation field and a conversion into some other form of energy, e.g. heat. Elastic scattering, by air molecules (Rayleigh scattering), or atmospheric

aerosol particles (Mie scattering), changes the direction of propagation of an individual photon, but not its energy. In contrast, inelastic scattering additionally changes the photon energy. Inelastic scattering by molecules is called Raman scattering, where the photon energy can be reduced (Stokes scattering) or increased (anti-Stokes scattering). The thermal emission from air molecules and aerosol particles in the infrared wavelength range is negligible for spectroscopic measurements in the UV/vis wavelength range (Platt and Stutz, 2008).

3.2.1 Absorption by molecules

Absorption of photons change the energetic states of molecules due to different phenomena. During these interactions, electronic, vibrational and rotational transitions occur. For small atoms, the energy level E_n of an electronic state n is in good approximation given by the Rydberg formula $E_n = -R_{Ry}/n^2$, where R_{Ry} denotes the Rydberg constant for the particular atom.

In contrast to atoms, molecules have electronic states of different energy and additional excitation schemes. The rotation of the entire molecule according to the angular momentum $\vec{J}$ and quantum number J, can be changed by the absorption of photons with wavelengths in the sub-mm or microwave range (e.g. a microwave oven heats by exciting rotational transitions in water molecules). The allowed rotational energy levels in a molecule are given by $E_j = BJ(J+1)$, where $B = \frac{\hbar}{2\Theta}$ denotes the rotational constant of the particular molecule and rotation axis with the moment of inertia Θ with respect to this axis. The energy difference of two consecutive states is $\Delta E_j = 2B(J+1)$. Transitions between states with different J are constrained by the selection rule, and comprise different branches depending on the angular momentum difference between the initial and final state, namely the O, P, Q, R and S-branches with $\Delta J = -2, -1, 0, +1, +2$, respectively.

The vibration of molecules can be approximated by a harmonic oscillator with energy levels $E_\nu = (\nu + 1/2)\hbar\omega_O$ quantized by the vibrational quantum number ν and the zero-point energy of the molecular oscillator $\frac{1}{2}\hbar\omega_0$. Photons in the UV/vis wavelength range are also able to excite electronic transitions.

Since the molecules are also rotationally excited, each vibrational transition splits into a series of rotational lines. As a consequence of the different excitation schemes, the energy levels of the molecular electronic shell are split into a set of vibrational and rotational levels (Figure 3.2). The described splitting up of energy levels leads to differential structures in the absorption spectra of molecules in the UV/vis wavelength range (see Figure 6.1). This allows the application of the DOAS method (chapter 6.1).

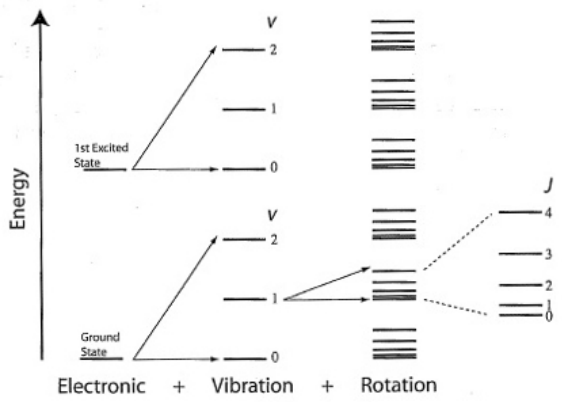

Figure 3.2: Schematic depiction of the superposition of electronic, vibrational and rotational energy levels. The absorption spectrum (cross section) of a molecule is determined by all non-forbidden transitions between two states. Adopted from http://www.patarnott.com.

3.2.2 Scattering by molecules and particles

Depending on the ratio of the wavelength of the incident radiation compared to the size of the target and whether the scattering process is elastic or inelastic, there are three main types of scattering processes in the atmosphere: Rayleigh, Mie and Raman scattering.

Rayleigh scattering

Rayleigh scattering describes elastic scattering on particles much smaller than the wavelength of the incident radiation. It has a strong wavelength dependency, scattering at shorter wavelengths is stronger than at longer wavelengths, which leads to the blue colour of the sky. The first empirical parametrisation of the Rayleigh cross section for standard air (especially regarding water vapor and CO_2) was given by Penndorf (1957):

$$\sigma = \frac{24\pi^3(n^2-1)^2}{\lambda^4 N^2(n^2+2)^2}\left(\frac{6+3\rho}{6-7\rho}\right), \tag{3.5}$$

where σ is the scattering cross section per molecule, N is molecular density, the term $(6+3\rho)/(6-7\rho)$ is called the depolarisation term or King factor, and ρ is the depolarisation factor which describes the effect of molecular anisotropy. A simplified parametrisation is given by Platt and Stutz (2008):

$$\sigma \approx \sigma_{R,0} \cdot \lambda^{-4} (\text{with } \sigma_{R,0} \approx 4.4 \times 10^{-16} \text{ cm}^2\text{nm}^4 \text{ for air}) \tag{3.6}$$

As the name implies Rayleigh scattering is a scattering and not an absorption process. However, in the narrow-beam approximation it can be treated as an absorption process (Platt et al., 2012). This approximation assumes that the probability of a photon that was scattered out of the light beam is scattered back into the light beam is negligible. The Rayleigh extinction coefficient ϵ_R for a number density of air molecules N_{air} is given by:

$$\epsilon_R(\lambda) = \sigma_R(\lambda) \cdot N_{air} \tag{3.7}$$

Bodhaine (1999) gives look-up table of Rayleigh cross sections for different types of air (pressure, water vapor, etc.) which is also implemented in the radiative transfer model McArtim (section 6.2.2) used within this work. The angular distribution of Rayleigh-scattered photons is given by the Rayleigh phase function:

$$\Theta(\vartheta) = \frac{3}{4}(1 + \cos(\vartheta)) = \frac{I(\vartheta)}{I_0} \tag{3.8}$$

Forward or backward scattering is stronger by up to a factor of 2, when compared to a scattering angle of $\vartheta = 90°$.

Scattering and absorption by particles

Photons can also interact with particles that have a size comparable to the wavelength of the incident radiation (via scattering or absorption). For spherical particles this process is described by the Mie theory which is named after the German physicist Gustav Mie. Because these particles can absorb and scatter radiation, the Mie extinction coefficient is divided into two parts

$$\epsilon_M(r, \lambda) = \epsilon_a(r, \lambda) + \epsilon_s(r, \lambda) \tag{3.9}$$

with the particle radius r, the scattering coefficient ϵ_s and the absorption coefficient ϵ_a. An overview on Mie theory in general would go beyond the scope of this work. The derivation and comprehensive discussions can be found in various textbooks. Therefore, a few general remarks from Platt and Stutz (2008) which are important for the present thesis will be given here.

The single scattering albedo (SSA) of an aerosol is defined as:

$$SSA = \frac{\epsilon_s(r, \lambda)}{\epsilon_a(r, \lambda) + \epsilon_s(r, \lambda)} \tag{3.10}$$

It defines the amount of radiation scattered by Mie particles, compared to the amount that was scattered or absorbed. An SSA of 1 describes pure scattering, whereas an SSA of 0 describes a particle that absorbs all radiation. Mie scattering is, similar to Rayleigh scattering, not an absorption process. However, it can be

described as an absorption process in the narrow-beam approximation as well. The wavelength dependency of the Mie extinction coefficient ϵ_M is:

$$\epsilon_M(\lambda) = \epsilon_{M,0} \cdot \lambda^{-\alpha} \tag{3.11}$$

where α is the so-called Ångström exponent, which is inversely related to the size of the particle (see e.g. Roedel (2000)). Mie scattering is less dependent on wavelength than Rayleigh scattering Typical Ångström exponents for aerosols in the UTLS range between 1.1 and 1.5.

The integrated aerosol extinction over a light path of length z yields the aerosol (or cloud) optical depth (OD) τ :

$$\tau(\lambda) = \int_0^z \epsilon(\lambda, z')dz' \tag{3.12}$$

The Mie phase function, and thus the scattering direction, depends on the size parameter x:

$$x = \frac{2\pi r}{\lambda} \tag{3.13}$$

In general it can be said, that forward scattering is more dominant in Mie scattering when compared to Rayleigh scattering, especially for increasing x. A common simple parametrisation for the phase function is given by Henyey and Greenstein (1941):

$$\Phi_{HG}(\cos\vartheta) = \frac{1 - g^2}{4\pi \cdot (1 + g^2 - 2g\cos\vartheta)^{3/2}} \tag{3.14}$$

where g is the average cosine of the scattering function $g =< \cos\vartheta >$ referred to as the asymmetry parameter. A value of 0 indicates an isotropic scattering behavior, while the value of 1 indicates a complete forward scattering. Typical values for stratospheric aerosols are $g \approx 0.6...0.8$.

Rotational Raman Scattering (RRS)

Additionally to elastic scattering, inelastic Raman scattering (i.e. the energy of the photon changes during the scattering process) may also occur in the atmosphere if the target molecule changes its excitation state during the scattering process. The photon can transfer energy to the molecule (Stokes process) or take up energy from the molecule (anti-Stokes process). If only the rotational state ($\delta\nu = 0$) of the molecule changes the process is called Rotational Raman scattering (RRS). When the vibrational excitation state changes as well, it is called rotational vibrational Raman scattering. The cross sections for Raman scattering are orders of magnitudes smaller than those for Rayleigh scattering (Platt and Stutz, 2008). However, the

influence of Raman scattering has to be considered for remote sensing applications. Due to the energy exchange during the scattering event, the incident photon has a different wavelength after the scattering process. This causes an effect known as the "Ring effect", which is named after Grainger and Ring (1962). The Ring effect describes a decrease in the optical depth of the Fraunhofer lines due to photons that are inelastically scattered. It has to be considered in the DOAS analysis (section 6.1). A detailed explanation of the Ring effect can be found in Platt and Stutz (2008).

Reflection at the sea surface

Sea surface reflection of sunlight is of specific importance for the analysis of the Global Hawk DOAS measurements since all flights were conducted above sea surface. The parametrisation of sun-glint and oceanic BRDF (Bidirectional reflectance distribution function) are based on the approach of Cox and Munk (1954). They retrieved the distribution of slopes of waves from photographs of sun-glint situations. The validity of their findings has in principal not been changed until today. This parametrisation is also implemented in the radiative transfer model McArtim (section 6.2.2).

3.3 The radiative transfer equation (RTE)

Taking into account the radiative processes described in the previous sections, the propagation of light through the atmosphere can be described by the radiative transfer equation (RTE). A change of the radiance $I(\lambda)$ at a given wavelength λ while travelling through an absorbing layer of the thickness ds is given by:

$$\frac{dI(\lambda)}{ds} = -I(\lambda) \cdot \epsilon_a(\lambda) = -I(\lambda) \cdot \sigma_a(\lambda) \cdot N_a, \tag{3.15}$$

with the absorption coefficient ϵ_a, the absorption cross-section σ_a and the number of absorbing molecules per unit volume N. Integration of Equation 3.15 over the layer thickness L results in the well-known Lambert-Beer law. Analogous to the absorption process, the attenuation of the incoming radiance due to scattering is given by:

$$\frac{dI(\lambda)}{ds} = -I(\lambda) \cdot \epsilon_s(\lambda) = -I(\lambda) \cdot \sigma_s(\lambda) \cdot N_s, \tag{3.16}$$

with ϵ_s being the scattering coefficient and σ_s the scattering cross-section. Often, a dimensionless scattering function $S(\theta, \phi)$ is used, which depends on the zenith angle θ and on the azimuth angle ϕ:

$$S(\theta, \phi) = \frac{4\pi}{\sigma_s(\lambda)} \cdot \frac{d\sigma_s(\lambda)}{d\Omega}. \tag{3.17}$$

If thermal emission is neglected, the total RTE can be expressed as:

$$\frac{dI(\lambda)}{ds} = -[\epsilon_a(\lambda)+\epsilon_s(\lambda)]\cdot I(\lambda)+\epsilon_s(\lambda)\int_0^{\pi}\int_0^{2\pi} I(\lambda,\theta,\phi)\cdot\frac{S(\theta,\phi)}{4\pi}d\phi\cdot\sin\theta d\theta. \quad (3.18)$$

The first part of this equation describes the attenuation of incoming radiation by absorption and scattering processes. The second part of the equation describes the radiance that is added to the propagation direction by scattering. The radiation field can be further separated into a direct and diffusive radiance.

Different radiative transfer modelling approaches can be applied to solve the RTE numerically. An overview of possible methods and the approach used in this study is presented in section 6.2.1.

4 The NASA ATTREX project

The NASA (Airborne Tropical TRopopause EXperiment) ATTREX [1] project is a five-year airborne science program aiming to study the chemical and physical properties, as well as the importance for global climate and stratospheric ozone, of the TTL over the Pacific.

The remoteness of the Pacific TTL makes it very hard to be reached and probed by in-situ instrumentation. Furthermore, satellite remote sensing is not able to resolve the small-scale dynamic and photochemical processes acting there. Hence, the TTL is still one of the least explored areas in the atmosphere. Because of its key feature as "the door to the stratosphere" small details in complex interplay of radiation, micro-physical and dynamical processes and photochemical reactions can have a huge impact on global climate. A lot of those details are yet not well understood

In order to investigate some core processes in more detail, the unmanned long-range high-altitude aircraft NASA Global Hawk (section 4.2) had been equipped with twelve different instruments (section 4.3.1) measuring various trace gases, water vapor and radiation. The overall ATTREX project is managed by the NASA Ames Research Center. The Global Hawk operations however are handled by the Dryden Flight Research Center (DFRC), southern California.

4.1 Objectives

As described in section 2 the TTL acts as a gate to the stratosphere and ultimately determines the chemical composition and humidity of air entering the stratosphere. The overarching goals of ATTREX are to improve:

- The understanding of how deep convection, slow large-scale ascent waves, and cloud microphysics control the humidity and chemical composition of air entering the stratosphere
- Global model predictions of feedbacks associated with future changes in TTL cirrus, stratospheric humidity, and stratospheric ozone in a changing climate.

[1] http://espo.nasa.gov/attrex/

Specific objectives of the mini-DOAS measurements during the NASA ATTREX project are:

- Measuring the abundance of the inorganic halogen compounds BrO and IO. Along with GWAS measurements (see 4.3.2) of major halogenated hydrocarbons the DOAS measurements provide constraints on the TTL and lower stratospheric Br_y and I_y budgets.
- The oxidation capacity in the TTL by observation of some relevant nitrogen (NO_x) and halogen compounds (BrO, and IO)
- Detection of ice particles (sub-visible cirrus clouds) and quantification of some of their optical properties

In order attain these objectives ATTREX provides a unprecedented data set of high spacial-resolution measurements in the TTL covering area-wide parts of the Eastern and Western Pacific.

4.2 The Global Hawk Aircraft

The Global Hawk (picture 4.1) is nearly ideal for sampling the TTL. It is an unmanned aerial vehicle (UAV) powered by a turbofan jet engine reaching a ceiling altitude from ∼16.5 km directly after take-off up to ∼18.9km in the latter part of the flight when most of the fuel is consumed. At a ground speed of 200 m/s and duration of ∼20 hours a flight distance of ∼15.000 km can be covered. The long endurance permits sampling of large regions of the Pacific TTL even with flights originating in southern California (see figure 4.4). The payload capacity of ∼680 kg allows to simultaneously carry several remote-sensing and in-situ instruments necessary to provide a comprehensive data set (see payload section 4.3.1).

The GH also provides communication via the K_u band[2], as well as a L-band (1616 - 1626.5 MHz, or Iridium[3]) satellite link to enable real-time communication of the investigators with their instruments to optimise settings and to monitor the instruments performance. In-situ instruments also provide real-time data which are useful to check on the conditions the GH is sampling. We used this connection to keep track of our detector temperature and to adapt the telescope elevation sequences to the flight patterns (see section 5). An internal navigation system (INS) provides 1 Hz real-time data of cf. the pitch of the GH with which our telescope positions are corrected automatically in time (see chapter 5).

[2]https://en.wikipedia.org/wiki/Ku_band
[3]https://iridium.com

Figure 4.1: The Global Hawk aircraft during flight. The telescopes of the mini-DOAS instrument are marked with a red circle. Credits: NASA Photo / Tom Miller

4.3 Observations - Available Data

This section gives first an overview on the complete GH payload during the 2013 NASA ATTREX deployment. After the overview, selected instruments which recorded complementary data, used during the data analysis of the DOAS measurements are specifically introduced.

4.3.1 Payload overview

The ATTREX GH payload is designed to address the key uncertainties in the understanding of TTL processes in chemistry, transport and especially cloud processes affecting water vapour and ice. Table 4.1 shows an overview of the instrument set-up. Instruments are chosen based on proven techniques, weight, size and possibility of accommodation on the GH. Figure 4.2 provides a sketch of where the instruments are installed on the aircraft. The mini-DOAS instrument is mounted at the so-called zone 25 which is located at the belly of the GH (details see chapter 5).

4.3.2 Complementary data of other instruments

Five other instruments besides the DOAS are of special interest for the data analysis performed in the thesis: The NOAA ozone monitor (Gao et al., 2012), the GH Whole Air Sampler GWAS, the Harvard University Ring Down Spectrometer (HUPCRS), the UCATS gas chromatograph and the Cloud Physics lidar (CPL). It follows a brief description for each of these instruments with focus on their precision and data rate.

Table 4.1: List of NASA ATTREX participants, instrumentation and measured parameters

Partner	Instrument	Instrument description	Measurements
In-situ			
University of Miami	GWAS	Global Hawk Whole Air Sampler	CFCs, halons HCFCs, N_2O, CH_4, HFCs, PFCs, hydrocarbonsetc(see4.3.2)
NOAA-ESRL	UCATS	UAS Chromatograph for Tracers	N_2O, SF_6, CH_4, H_2, CO, O_3, H_2O
Harvard	PCRS	Picarro Cavity Ringdown Spectrometer	CO_2, CO, CH_4
NASA Langley	DLH	Diode Laser Hygrometer	H_2O vapor
NOAA/CSD	NOAA Ozone	Tunable diode laser absorption	O_3
NOAA/Cires	NOAA Water	Tunable diode laser absorption	H_2O (vapor and total)
SPEC	Hawkeye & FCDP	Fast Cloud Droplet Probe	Ice crystal size distribution and habit
NASA ARC	MMS	Meteorological Measurement System	Temperature, pressure, 3D winds
Remote-Sensing			
NASA/GSFC	CPL	Cloud Physics Lidar	Aerosol/cloud backscattering and depolarisation ratio
University of Boulder, Colorado	SSFR	Solar and Infrared Spectral Flux Radiometer	Solar flux from below and above the GH, albedo
JPL/Caltech	MTP	Microwave Temperature Profiler	Temperature profile
UCLA / Univ. of Heidelberg	mini-DOAS	Optical absorption spectrometer	O_3, BrO, NO_2, IO,H_2O(vapor,ice)

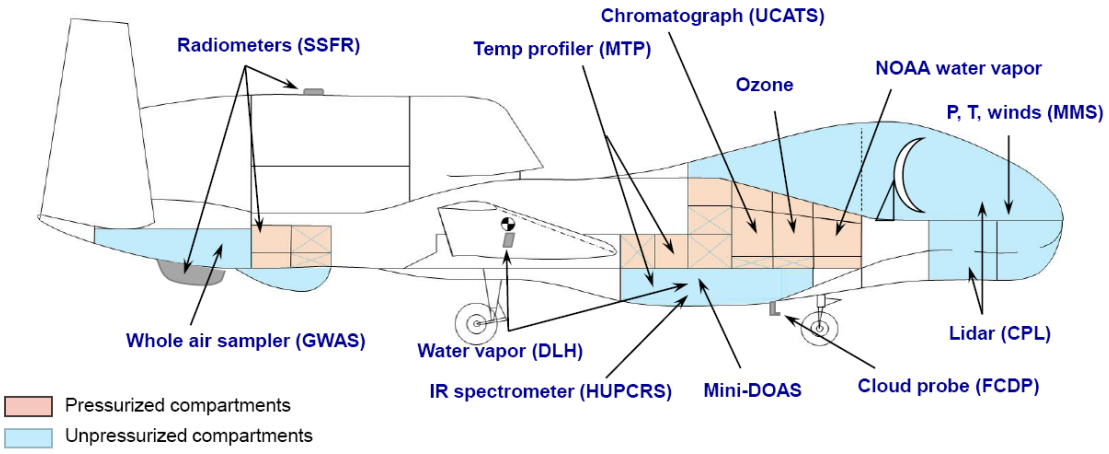

Figure 4.2: Sketch of the Global Hawk payload during the ATTREX deployments. (courtesy of Eric Jensen)

NOAA O_3 instrument

The NOAA ozone instrument is a dual-beam UV photometer. A polarisation optical-isolator configuration is utilised to fold the UV beam inside the absorption cells, yielding a 60-cm absorption length with a 30-cm cell. The instrument has a fast sampling rate (2 Hz at $<$ 200 hPa, 1 Hz at 200–500 hPa, and 0.5 Hz at $\leq$ 500 hPa), high accuracy (3% excluding operation in the 300 - 450 hPa range, where the accuracy may be degraded to about 5%), and excellent precision ($1.1 \cdot 10^{10}$ O_3 molecules/cm^3 at 2 Hz, which corresponds to 3.0 ppb at 200 K and 100 hPa, or 0.41 ppb at 273 K and 1013 hPa). The size (36 l), weight (18 kg), and power (50 - 200 W) make the instrument suitable for many unmanned aerial vehicle vehicles (UAV) and other airborne platforms. In-flight and laboratory inter-comparisons with existing O_3 instruments showed that measurement accuracy (3 %) was maintained in flight.

The NOAA O_3 data is used extensively in the data analysis in order to constrain the radiative transfer of the DOAS measurements. This so-called O_3-scaling-method is explained in detail in section 7.4.

HUPCRS

The Harvard University Picarro Cavity Ring down System (HUPCRS) provides precise, stable measurements of CO_2 and CH_4. The HUPCRS also includes a CO channel that provides useful data with some averaging. The CH_4 measurements are of specific importance for the data analysis performed in this thesis. The accuracy is given by 0.3 ppb for the 1/10 Hz frequency data.

Unfortunately, the HUPCRS instrument did not properly work during the first two

flights of the 2013 deployment (SF1-2013 and SF2-2013), mostly due to calibration issues (personal communication with J. Pittman, 2015).

UCATS GC

The UAS Gas Chromatograph for Atmospheric Trace Species (UCATS) provides measurements of N_2O, SF_6, H_2, CO (tropospheric), and CH_4, as well as additional measurements of ozone and water vapor. The accuracy ranges between 1% and 5%, depending on the species.

The UCATS CH_4 data with the much lower precision of ∼6 ppb is used for SF1-2013 and SF2-2013 during which the HUPCRS instrument did not work.

GWAS

The Global Hawk Whole Air Sampler (GWAS) consists of 90 gas canister samples that are spaced throughout each flight. The times for the GWAS samples are determined on a real-time basis depending on the atmospheric conditions and scientific relevance. During descents of the GH no GWAS samples can be taken due to power consumption issues. Post-flight, gas chromatographic analysis provides concentrations of a plethora of trace gases with sources from industrial mid-latitude emissions, biomass burning, and the marine boundary layer, with certain compounds (e.g. organic nitrates) that have a unique source in the equatorial surface ocean. GWAS also measures a full suite of halocarbons that provide information on the role of short-lived halocarbons in the tropical UTLS region, on halogen budgets in the UTLS region, and on trends of HCFCs, CFCs, and halogenated solvents. The measurement accuracy amounts from 5% up to 20% depending on the species.

In the framework of this thesis the DOAS measurements of Br_y^{inorg} are combined with the GWAS measurements of short-lived halocarbons and halons in order to infer the total $Br_y (= Br_y^{org} + Br_y^{inorg})$ budget.

CPL

The information given here is extracted from the CPL web page[4].

The Cloud Physics Lidar provides a complete battery of cloud physics information. Data products include:

- Cloud profiling with 30 m vertical and 200 m horizontal resolution at 1064 nm, 532 nm, and 355 nm, providing cloud location and internal backscatter structure.
- Aerosol, boundary layer, and smoke plume profiling at all three wavelengths.

[4] http://cpl.gsfc.nasa.gov/

- Depolarization ratio to determine the phase (e.g., ice or water) of clouds using the 1064 nm output.
- Cloud particle size determined from a multiple field-of-view measurement using the 532 nm output (off-nadir multiple scattering detection).
- Direct determination of the optical depth of cirrus clouds (up to ∼OD 3) using the 355 nm output.

The processed data resolution is 1 Hz temporally and 30 m (vertical) by 20 m (horizontal) spatially. Due to limited electric power supply from the GH jet engine the CPL instrument had to be shut down during the dives. Figure 4.3 shows an example of the processed data of a part from 23:00 UT (Feb 13) to 10:00 UT (Feb 14) which indicates a patchy shallow marine stratocumulus cloud (mSc) cover of SF3-2013. One can clearly see nice examples of shallow patchy marine stratocumulus cloud cover and a deck of high cirrus clouds (3:30 - 6:00 UTC)

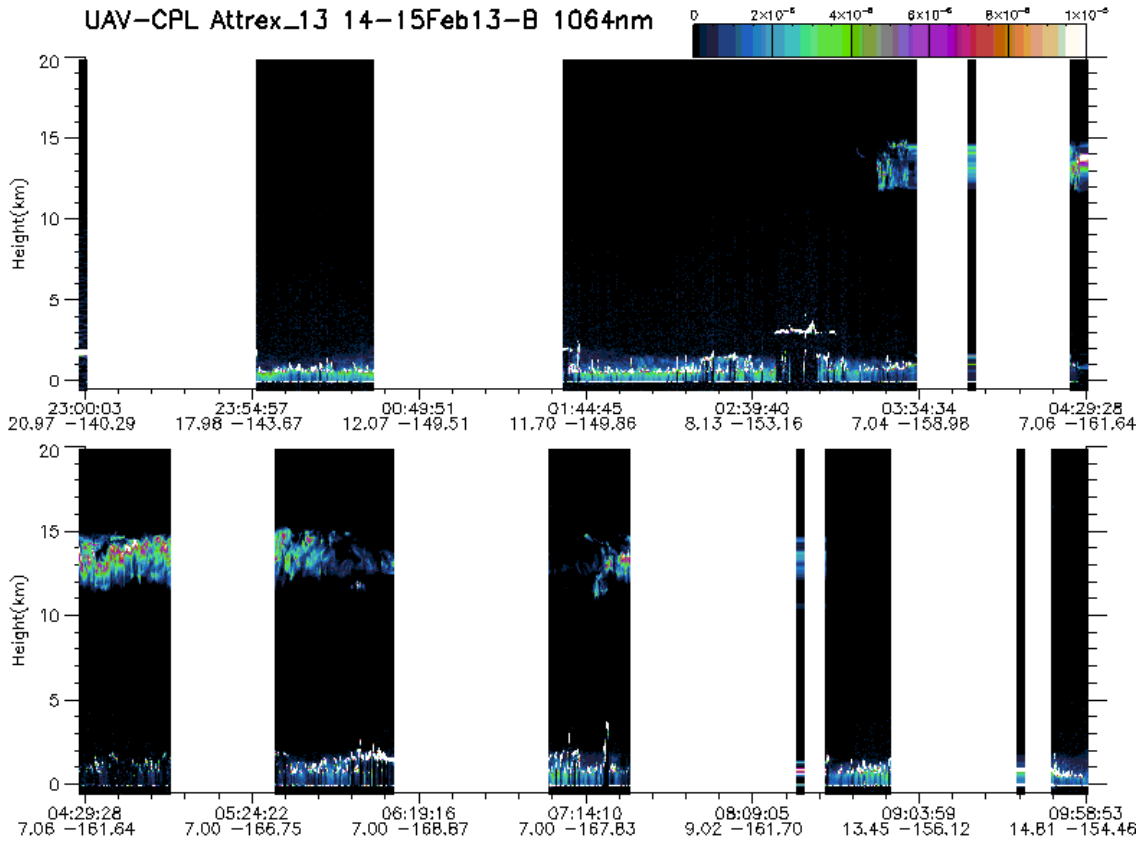

Figure 4.3: Record of the 1064 nm channel of the CPL data of a part of SF3-2013. White parts indicate the periods in which the CPL instrument had to be shut down. For details see text.

Table 4.2: List of NASA-ATTREX sorties

Flight	Date	Duration (sunlight)	Objective
Eastern Pacific (2013)			
Test flight	Jan 19	6.5	Technical check-up
SF1-2013	Feb 5-6	10	Central Pacific TTL profiling
SF2-2013	Feb 9-10	10	Meridional TTL cross section
SF3-2013	Feb 14-15	10	Central Pacific TTL profiling
SF4-2013	Feb 21-22	10	Eastern Pacific meridional cross section
SF5-2013	Feb 26-27	10	Central Pacific cold TTL cirrus profiling
SF6-2013	Mar 1-2	10	Eastern Pacific cold TTL cirrus profiling
Western Pacific (2014)			
SF1-2014	Feb 12	10	Western Pacific TTL composition survey TTL cirrus sampling
SF2-2014	Feb 16	10	Double-tropopause apparent in thermal structure and tracers
SF3-2014	Mar 4	10	Faxai-perturbed TTL sampling TTL cirrus produced by Faxai taifun
SF4-2014	Mar 6	10	TTL wave measurements TTL trace gas and cloud measurements
SF5-2014	Mar 9	10	Southern survey Fresh outflow from equatorial convection
SF6-2014	Mar 11	10	Northern survey
Transit back	Mar 13	10	TTL profiling across central Pacific

4.3.3 Sorties

Table 4.2 shows an overview of all sorties of the GH in the framework of the NASA-ATTREX project in 2011, 2013 and 2014. The numbering of the flights (column 1) is kept throughout this work.

Figure 4.4 shows all scientific sorties of the Global Hawk during both the 2013 (Dryden) and 2014 (Guam) deployment. The mini-DOAS instrument performed overall well and data was recorded during all flights.

All sorties are supported by the NASA-Ames Airborne Science Meteorological Support[5], which delivers various post-analysis products, satellite products, data from soundings, etc.

[5]http://bocachica.arc.nasa.gov/

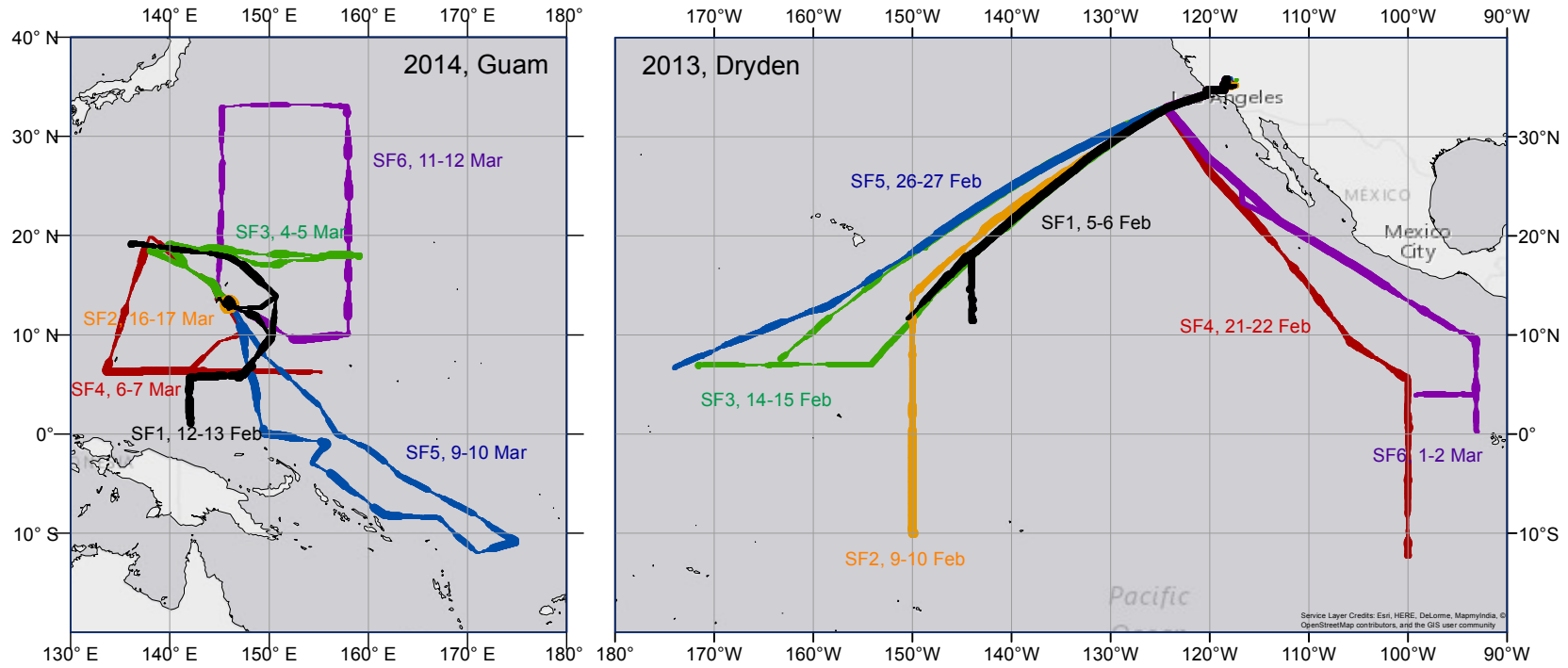

Figure 4.4: Sorties of the Global Hawk during the 2013 (Dryden) and 2014 (Guam) deployments. The thickness of the lines indicate the altitude of the GH. Thinner lines mean lower altitude (∼14 km), thicker lines larger altitudes (∼18 km)

5 The Global Hawk mini-DOAS instrument

This chapter provides a very short description of the Global Hawk mini-DOAS instrument and lists the most important specifications for this work. A comprehensive characterisation can be found in Raecke (2013) (chapter 4).

The Global Hawk mini-DOAS is a custom-built instrument based on the experiences from earlier deployments of balloon- and aircraft-borne (e.g. Ferlemann et al. (2000) Weidner et al. (2005), Kritten et al. (2010), Prados-Roman et al. (2011)) and ground-based (e.g. Hönninger et al. (2004), Frieß et al. (2006), Stutz et al. (2007)) DOAS measurements.

The heart of the instrument consists of three optical spectrometers which are pressure and temperature-stabilised (Figure 5.1). The instrument is mounted at the belly zone of the Global Hawk (Figure 5.2). It fits the strict requirements in terms of size, weight, power consumption and security to be deployed on the Global Hawk. The edge length of the cubic-shaped spectrometer assembly is ∼50 cm, the total weight is about 35 kg and the power consumption amounts to 100 W, including telescope heating.

Three rotating telescopes stick out of the GH fuselage and collect scattered sunlight in the UV, visible and near-IR wavelength range (Figure 5.3). The telescopes point into flight direction (assuming no shear winds, and no drift of the GH) and the telescope elevation angle is therefore sensitive to the pitch of the aircraft. In order to compensate the changing pitch of the aircraft (Figure 5.4) the telescopes are actively pitch-controlled at a 1 Hz frequency. The accuracy of the pitch correction is estimated to be approximately ±0.1°. Each telescope cover contains an embedded diffuser disk at the zenith position of the telescope. This provides recording of direct sunlight spectra in case the disk is directly illuminated by the sun. Direct sunlight spectra are useful because the light path length of the DOAS reference column (section 6.1) is short and they allow to calculate the light geometrically (section 7.4). The major optical specifications are listed in Table 5.1.

Table 5.1: Major optical specifications of the Global Hawk mini-DOAS instrument.

Channel	**Wavelength range (nm)**	**Resolution (nm)**	**Vertical field of view (°) FWHM**
UV	300 - 380 nm	0.8	0.265
VIS	410 - 530 nm	0.9	0.288
near-IR	900 - 1700 nm	20	0.254

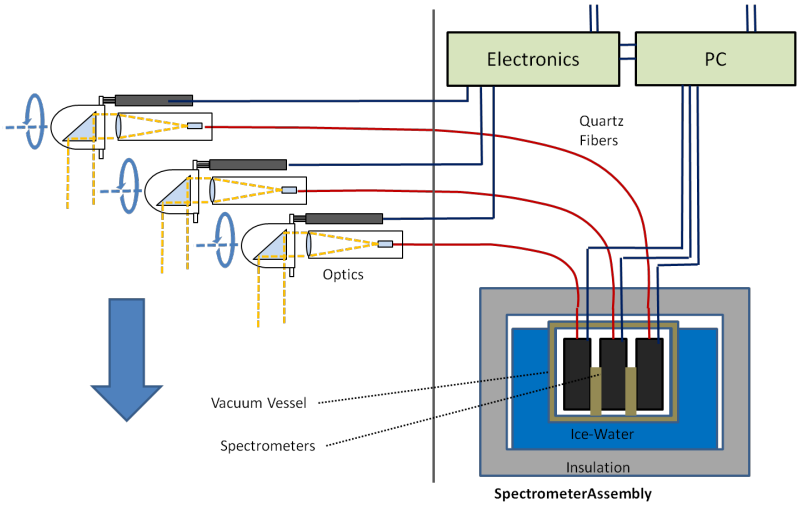

Figure 5.1: Sketch of the Global Hawk DOAS instrument. Left side: Optics for light intake, three rotating telescopes pointing into flight direction (blue arrow) for collecting scattered sunlight in three wavelength ranges: UV, VIS and near-IR. Right side: Assembly of the spectrometers in an vacuum housing which is bathed in an ice-water-mixture for temperature stabilisation.

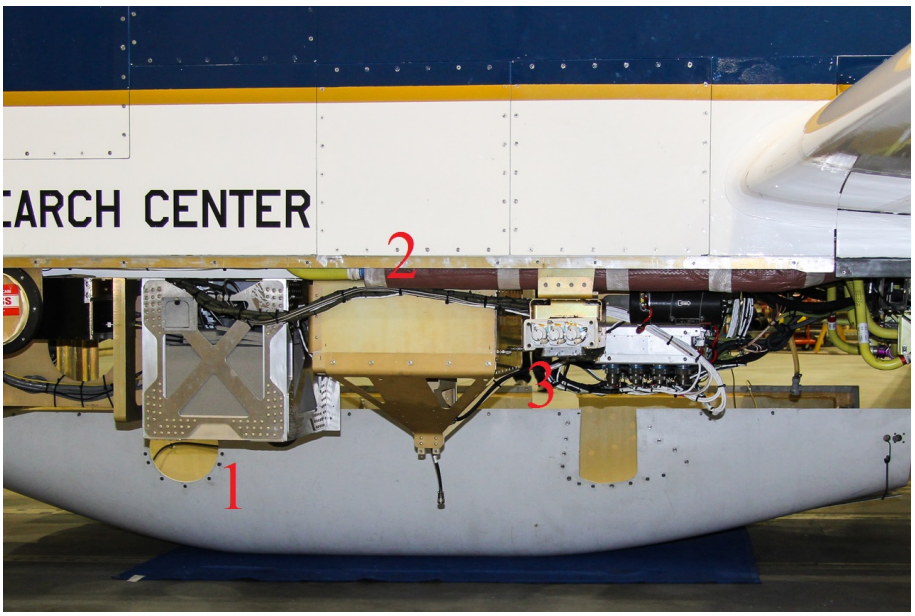

Figure 5.2: Photo of the instrument integrated in zone 25 (location see 4.2), the unpressurised belly pod of the GH, without fairing. 1) spectrometers assembly 2) fiber bundles 3) telescopes.

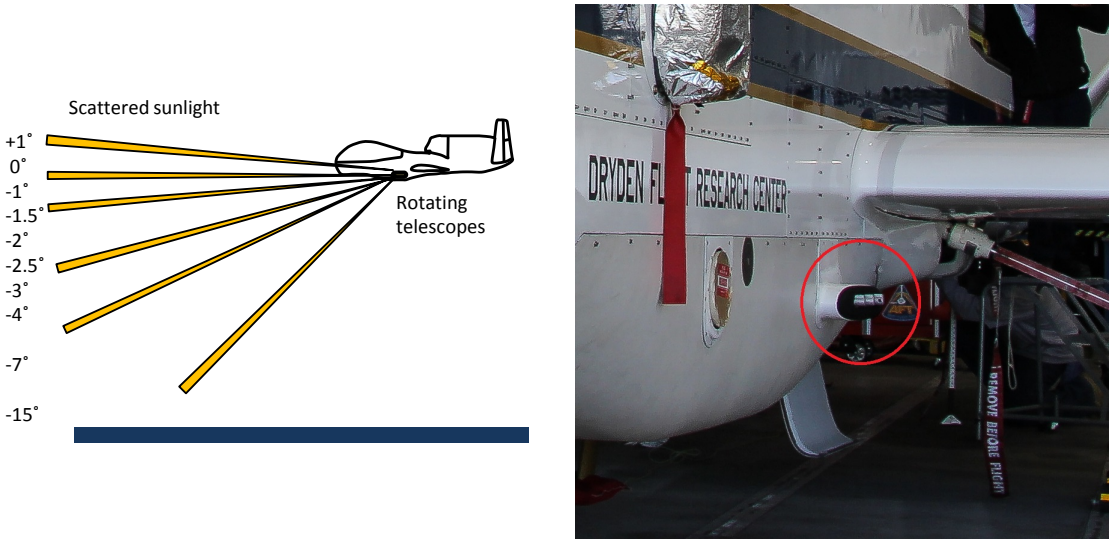

Figure 5.3: GH belly cam pictures taken at the end of the ascend of the second dive of SF3-2013.

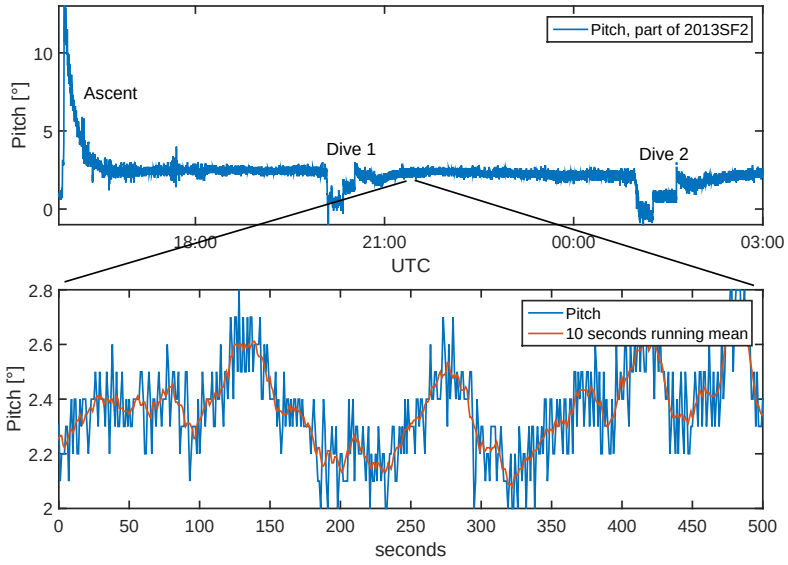

Figure 5.4: Upper panel: Pitch of the GH during the first part of 2013SF2. Lower panel: Zoom of a short period of cruising at level. As described in 4.2 the GH turbofan engine constantly switches between power on and idle in order to keep cruise altitude. The changing thrust of the engine and the corresponding change in pitch angle is demonstrated by the red curve which is a 10 seconds running average of the blue 1 Hz data. The time interval is arbitrarily chosen.

6 Methods and tools

This next two chapters give a comprehensive overview of the methods and tools used in the data analysis. It is shown step-by-step how concentrations of the targeted trace gases are retrieved from the raw spectra.

The first step of the analysis procedure is the spectral retrieval via the DOAS technique which is explained in section 6.1. Two different approaches are applied to infer mixing ratios from the spectrally retrieved differential slant column densities (dSCDs) - the optimal estimation method (section 7.1) and the scaling-method (section 7.4). Due to their extent, the inversion methods are discussed in a separate chapter 7. The present chapter introduces complementary tools that are used in the course of the inversions. Both inversion approaches include extensive radiative transfer calculations. Therefore, the radiative transfer equation and the approaches to solve it, are discussed in section 6.2. The use of predictions of chemical transport models (CTMs) during the analysis process is discussed in section 6.3.

6.1 Differential Optical Absorption Spectroscopy (DOAS)

The DOAS method is a well-established approach to analyse scattered sunlight spectra for molecular absorptions. It is based on the principle that every molecule has its own unique *absorption cross section* (see Figure 6.1) which is caused by electronic, vibrational or rotational transitions from the ground state to excited states of electrons in the molecule (section 3.2.1). The key idea of DOAS is that the narrow-band molecular absorptions can be separated from the broad-band scattering (section 3.2.2) structures in the fitting process. Technical details of the method and a very comprehensive overview can be found in Platt and Stutz (2008).

From the Beer-Lambert law

$$I(\lambda, L) = I_0 \cdot \exp\left(-\int_0^L \sigma(\lambda, p, T) \cdot c(l) dl\right), \tag{6.1}$$

one derives the attenuation factor, the optical density (OD, or τ), a quantity often used in this thesis:

$$\tau = -\ln\left(\frac{I(\lambda)}{I_0(\lambda)}\right) = -\int_0^L \sigma(\lambda, p, T) \cdot c(l) dl \tag{6.2}$$

The OD is connected with the light path integrated concentration, the so-called slant column density (SCD), via:

$$\tau(\lambda) = \int_0^L \sigma(\lambda) \cdot c(l) dl = \sigma(\lambda) \cdot SCD \tag{6.3}$$

Since in most cases the I_0 spectrum (reference spectrum), also contains absorption of the targeted trace gas, the primary output of the DOAS retrieval are the so-called differential slant column densities (dSCDs). The amount of absorption (in terms of a slant column density) contained in the reference spectrum needs to be added, i.e.

$$SCD = dSCD + SCD_{ref} \tag{6.4}$$

In the case of the Global Hawk DOAS measurements direct solar references (see section 5) are used as reference spectra. This allows a geometrical calculation of the light path in the reference spectrum (see equations 7.29 and 7.30). The solar reference spectrum recorded at the smallest possible SZA (for each flight) is chosen in order to keep the light path and therefore the absorption in the reference spectrum as small as possible. In the case of O_4 the absorption in the reference spectrum is only ∼1 % of the absorption contained in a scattered sunlight spectrum. In case of absorbers with high stratospheric concentration (O_3, BrO, NO_2) the situation is different and more complicated. A priori information of the overhead concentrations have to be used (see sections 6.3 and 7.4).

For the DOAS analysis of the Global Hawk spectra an I_0-correction is performed, the rotational Raman spectrum (also referred to as *Ring spectrum*, Grainger and Ring (1962)) is calculated from each scattered sunlight spectrum and the fitted cross sections are listed in Table 6.1.

Table 6.1: Reference spectra and settings of the DOAS trace gas retrievals

Retrieval	λ- interval	Reference	O_3	O_4	NO_2	BrO	H_2O	Polyn.	Comment
O_3-UV	343 - 355 nm	direct sun	203 K	293 K	203 K	298 K	203 K	2	O_4, NO_2, BrO linked O_3 Shift free for direct solar spectrum and O_3 Ring spectrum linked to solar spectrum
O_3-vis	437 - 485 nm	direct sun	203 K	293 K	203 K 223 K	-	203 K	2	O_4, NO_2, H_2O linked O_3 Shift/squeeze free for direct solar spectrum and O_3 Ring spectrum linked to solar spectrum
BrO-UV	345-360 nm	direct sun	203 K 213 K	293 K	203 K	298 K d	-	2	O_4, NO_2, O_3 linked BrO Shift/squeeze free for direct solar spectrum and BrO Ring spectrum linked to solar spectrum
NO_2-vis	424-460 nm	direct sun	203 K 213 K	293 K	203 K	-	203 K	2	O_4, H_2O, O_3 linked NO_2 Shift/squeeze free for direct solar spectrum and NO_2 Ring spectrum linked to solar spectrum

The wavelength interval for the O_3 DOAS analysis in the UV is chosen adjacent in wavelength to the BrO interval (table 6.1) in order to suppress wavelength dependent RT-related uncertainties in the O_3-scaling-method (section 7.4). The wavelength

intervals in the visible range for O_3 and NO_2 are slightly offset. This has to be taken into account when applying the O_3-scaling-method for NO_2.

Figures 6.2 and 6.3 show an example of the spectral analysis in the UV and visible wavelength range. Errors are not plotted for better visibility. One can nicely see the separation of the dSCDs for the different telescope elevation angles. Absorbers with high concentrations in the troposphere (e.g. O_4) show higher dSCDs for low elevation angles and absorbers with high concentrations in the stratosphere (e.g. O_3) vice versa.

Typical fit errors of the spectral retrieval are listed in table 6.2.

Table 6.2: Typical fit errors of the DOAS retrieval.

	UV			**VIS**		
trace gas	O_4	O_3	BrO	O_4	O_3	NO_2
fit error (molec./cm^2)	$4 \cdot 10^{41}$	$6 \cdot 10^{17}$	$2 \cdot 10^{13}$	$3 \cdot 10^{41}$	$7 \cdot 10^{17}$	$3 \cdot 10^{14}$

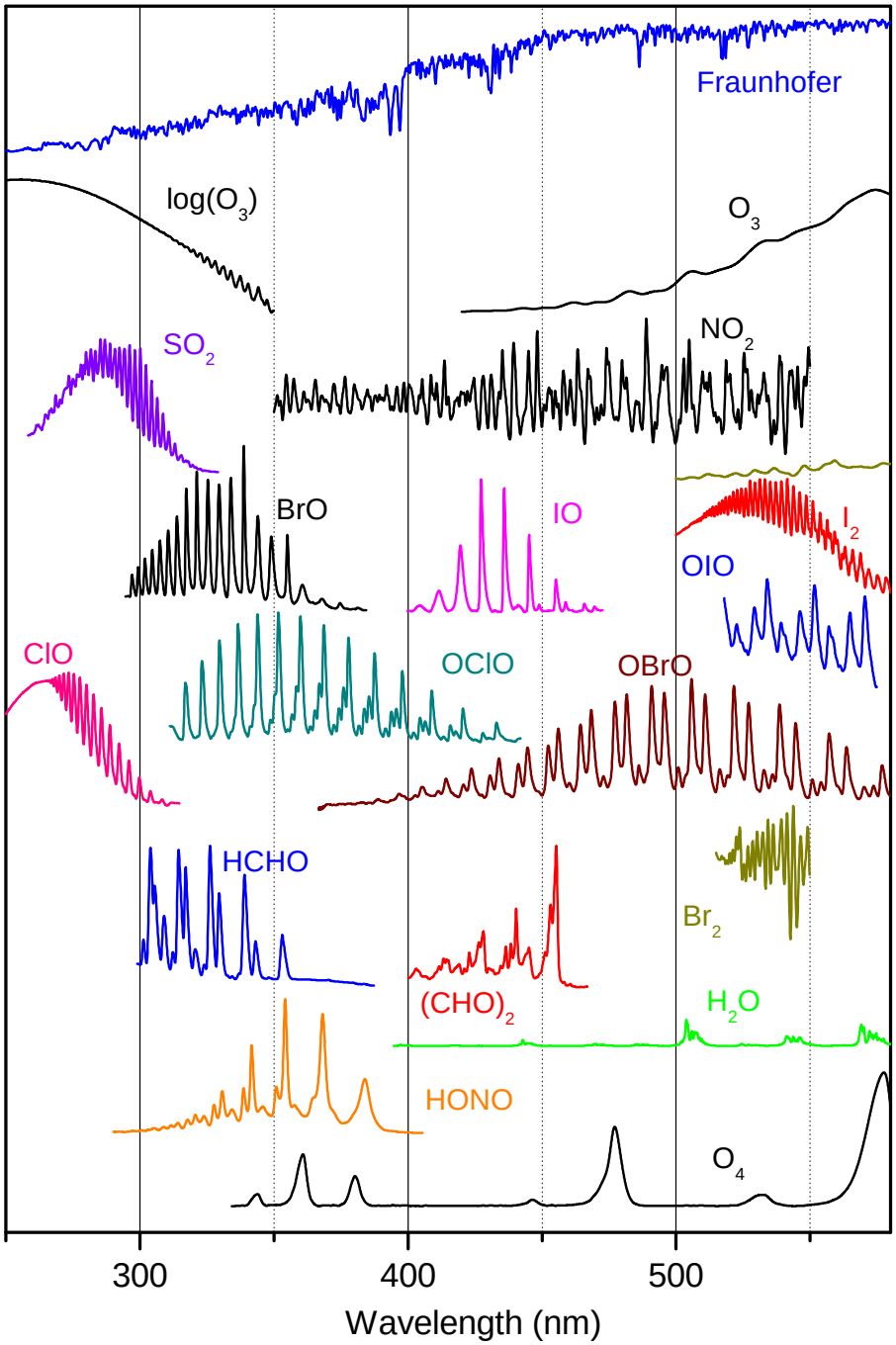

Figure 6.1: Absorption cross sections of UV/vis absorbing trace gases. The cross section of the gases relevant for this thesis are drawn in black. (Courtesy of Udo Friess)

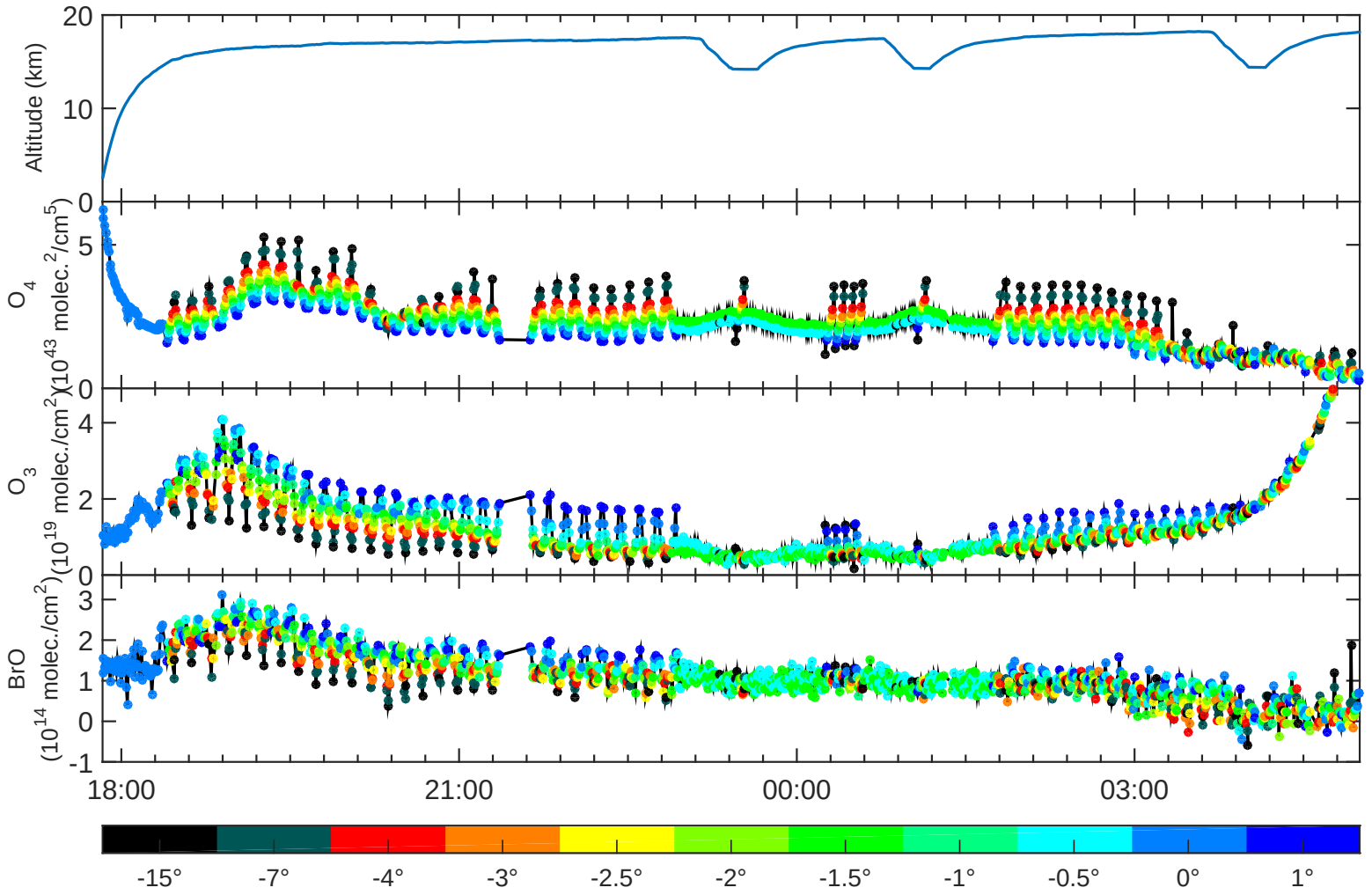

Figure 6.2: Result of the spectral retrieval in the UV range for SF3-2013. Panels top to down: Altitude, O_4 dSCDs, O_3 dSCDs, BrO dSCDs. The colour code indicates the telescope elevation angle.

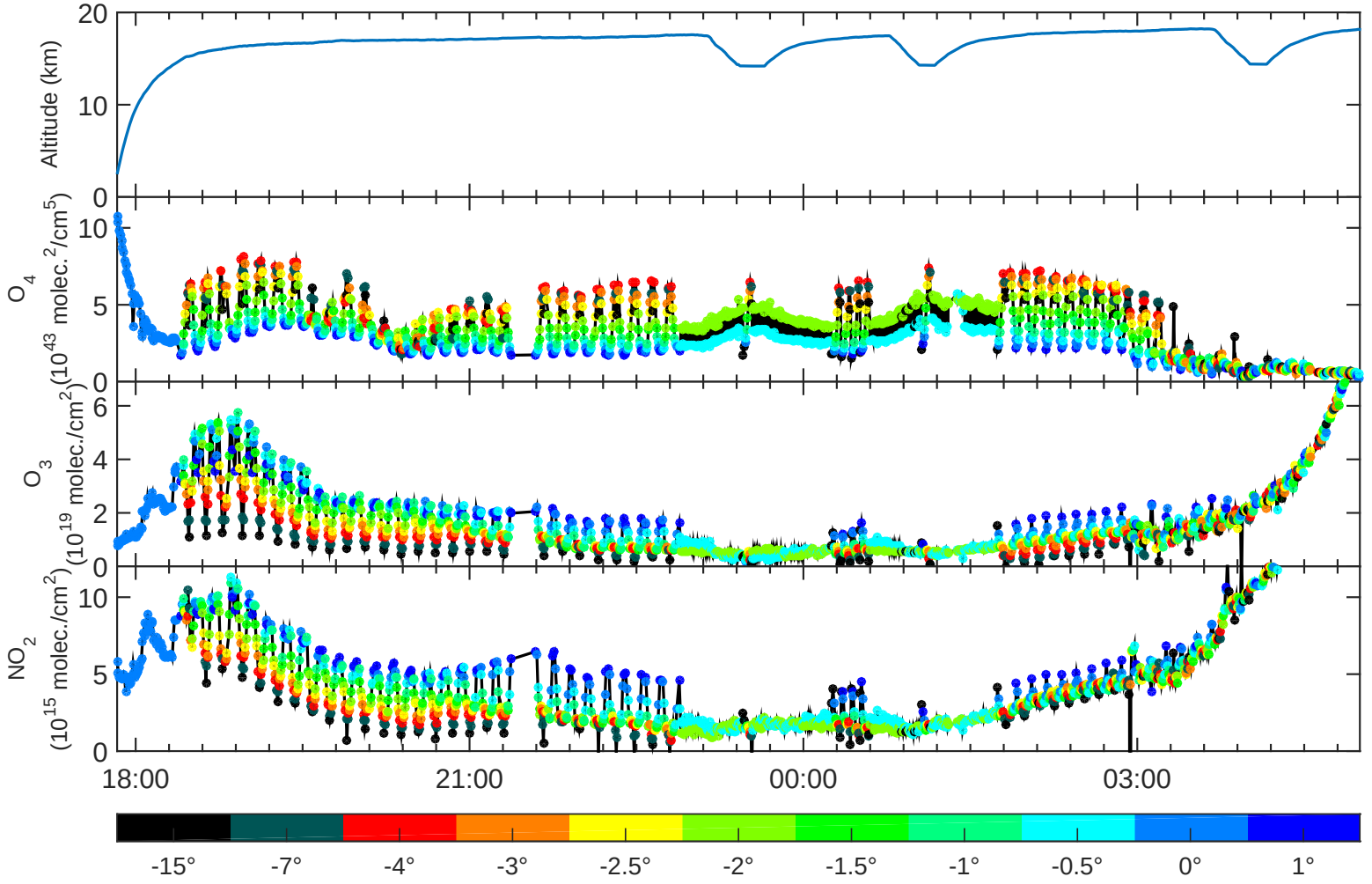

Figure 6.3: Result of the spectral retrieval in the visible range for SF3-2013. Panels top to down: Altitude, O_4 dSCDs, O_3 dSCDs, NO_2 dSCDs. The colour code indicates the telescope elevation angle.

6.2 Radiative transfer modelling

Radiative transfer modelling is used extensively throughout the data analysis process. The measured spectra are scattered sunlight spectra and the collected light made its way throughout the atmosphere before entering the telescope. To retrieve information on trace gas concentrations, it is necessary to determine the contribution of different layers of the atmosphere to the measured signal. Therefore, all radiative processes in the atmosphere of the collected light, have to be modelled. In order to do so, the RTE (section 3.3) has to be solved, or approximated in a sufficient way.

6.2.1 Methods to solve the RTE

An exact analytical solutions of the full RTE has not been found yet, mainly due to the challenge of weak boundary conditions and the 3D nature of radiative transfer (see e.g. Marshak and Davis (2005)). There are different ways of simplifying the RTE. Many approaches make more or less strong approximations in the boundary conditions which have to be justified for the targeted purpose. A very strong approximation is the two-stream approximation which is commonly used in parametrisations of radiative transport in global circulation models (GCM) or in weather forecasting models. Another approximation is to neglect multiple scattering, which is justified for thin atmospheres, i.e. in particular not in the troposphere or in the presence of clouds or high aerosol load. Further the curvature of the Earth (plane parallel models) or polarisation are not taken into account in some RTMs.

Prevalent methods to solve the RTE for the purpose of atmospheric remote sensing are *Discrete Ordinate* and *Monte Carlo* methods. There is no "discrete oridinate method" as such. It is a class of methods in which all relevant coordinates are divided into discrete grid points or cells. The advantage of those methods is that no noise is introduced into the results and the computational effort is relatively small. But this can give a false sense of comfort because discrete ordinate methods may introduce errors due to limited resolution of e.g. the angles.

Monte Carlo methods are the other popular approach of solving the RTE, and also the one which is used for radiative transfer calculations in the frame of the data analysis presented in this work.

6.2.2 The Monte Carlo approach - McArtim

Monte Carlo methods are named after the city of Monte Carlo, known for its casinos. As with gambling, Monte Carlo methods are based on chance. The idea is to follow the path of a photon from one scattering event to the next, and to use random numbers to decide in which direction the photons will proceed after each scattering event, or if it is absorbed, and finally what is the probability to hit the sun (backward) or the detector (forward). Monte Carlo methods basically allow any

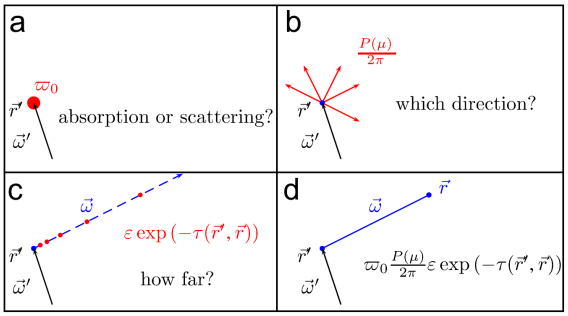

Figure 6.4: Schematic depiction of the random sampling of a) the single scattering albedo ω_0, b) the scatter angle, or phase function P c) the free light path, with ϵ being the extinction coefficient. Panel d) shows all multiplied probabilities which characterize one scatter event. Adopted from Deutschmann et al. (2011)

desired complexity of the RTE but the accuracy of the outputs, intensities, Jacobian or Hessian matrices, is dependent on the number of photons sampling the medium.

An advantage of Monte Carlo methods is that they are easy to understand in the way that they are a real-space approach. Objects influencing the radiative transfer like clouds (also 3D), mountains, etc, can be simply implemented in the domain.

In this study, the fully spherical 3D backward Monte Carlo RTM *McArtim*, developed by Deutschmann et al. (2011), is used for the radiative transfer calculations. Here only a brief summary of the McArtim features is given. For a comprehensive description, see Deutschmann (2008), Deutschmann et al. (2011) and Deutschmann (2014). Figure 6.4 shows the basic principle of the ray-tracing algorithm implemented in McArtim. As described in chapter 5, the FOV of the telescope is very small. Thus, very few photons entering the atmosphere are finally reaching the telescope. Numerical solutions of the RTE follow the so-called *principle of reciprocity*, i.e. that the solution of the time-reversed RTE, the so-called *adjoint RTE*, is the same like for the regular RTE. This works because photons, like all vector bosons, have an odd intrinsic parity. For details of the derivation see again Deutschmann et al. (2011), chapter 2.3.4. McArtim provides both forward and backward tracing of photon trajectory. Backward tracing means that the photon trajectories start at the detector at a given viewing direction and end at the sun. The probability of a photon path happing this way is much larger and the computing time to reach the same precision like in forward tracing is shorter. An illustration is shown in Figure 6.5. The FOV of the telescopes is taken into account by ”shooting” the photons not only directly into viewing direction but also within the range of the FOV opening angle off this direction, weighted by a Gaussian function in order to represent the telescope FOVs in an optimal way.

Figure 6.6 shows the scatter events for a typical viewing geometry. The atmosphere contains a deck of marine strato-cumulus clouds located between 1 and 2 km

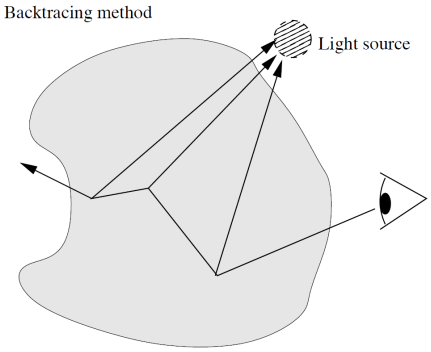

Figure 6.5: Illustration of the MC backtracing method. The starting point of the photons is the detector, indicated by the eye. Adopted from lecture notes of Prof. Dr. Cornelis P. Dullemond, University of Heidelberg (http://www.ita.uni-heidelberg.de/~dullemond/lectures/radtrans_2012/)

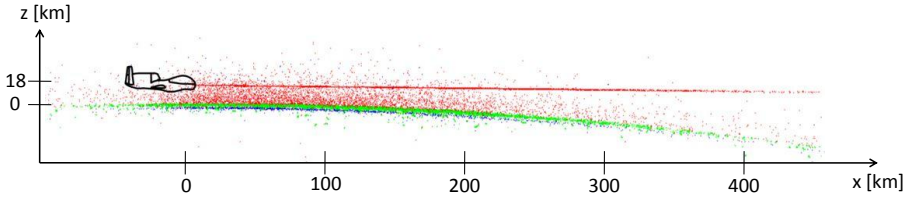

Figure 6.6: 3D simulation of the radiative transfer of the limb measurement at 18 km altitude and wavelength of 350 nm, elevation angle of the telescope -0.5°, 45° solar zenith angle, 90° relative angle between the limb line-of-sight and the sun's azimuth direction. The red, green and blue points mark each Rayleigh, Mie, and ground reflection scattering events, respectively. For details see text.

altitude with optical thickness of $\tau = 30$ and a ground (oceanic) albedo of A = 0.07. Since the RT model is a backward MC model, the line-of sight in limb direction becomes manifest as a bright line of collocated red points (Rayleigh scattering events) starting at aircraft position with a width representing the field of view of the mini-DOAS telescopes. The simulation demonstrates that the Earth's sphericity and atmospheric refraction is relevant for the interpretation of UV/vis/near-IR limb measurements made within the middle atmosphere.

Table 6.3 shows all parameters used in McArtim to describe the geometry and the atmosphere. McArtim allows many more options (e.g. 3D altitude profiles of the terrain) which are not needed for a sufficient model description of the Global Hawk's viewing geometry above the ocean. The last column shows the values (or source of the values) used for the data analysis within this work.

Table 6.3: Overview of the different variables and parameters required for the model atmosphere in McArtim.

Variable name	Description	Unit	Value/source
SZA	Angle between the position of the Sun and the zenith	°	GH INS (Global Hawk Internal Navigation System)
SAA	Azimuth angle of the Sun with respect to the North	°	GH INS
North azimuth	Azimuth viewing direction of the telescope (= viewing direction) towards the north pole meridian; north azimuth = heading direction of the aircraft	°	GH INS
SRAA	Sun relative azimuth angle: angle between the azimuth angle of the Sun and the azimuth viewing direction of the telescope; SRAA = SAA - north azimuth	°	GH INS
Elevation angle α	Angle between the horizon and the line of sight of the telescope: Alternating between	°	see chapter 5
Colatitude	90 ° - latitude	°	GH INS
Longitude		°	GH INS
Altitude	Altitude of the GH	km	GH INS
Ground albedo	Oceanic ground albedo	-	UV: 0.07, VIS:0.2
SSA	Singe scattering albedo (see equation 3.10)	-	Clouds: 0.999 aerosols: 0.97
ϵ (extinction)	Vertical extinction profile of aerosol or cloud particles (see equation 3.11)	km^{-1}	SAGEII
g	Asymmetry parameter of the Henyey-Greenstein parametrisation of the phase function (see equation 3.10)	-	Clouds: 0.75, aerosols: 0.72
Air data	Vertical profiles of temperature and pressure of the air	hPa, K	SLIMCAT
Strong absorbers	Concentration profiles of trace gases with high optical depth in the atmosphere (e.g. O_3, O_4, NO_2) that influence the light path	molec/cm^3	SLIMCAT
FOV	Field of view of the telescopes	°	UV: 0.265° (FWHM) VIS: 0.288° (FWHM)
λ	Wavelength, preferably, the middle wavelength of the analysed wavelength interval	nm	UV: 352 nm, VIS: 442 nm

6.2.3 The BoxAMFs concept

The primary output of the RT calculations are the so-called Box Air Mass Factors (*BoxAMFs*, or just B) which depend on the wavelength λ, the viewing geometry Ω (telescope elevation angle, SZA, SRAA) and the optical state ϵ (e.g. presence of clouds, AOD, strong absorbers like water vapor, etc.) of the atmosphere. They connect the measured and modelled SCDs with the vertical column densities (VCD) which are independent of wavelength, viewing geometry and optical state of the atmosphere:

$$BoxAMF(\lambda, \Omega, \epsilon) = \frac{SCD(\lambda, \Omega, \epsilon)}{VCD} \tag{6.5}$$

Technically in a 1D representation McArtim (or other RTMs) discretises the atmosphere vertically into layers of height h_i, called boxes. McArtim is also able to discretise the atmosphere in full 3D. The resulting voxels are called clusters. The 3D representation is used in section 7.4 when calculating the sensitivity of the measurements ahead of the aircraft. For the purpose of the optimal estimation inversion (7.1) or the other steps of the scaling-method the spherical 1D representation is used.

In the 1D representation the total AMF can be calculated from the BoxAMFs by

$$AMF(\lambda, \Omega, \epsilon) = \frac{\sum\limits_i BoxAMF_i(\lambda, \Omega, \epsilon) \cdot c_i \cdot h_i}{\sum\limits_i c_i \cdot h_i} \tag{6.6}$$

Figure 6.7 shows the BoxAMFs for one scanning sequence of the telescopes. The atmosphere is discretised in 1km high boxes. One can nicely see that the visibility into the lower atmosphere is better in the visible wavelength range (right panel) than in the UV wavelength range due to the larger efficiency of Rayleigh scattering in the UV. Figure 6.2.3 shows all BoxAMFs for SF3-2013. Please note that the plot only shows a "pseudo" 2D illustration of the BoxAMFs since just the complete sequence of the 1D BoxAMFs for each measurement geometry is plotted colour-coded.

Making use of this concept the modelled SCDs can be written as:

$$SCD = \sum_i BoxAMF_i(\lambda, \Omega, \epsilon) \cdot c_i \cdot h_i \tag{6.7}$$

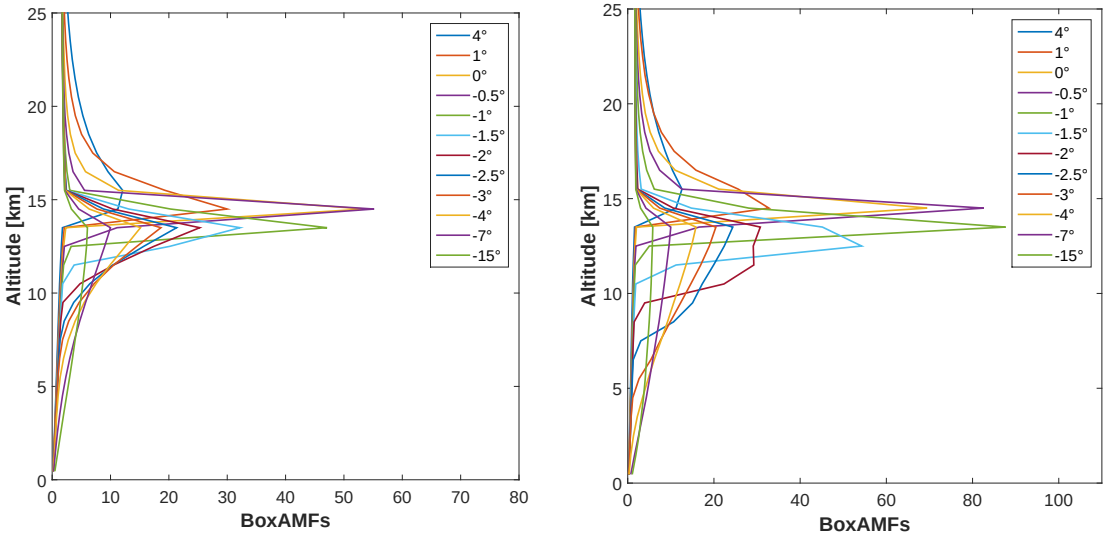

(a) BoxAMFs for 360 nm

(b) BoxAMFs for 477 nm

Figure 6.7: 1D BoxAMFs of one scanning sequence for an atmosphere with a SAGEII zonal mean (25-35°N) aerosol profile. The GH is located at 17.4 km altitude. The atmosphere is vertically discretized in 1 km altitude layers.

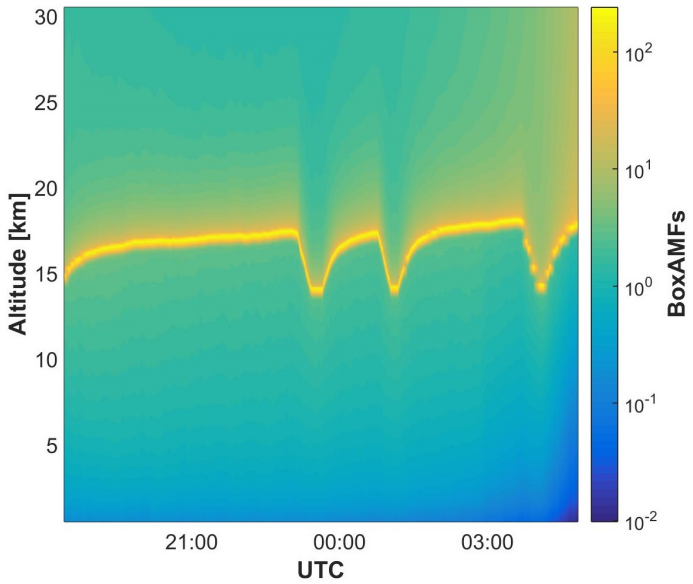

Figure 6.8: BoxAMFs for the complete sunlit part of SF3-2013. Please note the logarithmic colour scale.

6.3 Photochemical transport modelling

Chemical Transport Model (CTM) predictions are used for various purposes during the data analysis. For the present study data of the 3D CTM SLIMCAT (Chipperfield (1999) and Chipperfield (2006)) are used. SLIMCAT output has been used and validated in many studies carried out by the group "Upper Troposphere and Stratosphere" at the IUP Heidelberg (e.g. Weidner et al. (2005), Butz et al. (2006), Dorf et al. (2008), Butz et al. (2009), Kreycy et al. (2013)) during the last decade. The following sections give a description of the SLIMCAT CTM and the specific data product which is used in the frame of the present study.

6.3.1 SLIMCAT

The following description is adopted from the official TOMCAT/SLIMCAT (Chipperfield, 2006) web page [1].

TOMCAT/SLIMCAT is a three-dimensional (3D) off-line chemical transport model (CTM). The model uses winds and temperatures from meteorological analyses (e.g. from the UK Met Office or ECMWF) to specify the atmospheric transport and temperatures and calculates the abundances of chemical species in the troposphere and stratosphere. The model has the option of detailed chemical scheme(s) for the stratosphere and troposphere. The model can be used to simulate the past and current atmosphere, help interpret observations, and to diagnose the extent of problems such as stratospheric ozone depletion or tropospheric pollution.

The first version of TOMCAT was written by Martyn Chipperfield (MPC) Meteo-France in Toulouse in 1992 with the help of Pascal Simon. At this stage the model was used for stratospheric chemistry studies. From 1993 the use and development of the model followed MPC to the Department of Chemistry at the University of Cambridge. Around 1995 MPC wrote SLIMCAT. This was a stratosphere-only version of TOMCAT formulated on isentropic levels. At this time TOMCAT became a 'tropospheric' model and varrious people in Cambridge helped to add treatments of e.g. convection, boundary layer mixing, and tropospheric chemistry. MPC moved to Leeds in 1999 where the model development continues. Recently, SLIMCAT has been extended downwards to include the troposphere. As the two former models were so similar, it made maintenance/development easier to merge TOMCAT and SLIMCAT into a single library with a choice of vertical coordinate (and other things), so that one model covers all of the applications. Depending on the coordinate use, the model is still referred to as TOMCAT or SLIMCAT. For convenience the model is further on simply called SLIMCAT throughout this thesis.

[1] http://homepages.see.leeds.ac.uk/ lecmc/slimcat.html

Main Model Details

- Variable resolution. Typical resolutions are 5 × 5 degrees for multiannual runs to up to 1 × 1 degree.
- Forced by meteorological analyses, usually ECMWF and sometimes UKMO.
- Options of detailed stratospheric or tropospheric chemistry schemes.
- Options of detailed aerosol microphysics (GLOMAP) and PSCs (DLAPSE).
- Chemical data assimilation scheme.
- Embedded trajectory code.
- Written in Fortran (f77, f90). Runs on most platforms (including vector machines). Parallelised using OpenMP and MPI.

6.3.2 SLIMCAT setup for Global Hawk flights

The SLIMCAT model is driven by the ECMWF data with archived ERA-interim convective mass fluxes. Kinetic and photochemical data are from the JPL-2011 recommendations including recent updates (Sander et al., 2011). In the runs, the AGAGE and NOAA [2] CH_4 surface concentrations are assumed. For the brominated species, the following concentrations are assumed: [CH_3Br] = 6.9 ppt, [halons]= 7.99 ppt, [$CHBr_3$] = 1.4 ppt, [CH_2Br_2] = 1 ppt, and Br from $\sum$[$CHClBr_2$, $CHCl_2Br$, CH_2ClBr] = 1 ppt in agreement with recent reports (e.g., WMO (2014), Sala et al. (2014b)) totalling [Br_y^{org}] = 20.55 ppt at the surface. No other (c.f., unknown organic or inorganic) sources of bromine for UT, LS, and TTL are assumed (Fitzenberger et al. (2000), Salawitch et al. (2010),Wang et al. (2015), and others), except a lower limit of 0.5 ppt to the modelled tropospheric BrO is set in agreement with the findings discussed in section 7.4.3.

For the present study, SLIMCAT is run in the so-called trajectory mode. Vertical profiles of 27 species, temperature, pressure and humidity are calculated along the flight trajectories of all Global Hawk flights. The model run is allowed to spin-up since 1979 and from Jan 1., 2013, has a 1.2 x 1.2 degree horizontal resolution. The vertical resolution depends on the altitude. 36 vertical levels are unevenly distributed from ground up to ∼63 km with the highest resolution of 1 km around the UT/LS. Figure 6.9 shows an example of the curtain data of NO_2, BrO and O_3 for the flight SF3-2013. The SLIMCAT curtains for the other 2013 flights can be found in Appendix B. For the interpretation of the GH measurements the curtain data are further interpolated on finer grids and then vertically adjusted for small-scale dynamical features, e.g. due to small scale gravity waves. The details of the applied data processing in order to make it applicable for the GH measurements are described in section 7.4.2.

[2] https://agage.mit.edu/

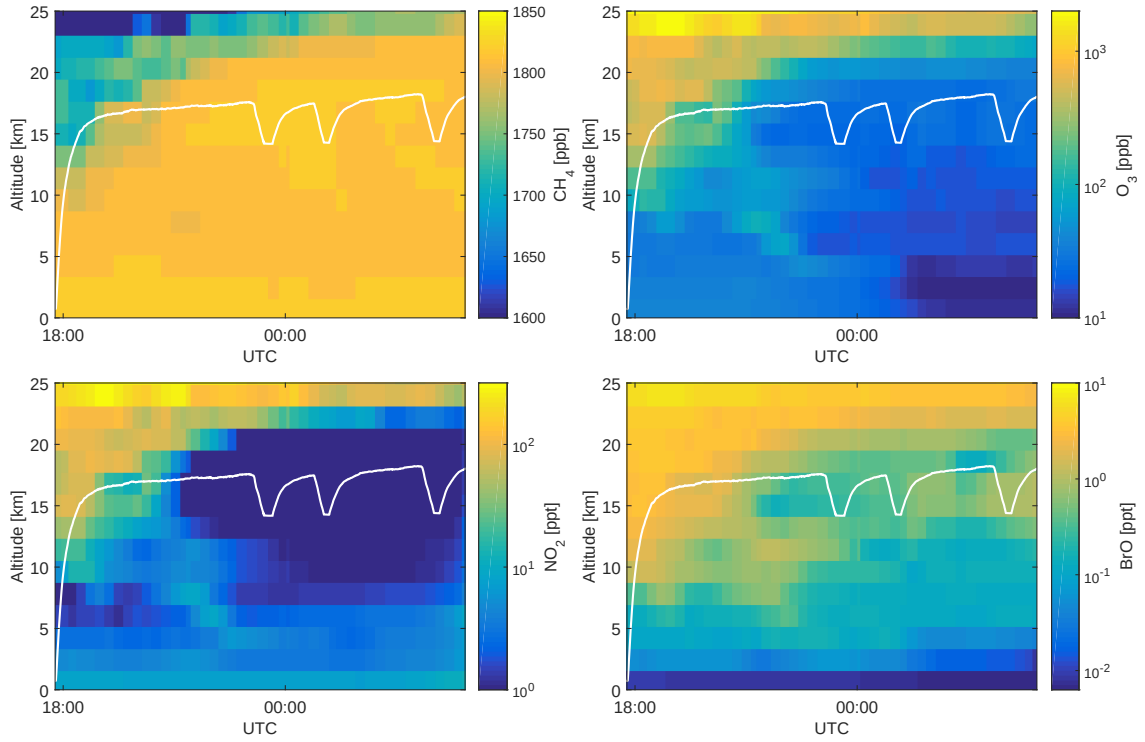

Figure 6.9: Example of SLIMCAT mixing ratio curtains along the flight track of SF3-2013. Upper left panel: CH_4, upper right panel: O_3, lower left panel: NO_2, lower right panel: BrO. The white lines indicate the altitude profile of the GH.

The inclusion of SLIMCAT curtains in this study was particularly necessary for (a) the retrieval of absolute concentrations using the O_3-scaling-method (see section 7.4), (b) for the estimate of errors and retrieval sensitivities to various parameters (see section 7.4.3 and Appendix A), (c) the separation of dynamical and photochemical processes in the interpretation of the DOAS data (chapter 8) and (d) the assessment of total Br_y^{inorg} (see section 7.7).

6.3.3 SLIMCAT photochemical sensitivity runs

The standard run with the kinetic and photochemical data according to Sander et al. (2011) is further on called run #583. Two other runs with modified chemical kinetics regarding inorganic bromine chemistry are performed:

- In run #584 the ratio of the photolysis frequency of $BrONO_2$ and the three-body association rate reaction coefficient $k_{BrO+NO2}$ is set to 1.75 according to the finding of e.g. Kreycy et al. (2013).
- In run #585 the two-body rate reaction coefficient k_{Br+O3} is set to the upper limit of the uncertainty range given in Sander et al. (2011) (Figure 6.10).

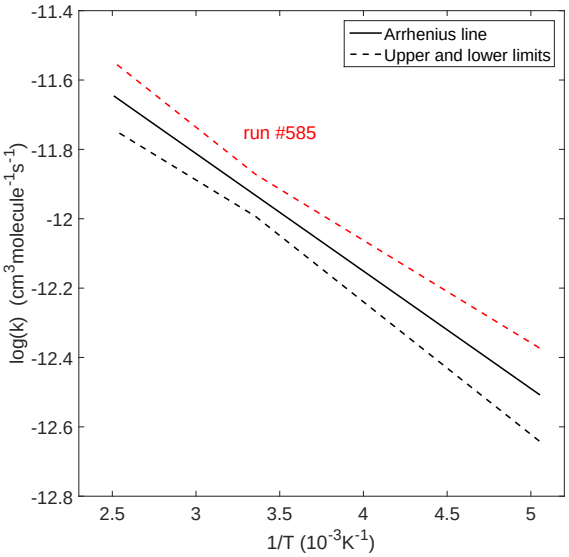

Figure 6.10: Arrhenius plot of Br + O_3 including the uncertainties given in Sander et al. (2011). The black solid line corresponds to the standard run #583, the red dashed line to run #585.

Both runs change the internal ratio of inorganic bromine species, called Br_y^{inorg} partitioning, in favour of an increased BrO formation.

7 Trace gas retrieval: Inversion, sensitivity studies and error analysis

This chapter introduces two approaches to invert the measured trace gas dSCDs to absolute concentrations. The first approach is the *optimal estimation (OE) inversion*. It is a wide-spread approach for the interpretation of e.g. ground-based MAX-DOAS (e.g. Frieß et al. (2011), ...), satellite-borne (e.g. Parrella et al. (2013), Rozanov et al. (2011), ...), or also aircraft-borne (e.g. Prados-Roman et al. (2011), Volkamer et al. (2015)) DOAS measurements. Section 7.1 explains the mathematical background, while section 7.2 illustrates the technical implementation. Section 7.3 shows why this approach is not well-suited for the Global Hawk measurements. In section 7.4 the second approach, the so-called *O_3-scaling-method* – a novel method to derive mixing ratios from the dSCDs by combining dSCDs, in-situ measured O_3 and radiative transfer modelling – is introduced. Section 7.5 compares both approaches.

7.1 Optimal Estimation Inversion

In atmospheric remote-sensing usually it is not possible to measure directly the quantities of interest but other quantities depending in some way on those. Following the nomenclature of Rodgers (2000) the quantities of interest are assembled in the state vector $\mathbf{x}$ ($dim = n$), the measurements in the vector $\mathbf{y}$ ($dim = m$). The measurement is connected with the state by the *forward function* $\mathbf{f}$

$$\mathbf{y} = \mathbf{f}(\mathbf{x}) \tag{7.1}$$

The exact forward function f is not known and has to be replaced by the forward model *forward model* $\mathbf{F}$ which contains a sufficient representation of the physical processes connecting $\mathbf{x}$ and $\mathbf{y}$:

$$\mathbf{y} \approx \mathbf{F}(\mathbf{x}, \mathbf{b}) + \epsilon \tag{7.2}$$

where $\mathbf{b}$ are parameters that shall not be obtained by the measurements but are needed in the forward model and ϵ is the measurement error vector. Often the relation 7.2 is not bijective and/or the inverse problem is ill-posed in the sense of information content of $\mathbf{x}$ and $\mathbf{y}$ and is therefore under-constrained. As a consequence the inverse forward function $\mathbf{F^{-1}}$ can not be found. In order to constrain the problem it is useful to introduce an *a priori* estimate $\mathbf{x_a} + \epsilon_\mathbf{a}$ of the state which represents the

best knowledge of $\mathbf{x}$ before the measurement. After making the measurement, one seeks an improved estimate $\hat{\mathbf{x}}$ of $\mathbf{x}$ which better fits the constraints imposed by the measurements and by the a priori estimate. Assuming Gaussian error distributions, the probability distribution of $\mathbf{x}$ and of $\mathbf{y}$ given $\mathbf{x}$ are:

$$P(\mathbf{x}) = \frac{1}{\mathbf{S}_a\sqrt{2\pi}^n} exp\left[-\frac{1}{2}(\mathbf{x}-\mathbf{x}_a)^T\mathbf{S}_a^{-1}(\mathbf{x}-\mathbf{x}_a)\right] \tag{7.3}$$

$$P(\mathbf{y}|\mathbf{x}) = \frac{1}{\mathbf{S}_\epsilon\sqrt{2\pi}^{mn}} exp\left[-\frac{1}{2}(\mathbf{F}(\mathbf{x})-\mathbf{y})^T\mathbf{S}_\epsilon{}^{-1}(\mathbf{F}(\mathbf{x})-\mathbf{y})\right] \tag{7.4}$$

S_ϵ and S_a are the measurement and a priori error covariance matrices containing as diagonal elements the squared errors of the measurement and the a priori, respectively.

Applying Bayes' theorem and ignoring the normalising terms that are independent of $\mathbf{x}$, one obtains

$$P(\mathbf{x}|\mathbf{y}) \sim exp(-\left[(\mathbf{F}(\mathbf{x})-\mathbf{y})^T\mathbf{S}_\epsilon^{-1}(\mathbf{F}(\mathbf{x})-\mathbf{y}) + (\mathbf{x}-\mathbf{x}_a)^T\mathbf{S}_a^{-1}(\mathbf{x}-\mathbf{x}_a)\right]) \tag{7.5}$$

Finding the maximum value for $P(\mathbf{x}|\mathbf{y})$ - the maximum likely state to describe the measurements - is equivalent to finding the minimum in the *cost function*:

$$\chi^2(\mathbf{x}) = \left[(\mathbf{F}(\mathbf{x})-\mathbf{y})^T\mathbf{S}_\epsilon^{-1}(\mathbf{F}(\mathbf{x})-\mathbf{y}) + (\mathbf{x}-\mathbf{x}_a)^T\mathbf{S}_a^{-1}(\mathbf{x}-\mathbf{x}_a)\right] \tag{7.6}$$

The optimal state $\hat{\mathbf{x}}$ is the solution to

$$\nabla_{\mathbf{x}}\chi^2(\mathbf{x}) = 0 \tag{7.7}$$

Depending on the nature of the forward model the solution $\hat{\mathbf{x}}$ can be found directly for the linear case or iteratively for the non-linear case.

Linear case

For the linear case the forward model can be formulated as::

$$F(\mathbf{x}) = \mathbf{K}\mathbf{x} \rightarrow \nabla_{\mathbf{x}}F(\mathbf{x}) = \mathbf{K} \tag{7.8}$$

where $\mathbf{K}$ is the so-called Kernel matrix or weighting function matrix, containing the partial derivates $K_{ij} = \partial F_i(\mathbf{x})/\partial x_j$. Combining 7.8 with 7.7 yields:

$$\hat{\mathbf{x}} = (\mathbf{S}_a^{-1} + \mathbf{K}^T\mathbf{S}_\epsilon^{-1}\mathbf{K})^{-1}(\mathbf{K}^T\mathbf{S}_\epsilon^{-1}\mathbf{y} + \mathbf{S}_a^{-1}\mathbf{x}_a) \tag{7.9}$$

Non-linear case

For the non-linear case the replacement 7.8 can not be made. Numerical methods must be applied to minimise the cost function. Major minimisation algorithms are the *Gauss-Newton algorithm* or the *Levenberg-Marquardt algorithm*. Starting from the gradient of the cost function:

$$\nabla_{\mathbf{x}}\chi^2(\mathbf{x}) = \frac{1}{2}\left[\mathbf{K}^T\mathbf{S}_\epsilon^{-1}(\mathbf{F}(\mathbf{x})-\mathbf{y}) + \mathbf{S}_a^{-1}(\mathbf{x}-\mathbf{x}_a)\right] := \mathbf{g}(\mathbf{x}) \tag{7.10}$$

The Gauss-Newton iteration scheme introduces:

$$\mathbf{x}_{i+1} = \mathbf{x}_i - \left[\nabla_{\mathbf{x}}\mathbf{g}(\mathbf{x}_i)\right]^{-1}\mathbf{g}(\mathbf{x}_i) \tag{7.11}$$

with the Hessian elements

$$\mathbf{H}_{GN} = \nabla_{\mathbf{x}}\mathbf{g}(\mathbf{x}) = \nabla_{\mathbf{x}}\mathbf{K}^T\mathbf{S}_\epsilon^{-1}(\mathbf{F}(\mathbf{x})-\mathbf{y}) + \mathbf{K}^T\mathbf{S}_\epsilon^{-1}\mathbf{K} + \mathbf{S}_a^{-1} \tag{7.12}$$

The second derivatives in the first term converge to zero near the minimum if the forward model sufficiently describes the real system and can therefore be neglected. Combining 7.11 and 7.12 yields:

$$\mathbf{x}_{i+1} = \mathbf{x}_i - (\mathbf{S}_a^{-1} + \mathbf{K}^T\mathbf{S}_\epsilon^{-1}\mathbf{K})^{-1}\left[\mathbf{K}^T\mathbf{S}_\epsilon^{-1}(\mathbf{F}(\mathbf{x})-\mathbf{y}) - \mathbf{S}_a^{-1}(\mathbf{x}-\mathbf{x}_a)\right] \tag{7.13}$$

There are cases in which the Gauss-Newton algorithm diverges. In order to guarantee the convergence of the iteration to the correct solution, Levenberg (Levenberg, 1944) and Marquardt (Marquardt, 1963) suggested to modify the Hessian elements of the Gauss-Newton method and to use:

$$\mathbf{H}_{LM} = \mathbf{H}_{GN} + \gamma\mathbf{S}_a^{-1} \tag{7.14}$$

The final Levenberg-Marquardt iteration scheme is then:

$$\mathbf{x}_{i+1} = \mathbf{x}_i - \left[(1+\gamma)\mathbf{S}_a^{-1} + \mathbf{K}^T\mathbf{S}_\epsilon^{-1}\mathbf{K})^{-1}\right]\left\{\mathbf{K}^T\mathbf{S}_\epsilon^{-1}(\mathbf{F}(\mathbf{x})-\mathbf{y}) - \mathbf{S}_a^{-1}(\mathbf{x}-\mathbf{x}_a)\right\} \tag{7.15}$$

The Levenberg-Marquardt algorithm combines the *steepest descent* and the Gauss-Newton method. Depending on the local situation of the χ^2-landscape the mixture is controlled by the parameter γ. If the gradient is strongly non-linear, γ should be increased. For very high γ the L.-M. algorithm converges to the slow but stable steepest descent method. If the $\mathbf{g}(\mathbf{x})$ is approximately linear, γ should be decreased that the method is more like the faster Gauss-Newton method.

Rodgers (2000) suggests the following strategy to adjust γ:

1. Find good estimate of $\mathbf{x}$, e.g. take $\mathbf{x}_a$

2. Apply 7.15 to find $\mathbf{x}_{i+1} := \mathbf{x}_{trial}$
3. Calculate $\chi^2(\mathbf{x}_{trial})$ with 7.6
4. Check if $\chi^2(\mathbf{x}_{trial}) < \chi^2(\mathbf{x}_i)$
   - if yes: set $\mathbf{x}_{i+1} = \mathbf{x}_{trial}$ and divide γ by a factor (e.g. 10)
   - if no: multiply γ by a factor (e.g. 10) and check again
5. Continue with step 2 until an abort criterion is reached

This strategy assures that each iteration step decreases the cost function. Step for step the algorithm iterates towards the optimal compromise between the forward modelled state and the measurements. Hence the name "optimal estimation".

7.2 MaRS retrieval

The initial intention was to retrieve a profile from the GH mini-DOAS measurement by a full inversion for each limb scan and ascent or descent. Full inversion means that in a first step the optical state, especially the aerosol and cloud profile, is retrieved by means of a non-linear inversion. In a second step the retrieved optical state is used to calculate the light paths in the atmosphere. In this case a linear inversion is used and the measurement vector is described by the slant column densities.

In the frame of the present work a full retrieval scheme was written in MATLAB[1] which uses the RTM McArtim (see section 6.2.2). The program is written in a way that it is easily suitable for other platforms or instruments than the Global Hawk instrument, e.g. other aircraft-borne instruments like the HALO instrument, ballon-borne instruments or ground-based MAX-DOAS instruments. Since it is possible to switch between different constraints (explained in the next paragraph) the software is called Master Retrieval Software "MaRS". The code was also already used in studies of Großmann (2014). Figure 7.1 shows an overview of the MaRS workflow.

MaRS uses *l multiple wavelengths* and works on a *1D altitude grid*, that means the atmosphere is divided into n vertical clusters (not necessarily equidistant) and allows to retrieve the aerosol/cloud extinction profile $\boldsymbol{\epsilon}(\lambda)$, the single scattering albedo $\boldsymbol{\omega}_0(\lambda)$, the asymmetry parameter $\mathbf{g}(\lambda)$ for the Henyey-Greenstein parametrisation (see section 3.2.2) of the phase function for each cluster as well as the Ångström exponent α (equation 3.11). Accordingly the state vector $\mathbf{x}$ consists of the aerosol extinction profile and optionally the optical parameters:

$$\mathbf{x} = [\boldsymbol{\epsilon}(\lambda_{ref}), \boldsymbol{\omega}_0(\lambda_1), .., \boldsymbol{\omega}_0(\lambda_l), \mathbf{g}(\lambda_1), .., \mathbf{g}(\lambda_l), \alpha]^T \tag{7.16}$$

where λ_{ref} denotes the reference wavelength for which the extinction profile is given. λ_l refer to the other wavelength which are considered in the retrieval. When several

[1] http://de.mathworks.com/

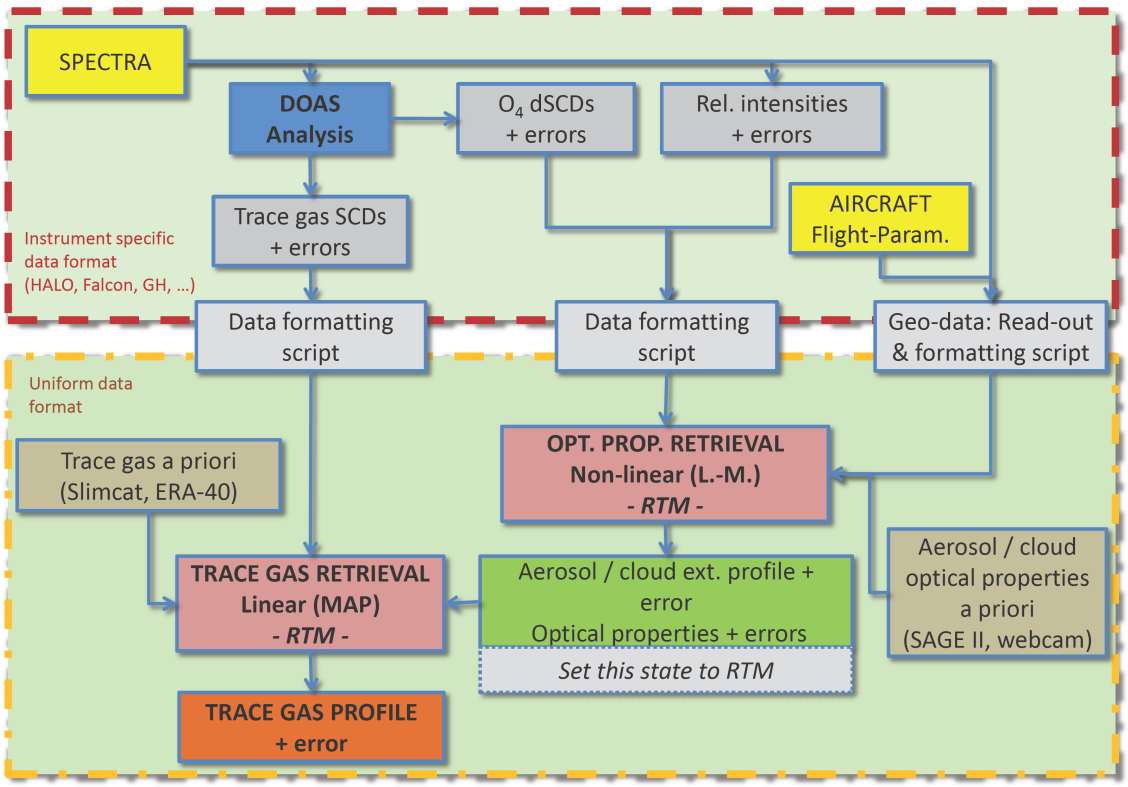

Figure 7.1: MaRS flow chart. The two main mathematic inversions happen in the red shaded boxes. The retrieval of the optical properties of the atmosphere needs a non-linear scheme while the trace gas retrieval is a linear process. The MaRS retrieval can be applied to other platforms and instruments adapting only the underlying functions in the red dashed box.

wavelengths are used simultaneously the aerosol extinction profile is converted to the according wavelength using α. In the case of a retrieval using only one wavelength and only the extinction profile should be retrieved, the state vector simply looks like:

$$\mathbf{x} = \boldsymbol{\epsilon}(\lambda_{ref}) \tag{7.17}$$

The retrieval can be constrained by either measured O_4 absorptions or measured radiances or both. When both are used at multiple wavelengths (O_4 absorption band respectively) the full measurement vector is

$$\mathbf{y} = (\mathbf{y}_{O_4}, \mathbf{y}_I)^T \tag{7.18}$$

$$= \left\{ [\mathbf{S}_{O_4}(\lambda_1), ..., \mathbf{S}_{O_4}(\lambda_l)]^T, [\mathbf{I}(\lambda_1), ..., \mathbf{I}(\lambda_l)]^T \right\} \tag{7.19}$$

where $\mathbf{S}_{O_4}$ and $\mathbf{I}$ are again vectors

$$\mathbf{S}_{O_4} = (S_{O_4,1}, ..., S_{O_4,m})^T \tag{7.20}$$

$$\mathbf{I} = (I_1, ..., I_m)^T \tag{7.21}$$

with m measurements. Since the measured and modelled intensities have different units, a normalization is necessary

$$I_{norm,i},(\lambda) = \frac{I_i(\lambda)}{I_{ref}(\lambda)}, \text{ with } i = 1...m \tag{7.22}$$

The forward modelled O_4 absorption, the relative intensities as well as the needed Jacobian matrix is calculated with the radiative transfer model. With the normalisation 7.22 also the partial derivatives have to be normalised:

$$\mathbf{K}_I = \frac{\partial \mathbf{y}_I(\lambda)}{\partial \mathbf{x}} \tag{7.23}$$

$$\rightarrow \mathbf{K}_{I,norm} = \frac{\partial \mathbf{y}_I(\lambda)}{\partial \mathbf{x}} \cdot \frac{1}{y_{I,ref}(\lambda)} - \frac{\partial y_{I,ref}(\lambda)}{\partial \mathbf{x}} \cdot \frac{\mathbf{y}_I(\lambda)}{y_{I,ref}(\lambda)} \tag{7.24}$$

7.3 O_4 as a proxy for atmospheric light path length

The optical state retrieved in the first step of the full optimal estimation inversion (in Figure 7.1 the upper right red box) represents the b parameters (see equation 7.2) of the following linear trace gas inversion (lower left red box). It is crucial to obtain the best retrieval for the optical state because its constraints on the trace gas inversion lead to more reliable results.

A wide-spread approach for retrieving the optical state is to make use of the oxygen collisional complex O_4 as light path proxy. This section first explains the physics of the O_4 and then shows why this approach is not well-suited for the purpose of analysing the Global Hawk DOAS measurements.

7.3.1 O_4 physics

O_4 is a collisional complex of two O_2 molecules. It is also called tetraoxygen and was first predicted in 1924 by Lewis (1924). Due to the unknown life time and rate coefficient of O_2+O_2 it is not possible to measure the absolute absorption cross section of O_4 but the product of the squared O_2 concentration multiplied by the equilibrium constant:

$$\epsilon_{O_4,measured} = [\mathrm{O_2}]^2 \cdot k_{eq} \cdot \sigma_{O_4} \tag{7.25}$$

Thus, the unit of the O_4 cross section is $[cm^5 \cdot molecule^{-2}]$ and the O_4 concentration is given in $[molecule^2 \cdot cm^{-5}]$.

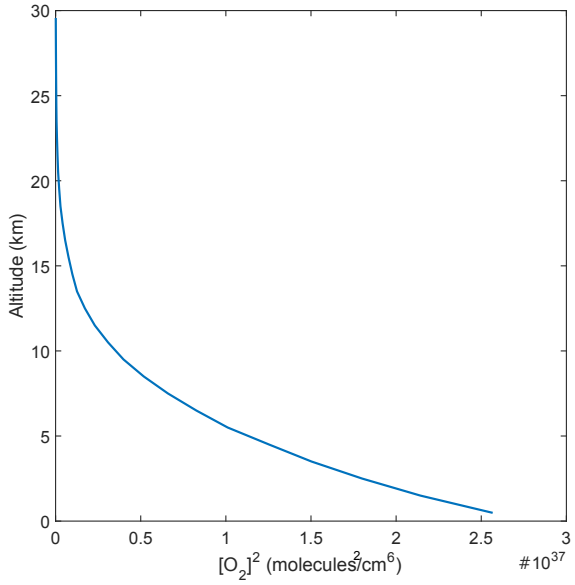

Figure 7.2: $[O_2]^2$ profile derived from pressure and temperature profile of SF3-2013.

Since O_2 has a constant atmospheric volume mixing ratio (20.9%) the concentration of O_4 decreases exponentially with altitude with a scale height of approximately 4 km. With a known pressure and temperature profile also the O_4 concentration profile can be evaluated as follow:

$$[O_4](z) = k_{eq} \cdot [O_2]^2(z) = k_{eq} \left(\frac{P(z)}{k_B \cdot T(z)} \cdot 0.209 \right)^2 . \tag{7.26}$$

Absorption bands of O_4 are caused by simultaneous transitions of two O_2 molecules from their ground states to electronically excited states. Of special interest for this work are the absorption bands at 360 nm and 477 nm. The 360 nm band is caused by the transition from the ground state ${}^3\Sigma_g^- + {}^3\Sigma_g^-$ to the excited state ${}^1\Sigma_g^+ + {}^1\Sigma_g^+$ with the vibrational quantum number $\nu = 1$. The excited state of the 477 nm band is ${}^1\Sigma_g^+ + {}^1\Delta_g$ with the vibrational quantum number $\nu = 0$.

By virtue of knowing the pressure and temperature profile, the extinction profile of O_4 is also known (equation 7.26), changes in O_4 absorption can be used as an indicator for changes in atmospheric light paths.

7.3.2 Problems when constraining the RT by O_4 on high-flying moving platforms

There are several studies with various observation geometries in which O_4 is used to constrain the radiative transfer, e.g. for ground-based MAX-DOAS measurement Hönninger et al. (2004), Wagner et al. (2004) Frieß et al. (2006), Irie et al. (2008), Irie

et al. (2011), Clémer et al. (2010) and Yilmaz (2012), or for airborne measurements Prados-Roman et al. (2011) and Volkamer et al. (2015).

Two major criteria are important for the quality of the optical state (here i.e. the aerosol/cloud profile) retrieval:

- the altitude of the observer
- the change of the aerosol/cloud profile during one observation period due to the movement of the observer (e.g. moving aircraft) or to time-dependent changes of particles (e.g. moving clouds)

It is important to understand the meaning of an observation period for the retrieval. An observation period includes all measured optical densities, or dSCDs respectively, which are taken into account for constraining an individual retrieval. This corresponds to a telescope elevation scanning sequence or an ascent/descent of the aircraft. All observations in this period are treated like simultaneous measurements, i.e. all measurements "see" the same atmosphere. However, e.g. an ascent of the GH takes about 45 min. The aerosol/cloud retrieval only operates on the altitude coordinate. No temporal or horizontal changes are considered. The retrieved optimal state vector is therefore an averaged compromise of all occurring situations during the regarded period.

Here, it has to be mentioned that there is a balloon-borne study of Kritten et al. (2010) that includes a time dependent kernel to account for changes of the a priori profile due to photochemistry. However, the atmospheric state that influences the RT is also not treated time dependent.

The altitude of the observer is an essential criterion considering that the O_4 concentration decreases exponentially with altitude. Frieß et al. (2006) states: "Since the bulk concentration of O_4 is located close to the surface, the optical depth of O_4 is very sensitive to changes in the light path distribution at low altitudes."

But the altitude criterion can not be considered without the second point. Platforms like the Global Hawk or the Gulf Stream V aircraft (NSF/NCAR GV), reach altitudes of 15 km to 19 km and horizontal air speeds of >200 m/s. This altitude is approximately 5 times the scale height of O_4, i.e. the concentration is only 0.7% of the concentration at ground level. Therefore it is evident that especially changes in the cloud coverage at low altitude (e.g. marine stratocumulus clouds, further "mSc") strongly influence the measured O_4 optical depths. Figure 7.3 shows the altitude dependent contribution to the measured O_4 optical depth (OD) for different cloud scenarios (see figure text). The contribution function is the layer-wise multiplication of the BoxAMFs (Figure 6.7) and the O_4 profile (Figure 7.2). The integral below the curve, which is the total OD, changes strongly due to the increasing amount of upwelling photons carrying O_4 absorption from the lower troposphere. Also the thicker the cloud the more the light path within the cloud is enhanced before photons leaving the cloud. Table 7.1 shows the exact values of the modelled ODs. Conversely,

Table 7.1: O_4 ODs ($\times 10^3$) corresponding to Figure 7.3. The rows indicate the telescope elevation angles, the columns the mSc ODs (panels in figure).

mSc OD	**0**	**1**	**5**	**10**	**20**	**50**
Elev. angle						
+1°	3.87	5.51	7.56	8.47	9.18	9.5
+0°	4.35	5.92	8.05	9	9.59	10.02
-0.5°	4.55	6.14	8.35	9.23	9.88	10.21
-1°	5	6.68	8.84	9.73	10.35	10.66
-1.5°	5.54	7.17	9.32	10.24	10.9	11.23
-2°	6.07	7.7	9.88	10.81	11.55	11.79
-2.5°	6.58	8.23	10.52	11.41	12.13	12.38
-3°	7.02	8.81	11.01	11.99	12.58	12.99
-4°	7.98	9.82	12.09	13.13	13.69	14.08
-7°	9.84	11.81	14.21	15.21	15.95	16.27

the contribution from flight altitude does not change. Small changes in O_4 ODs due to the aerosol load at high altitudes are completely masked by even slight changes in low cloud cover.

However, if there is clear sky or the cloud cover does not change in the course of an observation period (e.g. an ascent of the aircraft), the aerosol retrieval delivers reasonable results. Volkamer et al. (2015) shows a Mie extinction retrieval for two ascends of the aircraft (NSF/NCAR GV) during the TORERO campaign, Eastern Pacific from ground up to 12 km. The meteorological condition is commented as "Both flights were from/to San Jose, Costa Rica and headed West over the Northern Hemisphere tropical Eastern Pacific Ocean to probe mostly cloud free air". It is not stated what "mostly" exactly means. During all flights of both, 2013 and 2014, NASA-ATTREX missions (see Figure 4.4) there was no cloud-free area of the extent of the visual range of the mini-DOAS which is up to 300 km (see Figure 7.7). Figure 7.4 shows two pictures of the GH belly cam taken in a 10 min interval. Not only the horizontally averaged optical depth of the mSc changes but also the horizontal distribution of the cloud patches. This also affected the light paths in the lower troposphere.

Figure 7.5 shows the measured O_4 ODs during the ascent of the second dive of SF3-2013. There is elevated O_4 absorption when mSc patches are located in the line of sight. The changes in the OD due to changes in low cloud cover are in the range of $\sim 0.5 \cdot 10^{-3}$.

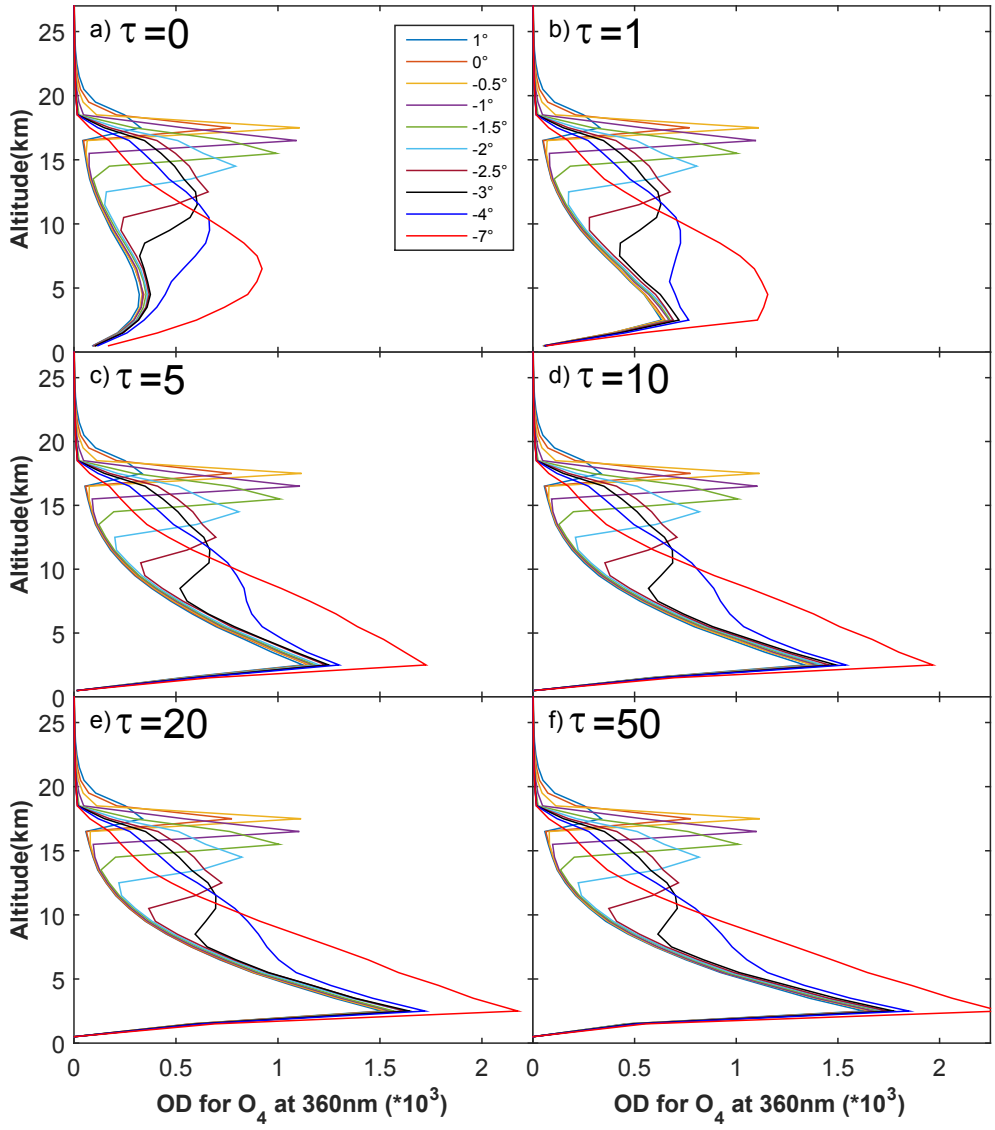

Figure 7.3: Altitude dependent contribution function to the simulated optical densities of the O_2 + O_2 collisional complex (O_4) at 360 nm for limb measurements at 18 km and different observation angles, as indicated in the legend of panel a.). In the simulations, a deck of marine stratocumulus clouds (mSc) located between 1 and 2 km with different cloud optical depth τ_{mSc} is assumed, since, according to the cloud physics Lidar measurements (CPL), mSc were frequently occurring during the NASA-ATTREX flights over the Eastern Pacific. Panel a.) is for clear skies, panel b.) for $\tau_{mSc} = 1$, panel c.) for $\tau_{mSc} = 5$, panel d.) for $\tau_{mSc} = 10$; panel e.) for $\tau_{mSc} = 20$, and panel f.) for $\tau_{mSc} = 50$. The integrals below the curves correspond to the optical density an observer would measure for the given conditions.

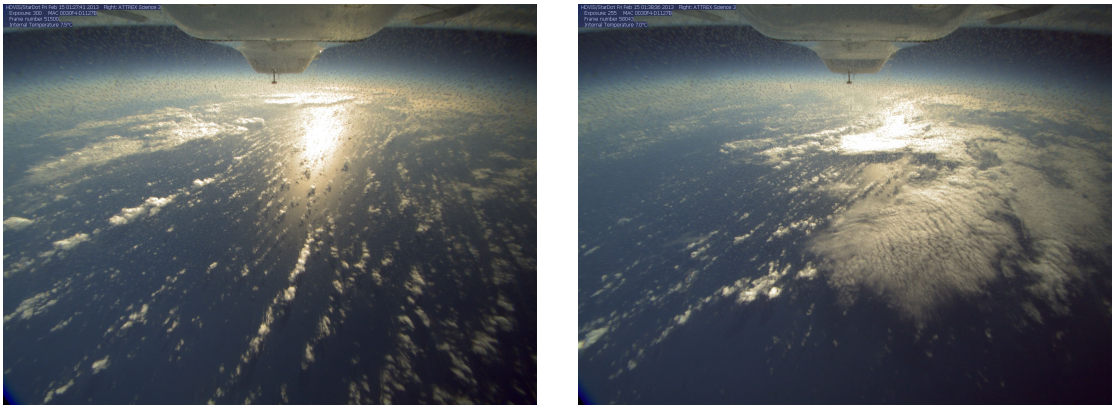

(a) Feb. 15, 01:27 UT. **(b)** Feb. 15, 01:37 UT.

Figure 7.4: GH belly cam pictures taken at the end of the ascent of the second dive in SF3-2013. The time difference between both pictures is only 10 minutes.

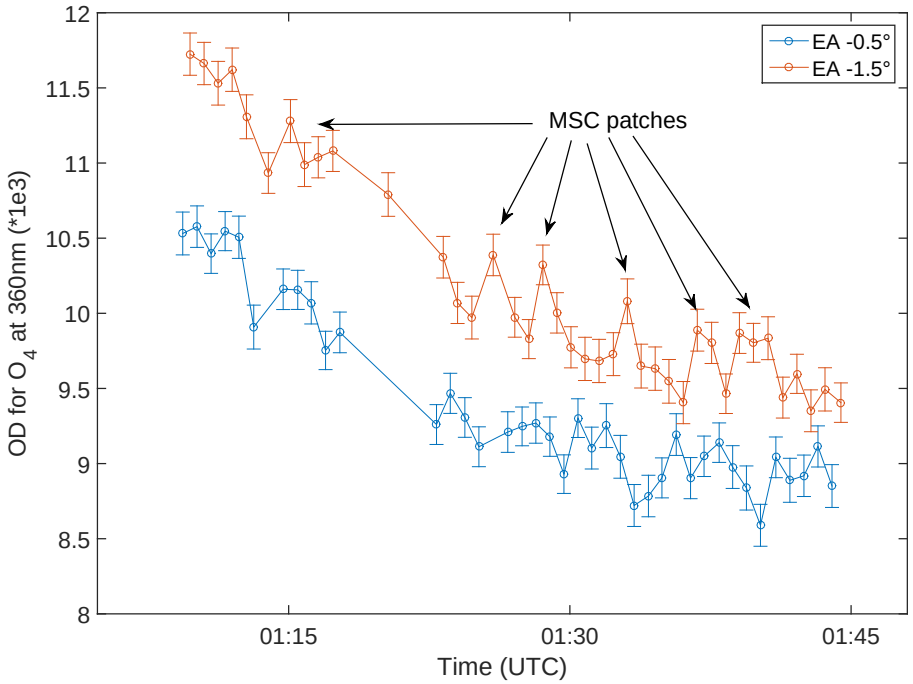

Figure 7.5: Measured O_4 ODs during the ascent of the second dive in SF3-2013. The telescope elevation angle alternates between -0.5° (blue) and -1.5° (red). The arrows indicate measurements in which a mSc patch was located in the line of sight.

7.4 Scaling method

To overcome the two major problems of an OE retrieval, essentially the lack of knowledge about the optical state, and the changing atmosphere (either the optical state or the a priori concentration profiles), a novel method is developed that overcomes these two problems in an elegant way. The knowledge about the light path is gained by comparing in-situ and remotely measured O_3. Hence, this method is further on called *O_3-scaling-method*.

The first part of this section explains the derivation of the formalism and the next part deals with a comprehensive analysis of the errors and uncertainties related to this method. It is shown that especially the two problems mentioned above play none or only a minor role.

7.4.1 Formalism

The key idea of the proxy gas scaling method combines the information of

1. in-situ measured concentration of the proxy gas [P] - collected by another instrument
2. model data to determine the overhead column density of the target trace gas in order to convert the measured dSCD in SCDs
3. the ratio of the measured SCDs of the trace gas X and the proxy gas P - measured by the mini-DOAS
4. the two contributions (S_x for the target trace gas and S_P for the proxy trace gas) due to the absorption at the flight altitude layer with respect to the total absorption, evaluated for the whole altitude range (modelled with a RTM)

in order to retrieve the concentration of the targeted trace gas X in flight altitude. In the case of the Global Hawk measurements the DOAS reference spectrum is a direct solar spectrum. Neglecting scattering into and out of the line of sight between the Global Hawk and the Sun the reference column can geometrically be calculated. From measured dSCDs (dS) to SCDs (S):

$$S_X = dS_X + S_{X,ref} \tag{7.27}$$

$$S_{X,ref} = \sum_{i=flightlevel}^{TOA} B_{\mathrm{X}_{i,ref}} \cdot [\mathrm{X}]_i \cdot z_i, \text{ with } TOA\text{: top of atmosphere} \tag{7.28}$$

$$B_{\mathrm{X}_{i,ref}} = \frac{1}{\cos(SZA_{ref})}, \text{ for } i > l \tag{7.29}$$

$$B_{\mathrm{X}_{i,ref}} = 0, \text{ for } i < l \tag{7.30}$$

with z_i being the thickness of altitude layer i and l being the flight level. Here the vertical concentration profile $[X]$ is taken from the SLIMCAT chemical transport

model at the time and location of the reference measurement.

The measured SCDs represent the total amount absorption along the light path throughout the atmosphere but they cannot distinguish the particular absorption contribution coming from a specific altitude layer within the atmosphere. This implies the total SCDs S_{x} and S_{P} are measured for every trace gas and for each measurement geometry.

On the other hand the SCDs can be modelled by an RTM (in this case McArtim) as:

$$S_X = \sum_i [\mathrm{X}]_i \cdot B_{\mathrm{X}_i} \cdot z_i \tag{7.31}$$

$$S_P = \sum_i [\mathrm{P}]_i \cdot B_{\mathrm{P}_i} \cdot z_i, \tag{7.32}$$

Rearranging these formula yields an expression for the concentration of X and P in the layer of interest j.

$$[\mathrm{X}]_j = \frac{S_X - \sum_{i \neq j} [\mathrm{X}]_i \cdot B_{\mathrm{X}_i} \cdot z_i}{B_{\mathrm{X}_j} \cdot z_j} \tag{7.33}$$

$$[\mathrm{P}]_j = \frac{S_P - \sum_{i \neq j} [\mathrm{P}]_i \cdot B_{\mathrm{P}_i} \cdot z_i}{B_{\mathrm{P}_j} \cdot z_j}. \tag{7.34}$$

The concentrations of the proxy gas P and trace gas X in the layer of interest can only be modelled because the measurements provide only the total SCDs. The ratio of these two equations yields:

$$\frac{[\mathrm{X}]_j}{[\mathrm{P}]_j} = \frac{\frac{S_X - \sum_{i \neq j} [\mathrm{X}]_i \cdot B_{\mathrm{X}_i} \cdot z_i}{B_{X_j} \cdot z_j}}{\frac{S_P - \sum_{i \neq j} [\mathrm{P}]_i \cdot B_{\mathrm{P}_i} \cdot z_i}{B_{P_j} \cdot z_j}} = \frac{B_{P_j}}{B_{X_j}} \cdot \left(\frac{S_X - \sum_{i \neq j} [\mathrm{X}]_i \cdot B_{\mathrm{X}_i} \cdot z_i}{S_P - \sum_{i \neq j} [\mathrm{P}]_i \cdot B_{\mathrm{P}_i} \cdot z_i} \right). \tag{7.35}$$

If the RT calculations for both gases are performed for the same wavelengths and same atmospheric conditions and since the geometry of the DOAS reference is the same, the ratio of B_{X_j} / B_{P_j} equals to 1.

We can now define the factors α_{X} and α_{P} as:

$$\alpha_{\mathrm{X}_j} = \frac{S_X - \sum_{i \neq j} [\mathrm{X}]_i \cdot B_{\mathrm{X}_i} \cdot z_i}{S_X} = \frac{[\mathrm{X}]_j \cdot B_{\mathrm{X}_j} \cdot z_j}{\sum_i [\mathrm{X}]_i \cdot B_{\mathrm{X}_i} \cdot z_i}, \tag{7.36}$$

$$\alpha_{\mathrm{P}_j} = \frac{S_P - \sum_{i \neq j} [\mathrm{P}]_i \cdot B_{\mathrm{P}_i} \cdot z_i}{S_P} = \frac{[\mathrm{P}]_j \cdot B_{\mathrm{P}_j} \cdot z_j}{\sum_i [\mathrm{P}]_i \cdot B_{\mathrm{P}_i} \cdot z_i}. \tag{7.37}$$

These factors correspond to the fractional part of the total SCD which stems from the layer of interest j. They can only be calculated using the RT model.

With this definition, the concentration of X in the layer of interest j can be written as:

$$[\mathrm{X}]_j = \frac{\alpha_{X_j}}{\alpha_{P_j}} \cdot \frac{S_X}{S_P} \cdot [\mathrm{P}]_j \tag{7.38}$$

The key assumption in the proxy gas scaling approach is that the ratio of both α is the same in the measurement and in the model:

$$\left.\frac{\alpha_X}{\alpha_P}\right|_{meas} = \left.\frac{\alpha_X}{\alpha_P}\right|_{model} \tag{7.39}$$

The α ratio takes into account the different vertical shape of the trace gas and proxy gas profiles and therefore a different contribution to the SCD deriving from flight altitude. With this reasonable assumption, formula 7.38 yields the concentration of the trace gas X at flight altitude.

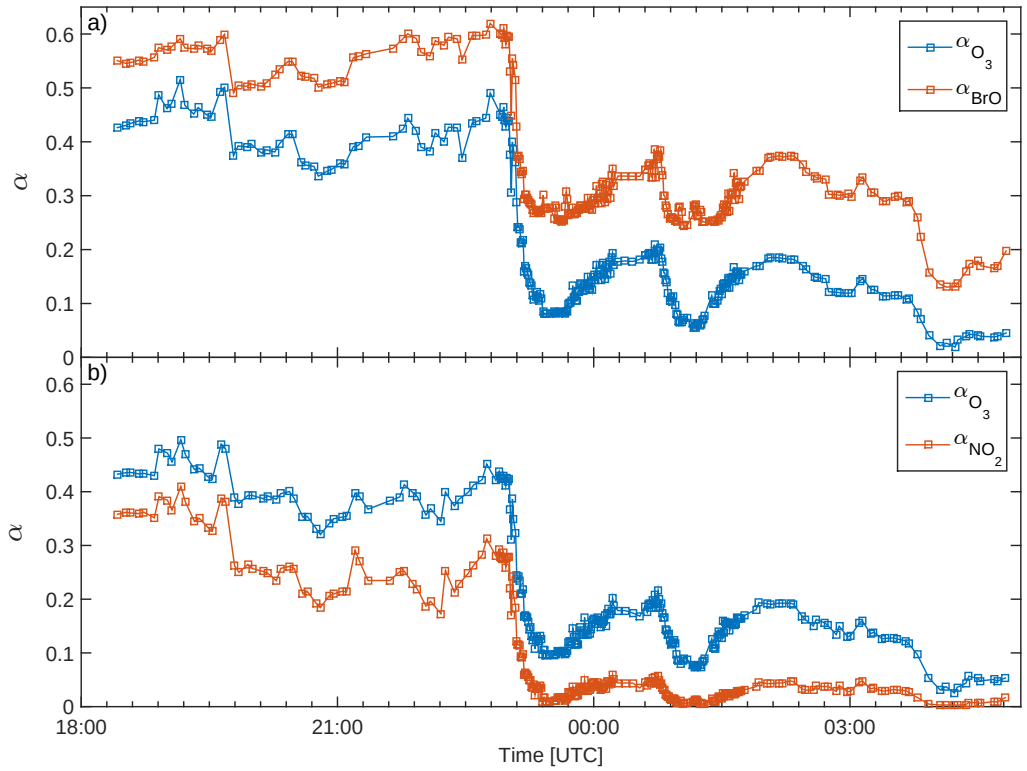

Figure 7.6: Alpha factors for O_3 and BrO in the UV range (upper panel) and for O_3 and NO_2 in the visible range (lower panel). Simulations done for SF3-2013. They show how much of the total measured absorption comes from the layer around flight altitude.

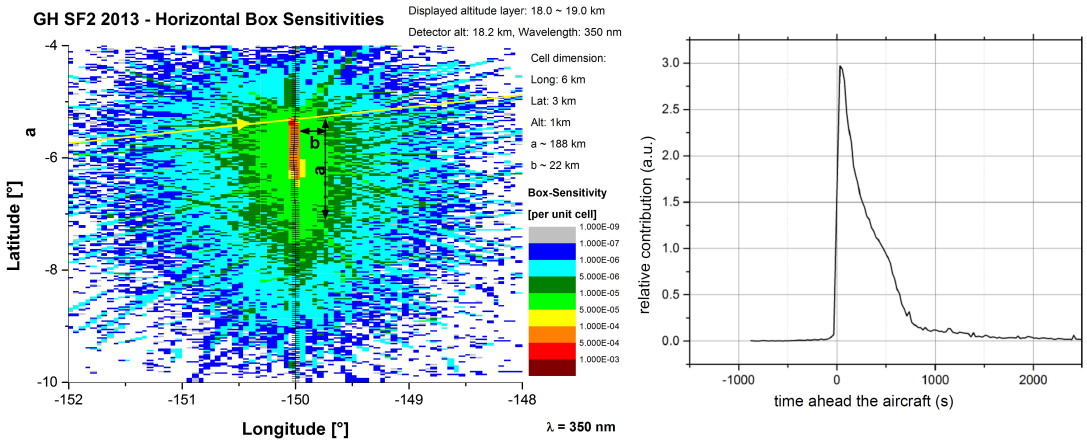

Figure 7.7: Left panel: horizontal sensitivity of a DOAS measurement recorded with the telescope pointing to the limb. The detector altitude is 18.2 km. The yellow arrowline denotes the incident direction of the sunlight. The black line is the flight path and every tick mark describes a recorded spectrum with a limb-pointing telescope. Right panel: Time weighting function for future in-situ measurements. (Courtesy of Rasmus Raecke)

7.4.2 Implementation for the Global Hawk data analysis

In the case of the GH measurements, $[\mathrm{P}]_j$ is the measured in-situ concentration of the proxy gas (O_3), but radiance, i.e., radiative transfer weighted averaged over the line-of-sight (Figure 6.6, Figure 7.7). This accounts for the remote-sensing nature of the DOAS measurements. The DOAS measurements are compared to in-situ measurements that happen up to hundreds of kilometres away from the GH and up to 15 minutes later in the future. Accordingly, the method is only reliable when the GH does not change its altitude because during dives the air mass probed straight ahead the aircraft is not probed by in-situ measurements in future. In case of dives the local in-situ concentration of $[\mathrm{P}]_j$ is taken. S_X, and S_P are obtained from equation 7.27. Finally the box air mass factors B_{X_i} and B_{P_i} of atmospheric layer i are calculated using RT model described in section section 6.2. The trace gas profiles $[\mathrm{X}]_i$ and $[\mathrm{P}]_i$ are taken from SLIMCAT simulations (section 6.3.2).

Figure 7.6 displays one simulation of the α-factors for the limb measurements of O_3 and BrO in the UV spectral range, and for O_3 and NO_2 in the visible spectral range (for the wavelength ranges see Table 6.1). They are simulated for the sunlit part of the GH flight track (SF3-2013) on Feb. 14/15, 2013. The figure indicates the varying sensitivities of the limb measurements for the layer around flight altitude as compared to the whole atmosphere (mostly overhead). The α-factors depend on various parameters, such as the wavelength, the solar illumination, the underlying concentration profiles, and other factors (for details see section 7.4.3). For exam-

ple, the α-factors tend to be larger (in the range of 0.3 to 0.6) for measurements within the extra-tropical lowermost stratosphere (from UT 18:00 until UT 23:20) and smaller (in the range of 0.02 to 0.3) within the TTL (lasting from UT 23:10 until UT 4:30 with the 3 dives occurring at UT 23:10 until UT 00:10, UT 00:45 until UT 01:45, and UT 02:30 until UT 4:30, respectively).

In other words, even though the line-of-sights within the limb layer j might be rather large (of the order of hundreds of kilometers), if the concentration of the targeted gas is very small, compared to other (mostly overhead) located atmospheric layers, the limb measurements are rather sensitive to any uncertainties in the radiative transfer and trace gas concentrations of non-directly probed layers. However, as it is shown below (section 7.4.3), the sensitivity of the inferred concentration coming from the layer j with respect to the RT and concentration in any other layers mostly cancels out when ratios of α-factors are considered (see equation 7.37).

As described in section 6.3.1 the horizontal resolution of SLIMCAT is $1.2° \times 1.2°$ which corresponds to approximately 130 km $\times$ 130 km which again corresponds to $\sim$10 min of flight time. Therefore dynamical processes taking place on a smaller scale can not be reproduced on the model. In order to account for these small-scale features and also for uncertainties in the dynamics of SLIMCAT (e.g. due to slightly wrong heating rates), the SLIMCAT data are vertically interpolated on a 100 m grid and then slightly shifted in the way that in-situ measured and SLIMCAT-simulated O_3 get into agreement.

Figure 7.8 shows an inter-comparison of measured (NOAA) and simulated (SLIMCAT) O_3 (trace c), CH_4 (HUPCRS) (trace b) NO_2 (mini-DOAS) (trace d), and BrO (mini-DOAS) (trace e) for the sunlit part of the GH flight track of SF3-2013, before the altitude adjustment of the SLIMCAT data. Figure 7.9 shows the same measured data but compared with the altitude adjusted SLIMCAT data. In principle it would be more reasonable to use a photochemically almost inert tracer like CH_4. Due to mathematical reasons, the altitude adjustment is performed via the (mostly) monotonically increasing O_3 profile. After the adjustment via O_3 one can clearly see that also the agreement of CH_4 is very good. Overall the NO_2 excellently and the BrO data compares reasonably well, but for some parts of the flight differences in the measured and predicted gas concentrations are seen as well. Before possible causes for these discrepancies are discussed, i.e., whether they are of dynamical and photochemical reasons (chapter 8), measurement errors and uncertainties of all parameters going into equations 7.37, 7.38, and 7.39 are discussed in following section 7.4.3.

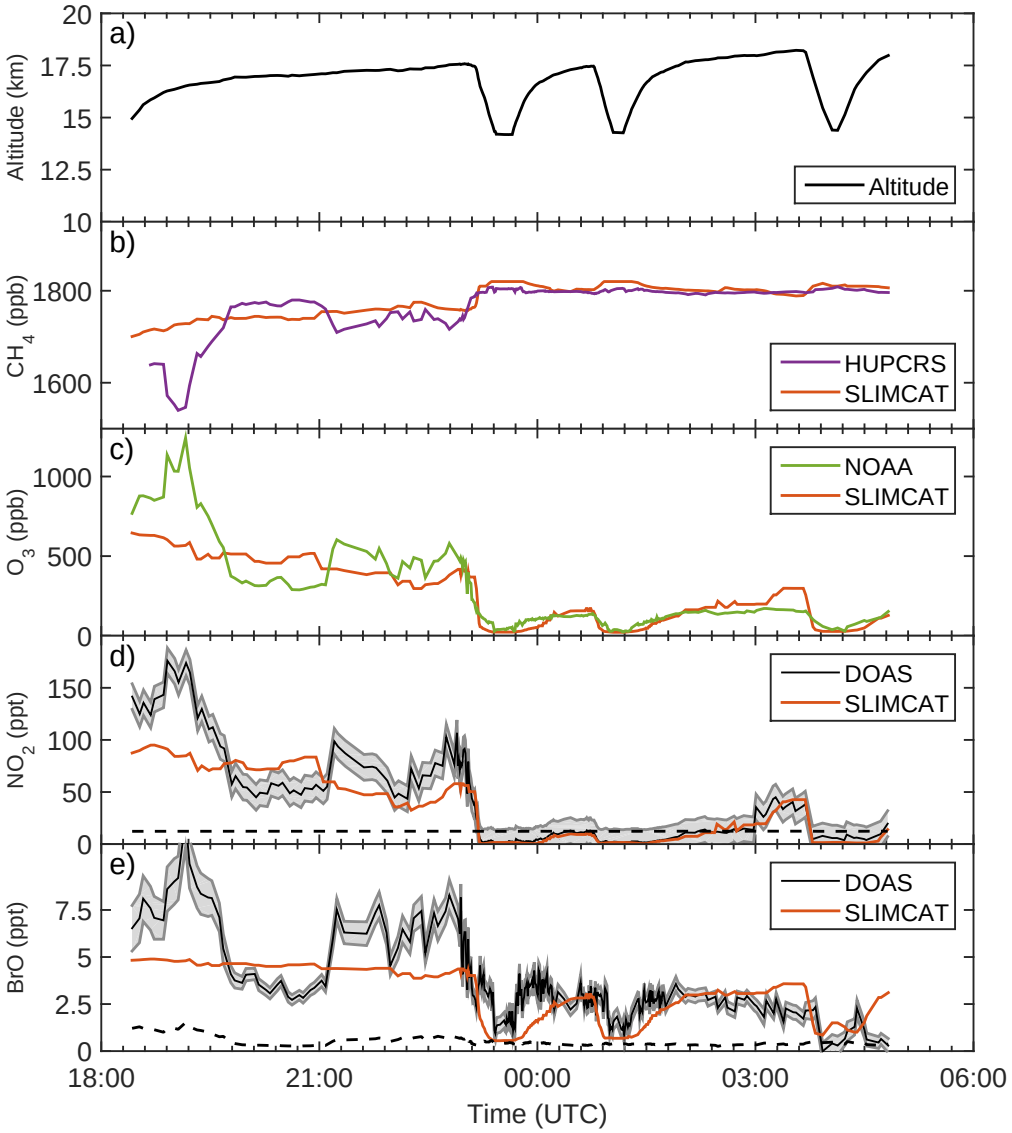

Figure 7.8: Inter-comparison of measured (NOAA) and SLIMCAT-simulated O_3 (trace a), CH_4 (UCATS) (trace b), NO_2 (mini-DOAS) (trace c), and BrO (mini-DOAS) (trace d) for the sunlit part of SF3-2013 on Feb. 14, 2013. The error bars for the mini-DOAS measured of NO_2, and BrO include all dominating errors, i.e., the spectral retrieval error, the overhead and the error due to a tropospheric contribution to the slant absorption.

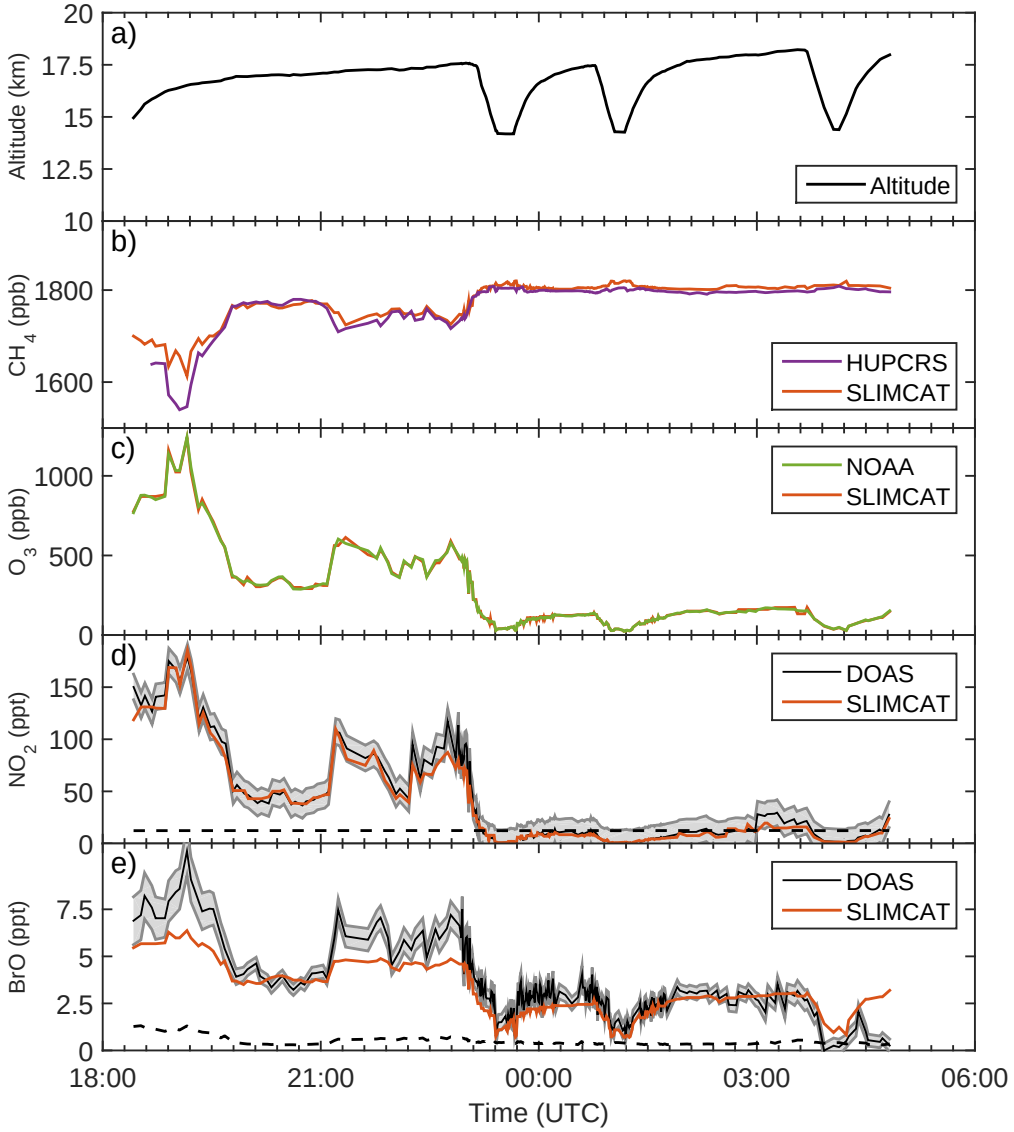

Figure 7.9: Same as Figure 7.8 but with altitude adjusted SLIMCAT data.

7.4.3 Sensitivities and errors in the trace gas retrieval

The error and uncertainties going into the O_3-scaling-method and its sensitivity towards all input parameters are addressed by inspection the Gaussian error propagation of all parameters that go into equations 6.4, 7.37, 7.37 (alpha factors), and 7.38. The Gaussian error inferred from equation 7.38 is

$$[\Delta \mathrm{X}]_j = [(\frac{\Delta\alpha_{X_j}}{\alpha_{X_j}})^2+(\frac{\Delta\alpha_{P_j}}{\alpha_{P_j}})^2+(\frac{\Delta SCD_X}{SCD_X})^2+(\frac{\Delta SCD_P}{SCD_P})^2+(\frac{\Delta[\mathrm{P}]_j}{[\mathrm{P}]_j})^2]^{0.5}\cdot[X]_j, \quad (7.40)$$

where j denotes the layer around flight altitude. Sensitivity studies of the α-factors α_{X_j} and α_{P_j} with respect to the parameters ($[\mathrm{X}]_j$, $[\mathrm{P}]_j$, B_{X_j}, B_{P_j} et cetera) of the equations 7.37, and 7.39 are investigated for the flight SF3-2013 by changing the input parameters. The studies comprise the shape and concentration of the O_3, NO_2, and BrO profiles, the amounts of tropospheric NO_2 and BrO, aerosol optical depth around flight altitude, the occurrence and optical depth of marine strato-cumulus clouds and cirrus clouds, ground albedo and error in the elevation angle within their reasonable ranges (see tables A.1 and A.2, runs 11 to 24). Further the sensitivity runs include simulations about the uncertainties of SCD_X, SCD_P, and $[\mathrm{P}]_j$ (runs 1 to 10), of the pointing error (runs 25, and 26), and of $\mathrm{P}]_j$. For the flight on SF3-2013, the results of all simulations are shown in the appendix A.

Major errors and uncertainties are due to spectral retrieval errors (see section 6.1), for small amounts of $[\mathrm{X}]_j$ the errors due to uncertainties of ΔSCD_{ref} (runs 3 to 10), and uncertainties due to the amount of the targeted gas in the troposphere below (runs 11, 12, and 13, for details see below). The impact of the overhead and tropospheric contribution is discussed in detail below.

In contrast, errors related to the in-situ measured ozone (runs 1, and 2), to the amount of aerosol and cirrus particles in flight altitude (runs 14, 15, and 19 to 21), to the occurrence of marine strato-cumulus clouds (runs 16, 17, and 18), to changes in the ground albedo (runs 22, 23, and 24), and to the pointing errors of the telescopes (runs 25, and 26) seem to play a minor role in the error budget. Mostly because the uncertainties of the α-factors cancel out in the α ratio used in equation 7.37.

The impact of the uncertainties in the $SCD_{X,ref}$ and $SCD_{P,ref}$ and the consecutive change of the SCD_X and SCD_P on the trace gas retrieval (e.g., for X = NO_2, BrO), is studied by varying the SLIMCAT-simulated overhead slant column amount within their likely errors, i.e. $\pm$ 15% for both NO_2, and for BrO (see the black points in Figure 7.13). The result in Figure 7.13 indicates errors for NO_2, and BrO in the range of 0 ppt to 2 ppt of 0.06 ppt to 0.2 ppt, respectively. The errors increase with the proximity (altitude) to the uncertain overhead stratospheric column.

Upwelling photons carrying some NO_2, and BrO absorption from the troposphere may have contaminated the limb observations made at EA = - 0.5°. This is estimated by inspecting the limb scanning observations made in the low level part (at 14.2 km altitude) of the second dive of SF3-2013. Here for the measurements made

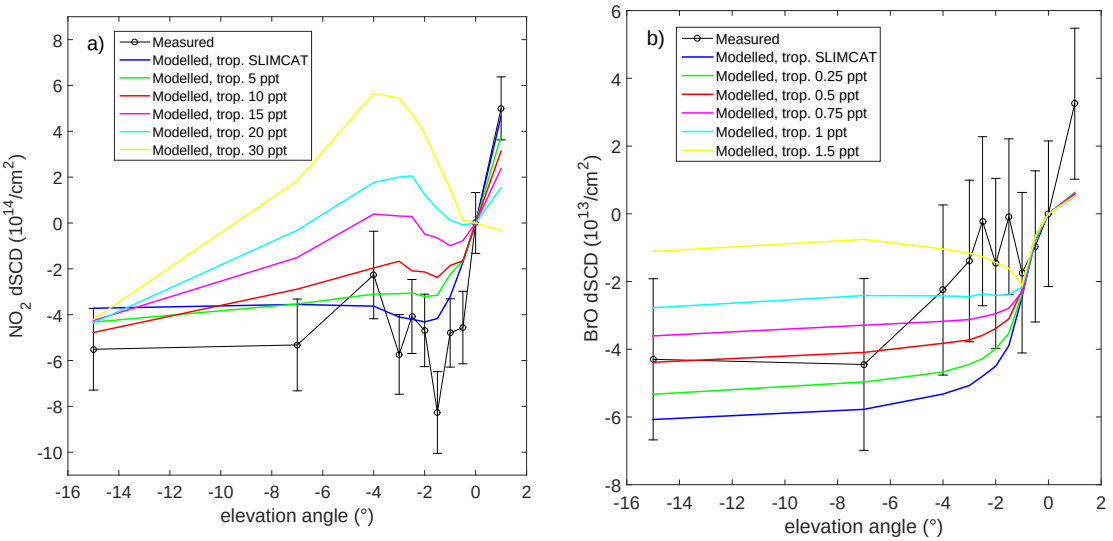

(a) NO_2 **(b)** BrO

Figure 7.10: Measured (black) and forward modelled (coloured) dSCDs relative to the 0° elevation angle for the limb scan sequence at the bottom (14.3 km) of the second dive of SF3-2013. The different colours of the forward modelled dSCDs indicate the assumed tropospheric mixing ratio of NO_2 (panel a) and BrO (panel b), respectively. For details and conclusions see text.

Table 7.2: Linear correlation coefficients belonging to Figure 7.11.

Tropospheric mixing ratio NO_2(ppt)	0	5	10	15	20	30
Linear correlation	0.9593	0.9558	0.9304	0.7716	0.3325	-0.1802

at elevations angles = 1°, -0.5°, -1.0°,-1.5°,-2.0°,-2.5°,-3.0°, -4.0°, -7.0°, and -15.0°, the dSCDs of NO_2 and BrO are evaluated against a limb spectrum taken at 0°, and compared to simulated dSCDs. It is either the prediction of SLIMCAT or constant mixing ratios but of varying amounts located in the troposphere, as indicated in Figure 7.10. For a better visualisation Figures 7.11 and 7.12 show the same data in a correlation plot. The comparison indicates that in the troposphere NO_2 mixing ratios ranged below 10 ppt, and BrO mixing ratio at around 0.5 ppt ± 0.5 ppt with an indication of a somewhat larger BrO mixing ratio [BrO].

This contribution coming from the troposphere and the contribution related to the assumption about the profiles of the targeted gases overhead are then combined (see Figure 7.13). Finally the total error is calculated by Gaussian adding the spectral retrieval error, and the combined error (the red dashed lines in Figure 7.13) due to uncertainties regarding the overhead error and the tropospheric error. In the

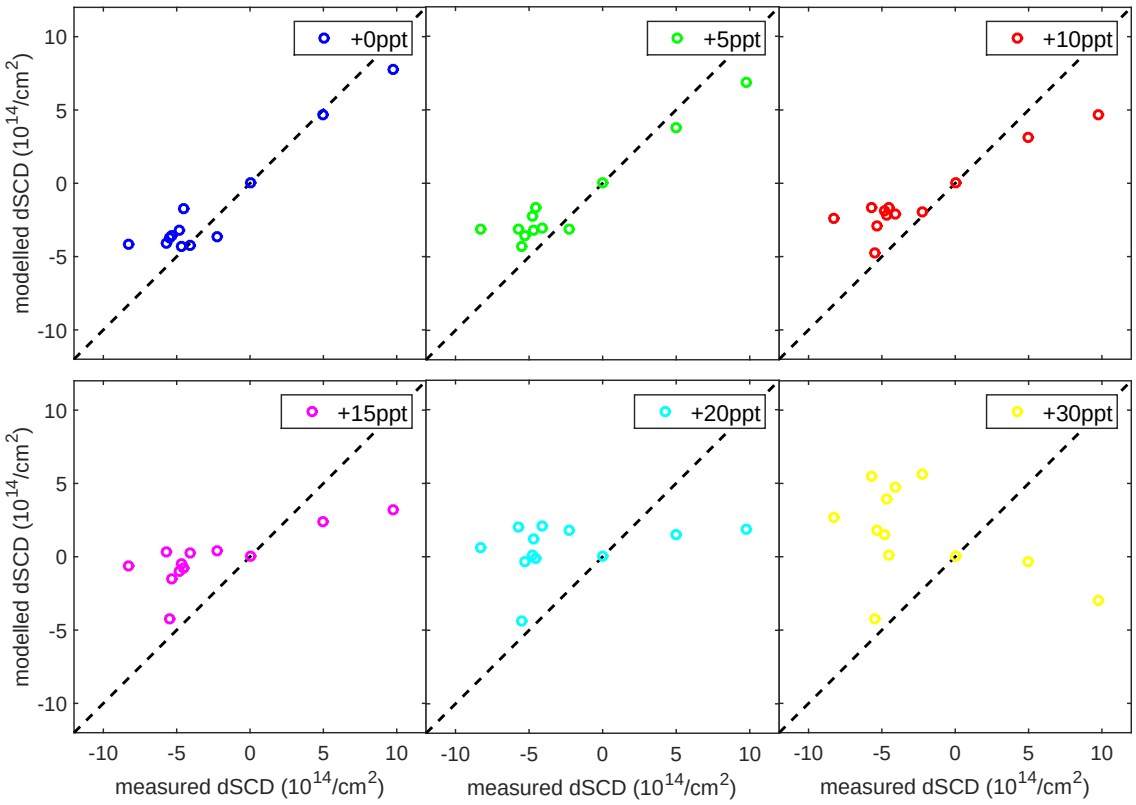

Figure 7.11: Correlation plot for measured and forward modelled NO_2 dSCDs of the limb scan sequence at the bottom (14.3 km) of the second dive of SF3-2013. The colours and assumed tropospheric mixing ratios are the same like in Figure 7.10, panel (a). The linear correlation coefficients are listed in Table 7.2.

following, this error is shown in all figures, for example in Figure 7.9, or Figures 8.4 to 8.9.

Finally it should be noted that for an estimate on the accuracy of our results as it is required when Br_y^{inorg} (chapter 8) is assessed, systematic errors due to uncertainties in the differential absorption cross section of the target gases need to be added to the random error, i.e., about ± 2.5% for O_3 in the UV and visible spectral range (Serdyuchenko et al., 2014), about ± 5% for NO_2 (Bogumil et al., 2003) in the visible spectral range, and about ± 10% for BrO in the UV spectral range (Harder et al., 2000) eventually need to be added.

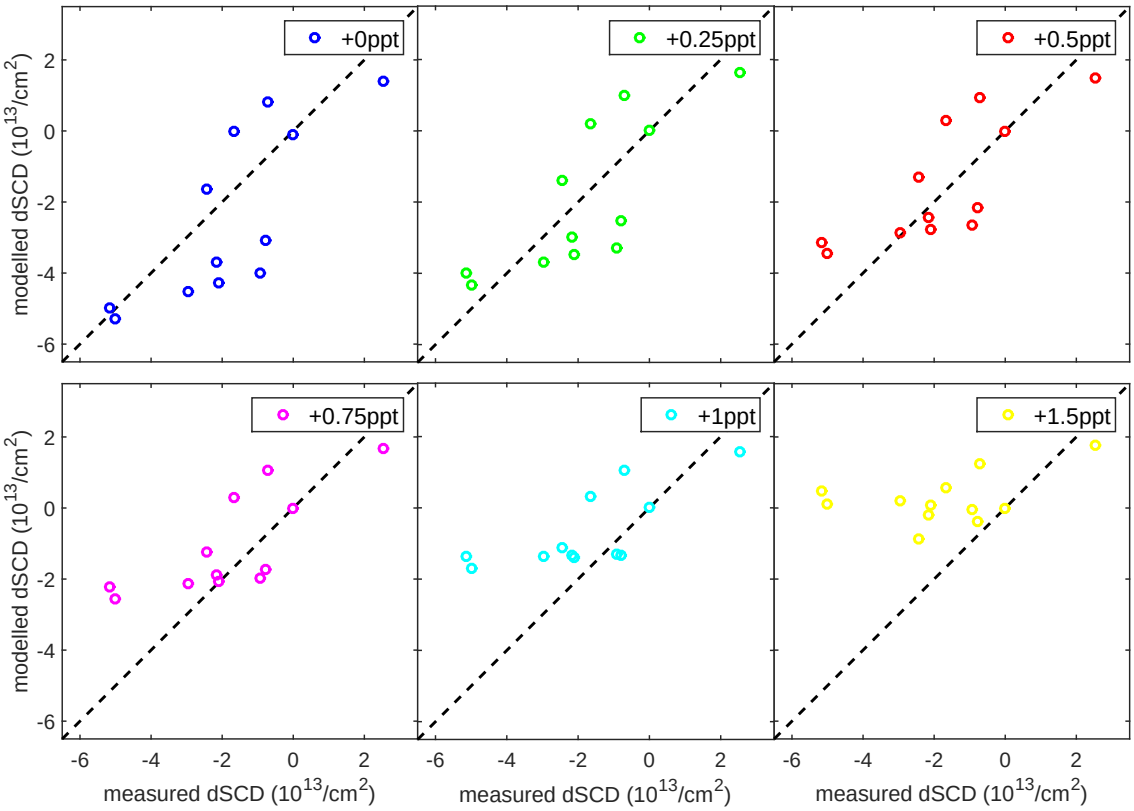

Figure 7.12: Correlation plot for measured and forward modelled BrO dSCDs of the limb scan sequence at the bottom (14.3 km) of the second dive of SF3-2013. The colours and assumed tropospheric mixing ratios are the same like in Figure 7.10, panel (b). The linear correlation coefficients are listed in Table 7.3.

Table 7.3: Linear correlation coefficients belonging to Figure 7.12.

Tropospheric mixing ratio BrO(ppt)	0	0.25	0.5	0.75	1	1.5
Linear correlation	0.7759	0.7768	0.7715	0.7657	0.7385	0.4304

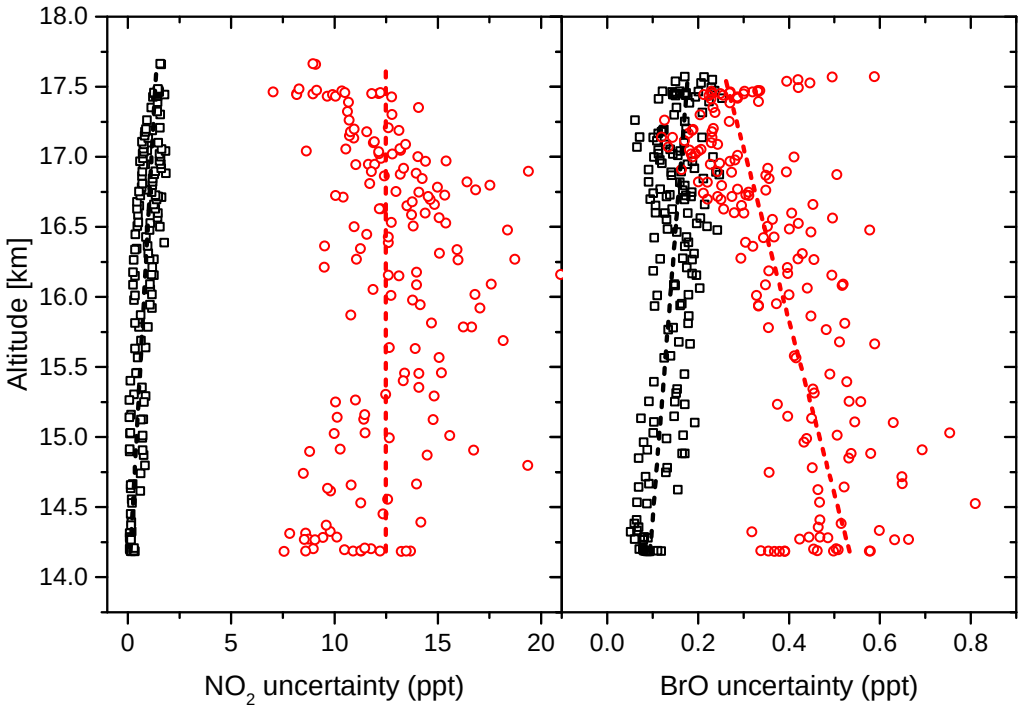

Figure 7.13: Uncertainty in the inferred NO_2 (left panel) and BrO (right panel) as a function of altitude due to uncertainties in the overhead (black squares), and in the column amounts located below the aircraft (red circles). For the overhead column amounts, uncertainties of ± 15% are assumed for both NO_2, and BrO. The uncertainty due to the changes of concentrations below the aircraft for both trace gases, NO_2, and BrO, is estimated by assuming uniform tropospheric mixing ratios of 15 ppt, and ± 0.5 ppt, respectively. The dashed lines indicate the linear regressions, which is used in the calculation of error propagation.

7.5 Optimal estimation vs. scaling method

This chapter compares the results of both methods, the O_3-scaling-method and the optimal estimation in the case of two ascents. For the second ascent of SF1-2013 (called "SF1-2013-Up2") the results of both methods excellently agree while for the second ascent of SF3-2013 (called "SF3-2013-Up2") the comparison shows a slight deviation in the first part of the ascent (lower TTL). Possible reasons for this deviation are discussed.

7.5.1 Atmosphere and model set-up

First the model atmosphere for calculating the BoxAMFs for the linear trace gas inversion has to be set up. The model atmosphere is a spherical 1D atmosphere and consists of a SLIMCAT pressure, temperature, O_3 and O_4 profile (0-60 km), taken in time from the middle of the respective ascent. The aerosol extinction profile for the UT is taken from SAGE II measurements and the optical thickness of the low cloud cover is obtained by a non-linear retrieval based on O_4 absorptions. The 1D retrieval yields an averaged optical thickness of $\tau = 5.1$ for SF1-2013-Up2 and $\tau = 7.9$ for SF3-2013-Up2 for a mSc deck located at 1-2 km. This is in by-eye agreement with the CPL backscatter ratio shown in Figure 4.3 (SF3-2013Up from 1:09 - 1:42 UT). At the times of the two ascents there is no exact Mie extinction data provided by the CPL instrument, therefore a quantitative comparison is not possible. The known shortcomings of those retrievals have been discussed in section 7.3.2, especially considering the horizontal heterogeneity during the time of SF3-2013-Up2.

7.5.2 Inversion results

Figures 7.14 and 7.15 show the results of the optimal estimation inversion for the two ascents. The left panels show the retrieved (red) BrO profile and the profile obtained by the O_3-scaling-method (green). As a priori profile a SLIMCAT BrO profile (0-60 km) averaged over the time of the ascent is taken. For the range of 14-18 km it is substituted by the O_3-scaled BrO profile interpolated (blue) to the retrieval grid which has a 1 km vertical resolution. The right panels show the corresponding averaging kernels. Between 14 km and 18 km altitude the averaging kernels amount to >0.8 for each layer, i.e. that the retrieved profile is almost independent from the a priori profile within this altitude range. The degrees of freedom (trace of the AK matrix) are 4.3 and 4.2, respectively. The degrees of freedom correspond to the retrieved data points which are independent from the a priori.

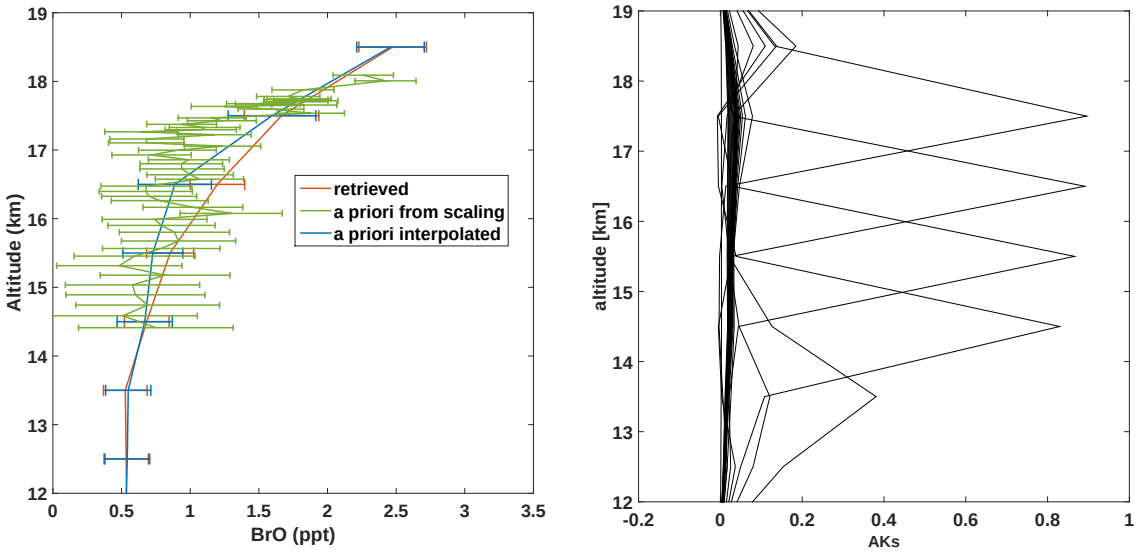

(a) BrO vmr profile

(b) Averaging kernels

Figure 7.14: Panel a: Optimal estimation result of SF1-2013, second ascent. Retrieved BrO profile (red), profile from O_3-scaling-method (green) used as a priori interpolated to the retrieval grid (blue). Panel b: Averaging kernels of the retrieval. Degrees of freedom: 4.3.

7.5.3 Intercomparison

For SF1-2013-Up2 the resulting profile of both methods compare very well within the error bars. There is only a small-scale feature at 17 km which is not reproduced by the OE inversion due to the 1 km grid. The results for SF3-2013-Up2 only agree in the upper half of the ascent but in the lower half the OE inversion yields larger concentrations than the scaling technique. This departure is mostly due to a changing atmosphere during the ascent. An ascent from 14 to 18km takes approximately 30-40 min. Regarding a horizontal air speed of ∼180 m/s the GH covers a distance of ∼400 km during the ascent. The heading during both ascents is southwest (∼270°) and therefore an ascent covers about 2-3 degrees of latitude. Within this distance both the overhead column as well as the aerosol/cloud profile may change. Figure 7.16 shows belly cam pictures of the period of both ascents. The cloud cover is very different. While during SF1-2013 the cloud patches are very small and regularly spread, SF3-2013 also shows huge clusters of clouds. If one imagines a smoothing in the size of the horizontal sensitivity (see Figure 7.7), the small-scaled cloud patches smear out and the cloud cover gets horizontally homogeneous for the ”eye” of the scattered sunlight measurements. In contrast to the huge cloud patches in SF3-2013 which are still heterogeneous. Also the aerosol load can change during the ascent but there are no means to check on this due to the problems pictured in

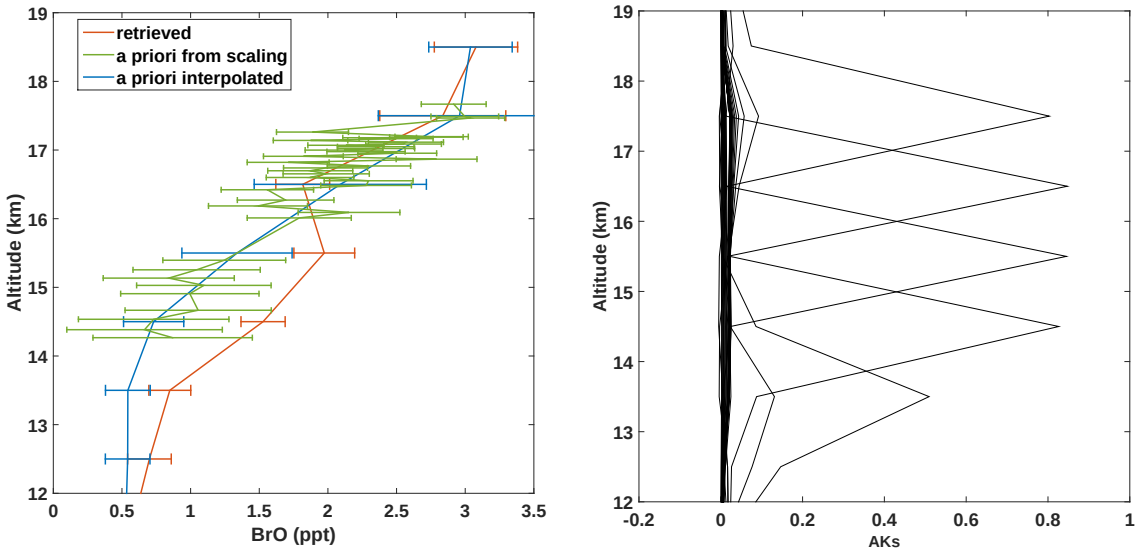

(a) BrO vmr profile **(b)** Averaging kernels

Figure 7.15: Panel a: Optimal estimation result of SF3-2013, second ascent. Retrieved BrO profile (red), profile from O_3-scaling-method (green) used as a priori interpolated to the retrieval grid (blue). Panel b: Averaging kernels of the retrieval. Degrees of freedom: 4.2

7.3.2. Figure 7.17 shows the result of an OE inversion with two different changes to the model atmosphere. In the atmosphere of the left panel an mSc with an OD of $\tau_{mod} = 20$ instead of $\tau = 7.9$ is introduced. This increases the effective albedo and reflects more photons from the lower troposphere which add additional absorption signal to the dSCDs and therefore the inversion algorithm needs less BrO at flight atltitude to obtain the same dSCDs. Much more influence on the result has an increase of the aerosol load within the TTL. In the right panel a linearly increasing aerosol extinction from $1{\cdot}10^{-3}$/km at 14 km up to $5{\cdot}10^{-3}$/km at 18 km is introduced.

In conclusion, the O_3-scaling-method is the better suited approach to analyse the GH data. Optimal estimation methods suffer from the following problems:

- The accuracy is rather limited, mostly due to Mie scattering contribution by aerosols and clouds not properly accounted for
- The assumptions on the optical of the atmosphere have a stronger impact on the result of the OE inversion as compared to the O_3-scaling-method (see sensitivity runs in section 7.4.3).
- OE inversions provide lower temporal and spacial resolution since one ascent/decent is seen as one state

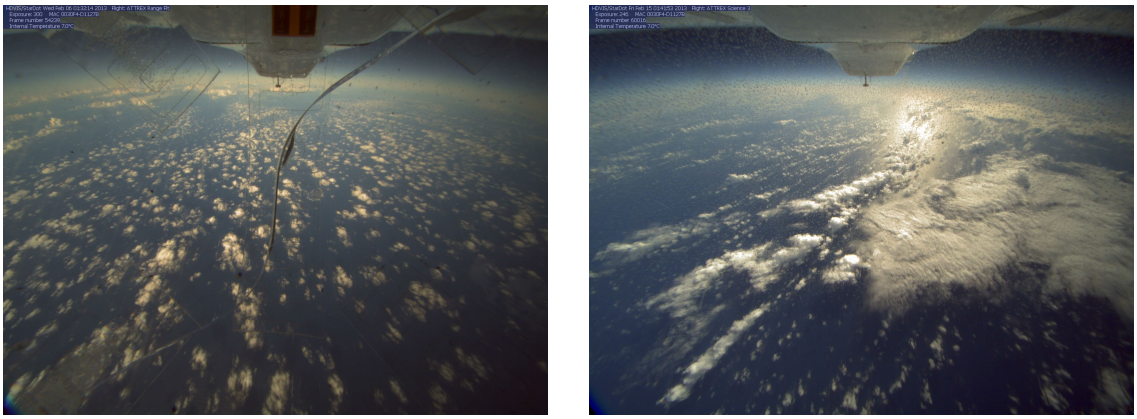

(a) SF1-2013-Up2 **(b)** SF3-2013-Up2

Figure 7.16: Belly cam pictures for the time of the ascents SF1-2013-Up1 and SF3-2013-Up1.

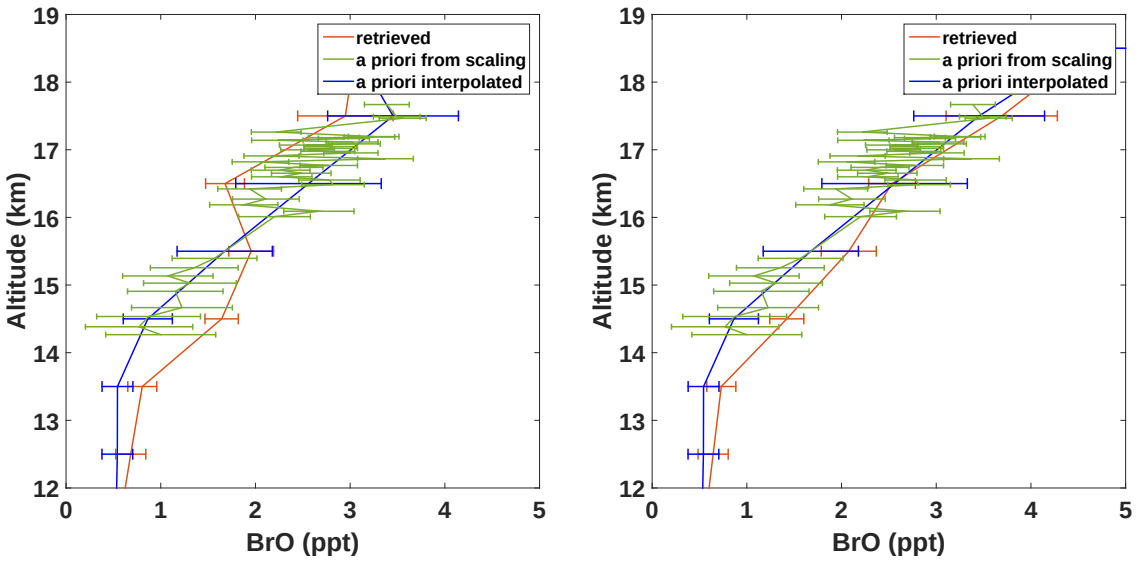

Figure 7.17: Left panel: Same like Figure 7.15 but with optical thicker mSc (OD=20). Right panel: Additionally added aerosol (for details see text).

7.6 Influence of the a priori profile on the retrieval

In the comparisons discussed above, an interpolated profile from the O_3-scaling-method is taken as an a priori. In the following inversion the profile from the recent publication of Wang et al. (2015) is taken. The profile from Wang et al. (2015) reaches from 0 to 14 km (Figure 7.18, black squares) and shows much higher concentrations than the profile obtained by the O_3-scaling-method or from SLIMCAT predictions. In order to avoid introducing an unrealistic profile shape, the Wang et al. (2015) profile is extrapolated (dashed blue lines) up to 20 km until it intersects with the SLIMCAT profile, which is taken as a priori from 20 km up to 64 km. The right panel in figure 7.18 shows the averaging kernels. AKs of almost 1 per layer indicate that the retrieved profile (left panel, red line) is independent of the a priori for the range of ∼13 - 18 km. It is emphasised that the BrO profile obtained by the O_3-scaling-method (left panel, green line) is only shown for illustration purposes. It has no influence at all on the inversion algebra.

The retrieved profile (red line) excellently agrees with the BrO profile obtained by the O_3-scaling-method. Even more important, it differs completely from the Wang et al. (2015) profile.The consequences of this findings are discussed in section 8.4.

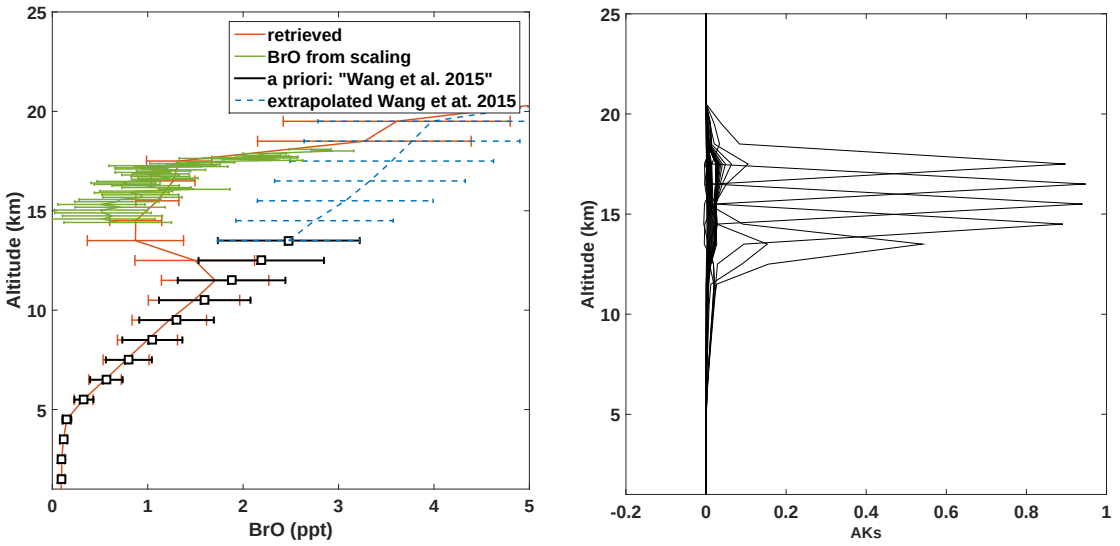

Figure 7.18: Left panel: Comparison of inferred BrO profile using the optimal estimation method (red line), and the O_3-scaling-method (green symbol) for the ascent from dive 2 during the flight on Feb. 5/6, 2013. Here, the a priori is taken from Wang et al. (2015) (black points), but for the probed altitude range (14.2 - 18 km) the solution (red line) tend to the BrO profile obtained from the O_3-scaling-method (green curve), indicating that Wang et al. (2015) profile is not compatible with the inferred BrO profile. Right panel: Averaging kernels.

7.7 Inference of inorganic bromine (Br_y^{inorg}) and error analysis

This section is a little bit out of the line of this chapter. It is explained how the total inorganic bromine (BrO_y^{inorg}) is inferred from the measured BrO concentrations. After that, it is discussed how the error of the BrO retrieval and the uncertainties in the required photochemical modelling are combined, and the error of BrO_y^{inorg} is deducted.

BrO_y^{inorg} is inferred by assuming the SLIMCAT-simulated BrO_y^{inorg} partitioning and apply it to the measured BrO:

$$[Br_y^{inorg}] = \left.\frac{[BrO]}{[Br_y^{inorg}]}\right|_{model} \cdot [BrO] \tag{7.41}$$

$$[Br_y^{inorg}] = [Br] + [BrO] + [BrONO_2] + [BrCl] + [HOBr] + [HBr] \tag{7.42}$$

The errors in estimating Br_y^{inorg} (= Br + BrO + $BrONO_2$ + HOBr + HBr) from the BrO measurements depend on the uncertainties in the related photochemistry. Since photochemical modelling (see panels (f) in figures 8.4 to 8.9) indicate that at daytime HOBr and HBr contribute to less than 10% to Br_y^{inorg}, the focus is on the photochemical model errors due to the presence of Br, and $BrONO_2$. These can best be assessed considering the major factors going into the $[Br_y^{inorg}]/[BrO]$ ratio

$$\frac{[Br_y^{inorg}]}{[BrO]} = 1 + \frac{[Br]}{[BrO]} + \frac{[BrONO_2]}{[BrO]} + ... \tag{7.43}$$

where in photochemical steady state at daytime the ratio on the right hand side can be calculated from $[Br]/[BrO] = J_{BrO}/k_{Br+O3} \cdot [O_3]$, and $[BrONO_2]/[BrO] = k_{BrO+NO2} \cdot [O_3] \cdot [M]/J_{BrONO_2}$. Gaussian error propagation then leads for the largely dominating errors due to the photochemical reaction rate constants and photolysis frequencies (Sander et al., 2011)

$$\begin{aligned} \Delta\frac{[Br_y^{inorg}]}{[BrO]}/\frac{[Br_y^{inorg}]}{[BrO]} &= [(\frac{[Br]}{[BrO]})^2 \cdot (\frac{\Delta k_{Br+O3}}{k_{Br+O3}})^2 \\ &+ (\frac{[BrONO_2]}{[BrO]})^2 \cdot (\Delta\frac{k_{BrO+NO2}}{J_{BrONO_2}})^2 \cdot (\frac{J_{BrONO_2}}{k_{BrO+NO2}})^2 + ...]^{0.5} \end{aligned} \tag{7.44}$$

Sander et al. (2011) estimate the uncertainty in the rate reaction coefficient k_{Br+O3} at low temperature (T = 190 K) to ± 40%. Inspecting in the JPL compilation comment (G31), however indicate a smaller uncertainty (28%) when only considering the

two studies which actually measured rather than extrapolated to the reaction rate constant at the relevant temperature range (T = 190 - 200 K) (Michael et al. (1978) and Nicovich et al. (1990)). Therefore in the following discussion, an uncertainty of 28% for k_{Br+O3} is used.

Further, in previous studies on the stratospheric bromine photochemistry Kreycy et al. (2013) found for T = 220 K the ratio $J_{BrONO_2}/k_{BrO+NO2}$ to be a factor of 1.7 (+0.4/-0.2) larger then recommended by the JPL-2011 compilation (Sander et al., 2011). How this change in the $J_{BrONO_2}/k_{BrO+NO2}$ ratio propagated into the estimate of Br_y^{inorg} is tested in a separate model run (see section 8.3).

Taking these uncertainties together with errors in the measured BrO (in section 7.4.3), the cross section error, and the errors in the modelled [Br]/[BrO], and [$BrONO_2$]/[BrO] ratios leads to the Br_y^{inorg} error, as indicated in panel (g) of the figures 8.4 to 8.9.

8 Results and discussion

This chapter presents a comprehensive analysis of all 2013 NASA-ATTREX flights. First some general remarks on the measurement bias, which is due (a) the season (late winter), (b) the region (Eastern Pacific) and (c) the time of day (need of sunlight), are given. Second, section 8.2 discusses how the adopted dynamical atmospheric transport in the model is validated by comparing model predicted and measured CH_4, as well as major brominated source gases. Then, section 8.3 provides a flight-by-flight analysis of the retrieved NO_2 and BrO concentrations and the inferred Br_y^{inorg} budget. The major focus is on comparisons of the BrO measurements with predictions of SLIMCAT simulations and estimates of Br_y^{inorg}. Section 8.4 discusses BrO altitude profiles inferred from measurements during the dives in the context of recent studies. The last section combines the Br_y^{inorg} measurements with GWAS measurements of organic source gases in order to infer the total Br_y budget.

8.1 Preliminary remarks

In February and March 2013, the NASA-ATTREX flights of the NASA Global Hawk were strongly biased with respect to the probed air masses, mostly because the scientific interest was primarily put on probing the TTL over the Eastern Pacific for aerosols and cirrus cloud particles during the convective season, rather than the photochemistry of bromine in the LS, UT, and TTL (see Figure 4.4). Therefore typical flight patterns led from Dryden/California into southern, or south-western direction. The dives were then performed within the TTL, but not within the subtropical lowermost stratosphere which was only crossed at almost constant pressure altitude. Further, since the take-offs were carried out during the local mornings, the leg into southern, or south-western direction occurred at daylight until a turning point was reached, and the legs into the north-eastern or northern directions back to Dryden were performed during the night. Finally the landings at Dryden were scheduled for the early local morning, mostly due to operational constraints. Therefore, no profiles of the targeted radicals were taken in the subtropical lowermost stratosphere, but a larger number within the UT and TTL at daytime.

Further in the analysis only those data are considered which were taken at solar zenith angles (SZA) $\leq 85^o$, because for increasing SZAs the received skylight radiance required increasingly longer signal integration times, and thus averaged over longer distances ahead the aircraft. Moreover as the SZA was increasing the sky-

light was expected to traverse an increasingly inhomogeneous curtain of the probed radicals due to photochemical reasons (e.g., inspect Figures 6.6 and 7.7). As a consequence, the spatial grid of SLIMCAT (1.2 × 1.2 degree) on which the photochemistry is simulated appeares too coarse for a useful interpretation of the measurements at large SZAs. Therefore for a tighter interpretation of the data a spatially higher resolved model than SLIMCAT would be required. Such an approach is for example followed in the balloon-borne studies of Harder et al. (2000), Butz et al. (2009), Kreycy et al. (2013), and others. However, since both processes are likely to increase the error of our analysis, and since large SZA ($\geq 85^o$) measurements only constituted a very minor part of all measurements, these data are not analysed in greater detail.

Further it should be noted that, for the flight on Feb. 21/22, 2013 (SF4-2013), the DOAS retrievals are much less robust than for all the other flights, most likely because the Fraunhofer reference spectra (taken via a diffuser) are affected by temporally changing residual structures most likely due to ice deposits on the diffuser disk. Therefore the data of this flight are not analysed in more detail, but they are only reported for completeness here.

8.2 Dynamics and source gases

Before measured and modelled NO_2, BrO and inferred Br_y^{inorg} can be compared quantitatively, it has to be assured that both the surface concentrations of the SGs and the convection scheme are represented correctly in the model. This is of major importance since the SLIMCAT simulations partly influence the outcome of the BrO and NO_2 concentrations via the O_3-scaling-method and the simulated Br_y^{inorg} partitioning is used to infer measured Br_y^{inorg} (see section 7.7).

8.2.1 Dynamics

Methane is a suitable tracer for transport and age of air (e.g. Johnson et al. (1999), Remsberg (2015)), because it reaches the middle stratosphere before it is chemically broken down (Waugh and Hall, 2002). ECMWF meteorological data including archived ERA-Interim convective mass fluxes and NOAA/AGAGE[1] surface concentrations of CH_4 yield a good agreement with SLIMCAT predictions and measurements in the LS, UT, and TTL. Figure 8.1 shows a comparison of the modelled and in-situ measured ratio of O_3 to CH_4 for all six flights. As mentioned in section 4.3.2 the HUPCRS instrument did not work properly during the first two flights mainly due to calibration issues. Therefore the used methane data of the first two flights was recorded by the UCATS GC instrument while for the other flights the more

[1] https://agage.mit.edu/data/agage-data

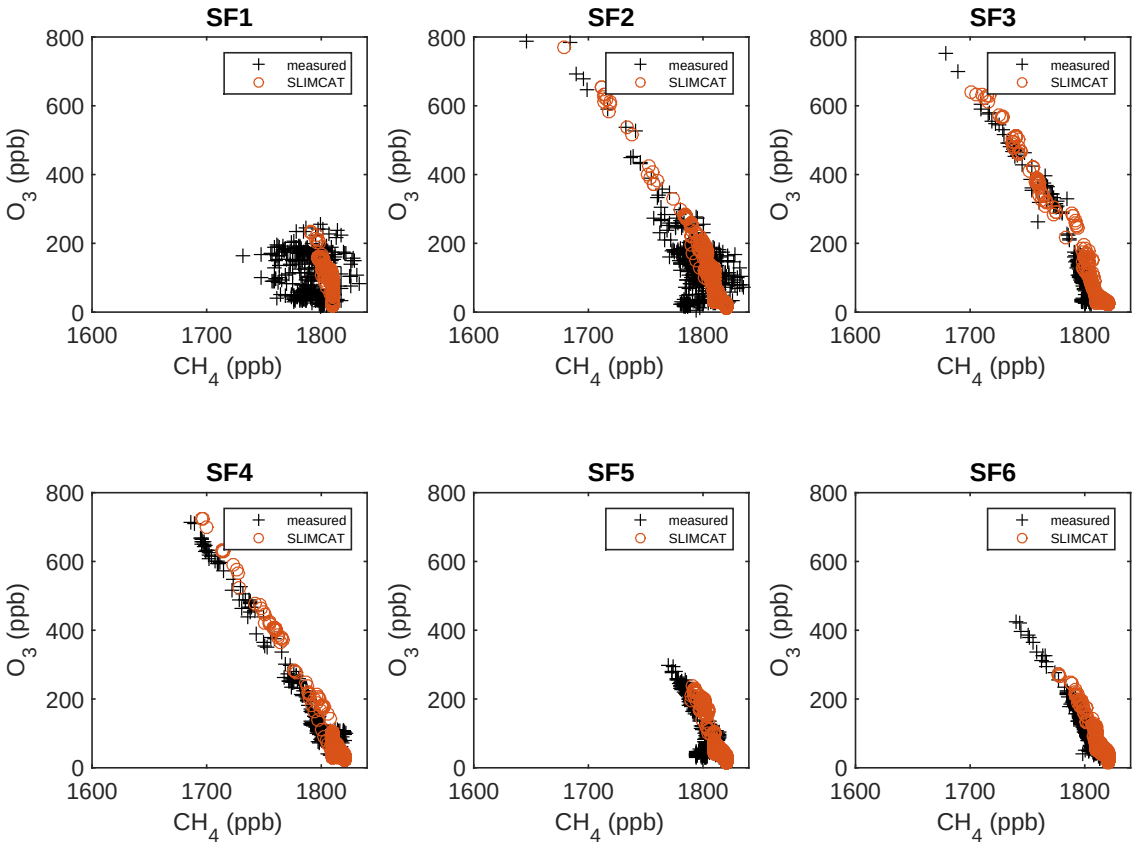

Figure 8.1: Comparison of the SLIMCAT-simulated and in-situ measured CH_4/O_3 ratio for all six flights in 2013. In-situ CH_4: SF1-2013 and SF2-2013, UCATS GC; SF3-2013 to SF6-2013, HUPCRS.

precise HUPCRS CH_4 data is used. For all flights the agreement of the observed and modelled O_3 to CH_4 correlation is reasonably good, except for SF1-2013 and SF2-2013 where the UCATS measured CH_4 scattered around the predicted CH_4 concentrations. Most likely this scatter is due to a calibration errors of UCATS, rather than it expressed the real behaviour of the atmosphere. Evidence for this conclusion is provided by the CH_4 comparisons of SF3-2013 to SF6-2013, where the HUPCRS CH_4 data are used, which do not show any scatter and which compare well with the model prediction.

The achieved excellent agreement between measured and modelled CH_4, and O_3 provides confidence that the SLIMCAT model reproduces well the key dynamical and photochemical processes of the probed air masses.

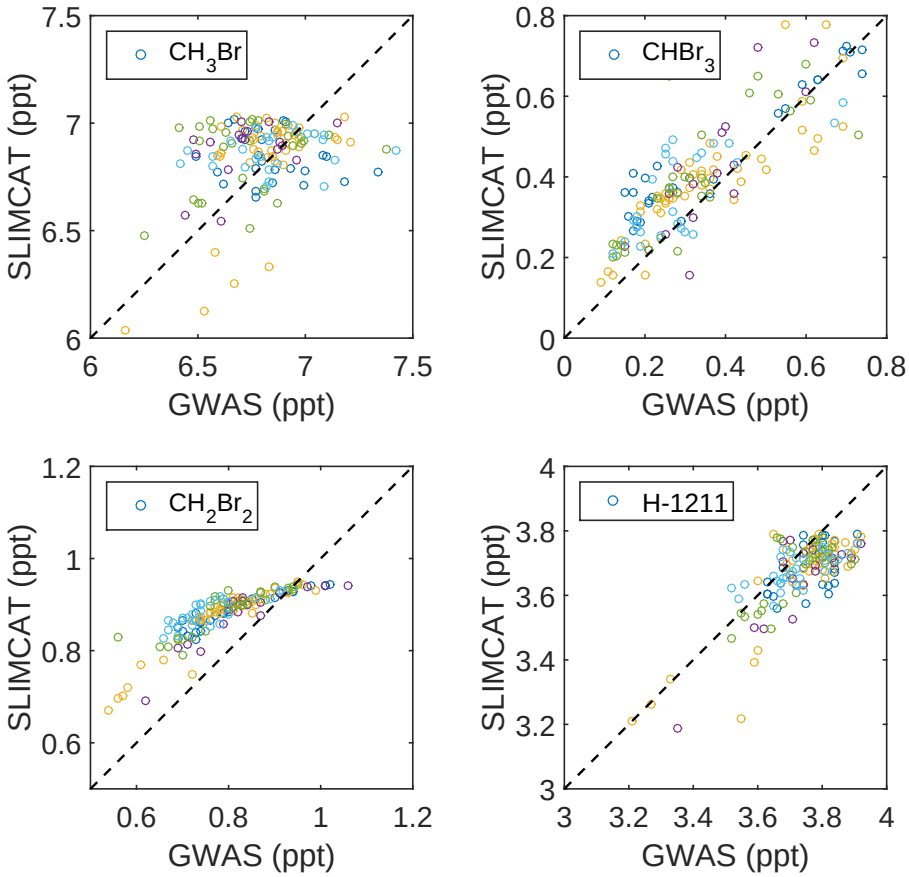

Figure 8.2: Comparison of in-situ measured and SLIMCAT-simulated brominated source gases. The colour indicate the flight number: SF1-2013 blue, SF3-2013 orange, SF4-2013 purple, SF5-2013 green, SF6-2013 light blue (same colours is in Figure 8.11)

8.2.2 Budget of brominated source gases

Organic bromine (Br_y^{org}) has three contributions (see chapter 2.4): Methyl bromide (CH_3Br), halons and very short-lived species (VSLS). The in SLIMCAT implemented long-lived SGs emissions (methyl bromide and halons) follow the A1 scenario in chapter 5, table 5A-2 of WMO (2011). The accordingly calculated surface mixing ratios are listed in table 5A-3. The contribution of VSLS to total organic bromine has a high uncertainty due to only poor constraints on the magnitude and distribution of emissions (Hossaini et al. (2013)) and a limited understanding of tropospheric processing. The overall agreement of the brominated source gases is good (Figure 8.2). For CH_2Br_2 however, the run #583 of the SLIMCAT model under-predicted dibromomethane for high concentrations (by 0.1 ppt) and over-predicted it by up to 0.2 ppt for low concentrations (lower left panel), most likely due to underesti-

mated surface concentration (1.05 ppt), and incorrectly calculated atmospheric life times by reactions of CH_2Br_2 with OH radicals in the model (e.g. Mellouki et al. (1992), Ko et al. (2013), WMO (2014)). $CHBr_2Cl$, $CHBrCl_2$ and CH_2BrCl are not treated as specific tracers in SLIMCAT. Rather they are lumped to the major VSLS with similar lifetime. According to WMO (2014) they contribute 0.3 ppt, which are lumped to $CHBr_3$ and 0.1 ppt to CH_2Br_2, respectively, This assumption is in agreement with GWAS measurements of SF3-2013 (Figure 8.3) when interpolated to the surface ($\theta \approx 300$ K). All together this results in effectively 1.7 ppt $CHBr_3$ and 1.05 ppt CH_2Br_2. In the upcoming paper by Navarro (2015) it is argued that the

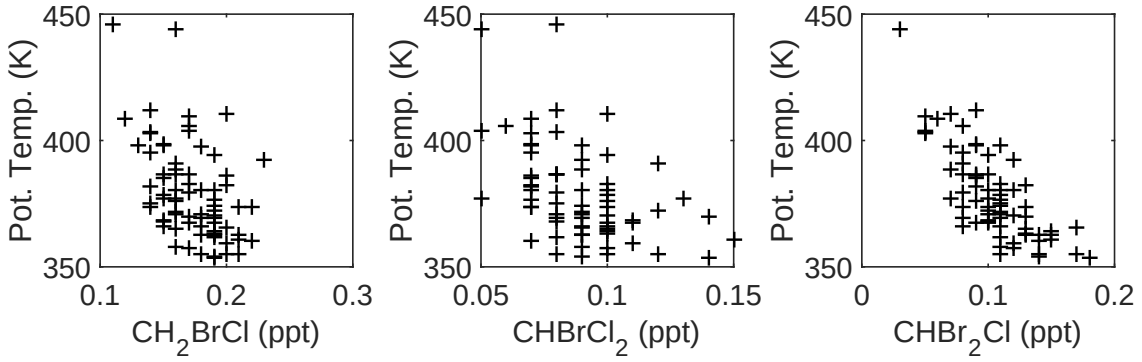

Figure 8.3: GWAS measurements of minor VSLS (mixed Br−Cl species) during SF3-2013.

scatter in CH_3Br and $CHBr_3$ from flight-to-flight and sample-to-sample is mostly due to different source regions of the air masses probed during SF1-2013 to SF6-2013, implying a spatially (and possibly time dependent) varying source strengths of the brominated natural source gases (e.g., Hossaini et al. (2013), Ziska et al. (2013), and others).

With the present version of the SLIMCAT simulations, this scatter introduces an estimated uncertainty of ± 0.8 ppt into Br_y^{org}, and potentially in Br_y^{inorg} available in the TTL. The systematic under-prediction of 0.1 ppt at high CH_2Br_2 concentrations, and its too long life time in the TTL leading to too large CH_2Br_2 concentrations in the model for old air (by up to 0.2 ppt) may cause an additional and systematic under-prediction of Br_y^{inorg} of $\leq$ 0.4 ppt in the model. Both contributions to the uncertainty of Br_y^{org} are considered in the comparison of measured and modelled BrO, and Br_y^{inorg} (see section 8.3 below).

8.3 Comparison of measured and modelled NO_2, BrO and Br_y^{inorg}

Figures 8.4 to 8.9 provide overviews on the measured data together with the SLIMCAT simulations of CH_4, O_3, NO_2, BrO, the Br_y^{inorg} partitioning and inferred total Br_y^{inorg} as a function of time, for each flight. The different measurements and comparisons are discussed in the following. For better visibility, the figures are scaled to the full extent of a page and the panels are listed here and the individual panels show:

(a) Altitude (km)

(b) In-situ measured CH_4 (Flights 1-2 UCATS GC, flights 3-6 HUPCRS)

(c) In-situ measured O_3 (NOAA)

(d) NO_2 (black: DOAS with error bars, orange: SLIMCAT)

(e) BrO (black: DOAS with error bars, orange: SLIMCAT)

(f) SLIMCAT BrO_y^{inorg} partitioning

(g) Inferred BrO_y^{inorg}, according to equation 7.41

The error bars of the NO_2 and BrO measurements include all dominating errors (equation 7.40), i.e. the error of the spectral analysis, the error due to the propagation of the overhead column error and the error due to the uncertainty of the tropospheric contribution to the slant absorption. The error bars of Br_y^{inorg} also include the uncertainties in the $BrONO_2$ photolysis frequency and the $Br+O_3+M$ reaction rate (equation 7.45). Dashed vertical lines separate the different regimes of probed air according to the criteria introduced in section 2.4.

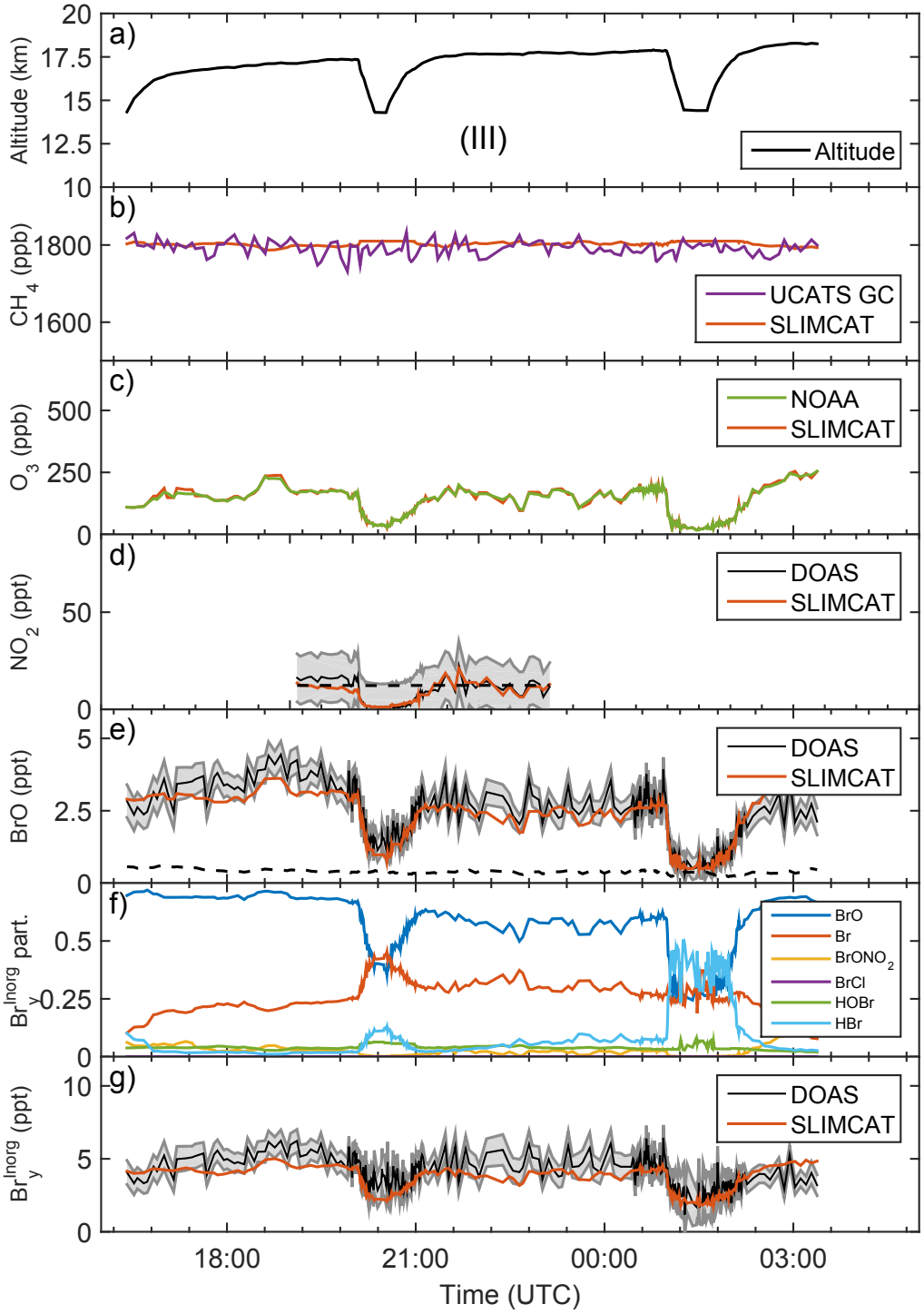

Figure 8.4: SF1-2013, on Feb. 5, 2013. The different panels are explained in the text.

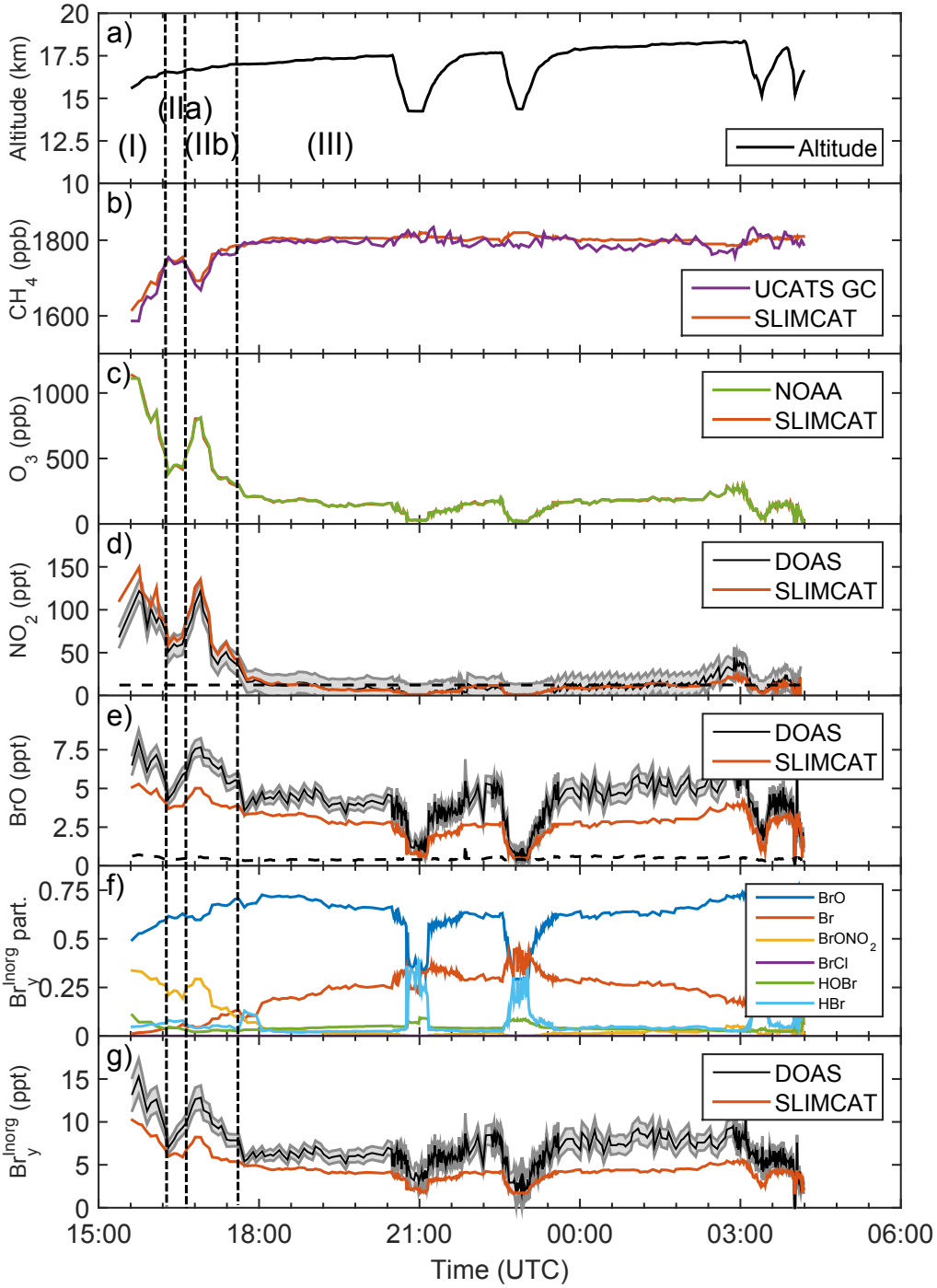

Figure 8.5: Same as Figure 8.4, but for SF2-2013, on Feb. 9, 2013.

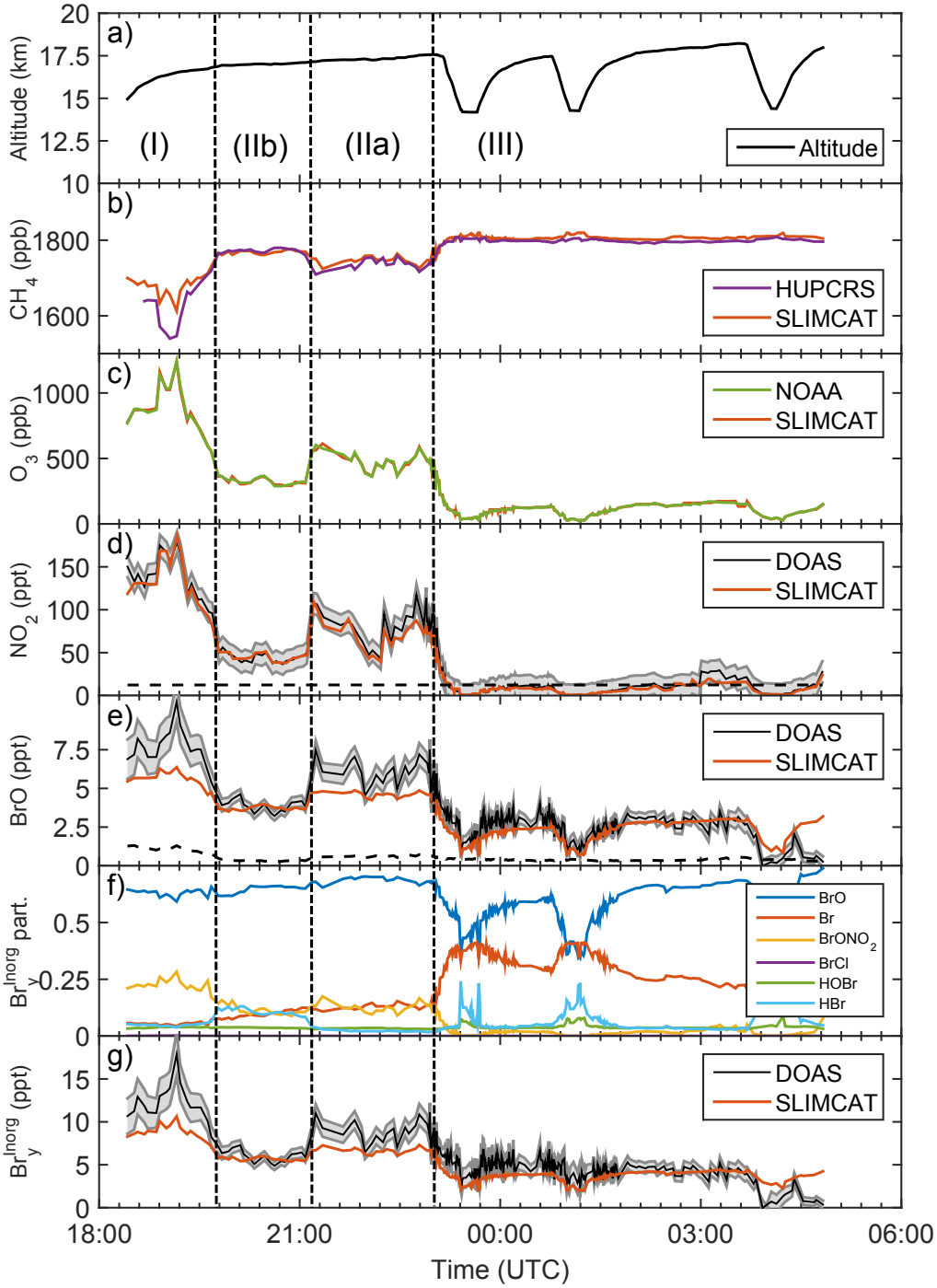

Figure 8.6: Same as Figure 8.4, but for SF3-2013, on Feb. 14, 2013.

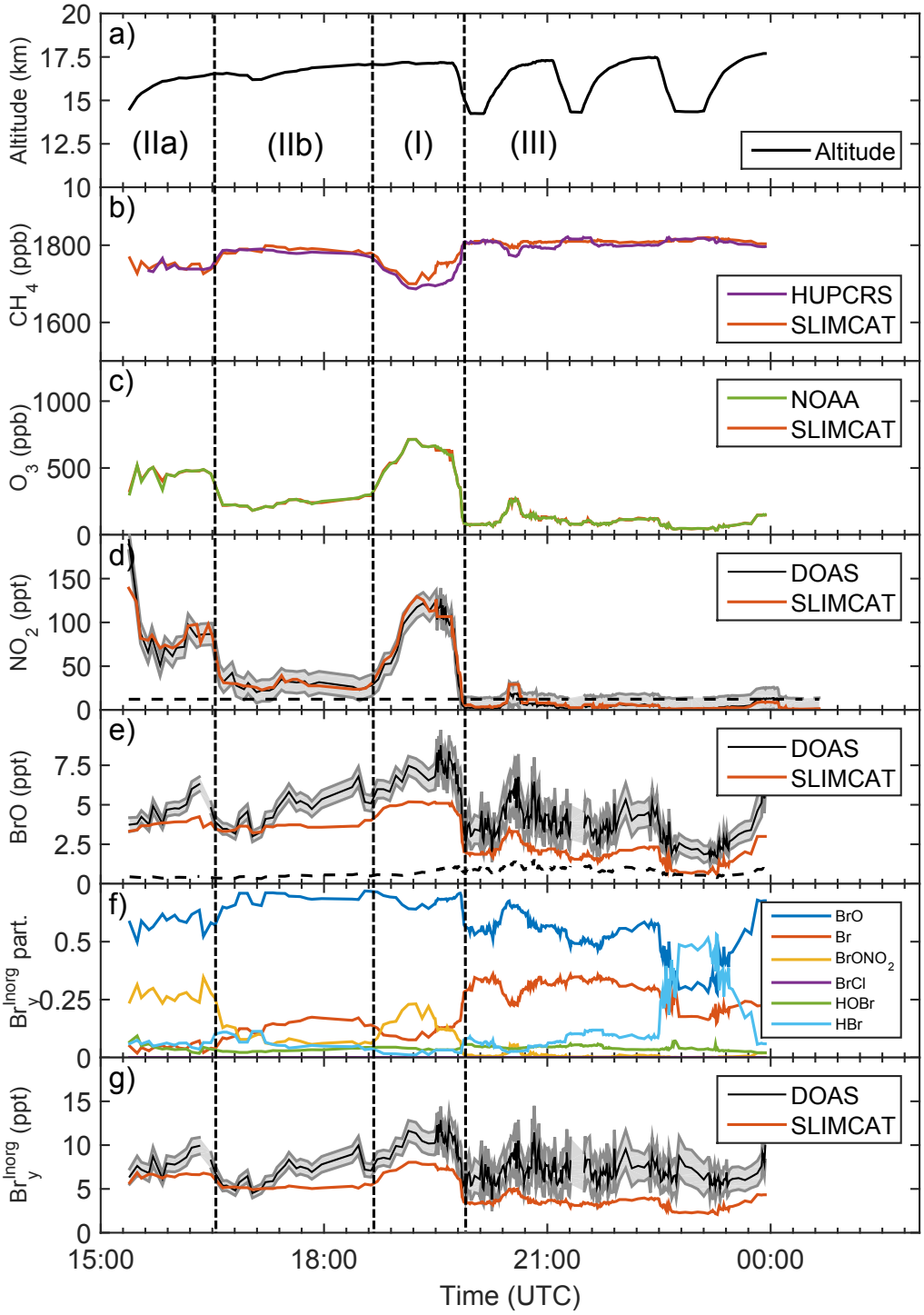

Figure 8.7: Same as Figure 8.4, but for SF4-2013, on Feb. 21, 2013.

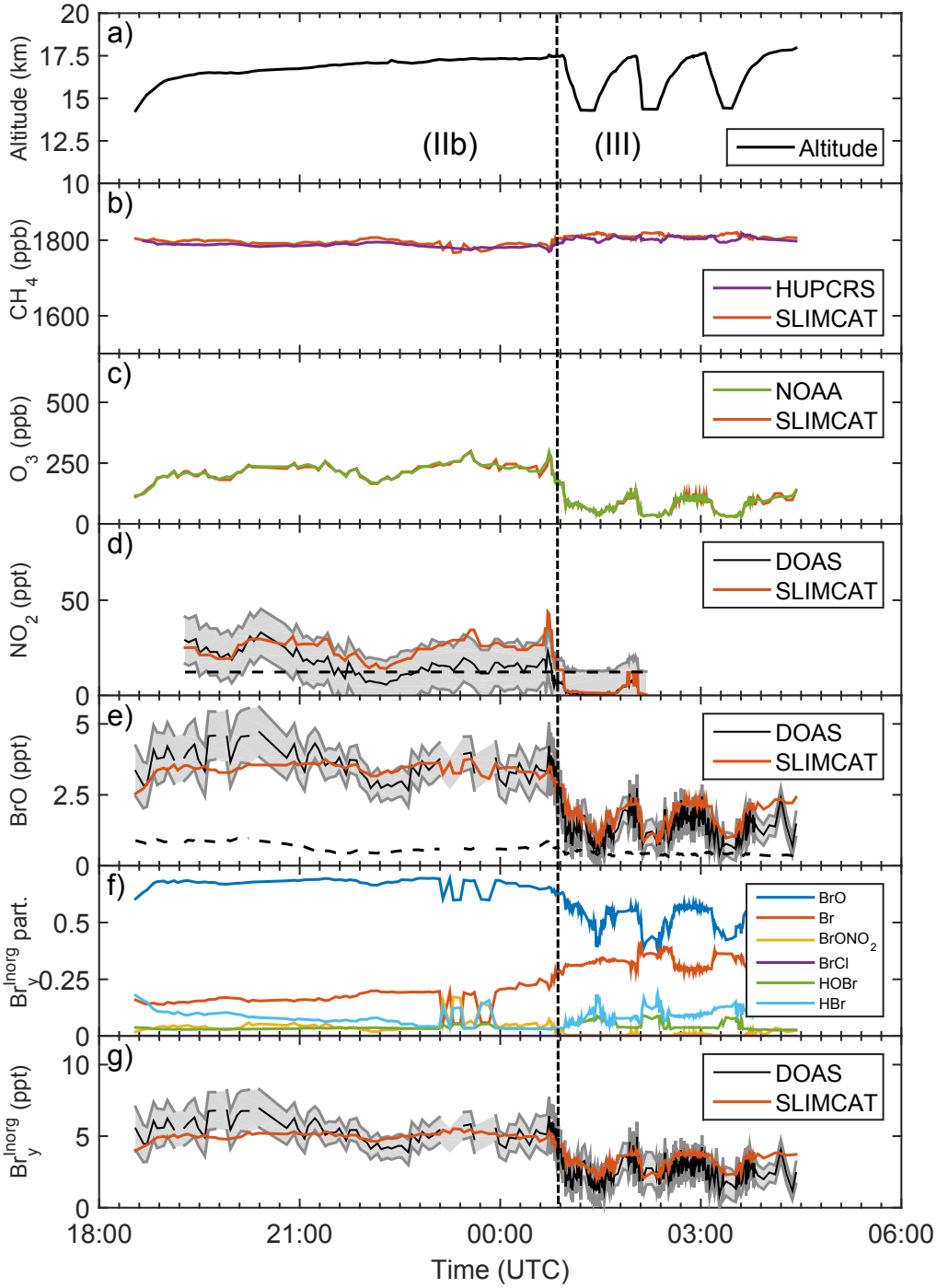

Figure 8.8: Same as Figure 8.4, but for SF5-2013, on Feb. 26, 2013.

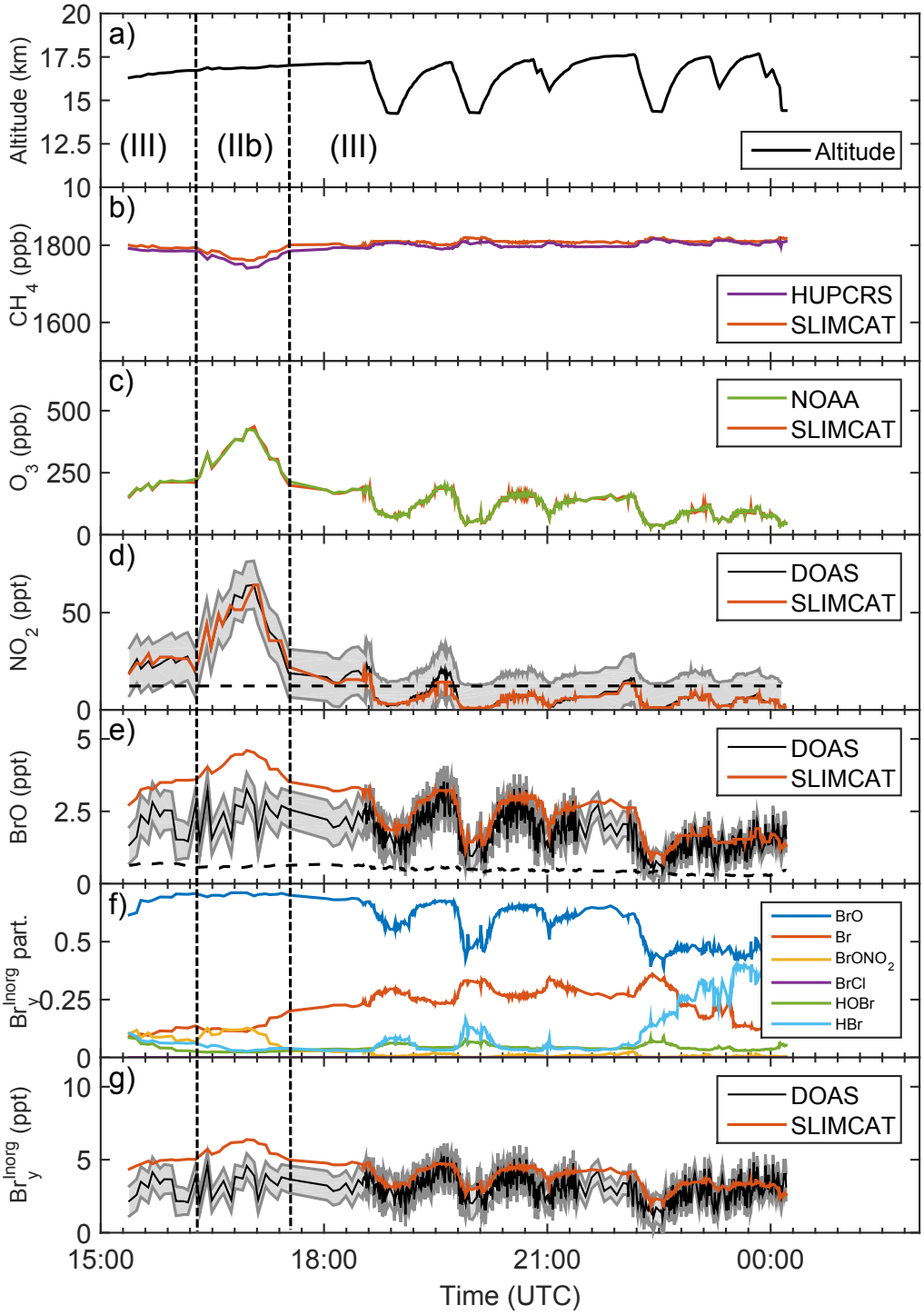

Figure 8.9: Same as Figure 8.4, but for SF6-2013, on Mar. 1, 2013.

Panels (b), and (c) of Figures 8.4 to 8.9 show comparisons of measured and modelled CH_4, and O_3 concentrations. The measured and modelled species show excellent agreement within the given error bars, after the modelled curtains were altitude adjusted (see section 6.3.2), which is not surprising after the agreement in Figure 8.1.

Panels (d) compare measured and modelled NO_2. Overall the measured (and modelled) NO_2 concentrations meet the expectations for NO_x (= NO, NO_2, and NO_3) abundances in the LS, UT, and TTL over the pristine Pacific. Elevated NO_2 concentrations (range 70 ppt to 170 ppt) are measured within the subtropical lowermost stratosphere, where aged air masses are probed as indicated by the decreased CH_4 concentrations, elevated O_3 concentrations, and presumably decreased N_2O concentrations. Remind here that N_2O is the primary source for stratospheric NO_x, and in the stratosphere CH_4, and N_2O destruction closely follow each other (e.g., Michelsen et al. (1998), Ravishankara et al. (2009), and others). Very low NO_2 concentrations ($\leq$ 30 ppt) are detected within the UT and TTL, indicating that the analysed air did not originate from recently polluted, or lightning affected regions. Further, the modelled NO_2 concentrations (red line in panel d) are found to fall into the given range of errors of the measured NO_2 concentrations. This finding strongly indicates that the NO_x, and NO_y (= NO_x, N_2O_5, HNO_3, HO_2NO_2,...) budget and photochemistry of the LS, UT and TTL is reproduced well in the SLIMCAT simulations, and that overall the O_3-scaling-method works well for NO_2.

Next the discussion addresses the findings on measured and modelled BrO, and what conclusions can be drawn for the amount and fate of inorganic bromine within the tropical LS, UT, and TTL. Measured and modelled BrO is displayed in Figures 8.4 to 8.9 (panel e), together with the modelled Br_y^{inorg} partitioning (panel f) and inferred Br_y^{inorg}. Again elevated BrO concentrations are measured within the LS (range 3 - 9 ppt), and lower BrO concentrations in the TTL (range 0.5 ppt - 5 ppt) with the smallest BrO concentrations (0.5 ppt - 1 ppt) occurring near the LZRH, i.e. the bottom of the TTL. Overall this behavior is expected from the arguments based on the amount and composition of the brominated organic and inorganic source gases, their life time, and atmospheric transport (e.g., Fueglistaler et al. (2009), Aschmann et al. (2009), Hossaini et al. (2012b), Ashfold et al. (2012), WMO (2014), and others).

With these caveats in mind, Figure 8.10 (black crosses) compares measured and modelled BrO. For all flights (except flight SF4-2013, for which a DOAS retrieval problem exists which caused a bias of 2 ppt in inferred BrO), measured and modelled BrO corresponds excellently for low concentrations (i.e. closed to LZRH), or very young air. For larger BrO concentrations (and older air) good agreement between measurement and model is found for SF1-2013, SF5-2013, and SF6-2013, when mostly air with low NO_2 concentrations (and predicted low $BrONO_2$ concentrations) was probed. For large BrO concentrations measured during flights SF2-2013, and

SF3-2013, the measured BrO is up to 2 ppt, or 25% larger than what the model predicted. In part, this gap could (tentatively) be closed by (1) adjusting the CH_2Br_2 surface concentration and atmospheric life time which potentially may add 0.4 ppt of Br_y^{inorg}, or $\approx$ 0.3 ppt in BrO when considering the bromine partitioning, and (2) by removing the flight to flight scatter in source gas concentrations ($\pm$ 0.8 ppt) in Br_y^{inorg}. The latter can for example be performed by a detailed back-trajectory and source appointment analysis (e.g. for details see Navarro (2015)).

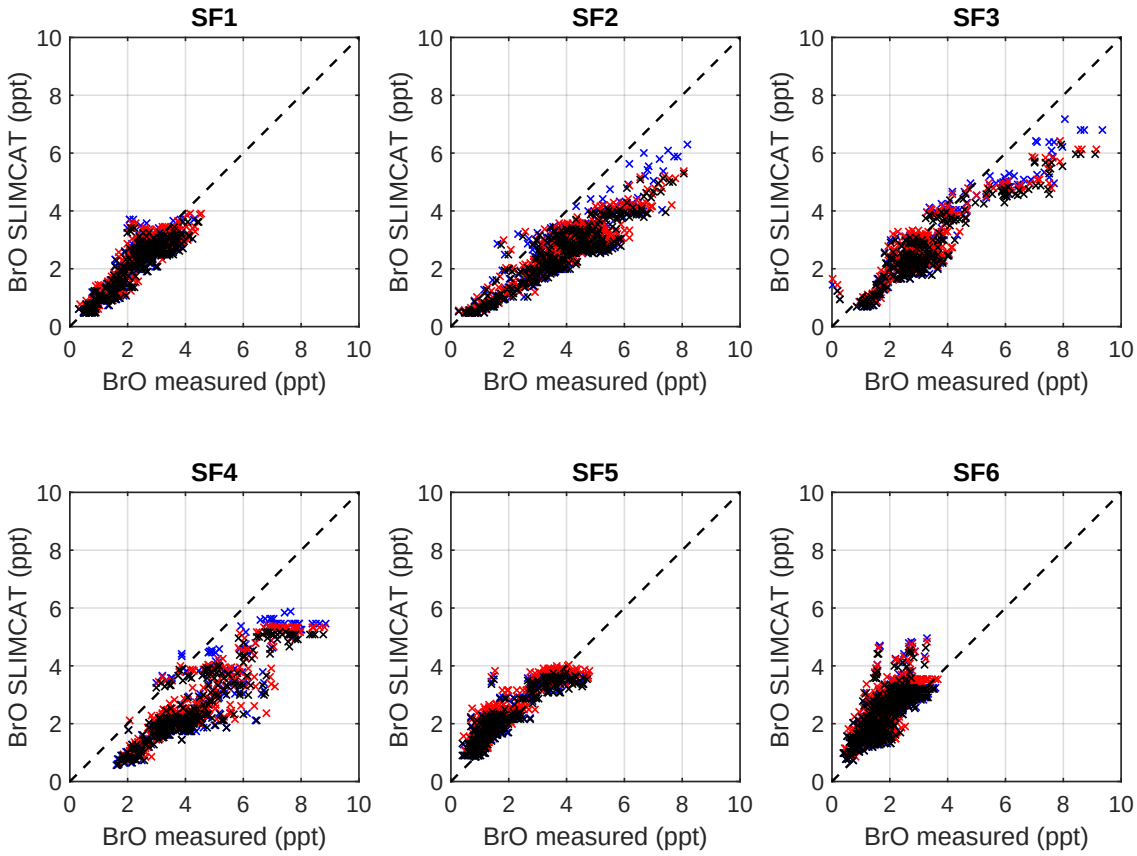

Figure 8.10: Comparison of measured and modelled BrO for all NASA-ATTREX science flights in 2013. Black crosses are for model run #583, blue crosses for run #584, and red crosses run #585.

Other reasons for the gap could come from uncertainties in the used kinetic constants, for example for the reaction BrO + NO_2 + M $\rightarrow$ $BrONO_2$ + M followed by the photolysis of $BrONO_2$, or the reaction Br + O_3 $\rightarrow$ BrO + O_2 (see section 7.7). How the assumed kinetic constants affect the result is tested in model run #584, by adopting for $BrONO_2$ J/k a factor 1.75 larger than recommended by JPL (Sander et al., 2011) according to the finding of Kreycy et al. (2013) (see the blue crosses in Figure 8.10). Evidently increasing J/k helps to close the remaining gap in measured

versus modelled BrO, which becomes particularly evident for large BrO and NO_2 concentrations i.e., for the bromine partitioning of the LS.

Alternatively, in model run #585 the rate reaction coefficient k_{Br+O3} for Br + O_3 is increased to the upper limit of the given uncertainty range of the JPL compilation. Overall increasing k_{Br+O3} changes very little in the measured vs modelled correlation for BrO (see the red crosses in Figure 8.10), but it would change the Br_y^{inorg} partitioning so that BrO was always largely prevalent over Br even at the lowest altitudes of the TTL (e.g., inspect panel (f) in Figures 8.4 to 8.9). In conclusion, our joint measurement of O_3, NO_2, and BrO, and the supporting CTM simulations do not support the speculation of Fernandez et al. (2014) on the existence of a 'ring of Br atoms' in the UT, and TTL to surround the globe at daytime, irrespective of what is assumed for k_{Br+O3}.

8.4 Comparison of BrO measurements with previous studies

Next the measurements are compared with previous BrO measurements in the UT, and TTL (e.g., Dorf et al. (2008), and Wang et al. (2015)). Overall the balloon-borne BrO profile measurements of Dorf et al. (2008) performed over tropical Brazil during the dry i.e., the non-convective season in June 2005, and June 2008 excellently compare with the BrO profiles inferred from our measurements for the UT and TTL (i.e., typically [BrO] = 0.5 ppt -1.0 ppt in the UT and around LZRH, and up to 5 ppt at the cold point tropopause), e.g., compare Figure 1 in Dorf et al. (2008) and Figures 7.15 and 7.14.

The present BrO measurements, as well as the BrO profile measurement of Dorf et al. (2008) are however in contrast to recent reports on the presence of BrO amounting up to 3 ppt in the tropical and subtropical UT, and around the bottom of the TTL (Wang et al., 2015) (compare Figure 2, panel A in Wang et al. (2015) with the left panel in Figure 7.18). Here it should be emphasized again that in the present data no indication is found for unexpected high or elevated BrO concentrations in the UT, and TTL, neither from inspecting the UT from above (e.g., see Figure 7.10), nor when directly probing the TTL (see above).

Between Wang et al. (2015) and this study some similarities exist, but also some dissimilarities. First of all, Wang et al. (2015) probed the UT and the bottom of the TTL for BrO, adjacent to the part of the Pacific as the Global Hawk sorties did in early 2013, i.e., mostly off the Western coasts of South and middle America during the same season but more to the south. Therefore it could be just a matter of chance, or due to the different regions probed in both studies, that during NASA-ATTREX it was missed to detect elevated BrO concentration in the UT, and the bottom of the TTL as reported by Wang et al. (2015), and Volkamer et al. (2015).

Second even though Wang et al. (2015) used a similar technique as used for the present study, and in particular they used the same radiative transfer code (i.e. McArtim, see Deutschmann et al. (2011)), they solely relied on using the optimal estimation technique for the interpretation of their measurements, i.e. for the profile retrieval (Volkamer et al., 2015). It is known that this technique may deliver robust results, if the region of interest is carefully sampled, and if the forward model (equation 7.2) reasonably well describes the physical reality (Rodgers, 2000). Accordingly, Wang et al. (2015), and Volkamer et al. (2015) invested quite some effort to constrain well their radiative transfer, for example by using information on the aerosol type and their optical properties gained by other instrumentation and/or by constraining the radiative transfer with measured information on the absorption of the O_4 collisional complex (see for example Figure 3 in Volkamer et al. (2015), and the complementary Figure 7.3 in the present study). The study on the sensitivity of the O_4 absorption in limb direction as a function of the cloud cover underneath (see section 7.3.2) as well as the results presented by Volkamer et al. (2015) in their Figure 3 clearly demonstrate the limitation of the O_4 method to constrain the radiative transfer for UV/vis studies above 10 km, mostly because the bulk of O_4 collisional complex is located near the surface. Therefore, any skylight analysed for the O_4 absorption in limb direction may carry additional, or even predominantly information on the radiative transfer of lower atmospheric layers (see Figure 7.3), rather than of the targeted atmospheric layers.

Finally Wang et al. (2015), and Volkamer et al. (2015) did not use a stratospheric CTM to study the potential influence of changing overhead BrO concentrations on their results. As a result, the predominant occurrence of atmospheric BrO in the stratosphere at daytime, and its potential column changes mostly due to a changing tropopause height may have mimicked the presence of BrO in limb direction, or flight altitude, in Wang et al. (2015), and Volkamer et al. (2015) (see Figure 7.13 of this study).

In conclusion, even though most of the TORERO (data basis for Volkamer et al. (2015) and Wang et al. (2015)) flights were performed under clear-skies (Volkamer et al., 2015), it is not clear how much unaccounted scattering due to aerosols and (probably) optically thin upper tropospheric clouds, lower level clouds, or changing overhead stratospheric BrO contributed to the inferred elevated BrO in the UT, or bottom of the TTL.

8.5 Distribution of inorganic bromine (Br_y^{inorg})

Next, the implication of the measurements and modelling of Br_y^{inorg} (contribution 4) present in the LS, UT, and TTL over the Eastern Pacific during the convective season (Figure 8.11) is discussed. Br_y^{inorg} is calculated from measured BrO and the modelled Br_y^{inorg} partitioning (see panels (f), and (g) in Figures 8.4 to 8.9). The

histograms in Figure 8.11 clearly indicate, that Br_y^{inorg} increases with increasing potential temperatures i.e., from (2.63 ± 1.04) ppt at θ = 350 K - 360 K (at the bottom of the TTL) to (4.22 ± 1.37) ppt for θ = 390 K - 400 K (just above the cold point tropopause).

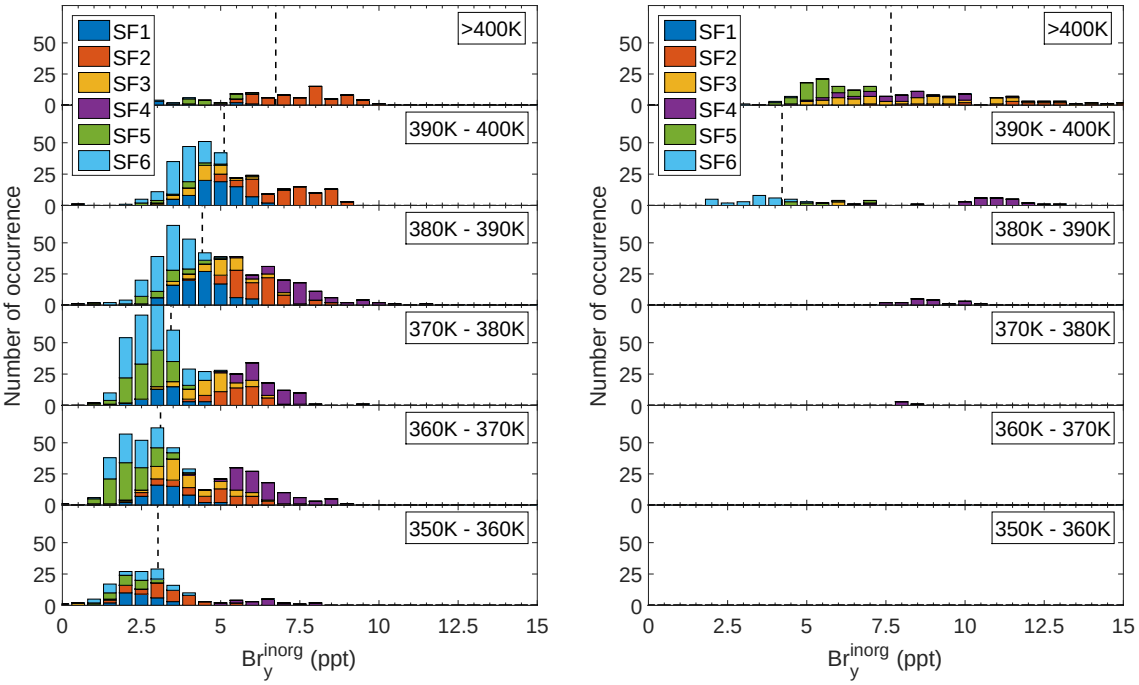

Figure 8.11: Left panel: Histogram of BrO_y^{inorg} occurrence as function of potential temperature for all NASA-ATTREX flights in 2013. Shown are data for $[CH_4]$≥1790 ppb, which can be considered as young air mostly found in the ventilated TTL. The mean concentration (black dashed vertical lines) and the variance are for θ = 350 K - 360 K, (2.63 ± 1.04) ppt; θ = 360 K - 370 K, (3.1 ± 1.28) ppt; θ = 370 K - 380 K, (3.43 ± 1.25) ppt; θ = 380 K - 390 K, (4.42 ± 1.35) ppt; θ = 390 K - 400 K, (5.1 ± 1.57) ppt, and θ ≥ 400 K, (6.74 ± 1.79) ppt, respectively. Data from SF4-2013 are shown for completeness but excluded from the calculation of averages. Right panel: Same as left panel but for $[CH_4]$≤1790 ppb, which can be considered as aged air mostly found in the subtropical lowermost stratosphere. The means and variances are for θ = 390 K - 400 K, (4.22±1.37) ppt, and θ ≥400 K, (7.67±2.72) ppt, respectively.

Remarkable are the non-negligible amounts of Br_y^{inorg} (2.63 ppt ± 1.04 ppt, range from 0.5 ppt to 5.25 ppt, which is from close to zero to 25% of all TTL bromine) inferred for altitudes just above the LZRH (θ = 350 K - 360 K), of which 40 to 50% consists of BrO. This finding clearly sets a range and an upper limit for the Br_y^{inorg} influx into the TTL due to entrained air masses of tropospheric origin

(contribution 4). Again the latter can most likely be attributed to different source regions (and thus emission strengths) of the brominated VSLS, and a varying degree of photochemical processing of the air masses transported from the surface to the TTL. Noteworthy is also the increase in variance found for Br_y^{inorg}, which increase in absolute terms, but decrease in relative terms (i.e. from 0.4 at θ = 350 K - 360 K to 0.3 at θ = 390 K - 400 K) with increasing θ. This may indicate a subsequent flattening-out of the air-mass-to-air-mass variability of Br_y^{inorg} in aging air due to the photochemical decay of the brominated organic source gases and atmospheric mixing processes.

8.6 Inferred total bromine (Br_y)

Figure 8.13 displays inferred total Br_y for the individual flights from where measurements of the organic bromine species are available and inferred Br_y^{inorg} is reliable. For individual samples Br_y ranges between (20.55 - 23.34) ppt for SF1-2013, (19.99 - 24.25) ppt for SF3-2013, (19.57 - 23.06) ppt for SF5-2013, and (19.25 - 20.36) ppt for SF6-2013. Averaged over each flight the concentrations range from 20.3 ppt for SF6-2013 up to 22.3 ppt for SF3-2013, with a standard deviation of ∼1.5 ppt per flight. The mean concentrations per flight are also shown in Figure 8.14 which is an updated version of Figure 2.8 (WMO, 2014). On the basis of Figures 8.13 and 8.14 the different contributions 1 - 4 to total Br_y are discussed.

Methyl bromide CH_3Br (dark blue, contribution 1) and the halons (purple, contribution 2) constantly contribute with 14.6 ppt to total Br_y for the air analysed in early 2013. This concentration is in excellent agreement with expectations based on the trend in CH_3Br and the halons (blue and purple lines in Figure 2.8), and the recent update of surface measurements (J. Elkins, private communication, 2015).

The contribution of the brominated VSLS (contribution 3) ranges between 2 ppt and 5 ppt for individual samples (Figure 8.12) and between 3.0 ppt and 3.3 ppt for the mean concentration of each flight. The increase in Br_y^{inorg} (contribution 4) with increasing potential temperature θ (and decreasing CH_4) mostly corresponds to a decrease in concentrations of the brominated VSLS, however, only if the same young air masses of large CH_4 concentrations were probed (Figure 8.12). For example for SF1-2013, SF5-2013, and SF6-2013 when mostly the TTL was probed, all data points fall into a band of about ±1 ppt in width, next to a flight dependent diagonal line (not shown). An exception is SF3-2013 when the LS (and thus older air) and TTL was probed. When extrapolating the corresponding diagonals for SF1-2013, SF5-2013, and SF6-2013 to $[Br_y^{inorg}] = 0$, and assuming no bromine is effectively lost, then the apparent concentrations of brominated VSLS at the surface should range between 4 ppt - 8.5 ppt. However, frequently much larger concentrations of brominated VSLS (up to 50 ppt) were measured in surface air of the Pacific (e.g., Yokouchi et al. (1997), Schauffler et al. (1998), Wamsley et al. (1998) Yokouchi et al.

(2005), Tegtmeier et al. (2012), Ashfold et al. (2012), Ziska et al. (2013), Sala et al. (2014b), and others). Therefore effective loss processes for bromine, for example by heterogeneous uptake of inorganic bromine on aerosol and cloud particles must act in the atmosphere.

As a consequence the photochemical destruction of the organic brominated VSLS and the concordant increase in inorganic bromine keeps Br_y almost constant within the TTL during an individual flight, but Br_y varies from flight to flight in a range of 20.3 ppt to 22.3 ppt (mean concentration per flight). In summary, subtracting from the given range (20.3 ppt to 22.3 ppt) of Br_y the contribution of CH_3Br and the halons to total stratospheric bromine (14.6 ppt) points to a variable contribution from VSLS bromine (contribution 3), and Br_y^{inorg} (contribution 4) to TTL bromine in the range of 5.7 ppt to 7.7 ppt (± 1.5 ppt). This range falls well into the range (2 ppt - 8 ppt) assessed in WMO (2014) for contribution 3 and 4, but it is somewhat (up to 3 ppt, see Figure 8.14) larger than some of the earlier studies indicated (see section 2.4). Here one may wonder whether (a) this results is significant, or if (b) some Br_y^{inorg} is actually removed by heterogeneous processes in the TTL (e.g., Aschmann et al. (2011), Aschmann and Sinnhuber (2013), and others), or if (c) TTL Br_y shows some seasonality (e.g., Levine et al. (2008), Krüger et al. (2008), Fueglistaler et al. (2009), Schofield et al. (2011), Ploeger et al. (2011), and others).

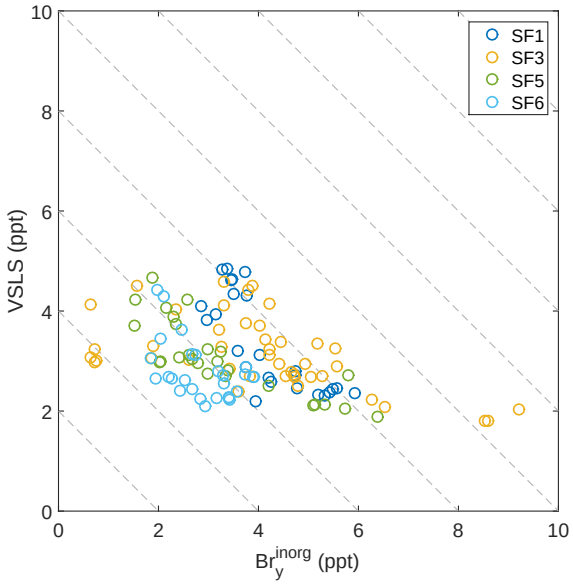

Figure 8.12: Br_y^{inorg} as a function of the sum of all brominated VSLS using the colour code of Figures 8.2 and 8.11. The data points should follow individual diagonal lines, if all Br_y^{inorg} would be produced from the same VSLS concentration at the surface.

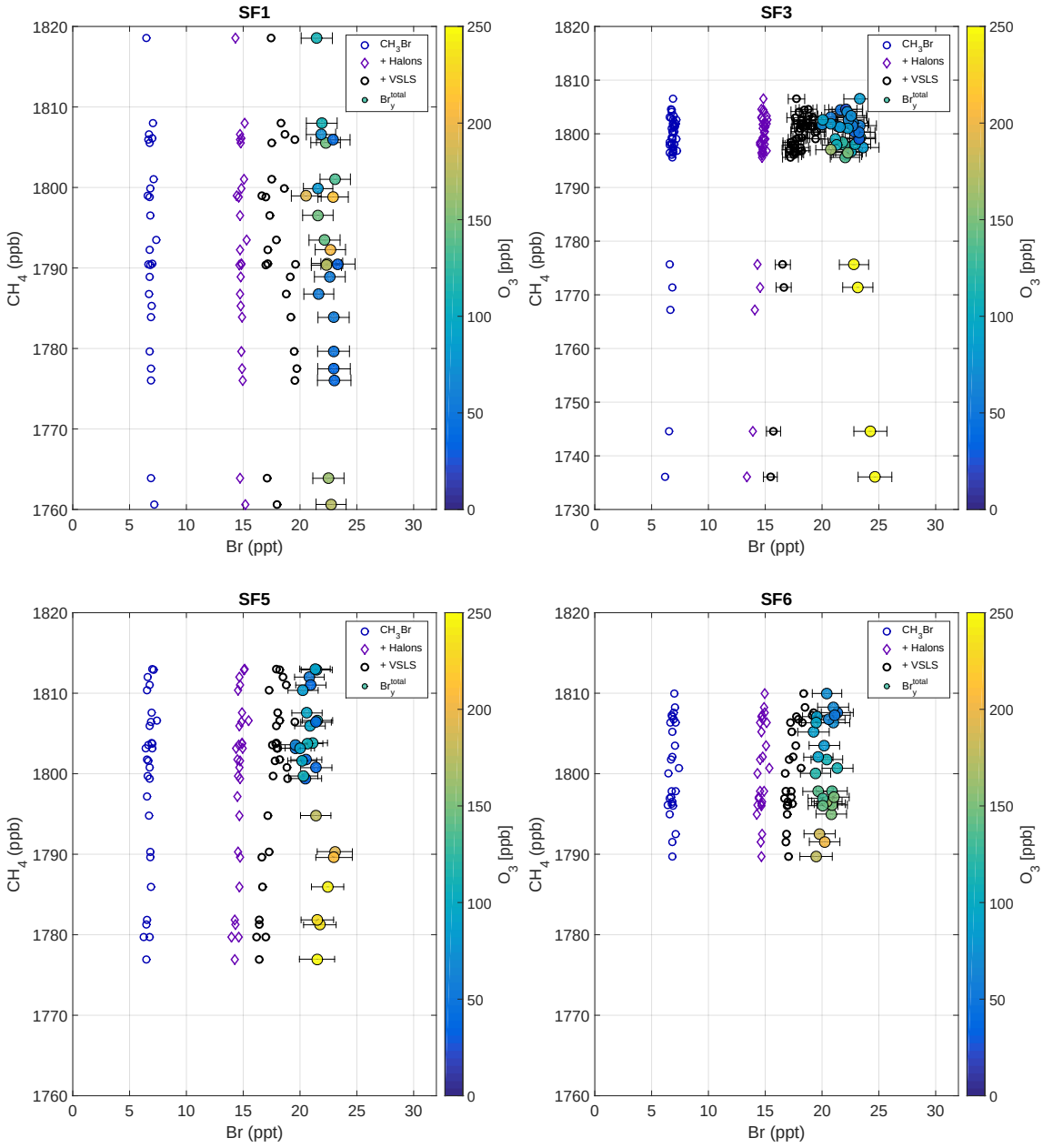

Figure 8.13: Inferred total Br_y ($= CH_3Br + Halons + VSLS + Br_y^{inorg}$) as a function of CH_4 for the flights SF1-2013, SF3-2013, SF5-2013 and SF6-2013. Please notice the different CH_4 range for SF3-2013, which is the only flight in which older air in the LS was sampled. For a single flight total Br_y is almost constant. Including all individual measurements from all flights, concentrations range from 19.25 ppt to 24.25 ppt with errors of ∼1.5 ppt for the single measurement. Mean concentrations and standard deviation per flight are (22.3 ± 0.7) ppt for SF1-2013, (22.2 ± 1.1) ppt for SF3-2013, (21.0 ± 0.9) ppt for SF5-2013, (20.3 ± 0.6) ppt for SF6-2013.

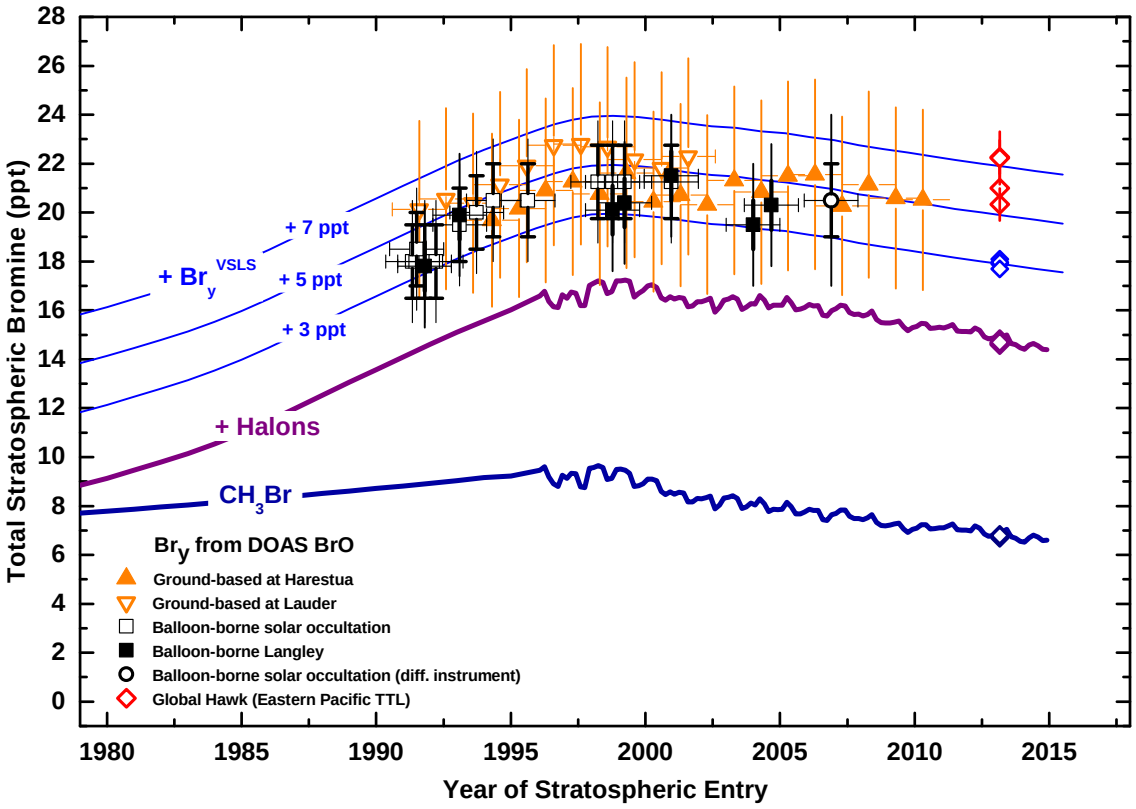

Figure 8.14: Same as Figure 2.8, including the data of the NASA-ATTREX flights SF1-2013, SF3-2013, SF5-2013 and SF6-2013. Each data point of Br_y corresponds to a flight mean concentration. Measurements of the long-lived SGs (CH_3Br and halons) follow exactly the expected trend but neither for the brominated VSLS nor for total Br_y. The red error bars represent the standard deviation from the mean, determined from all data of an individual flight (see caption of Figure 8.13).

9 Conclusions and outlook

9.1 Conclusions

The extra-tropical lowermost stratosphere, upper troposphere, and tropopause layer of the Eastern Pacific was probed for inorganic bromine during the convective season (February and March 2013). The measurements of CH_4, O_3, NO_2, BrO, and of some organic brominated source gases are inter-compared with SLIMCAT simulations. The simulated and measured in-situ concentrations of the dynamical tracer CH_4 agree well on a large scale but some small scale variations are not captured in the model. After the simulated SLIMCAT curtains of O_3 are projected on the measured O_3 concentrations, an overall excellent agreement for the CH_4 is found between the measurement and simulation of both tracers. When the simulated curtains of NO_2 are adjusted with the same parameters as inferred above, excellent agreement is again found between measured and modelled NO_2, thus providing further confidence in the measurement technique, in the modelled NO_y photochemistry, and in the overall approach.

Next, the measured and modelled TTL concentrations of CH_2Br_2, $CHBr_3$ are found to compare well after the surface concentrations and atmospheric life-times of both species are adjusted in the model (e.g., $[CHBr_3] = 1.4$ ppt, $[CH_2Br_2] = 1.05$ ppt at the surface). Further the contribution to bromine in the LS, UT, and TTL by some other VSLS chloro-bromo-hydrocabrons (e.g., $\Sigma[CHClBr_2CHCl_2BrCH_2ClBr\cdots]$) is accounted for by assuming a constant surface concentration of 1 ppt in the model. Total organic bromine inferred from these VSLS species is found to vary by $\pm$ 1 ppt from flight to flight in the TTL over the Eastern Pacific in early 2013. This clearly indicates different origins and possibly atmospheric processing of the investigated air masses (for details see the upcoming paper of Navarro (2015)).

The measured BrO concentrations ranged between 3 ppt - 9 ppt in the subtropical LS. In the TTL they ranged between (0.5 $\pm$ 0.5) ppt at the LZRH, and about 5 ppt at $\theta = 400$ K, in overall good agreement with the model simulations, and the expectation based on the decay of the brominated source gases, and atmospheric transport. In the TTL, the inferred Br_y^{inorg} is found to increase from a mean of (2.63 $\pm$ 1.04) ppt for θ's in the range of 350 K - 360 K to (5.11 $\pm$ 1.57) ppt for $\theta = 390$ K $-$ 400 K, respectively, whereas in the subtropical LS it reached (7.66 $\pm$ 2.95) ppt for θ's in the range of 390 K - 400 K. The non-negligible Br_y^{inorg} found for the lowest altitudes of the TTL i.e., (2.63 $\pm$ 1.04) ppt with a range from 0.5 ppt to 5.25 ppt (or close to zero to 25% of all TTL bromine) is also remarkable. This

may indicate a sizeable, but rather variable influx of inorganic bromine into the TTL, largely depending on the air mass history, i.e. source region, and atmospheric transport and processing.

The findings on Br_y^{inorg} in the LS and TTL are in broad agreement with past experimental and theoretical studies on the processes and amount of bromine injected by source gas and product gases into the TTL, and eventually into the extratropical lowermost stratosphere (Ko et al. (1997), Schauffler et al. (1998), Wamsley et al. (1998), Dvortsov et al. (1999), Pfeilsticker et al. (2000), Montzka et al. (2003), Salawitch (2006), Sinnhuber and Folkins (2006), Laube et al. (2008), Dorf et al. (2006), Dorf et al. (2008), Sinnhuber et al. (2009), Salawitch et al. (2010), Schofield et al. (2011), Aschmann et al. (2011), Hossaini et al. (2012b), Ashfold et al. (2012), Hossaini et al. (2012a), Aschmann and Sinnhuber (2013), Sala et al. (2014b), Wang et al. (2015), WMO (2014), and many others). The variable contribution from VSLS bromine (contribution 3), and Br_y^{inorg} (contribution 4) to TTL bromine ranges between 5.7 ppt to 7.7 ppt ($\pm$ 1.5 ppt) per flight. This range falls well into the range (2 ppt - 8 ppt) assessed in WMO (2014) for contribution 3 and 4, but it is somewhat larger than some of the earlier studies indicated (see section 2.4). This study, however sets tighter limits on the amount of inorganic bromine (Br_y^{inorg}), the influx of brominated source gases (Br_y^{org}), product gases, and the photochemistry of bromine in the TTL and LS than previously existing studies. In particular, it (re-)emphasizes that (a) variable, but non-negligible amounts of Br_y^{inorg} are transported into the TTL, (b) that TTL Br_y is rather variable (20.3 ppt to 22.3 ppt), and (c) that Br_y likely does not only depend on the source region of the air masses and thus the loading with VSLS bromine, but (d) possibly also on the efficiency of heterogeneous processing and removal of some Br_y^{inorg} by atmospheric (ice) clouds and aerosols (e.g., Aschmann et al. (2011), and Aschmann and Sinnhuber (2013)).

The amount of assessed Br_y over the Eastern Pacific during the convective season is found larger (up to 3 ppt) than the average concentrations found for the stratosphere presently (e.g., Dorf et al. (2006), Dorf et al. (2008), and WMO (2014)). By assuming that this gap is significant, additional processes may come into to the focus of stratospheric bromine research, i.e., the seasonality and possibly long term trend of the bromine transported into the stratosphere (e.g., Levine et al. (2008), Krüger et al. (2008), Fueglistaler et al. (2009), Schofield et al. (2011), Ploeger et al. (2011), and others).

9.2 Outlook

The outlook is twofold. First, it focusses on recommendations for the technical issues of the data analysis of the NASA-ATTREX 2013, and especially the 2014 flights. Recommendations are made of how the collected data from largely cloud affected NASA-ATTREX deployments in the Western Pacific in 2014 missions can be

processed. Second, open scientific questions arising from the results of the present thesis are addressed. It is discussed how future studies would help to improve further our knowledge on the photochemistry and budget of bromine in the TTL and stratosphere.

9.2.1 Recommendations for improvement of the data analysis

The following remaining open issues regarding the data analysis are:

First, an obvious issue is the spectral retrieval of SF4-2013. Due to some untraceable reasons the direct solar references of this flight are corrupted. Most probably there was ice formation on the diffuser disk. Also direct solar references from other flights were tried in the spectral retrieval but that did not work properly either. Eventually with more effort on re-calibrating solar references from other flights the data of SF4-2013 could be restored.

Second, the 2014 flights above the Western Pacific may give a spatially more complete picture of the TTL bromine budget during the wet and convective season. However cirrus clouds were much more abundant during the 2014 than during the 2013 deployment. The radiative transfer of cirrus clouds (ice particles) at high altitudes is very complex and requires a more complex parametrisation for the phase function than obtained from the Henyey-Greenstein parametrisation or Mie calculations. The sensitivity studies on cirrus clouds (19, 20, 21) revealed that the impact of cirrus clouds on the retrieved BrO concentrations via the O_3-scaling-method can be sizeable (up to 20% deviation, when flying within the cloud), remembering that the cirrus cloud in this study are rather thin (OD=1). Tricoli et al. (2015) developed a fully 3D scattering code for arbitrary shaped particles which could be used for calculating the Jacobians for a retrieval.

The biggest challenge however is the lack of a priori knowledge on the optical state of the atmosphere which makes the use of optimal estimation methods almost impossible. Also the O_3-scaling-method reaches its limits due to the light path modifications for cirrus clouds at high altitudes which makes the calculation of the α-factors more uncertain. Nevertheless the O_3-scaling-method can provide precise results for the cloud-free sections of the 2014 flights and results with a higher uncertainty for cloudy sections. Furthermore by utilising the near-IR data it is probably possible to distinguish the phase composition (ice, liquid water, water vapor) of the encountered clouds and thus improve the forward model.

Third, the O_3-scaling-method overcomes to a certain degree the 3D nature of the remote-sensing measurements (see chapter 7). However, a full 3D inversion would probably provide even more insight on the vertical and horizontal distribution of the targeted trace gases. I suggest an optimal estimation method but not based on 1D (altitude) but on a full 3D, or 2D (e.g. no horizontal heterogeneity assumed

perpendicular to the GH flight track) grid. By subdividing the atmosphere in 2D, or 3D, the layers become to clusters, or voxels. Depending the information content (via BoxAMFs and a priori contribution functions) the atmosphere would be subdivided in an appropriate way. Then a more realistic forward model would support a more reliable inversion, which however would likely carry (or require) more (2D, or 3D) a priori information. According to my knowledge this has not been tried for aircraft measurements so far. There are satellite retrievals which work on 2D or even 3D discretisations of the atmosphere (e.g. Pukite et al. (2010)). The major challenge of this approach is the adaptive clustering of the atmosphere in order to constrain the inversion accordingly to its information content. However, this approach would require quite some programming effort and would require a study on its own.

9.2.2 Open scientific questions

The observation of (a) higher Br_y concentrations than found in previous stratospheric measurements (e.g. Dorf et al. (2006), Dorf et al. (2008), and WMO (2014)) and (b) the observed variability from flight to flight, point to the following major causes, processes, and/or questions:

1. Does TTL total bromine determined for the wet season in early 2013 not reflect total stratospheric bromine, since there are efficient heterogeneous loss processes acting in the TTL (Aschmann et al. (2009), Aschmann et al. (2011), Aschmann and Sinnhuber (2013))?
2. Is there a sizeable seasonality in the transport of TTL bromine into the stratosphere ((e.g., Levine et al. (2008), Krüger et al. (2008), Fueglistaler et al. (2009), Schofield et al. (2011), Ploeger et al. (2011), and others)?
3. Does the trend in stratospheric total bromine continue as expected from change in surface concentrations of CH_3Br and the halons (Figure 8.14), or does in a changing climate the contribution of the VSLS and Br_y^{inorg} to stratospheric bromine becomes larger on a relative or even absolute basis (e.g. Hossaini et al. (2012a) and Yang et al. (2014))?

These questions however can only be answered when more Br_y data from the TTL and stratosphere become available in future. The measurements should provide complementary information to the already gained knowledge with respect to time and place. Further analysis of the NASA-ATTREX 2014 flights and studying the air back trajectories of the both, the 2013 and 2014 flights, (upcoming publication of Navarro (2015)) can already provide a more comprehensive picture of the distribution of the different contributions to Br_y across the whole Pacific during the wet season 2013. A project, similar to NASA-ATTREX, during the dry season would provide more information on the seasonality of bromine transport. This is of specific importance for the VSLS and Br_y^{inorg} contribution since they are not well-mixed

within the troposphere, in contrast to CH_3Br and the halons. Ashfold et al. (2012) also shows that the strength of El Niño and Southern Oscillation (ENSO) conditions have a strong impact on the air back trajectories of air parcels reaching the TTL. Future aircraft-borne measurements could monitor how changing ENSO conditions eventually change the production and distribution of VSLS.

Regular future balloon-borne soundings throughout the UT, TTL and LS (up to ∼35 km) of the different contributions to stratospheric Br_y would supply more information on heterogeneous loss processes and allow a monitoring of the long-term trend of Br_y.

There is also the open question regarding the formation rate constant of bromine nitrate ($BrONO_2$), which is the most important BrO_x reservoir species in the lower stratosphere (see inorganic bromine partitioning in panels (f) in Figures 8.4 to 8.9). The rate constant k_{BrONO_2} of the termolecular formation reaction $BrO+NO_2 \xrightarrow{M} BrONO_2$ has a large uncertainty which mostly arises from the extrapolation of the laboratory measurements of k_{BrONO_2} from high to low temperatures. E.g. a measurement of by Thorn et al. (1993), which is recommended by Sander et al. (2011), was performed within a temperature range of 248 K - 346 K. The findings of Kreycy et al. (2013), as well as of the present study, support a larger ratio of $J(BrONO_2)/k_{BrONO_2}$ (by a factor of 1.7 at 220 K). This is located within the large uncertainty range given in Sander et al. (2011). However, laboratory measurements of k_{BrONO_2} under controlled conditions at low temperatures, as encountered in the TTL (down to ∼190 K), would provide preciser results in the simulation of the inorganic bromine partitioning.

A Appendix: O_3-scaling-method sensitivity runs

This appendix contains a complete register of all performed sensitivity runs. Table A.1 and table A.2 show the numbers of the runs, the modifications made for each run, as well as the range and the typical impact on the derived NO_2 and BrO mixing ratio, respectively.

Figures A.1 to A.8 show the absolute (middle panel) and the relative (bottom panel) deviation of the BrO concentrations from the base run. The same runs for NO_2 are not shown because the behaviour is basically the same like for BrO. The base run specifications are listed in Table 6.3.

Table A.1: Sensitivity runs for inferred NO_2, according to the O_3-scaling-method.

Run #	Parameter	Modification	Δ NO_2			
			absolute		relative[%]	
			range	typical	range	typical
1 / 2	In-situ O_3	× 0.97/1.03	± 10 ppt	4/2 ppt	±6	± 3
3 / 4	NO_2 profile > 17.5 km	× 0.85/1.15	± 9 ppt	±3 ppt	± 3	± 5
5 / 6		× 0.7/1.3	± 25 ppt	±13 ppt	±30	± 15
7 / 8	O_3 profile >17.5 km	× 0.9/1.1	± 9 ppt	±3 ppt	±18	± 13
9 / 10		× 0.97/1.03	± 3 ppt	±1.5 ppt	±5	±3
11, 12, 13	Tropospheric NO_2	+ 10/+ 15/+ 20 ppt	±15/±20/±50 ppt	±10/±15/±25 ppt	±1000/±1500/±2000	±500/±750/±1000
14 / 15	Aerosol extinction	× 0.5/2	±4/±2 ppt	±1.5/±1.5 ppt	±4/±4	±3/±3
16, 17, 18	Marine strato-cumulus	OD=5/10/20 from 1-2 km	±3.5/±3.5/±3.5 ppt	±1.5/±1.5/±1.5 ppt	±4/±5/±5	±5/±6/±7
19, 20, 21	Cirrus cloud	OD = 1 from 13-14/ 14-15/15-16 km	±5/±5/±35 ppt	±3/±3/±3 ppt	±20/±30/±50	±5/±15/±20
22, 23, 24	Visible ground albedo	A = 0.1/0.3/0.4	±3/±4/±6 ppt	±2/±2/±2 ppt	±2/±3/±4	±2/±2/±
25 / 26	Pointing error	± 0.2°	±10/±3 ppt	±4 ppt	±30	±30/±3

Table A.2: Sensitivity runs for inferred BrO, according to the O_3-scaling-method.

Run #	Parameter	Modification	Δ BrO			
			absolute		relative[%]	
			range	typical	range	typical
1 / 2	In-situ O_3	× 0.97/1.03	±0.2 ppt	±0.15 ppt	±4	±3
3 / 4	BrO profile > 17.5 km	× 0.85/1.15	±0.6 ppt	±0.2 ppt	± 30	± 10
5 / 6		× 0.7/1.3	±0.6 ppt	±0.2 ppt	± 30	± 10
7 / 8	O_3 profile >17.5 km	× 0.9/1.1	±0.4 ppt	±0.2 ppt	± 8	± 5
9 / 10		× 0.97/1.03	±0.2 ppt	±0.1 ppt	± 4	± 3
11, 12, 13	Tropospheric BrO	+ 0 ppt, + 1/+ 1.5 ppt	±0.5/±0.5/±1 ppt	±0.3/±0.3/±0.6 ppt	±70/±50/±100	±15,±8,±20
14 / 15	Aerosol extinction	× 0.5/2	±0.04/0.06 ppt	±0.03/±0.015 ppt	±1/±1	±0.5/±0.5
16, 17, 18	Marine strato-cumulus	OD=5/10/20 from 1-2 km	±0.1/±0.2/±0.3 ppt	±0.07/±0.1/±0.25 ppt	±4/±6/±8	±3/±4/±5
19, 20, 21	Cirrus cloud	OD = 1 from 13-14/ 14-15/15-16 km	±0.1/±0.3/±0.5 ppt	±0.07/±0.15/±0.20 ppt	±10/±35/±25	±4/±6/±8
22, 23, 24	UV ground albedo	A = 0/0.1/0.2	±0.05/±0.05/±0.1 ppt	±0.025/±0.025/±0.05 ppt	±1/±1/±3	±0.5/±0.5/±2
25 / 26	Pointing error	± 0.2°	±0.3 ppt	±0.1/±0.3 ppt	±17	±3/±15

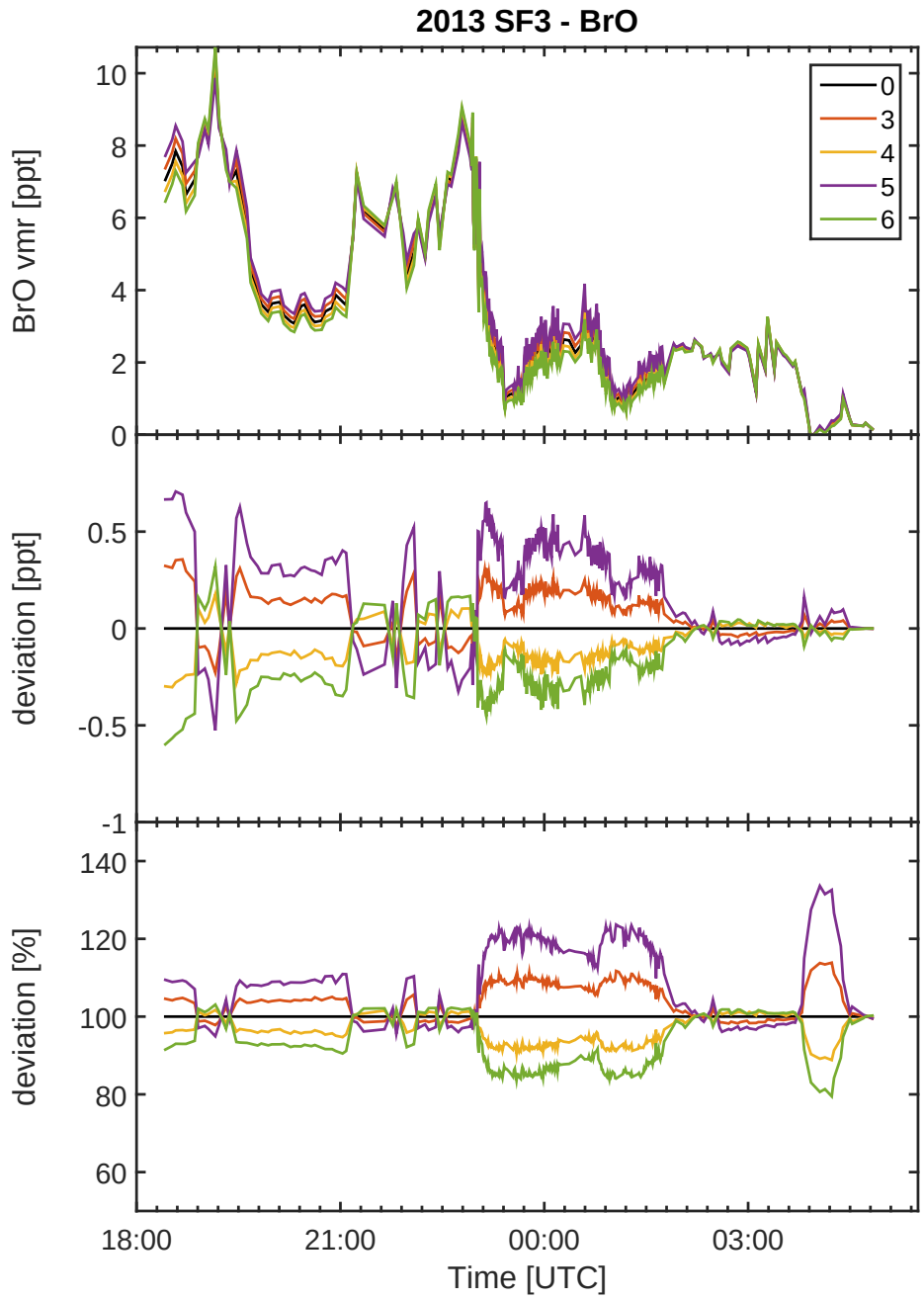

Figure A.1: Sensitivity runs 3, 4, 5, 6.

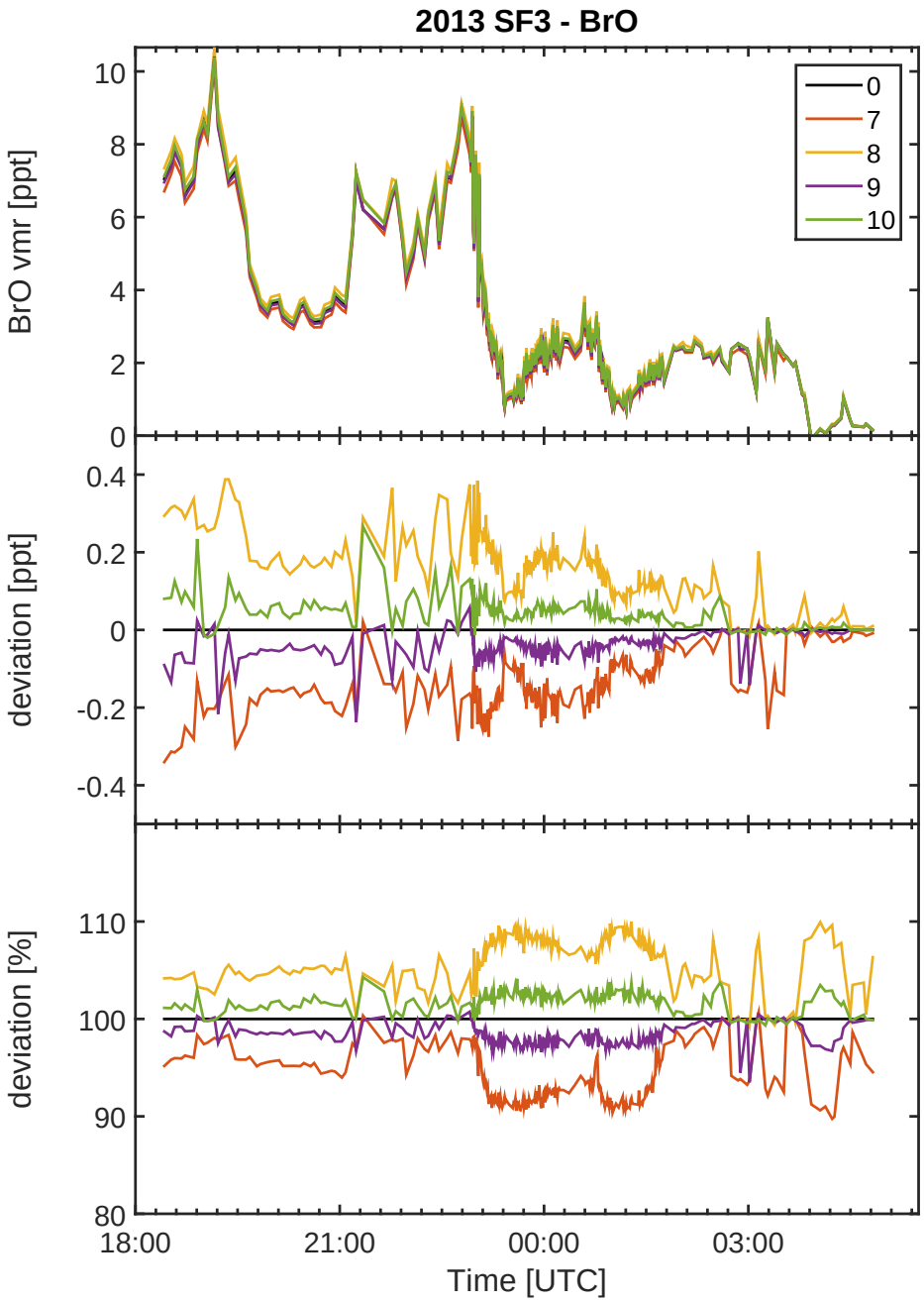

Figure A.2: Sensitivity runs 7, 8, 9, 10.

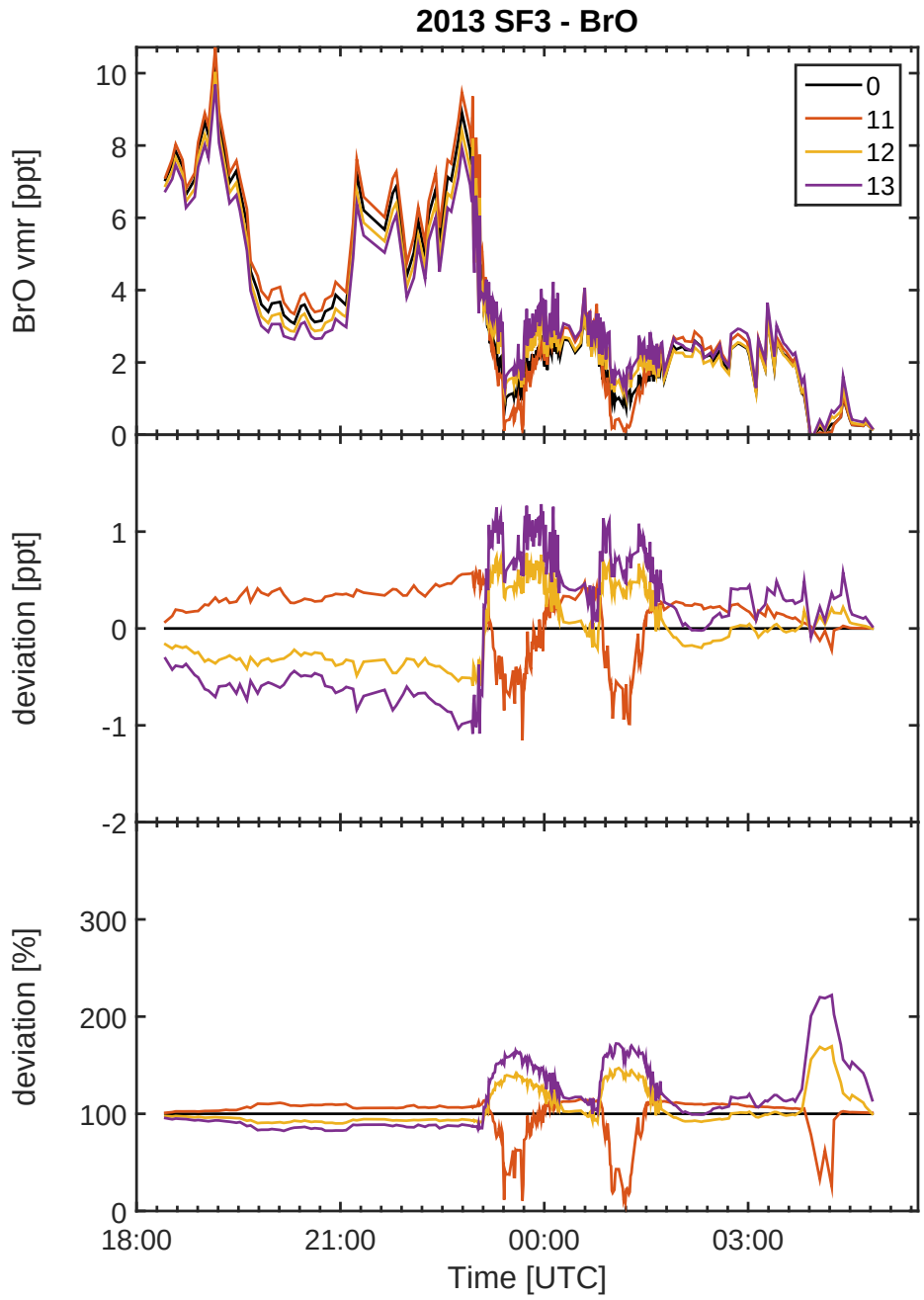

Figure A.3: Sensitivity runs 11, 12, 13.

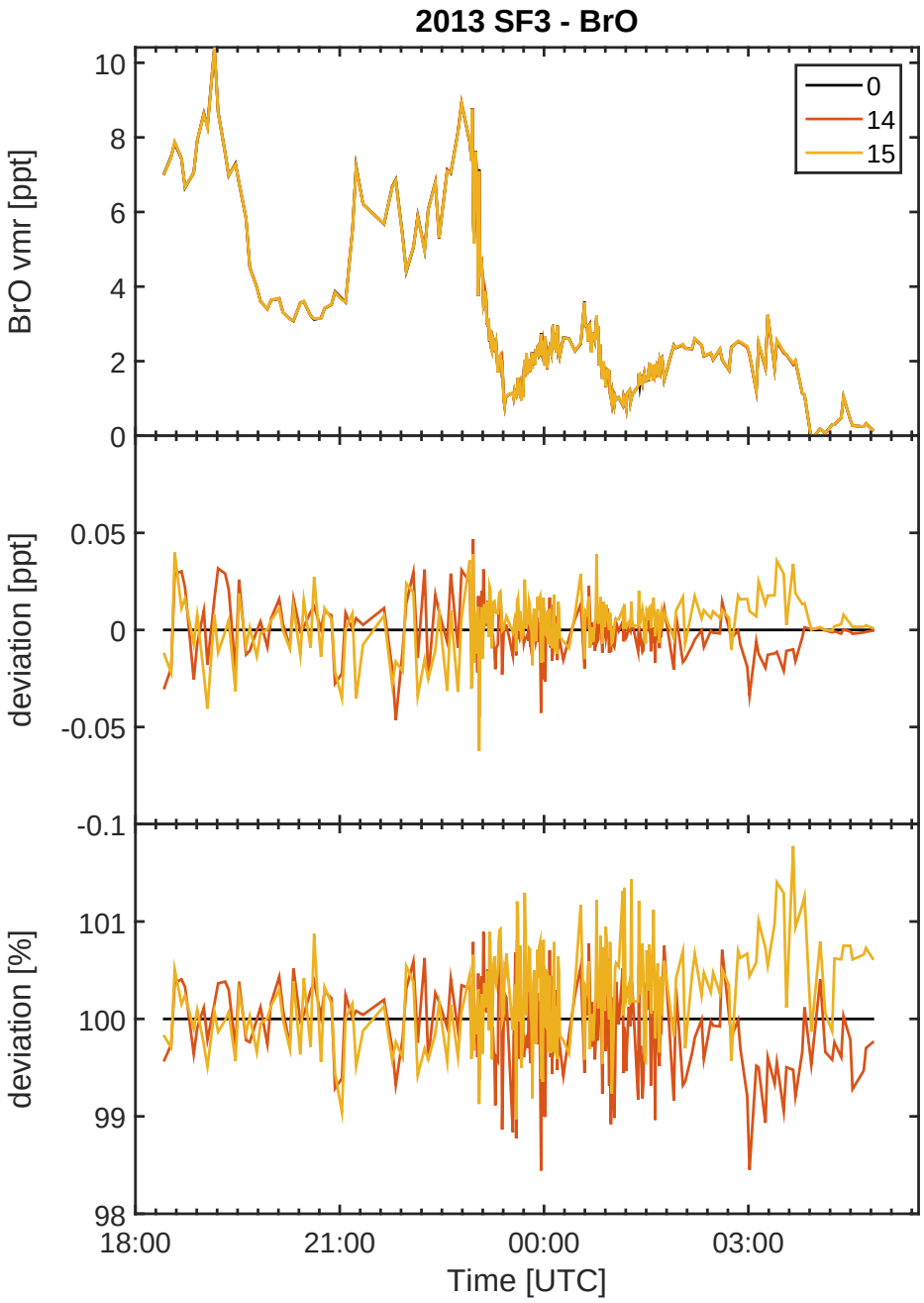

Figure A.4: Sensitivity runs 14, 15.

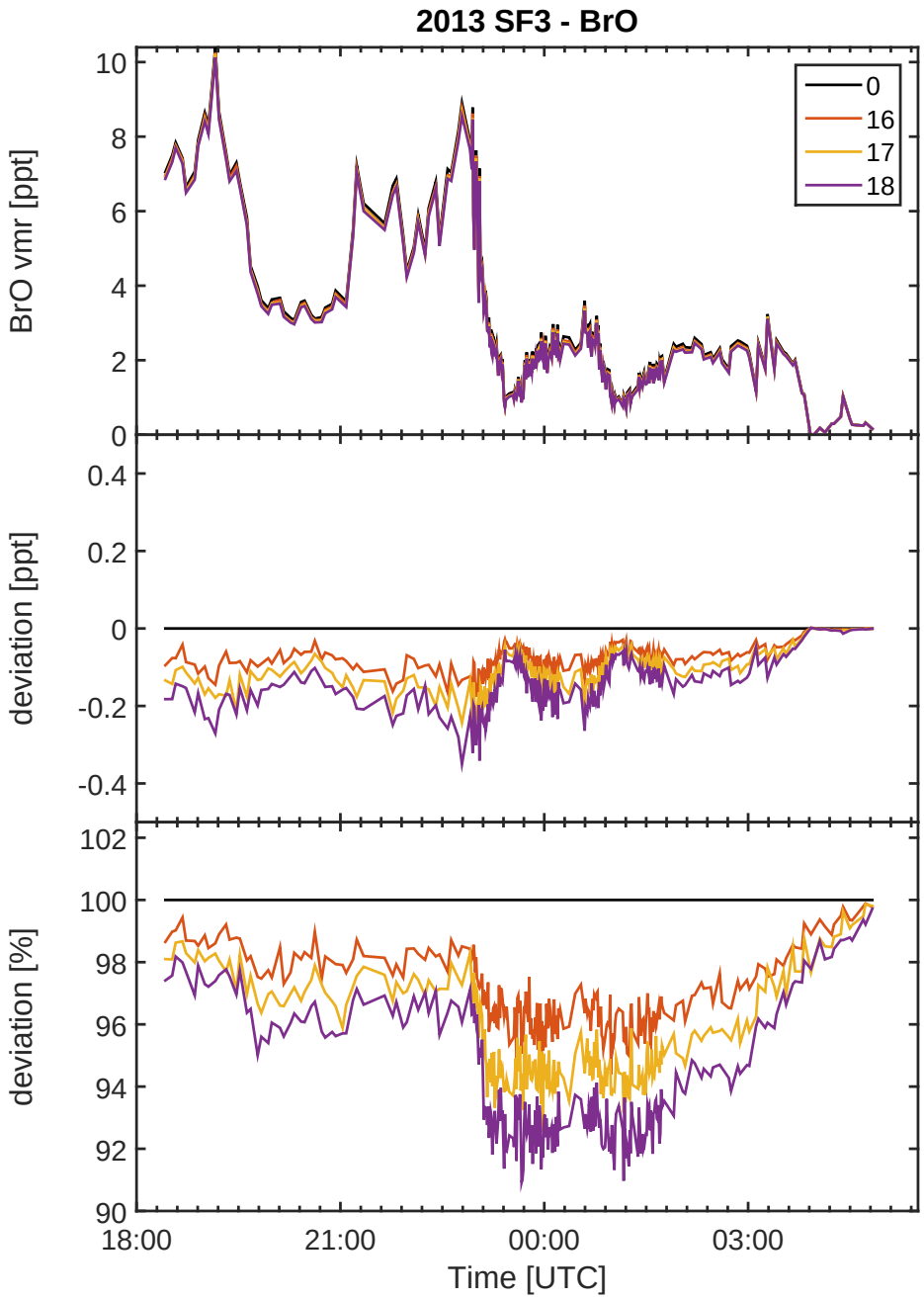

Figure A.5: Sensitivity runs 16, 17, 18.

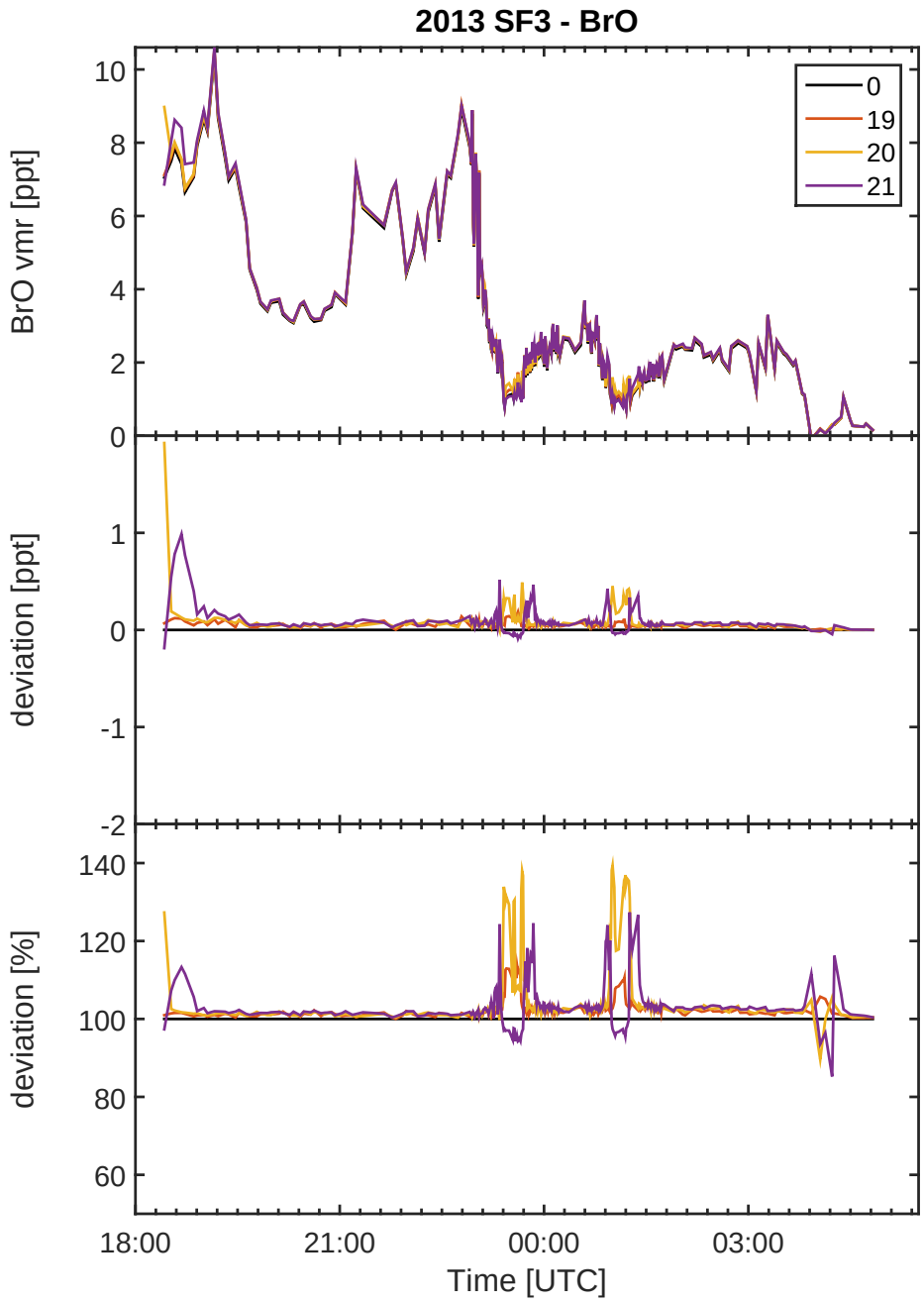

Figure A.6: Sensitivity runs 19, 20, 21.

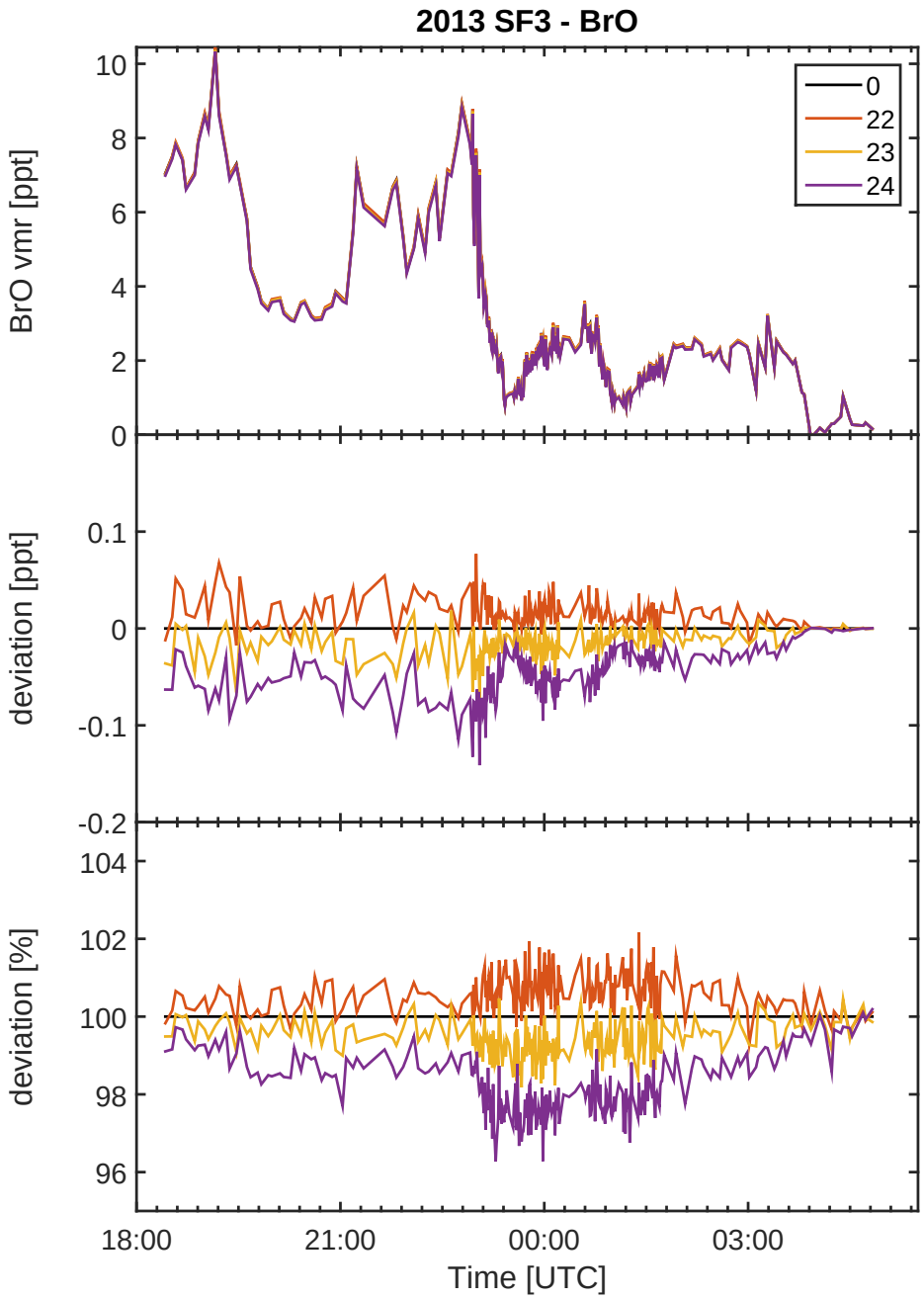

Figure A.7: Sensitivity runs 22, 23, 24.

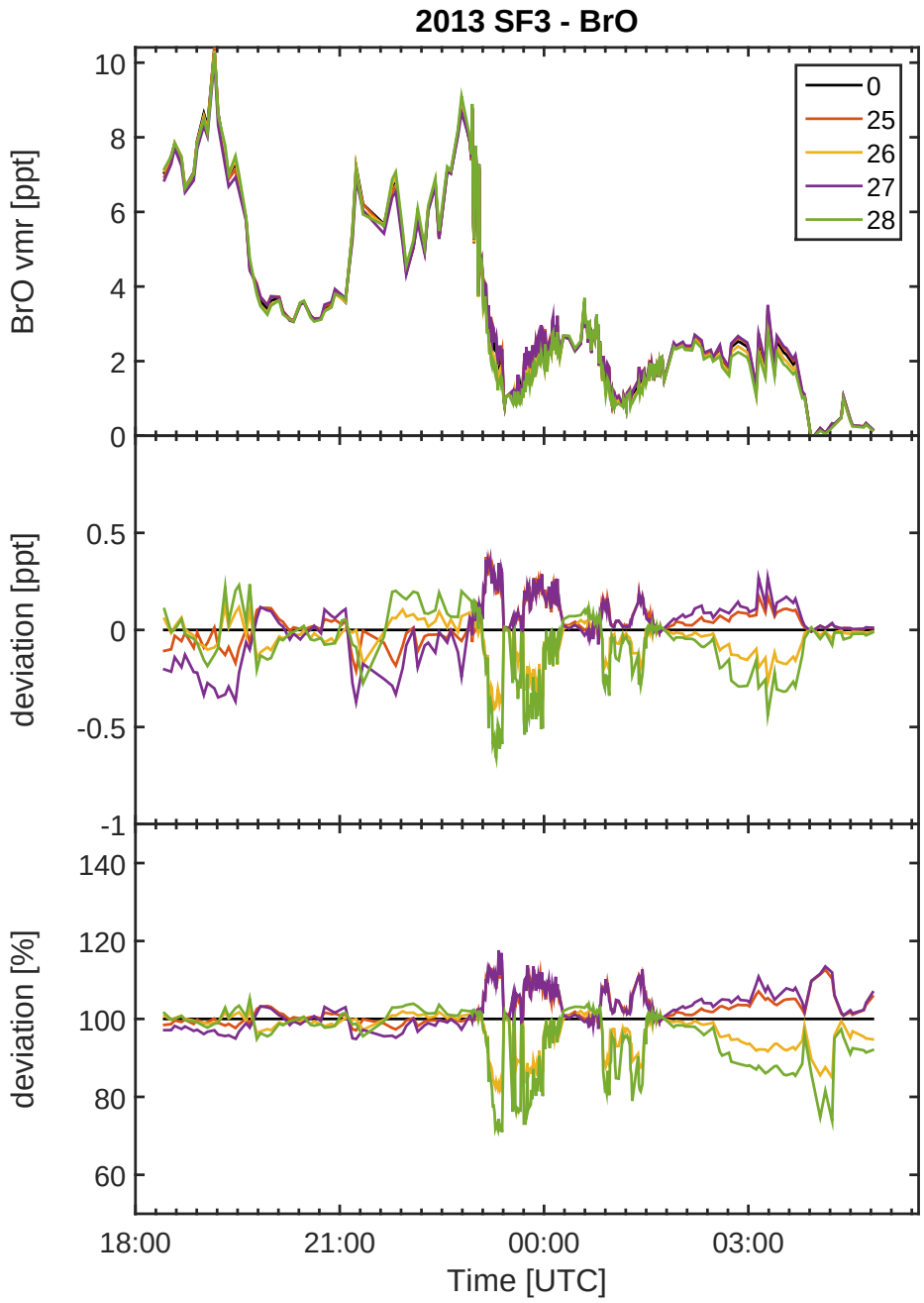

Figure A.8: Sensitivity runs 25, 26, 27, 28.

B Appendix: SLIMCAT curtain data

This chapter shows the major SLIMCAT curtain data used within the data analysis of all 2013 flights (Upper left: CH_4, upper right: O_3, lower left: NO_2, lower right: BrO).

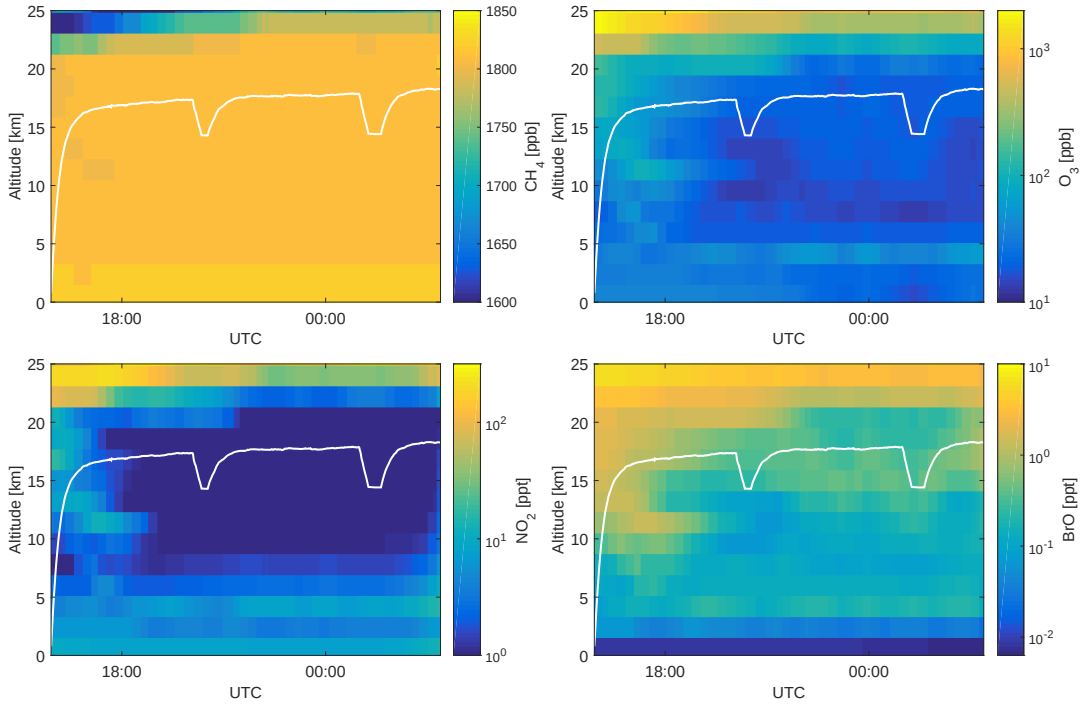

Figure B.1: Same as Figure 6.9 but for flight SF1-2013.

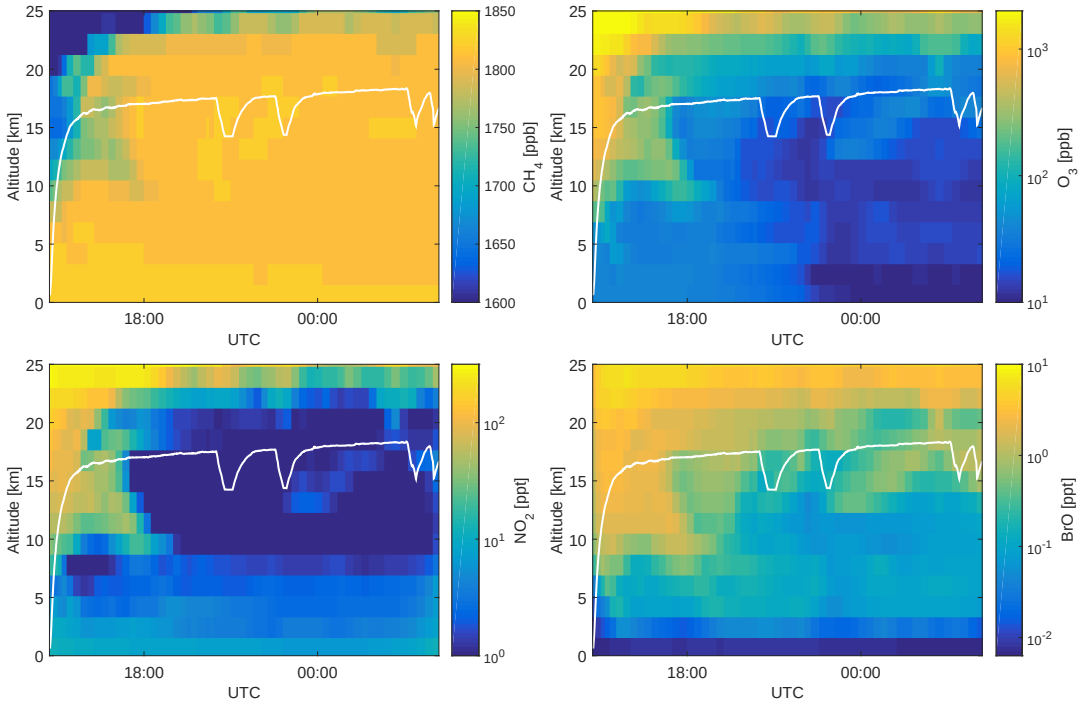

Figure B.2: Same as Figure 6.9 but for flight SF2-2013.

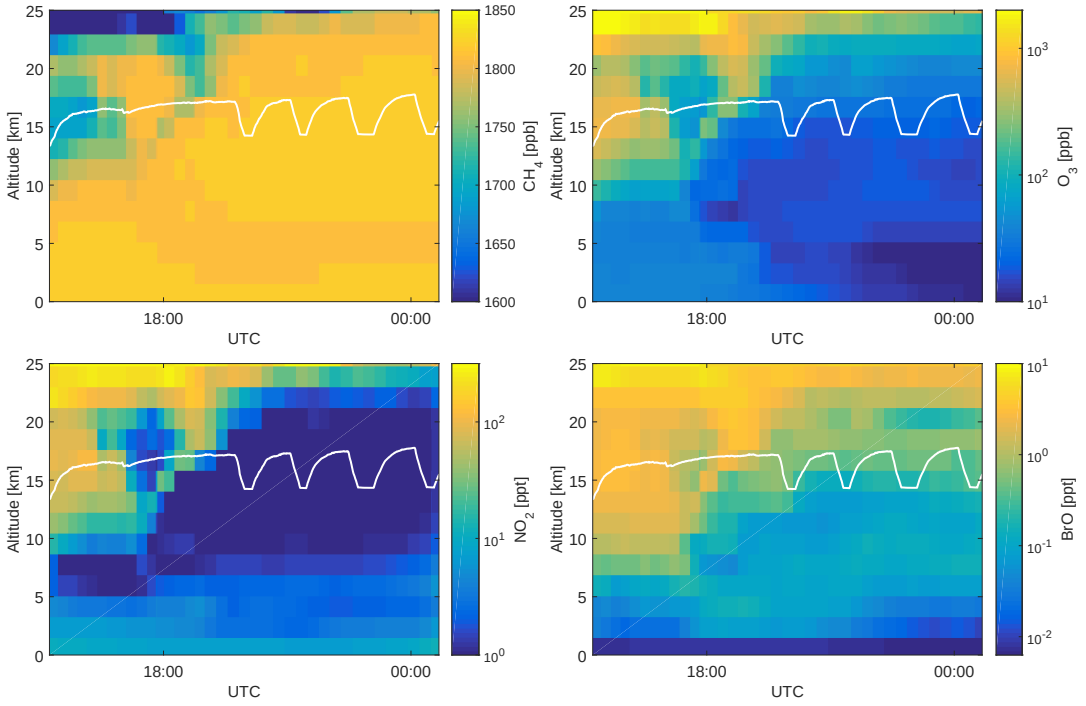

Figure B.3: Same as Figure 6.9 but for flight SF4-2013.

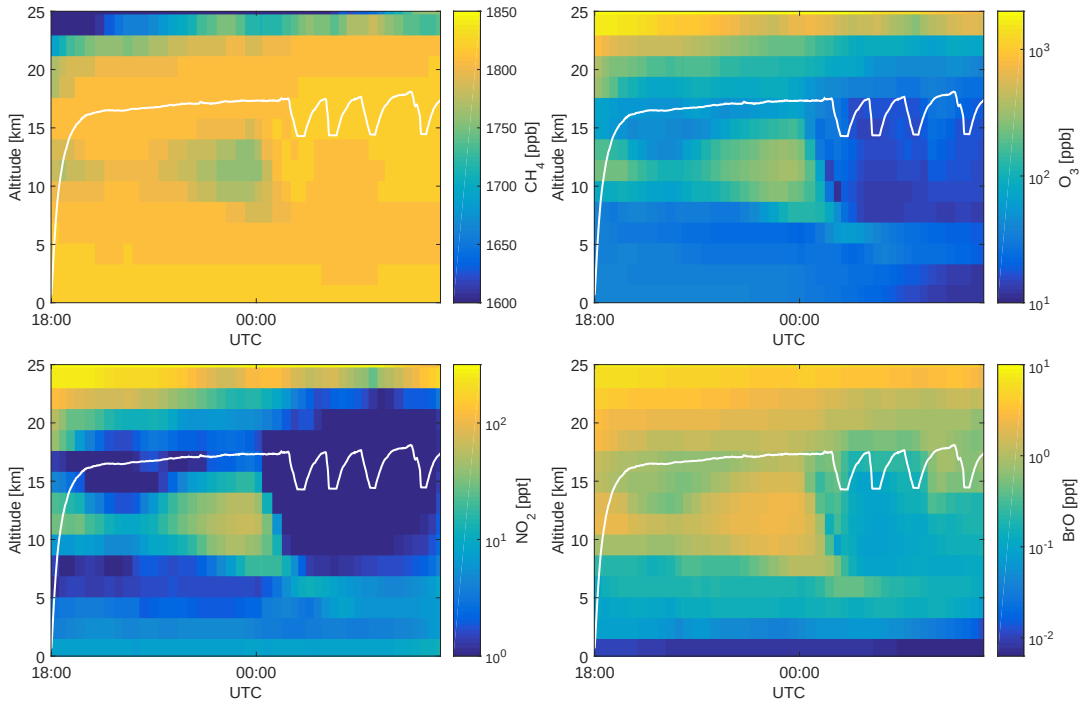

Figure B.4: Same as Figure 6.9 but for flight SF5-2013.

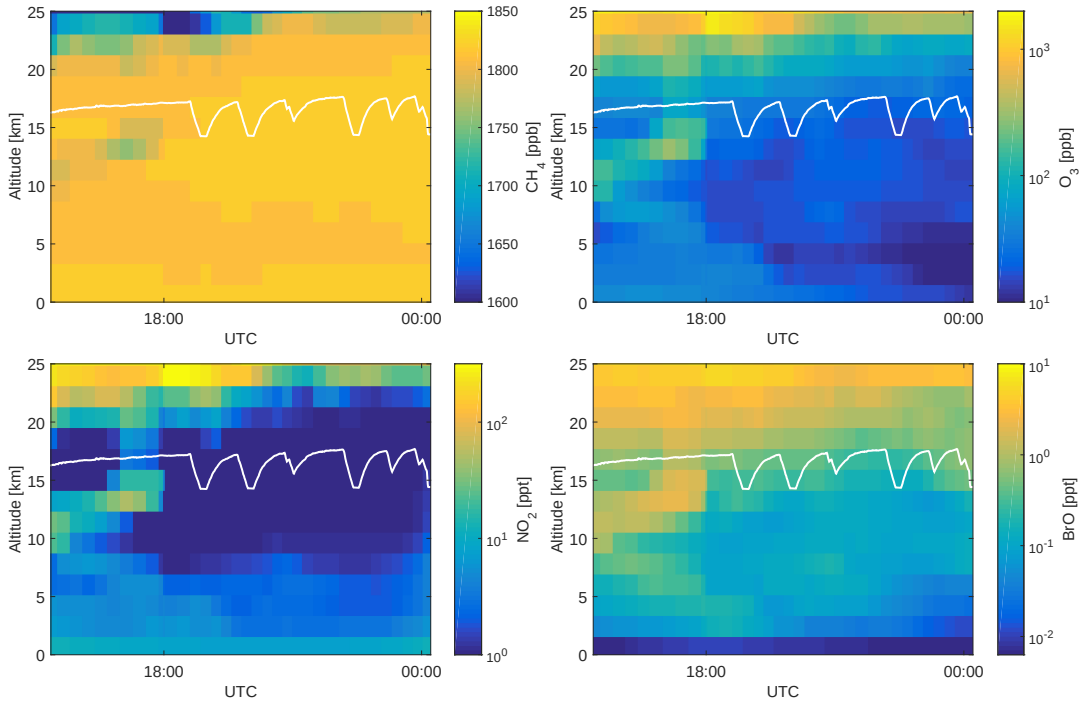

Figure B.5: Same as Figure 6.9 but for flight SF6-2013.

C Bibliography

J. Aschmann and B.-M. Sinnhuber. Contribution of very short-lived substances to stratospheric bromine loading: uncertainties and constraints. *Atmospheric Chemistry and Physics*, 13(3):1203–1219, 2013. doi: 10.5194/acp-13-1203-2013. URL http://www.atmos-chem-phys.net/13/1203/2013/.

J. Aschmann, B.-M. , Sinnhuber, E. L. Atlas, and S. M. Schauffler. Modeling the transport of very short-lived substances into the tropical upper troposphere and lower stratosphere. *Atmospheric Chemistry and Physics*, 9(23):9237–9247, 2009. doi: 10.5194/acp-9-9237-2009. URL http://www.atmos-chem-phys.net/9/9237/2009/.

J. Aschmann, B.-M. Sinnhuber, M. P. Chipperfield, and R. Hossaini. Impact of deep convection and dehydration on bromine loading in the upper troposphere and lower stratosphere. *Atmospheric Chemistry and Physics*, 11(6):2671–2687, 2011. doi: 10.5194/acp-11-2671-2011. URL http://www.atmos-chem-phys.net/11/2671/2011/.

M. J. Ashfold, N. R. P. Harris, E. L. Atlas, A. J. Manning, and J. A. Pyle. Transport of short-lived species into the tropical tropopause layer. *Atmospheric Chemistry and Physics*, 12(14):6309–6322, 2012. doi: 10.5194/acp-12-6309-2012. URL http://www.atmos-chem-phys.net/12/6309/2012/.

M. J. Ashfold, N. R. P. Harris, A. J. Manning, A. D. Robinson, N. J. Warwick, and J. A. Pyle. Estimates of tropical bromoform emissions using an inversion method. *Atmospheric Chemistry and Physics*, 14(2):979–994, 2014. doi: 10.5194/acp-14-979-2014. URL http://www.atmos-chem-phys.net/14/979/2014/.

Richard Aßmann. Über die Existenz eines wärmeren Luftstromes in der Höhe von 10 bis 15 km. *Sitzungsberichte der Königlich Preußischen Akademie der Wissenschaften zu Berlin (Sitzung der physikalisch-mathematischen Klasse vom 1. Mai 1902)*, 24:495–504, 1902.

Mark P. Baldwin and Timothy J. Dunkerton. Stratospheric harbingers of anomalous weather regimes. *Science*, 294(5542):581–584, 2001. doi: 10.1126/science.1063315. URL http://www.sciencemag.org/content/294/5542/581.abstract.

David R. Bates and Marcel Nicolet. The photochemistry of atmospheric water vapor. *Journal of Geophysical Research*, 55(3):301–327, 1950. ISSN 2156-2202. doi: 10.1029/JZ055i003p00301. URL http://dx.doi.org/10.1029/JZ055i003p00301.

Berson, A. and Süring, R. Ein ballonaufstieg bis 10500 m. *Illustrierte Aeronautische Mitteilungen*, 4:117–119, 1901.

Wood N. B. Dutton E. G. Slusser J. R. Bodhaine, A. B. On rayleigh optical depth calculations. *JOURNAL OF ATMOSPHERIC AND OCEANIC TECHNOLOGY*, 16, 1999.

K Bogumil, J Orphal, T Homann, S Voigt, P Spietz, O.C Fleischmann, A Vogel, M Hartmann, H Kromminga, H Bovensmann, J Frerick, and J.P Burrows. Measurements of molecular absorption spectra with the {SCIAMACHY} pre-flight model: instrument characterization and reference data for atmospheric remote-sensing in the 230–2380 nm region. *Journal of Photochemistry and Photobiology A: Chemistry*, 157(2–3):167 – 184, 2003. ISSN 1010-6030. doi: http://dx.doi.org/10.1016/S1010-6030(03)00062-5. URL http://www.sciencedirect.com/science/article/pii/S1010603003000625. Atmospheric Photochemistry.

H. Bönisch, A. Engel, Th. Birner, P. Hoor, D. W. Tarasick, and E. A. Ray. On the structural changes in the brewer-dobson circulation after 2000. *Atmospheric Chemistry and Physics*, 11(8):3937–3948, 2011. doi: 10.5194/acp-11-3937-2011. URL http://www.atmos-chem-phys.net/11/3937/2011/.

H. Bösch, C. Camy-Peyret, M. P. Chipperfield, R. Fitzenberger, H. Harder, U. Platt, and K. Pfeilsticker. Upper limits of stratospheric io and oio inferred from center-to-limb-darkening-corrected balloon-borne solar occultation visible spectra: Implications for total gaseous iodine and stratospheric ozone. *Journal of Geophysical Research: Atmospheres*, 108(D15), 2003. ISSN 2156-2202. doi: 10.1029/2002JD003078. URL http://dx.doi.org/10.1029/2002JD003078.

G. Brasseur and S. Solomon. *Aeronomy of the middle atmosphere*. D. Reidel Publishing Company, Dordrecht, 1986.

G. Brasseur and S. Solomon. *Aeronomy of the middle atmosphere*. Springer, P.OBox 17, 3300 AADordrecht, The Netherlands, 2005.

Guy P. Brasseur, Claire Granier, and Stacy Walters. Future changes in stratospheric ozone and the role of heterogeneous chemistry. *Nature*, 248:626 – 628, 1990. ISSN 2156-2202. URL http://www.nature.com/nature/journal/v348/n6302/abs/348626a0.html.

A. W. Brewer. Evidence for a world circulation provided by the measurements of helium and water vapour distribution in the stratosphere. *Quarterly Journal of the Royal Meteorological Society*, 75(326):351–363, 1949. ISSN 1477-870X. doi: 10.1002/qj.49707532603. URL http://dx.doi.org/10.1002/qj.49707532603.

S. Brinckmann, E. Engel, H. Bönisch, B. Quack, and Atlas E. Short-lived brominated hydrocarbons – observations in the source regions and the tropical tropopause layer. *Atmos. Chem. Phys.*, 12:1213–1228, 2012.

J. H. Butler, M. Battle, M. Bender, S. A. Montzka, A. D. Clarke, E.S. Saltzman, C. Sucher, J. Severinghaus, and J. W. Elkins. A twentieth century record of atmospheric halocarbons in polar firn air. *Nature*, 399:749–755, 1999.

A. Butz, H. Bösch, C. Camy-Peyret, M. Chipperfield, M. Dorf, G. Dufour, K. Grunow, P. Jeseck, S. Kühl, S. Payan, I. Pepin, J. Pukite, A. Rozanov, C. von Savigny, C. Sioris, T. Wagner, F. Weidner, and K. Pfeilsticker. Inter-comparison of stratospheric o_3 and no_2 abundances retrieved from balloon borne direct sun observations and envisat/sciamachy limb measurements. *Atmospheric Chemistry and Physics*, 6(5):1293–1314, 2006. doi: 10.5194/acp-6-1293-2006. URL http://www.atmos-chem-phys.net/6/1293/2006/.

A. Butz, H. Bösch, C. Camy-Peyret, M. P. Chipperfield, M. Dorf, S. Kreycy, L. Kritten, C. Prados-Roman, J. Schwärzle, and K. Pfeilsticker. Constraints on inorganic gaseous iodine in the tropical upper troposphere and stratosphere inferred from balloon-borne solar occultation observations. *Atmos. Chem. Phys.*, 9(18):7229–7242, 2009. doi: 10.5194/acp-9-7229-2009.

L. J. Carpenter, W. T. Sturges, S. A. Penkett, P. S. Liss, B. Alicke, K. Hebestreit, and U. Platt. Short-lived alkyl iodides and bromides at mace head, ireland: Links to biogenic sources and halogen oxide production. *Journal of Geophysical Research: Atmospheres*, 104(D1):1679–1689, 1999. ISSN 2156-2202. doi: 10.1029/98JD02746. URL http://dx.doi.org/10.1029/98JD02746.

S. Chapman. On ozone and atomic oxygen in the upper atmosphere. *Philos. Mag.*, 10:369–383, 1930.

M. P. Chipperfield. Multiannual simulations with a three-dimensional chemical transport model. *J. Geophys. Res.*, 104(D1):1781–1805, 1999.

M. P. Chipperfield. New version of the tomcat/slimcat off-line chemical transport model: Intercomparison of stratospheric tracer experiments. *Quarterly Journal of the Royal Meteorological Society*, 132(617):1179–1203, 2006. ISSN 1477-870X. doi: 10.1256/qj.05.51. URL http://dx.doi.org/10.1256/qj.05.51.

K. Clémer, M. Van Roozendael, C. Fayt, F. Hendrick, C. Hermans, G. Pinardi, R. Spurr, P. Wang, and M. De Mazière. Multiple wavelength retrieval of tropospheric aerosol optical properties from MAXDOAS measurements in Beijing. *Atmos. Meas. Tech.*, 3(1):111–145, 2010.

C. Cox and W. Munk. Measurement of the roughness of the sea surface from photographs of the sun's glitter. *J. Mar. Res*, 44:838–850, 1954.

P. J. Crutzen. The influence of nitrogen oxide on the atmospheric ozone content. *Q.J.R. Meteorol. Soc.*, 96:320–325, 1970. doi: 10.1002/qj.49709640815. URL http://dx.doi.org/10.1002/qj.49709640815.

P. J. Crutzen. Ozone production rates in an oxygen-hydrogen-nitrogen oxide atmosphere. *Journal of Geophysical Research*, 76(30):7311–7327, 1971. ISSN 2156-2202. doi: 10.1029/JC076i030p07311. URL http://dx.doi.org/10.1029/JC076i030p07311.

O. Dessens, G. Zeng, N. Warwick, and J. Pyle. Short-lived bromine compounds in the lower stratosphere; impact of climate change on ozone. *Atmosph. Sci. Lett.*, 10:201–206, 2009. doi: doi:10.1002/asl.236.

T. Deutschmann. *On Modeling Elastic and Inelastic Polarized Radiation Transport in the Earth Atmosphere with Monte Carlo Method*. PhD thesis, University of Leipzig, 2014.

Tim Deutschmann. Atmospheric radiative transfer modelling using Monte Carlo methods. Diploma thesis, University of Heidelberg, 2008.

Tim Deutschmann, Steffen Beirle, Udo Frieß, Michael Grzegorski, Christoph Kern, Lena Kritten, Ulrich Platt, Cristina Prados-Roman, Janis Pukite, Thomas Wagner, Bodo Werner, and Klaus Pfeilsticker. The monte carlo atmospheric radiative transfer model mcartim: Introduction and validation of jacobians and 3d features. *Journal of Quantitative Spectroscopy &Radiative Transfer*, page 19, 2011.

G. M. B. Dobson, D. N. Harrison, and J. Lawrence. Measurements of the amount of ozone in the earth's atmosphere and its relation to other geophysical conditions. part iii. *Proceedings of the Royal Society of London A: Mathematical, Physical and Engineering Sciences*, 122(790):456–486, 1926. ISSN 0950-1207. doi: 10.1098/rspa.1929.0034.

M. Dorf, JH Butler, A. Butz, C. Camy-Peyret, M.P. Chipperfield, L. Kritten, SA Montzka, B. Simmes, F. Weidner, and K. Pfeilsticker. Long-term observations of stratospheric bromine reveal slow down in growth. *Geophys. Res. Lett*, 33, 2006.

M. Dorf, A. Butz, C. Camy-Peyret, M. P. Chipperfield, L. Kritten, and K. Pfeilsticker. Bromine in the tropical troposphere and stratosphere as derived from balloon-borne bro observations. *Atmospheric Chemistry and Physics*, 8(23):7265–7271, 2008. doi: 10.5194/acp-8-7265-2008. URL http://www.atmos-chem-phys.net/8/7265/2008/.

Anne R. Douglass and Richard S. Stolarski. Impact of heterogeneous reactions on stratospheric chemistry of the arctic. *Geophysical Research Letters*, 16(2): 131–134, 1989. ISSN 1944-8007. doi: 10.1029/GL016i002p00131. URL http://dx.doi.org/10.1029/GL016i002p00131.

V. Dvortsov, M. A. Geller, S. Solomon, S. M. Schauffler, E. L. Atlas, and D. R. Blake. Rethinking reactive halogen budget in the midlatitude stratosphere. *Geophys. Res. Lett.*, 26(12):1699–1702, 1999.

C. Fabry and H. Buisson. L'absorption de l'ultra-violet par l'ozone et la limite du spectre solaire. *J. de Phys.*, 3(5):196–206, 1913.

J. C. Farman, B. G. Gardiner, and J. D. Shanklin. Large losses of total ozone in antarctica reveal seasonal ClO_x/NO_x interaction. *Nature*, 315:207–210, 1985.

F. Ferlemann, N. Bauer, R. Fitzenberger, H. Harder, H. Osterkamp, D. Perner, U. Platt, M. Scheider, P. Vradelis, and K. Pfeilsticker. Differential optical absorption spectroscopy instrument for stratospheric balloon-borne trace gas studies. *Appl. Opt.*, 39:2377–2386, 2000.

R. P. Fernandez, R. J. Salawitch, D. E. Kinnison, J.-F. Lamarque, and A. Saiz-Lopez. Bromine partitioning in the tropical tropopause layer: implications for stratospheric injection. *Atmospheric Chemistry and Physics Discussions*, 14 (12):17857–17905, 2014. doi: 10.5194/acpd-14-17857-2014. URL http://www.atmos-chem-phys-discuss.net/14/17857/2014/.

Barbara J. Finlayson-Pitts and James N. Pitts Jr. *Chemistry of the upper and lower atmosphere: Theory, experiments and applications*. Academic Press, San Diego, 2000. ISBN ISBN: 978-0-12-257060-5. doi: http://dx.doi.org/10.1016/B978-012257060-5/50000-9.

R. Fitzenberger, H. Bösch, C. Camy-Peyret, M.P. Chpperfield, H. Harder, U. Platt, J. Pyle, T. Wagner, and K. Pfeilsticker. First profile measurement of tropospheric BrO. *Geophys. Res. Lett.*, 27:2921–2924, 2000.

P. J. Fraser, D. E. Oram, C. E. Reeves, and S. A. Penkett. Southern hemisphere halon trends (1987-1998) and global halon emissions. *J. Geophys. Res.*, 1999.

Joseph Fraunhofer. Bestimmung des brechungs- und des farbenzerstreungs-vermögens verschiedener glasarten, in bezug auf die vervollkommnung achromatischer fernröhre. *Annalen der Physik*, 56(7):264–313, 1817. ISSN 1521-3889. doi: 10.1002/andp.18170560706. URL http://dx.doi.org/10.1002/andp.18170560706.

U. Frieß, P.S. Monks, J.J. Remedios, A. Rozanov, R. Sinreich, T. Wagner, and U. Platt. MAX-DOAS O_4 measurements: A new technique to derive information on atmospheric aerosols: 2. Modeling studies. *J. Geophys. Res.*, 111(14203): D14203, 2006. doi: 10.1029/2005JD006618.

U. Frieß, H. Sihler, R. Sander, D. Pöhler, S. Yilmaz, and U. Platt. The vertical distribution of bro and aerosols in the arctic: Measurements by active and passive differential optical absorption spectroscopy. *J. Geophys. Res.*, 116:D00R04–, September 2011. ISSN 0148-0227.

S. Fueglistaler, A. E. Dessler, T. J. Dunkerton, I. Folkins, Q. Fu, and P. W. Mote. Tropical tropopause layer. *Reviews of Geophysics*, 47(1), 2009. ISSN 1944-9208. doi: 10.1029/2008RG000267. URL http://dx.doi.org/10.1029/2008RG000267.

R. S. Gao, J. Ballard, L. A. Watts, T. D. Thornberry, S. J. Ciciora, R. J. McLaughlin, and D. W. Fahey. A compact, fast uv photometer for measurement of ozone from research aircraft. *Atmospheric Measurement Techniques*, 5(9):2201–2210, 2012. doi: 10.5194/amt-5-2201-2012. URL http://www.atmos-meas-tech.net/5/2201/2012/.

A. Gettelman and P.M.d.F. Forster. A climatology of the tropical tropopause layer. *Journal of the Meteorological Society of Japan*, 80(4B):911–924, 2002. doi: 10.2151/jmsj.80.911. URL https://www.jstage.jst.go.jp/article/jmsj/80/4B/80_4B_911/_pdf.

A. Gettelman, P. Hoor, L. L. Pan, W. J. Randel, M. I. Hegglin, and T. Birner. The extratropical upper troposphere and lower stratosphere. *Reviews of Geophysics*, 49(3):n/a–n/a, 2011. ISSN 1944-9208. doi: 10.1029/2011RG000355. URL http://dx.doi.org/10.1029/2011RG000355. RG3003.

J.F. Grainger and J. Ring. Anomalous fraunhofer line profiles. *Nature*, 193:762, 1962.

Katja Großmann. *Aircraft-borne DOAS limb observations of UV/visible absorbing trace gas species over Borneo: Implications for the photochemistry of iodine, volatile organic oxide degradation, and lightning-produced radicals*. PhD thesis, Institute of Environmental Physics, University of Heidelberg, 2014.

David R. Hanson, A. R. Ravishankara, and Susan Solomon. Heterogeneous reactions in sulfuric acid aerosols: A framework for model calculations. *Journal of Geophysical Research: Atmospheres*, 99(D2):3615–3629, 1994. ISSN 2156-2202. doi: 10.1029/93JD02932. URL http://dx.doi.org/10.1029/93JD02932.

H. Harder, H. Bösch, C. Camy-Peyret, M. P. Chipperfield, R. Fitzenberger, S. Payan, D. Perner, U. Platt, B.-M. Sinnhuber, and K. Pfeilsticker. Comparison of measured and modeled stratospheric bro: Implications for the total amount of stratospheric bromine. *Geophysical Research Letters*, 27(22):3695–3698, 2000. ISSN 1944-8007. doi: 10.1029/1999GL011215. URL http://dx.doi.org/10.1029/1999GL011215.

F. Hendrick, M. Van Roozendael, M. P. Chipperfield, M. Dorf, F. Goutail, X. Yang, C. Fayt, C. Hermans, K. Pfeilsticker, J.-P. Pommereau, J. A. Pyle, N. Theys, and M. De Mazière. Retrieval of stratospheric and tropospheric bro profiles and columns using ground-based zenith-sky doas observations at harestua, 60° n. *Atmospheric Chemistry and Physics*, 7(18):4869–4885, 2007. doi: 10.5194/acp-7-4869-2007. URL http://www.atmos-chem-phys.net/7/4869/2007/.

L.G. Henyey and J.L. Greenstein. Diffuse radiation in the galaxy. *Astrophysical Journal*, 93:70–83, 1941. doi: 10.1086/144246.

H. Hepach, B. Quack, F. Ziska, S. Fuhlbrügge, E. L. Atlas, K. Krüger, I. Peeken, and D. W. R. Wallace. Drivers of diel and regional variations of halocarbon emissions from the tropical north east atlantic. *Atmospheric Chemistry and Physics*, 14(3):1255–1275, 2014. doi: 10.5194/acp-14-1255-2014. URL http://www.atmos-chem-phys.net/14/1255/2014/.

J. R. Holton, P. H. Haynes, M. E. McIntyre, A. R. Douglass, Rood R. B., and L. Pfister. Stratosphere–troposphere exchange. *Rev. Geophys.*, 33:403–439, 1995.

G. Hönninger, C. von Friedeburg, and U. Platt. Multi axis differential optical absorption spectroscopy (max-doas). *Atmos. Chem. Phys.*, 4(1):231–254, 2004. ISSN 1680-7316.

R. Hossaini, M. P. Chipperfield, S. Dhomse, C. Ordóñez, A. Saiz-Lopez, N. L. Abraham, A. Archibald, P. Braesicke, P. Telford, N. Warwick, X. Yang, and J. Pyle. Modelling future changes to the stratospheric source gas injection of biogenic bromocarbons. *Geophysical Research Letters*, 39(20):n/a–n/a, 2012a. ISSN 1944-8007. doi: 10.1029/2012GL053401. URL http://dx.doi.org/10.1029/2012GL053401. L20813.

R. Hossaini, M. P. Chipperfield, W. Feng, T. J. Breider, E. Atlas, S. A. Montzka, B. R. Miller, F. Moore, and J. Elkins. The contribution of natural and anthropogenic very short-lived species to stratospheric bromine. *Atmospheric Chemistry and Physics*, 12(1):371–380, 2012b. doi: 10.5194/acp-12-371-2012. URL http://www.atmos-chem-phys.net/12/371/2012/.

R. Hossaini, H. Mantle, M. P. Chipperfield, S. A. Montzka, P. Hamer, F. Ziska, B. Quack, K. Krüger, S. Tegtmeier, E. Atlas, S. Sala, A. Engel, H. Bönisch,

T. Keber, D. Oram, G. Mills, C. Ordóñez, A. Saiz-Lopez, N. Warwick, Q. Liang, W. Feng, F. Moore, B. R. Miller, V. Marécal, N. A. D. Richards, M. Dorf, and K. Pfeilsticker. Evaluating global emission inventories of biogenic bromocarbons. *Atmospheric Chemistry and Physics*, 13(23):11819–11838, 2013. doi: 10.5194/acp-13-11819-2013. URL http://www.atmos-chem-phys.net/13/11819/2013/.

R. Hossaini, S. A Chipperfield, M. P. and. Montzka, A. Rap, S. Dhomse, and W. Feng. Effciency of short-lived halogens at influencing climate through depletion of stratospheric ozone. *Nature Geoscience*, 8(2), 2015. doi: doi:10.1038/ngeo2363. URL http://www.nature.com/ngeo/journal/vaop/ncurrent/full/ngeo2363.html.

IPCC. Climate change 2013: The physical science basis, working group i contribution to the fifth assessment report of the intergovernmental panel on climate change, working group i technical support unit. *Cambridge University Press*, page 1552, 2013. URL https://www.ipcc.ch/report/ar5/wg1/.

H. Irie, Y. Kanaya, H. Akimoto, H. Iwabuchi, A. Shimizu, and K. Aoki. First retrieval of tropospheric aerosol profiles using max-doas and comparison with lidar and sky radiometer measurements. *Atmospheric Chemistry and Physics*, 8(2):341–350, 2008. doi: 10.5194/acp-8-341-2008. URL http://www.atmos-chem-phys.net/8/341/2008/.

H. Irie, H. Takashima, Y. Kanaya, K. F. Boersma, L. Gast, F. Wittrock, D. Brunner, Y. Zhou, and M. Van Roozendael. Eight-component retrievals from ground-based max-doas observations. *Atmospheric Measurement Techniques*, 4(6):1027–1044, 2011. doi: 10.5194/amt-4-1027-2011. URL http://www.atmos-meas-tech.net/4/1027/2011/.

David G. Johnson, Kenneth W. Jucks, Wesley A. Traub, Kelly V. Chance, Geoffrey C. Toon, James M. Russell, and M. Patrick McCormick. Stratospheric age spectra derived from observations of water vapor and methane. *Journal of Geophysical Research: Atmospheres*, 104(D17):21595–21602, 1999. ISSN 2156-2202. doi: 10.1029/1999JD900363. URL http://dx.doi.org/10.1029/1999JD900363.

H. S. Johnston. Reduction of stratospheric ozone by nitrogen oxide catalysts from supersonic transport exhaust. *Science*, 173:517–522, 1971. doi: 10.1126/science.173.3996.517.

G. Kirchhoff. Ueber die fraunhofer'schen linien. *Annalen der Physik*, 185(1):148–150, 1860. ISSN 1521-3889. doi: 10.1002/andp.18601850115. URL http://dx.doi.org/10.1002/andp.18601850115.

M. K. W. Ko, P. A. Newman, S. Reimann, and E.S. Strahan. Lifetimes of stratospheric ozone-depleting substances, their replacements, and related species. *SPARC Report*, WCRP-15/2013(6):1 – 255, 2013.

M.K.W. Ko, N.D Sze, C.J Scott, and D.K. Weisenstein. On the relation between chlorine/bromine loading and short-lived tropospheric source gases. *J. Geophys. Res.*, 102:25,507 – 25,517, 1997.

S. Kreycy. *Investigation of the Stratospheric Bromine Chemistry by Balloon-Borne Spectroscopic Observations and Photochemical Modelling: A Case Study of J($BrONO_2$)/$k_{BrO+NO2}$*. PhD thesis, Institute of Environmental Physics, University of Heidelberg, 2012.

S. Kreycy, C. Camy-Peyret, M. P. Chipperfield, M. Dorf, W. Feng, R. Hossaini, L. Kritten, B. Werner, and K. Pfeilsticker. Atmospheric test of the $j(brono_2)/k_{BrO+NO2}$ ratio: implications for total stratospheric br_y and bromine-mediated ozone loss. *Atmospheric Chemistry and Physics*, 13(13):6263–6274, 2013. doi: 10.5194/acp-13-6263-2013. URL http://www.atmos-chem-phys.net/13/6263/2013/.

L. Kritten, A. Butz, M. Dorf, T. Deutschmann, S. Kühl, C. Prados-Roman, J. Pukite, A. Rozanov, R. Schofield, and K. Pfeilsticker. Time dependent profile retrieval of uv/vis absorbing radicals from balloon-borne limb measurements - a case study on no_2 and o_3. *Atmospheric Measurement Techniques*, 3(4):933–946, 2010. doi: 10.5194/amt-3-933-2010. URL http://www.atmos-meas-tech.net/3/933/2010/.

K. Krüger, S. Tegtmeier, and M. Rex. Long-term climatology of air mass transport through the tropical tropopause layer (ttl) during nh winter. *Atmos. Chem. Phys.*, 8(8):813–823, 2008. doi: 10.5194/acp-8-813-2008.

J. C. Laube, A. Engel, H. Bönisch, T. Möbius, D. R. Worton, W. T. Sturges, K. Grunow, and U. Schmidt. Contribution of very short-lived organic substances to stratospheric chlorine and bromine in the tropics – a case study. *Atmospheric Chemistry and Physics*, 8(23):7325–7334, 2008. doi: 10.5194/acp-8-7325-2008. URL http://www.atmos-chem-phys.net/8/7325/2008/.

K. S. Law and W. T. Sturges. Halogenated very short-lived substances. *Scientific Assessment of Ozone Depletion: 2006, Global Ozone Research and Monitoring Project*, 59, 2007.

E. C. Leedham, C. Hughes, F. S. L. Keng, S.-M. Phang, G. Malin, and W. T. Sturges. Emission of atmospherically significant halocarbons by naturally occurring and farmed tropical macroalgae. *Biogeosciences*, 10(6):3615–3633, 2013. doi: 10.5194/bg-10-3615-2013. URL http://www.biogeosciences.net/10/3615/2013/.

K. Levenberg. A method for the solution of certain non-linear problems in least squares. *Quart. Appl., Math.*, 2:164–168, 1944.

J. G. Levine, P. Braesicke, N. R. P. Harris, and J. A. Pyle. Seasonal and inter-annual variations in troposphere-to-stratosphere transport from the tropical tropopause layer. *Atmospheric Chemistry and Physics*, 8(13):3689 – 3703, 2008. doi: 10.5194/acp-8-3689-2008. URL http://www.atmos-chem-phys.net/8/3689/2008/.

Gilbert N. Lewis. The magnetism of oxygen and the molecule o4. *Journal of the American Chemical Society*, 46(9):2027–2032, 1924. doi: 10.1021/ja01674a008. URL http://dx.doi.org/10.1021/ja01674a008.

D. W. Marquardt. An algorithm for least-squares estimation of nonlinear parameters. *J. Soc. Indust. Math.*, 11:431–441, 1963.

A. Marshak and A.B. Davis. *3D Radiative Transfer in Cloudy Atmospheres*. Springer-Verlag, Heidelberg, 2005. ISBN ISBN-10 3-540-23958-8.

A. Mellouki, R. K. Talukdar, A.-M. Schmoltner, T. Gierczak, M. J. Mills, S. Solomon, and A. R. Ravishankara. Atmospheric lifetimes and ozone depletion potentials of methyl bromide (ch_3br) and dibromomethane (ch_2br_2). *Geophys. Res. Lett.*, 19:2059 – 2062, 1992.

J. V. Michael, J. H. Lee, W. A . Payne, and L. J. Stief. Absolute rate of reaction of bromine atoms with ozone from 200 - 360 k. *J. Atmos. Chem.*, 68:4093 – 4097, 1978.

H. A. Michelsen, G. L. Manney, M. R. Gunson, C. P. Rinsland, and R. Zander. Correlations of stratospheric abundances of ch4 and n2o derived from atmos measurements. *Geophysical Research Letters*, 25(15):2777–2780, 1998. ISSN 1944-8007. doi: 10.1029/98GL01977. URL http://dx.doi.org/10.1029/98GL01977.

K. Minschwaner, A. E. Dessler, J. W. Elkins, C. M. Volk, D. W. Fahey, M. Loewenstein, J. R. Podolske, A. E. Roche, and K. R. Chan. Bulk properties of isentropic mixing into the tropics in the lower stratosphere. *Journal of Geophysical Research: Atmospheres*, 101(D5):9433–9439, 1996. ISSN 2156-2202. doi: 10.1029/96JD00335. URL http://dx.doi.org/10.1029/96JD00335.

Mario J. Molina and F. S. Rowland. Stratospheric sink for chlorofluoromethanes: chlorine atomc-atalysed destruction of ozone. *Nature*, 249(5460):810–812, June 1974. doi: 10.1038/249810a0.

S. A. Montzka, J. H. Butler, B. D. Hall, D. J. Mondeel, and J. W. Elkins. A decline in tropospheric organic bromine. *Geophysical Research Letters*, 30(15):n/a–n/a, 2003. ISSN 1944-8007. doi: 10.1029/2003GL017745. URL http://dx.doi.org/10.1029/2003GL017745. 1826.

Maria Navarro. In prep. 2015.

J. M. Nicovich, K. D. Kreutter, and P. H. Wine. Kinetics of the reactions of cl(^2p_j) and br($^2p_{3/2}$) with o_3. *Int. J. Chem. Kinet.*, 22:399 –414, 1990.

J. P. Parrella, K. Chance, R. J. Salawitch, T. Canty, M. Dorf, and K. Pfeilsticker. New retrieval of bro from sciamachy limb: an estimate of the stratospheric bromine loading during april 2008. *Atmospheric Measurement Techniques*, 6(10):2549–2561, 2013. doi: 10.5194/amt-6-2549-2013. URL http://www.atmos-meas-tech.net/6/2549/2013/.

Rudolf Penndorf. Tables of the refractive index for standard air and the rayleigh scattering coefficient for the spectral region between 0.2 and 20.0 μ and their application to atmospheric optics. *J. Opt. Soc. Am.*, 47(2):176–182, Feb 1957. doi: 10.1364/JOSA.47.000176. URL http://www.opticsinfobase.org/abstract.cfm?URI=josa-47-2-176.

K. Pfeilsticker, W. T: Sturges, H. Bösch, C. Camy-Peyret, M. P. , A. Engel, R. Fitzenberger, M. Müller, S. Payan, and B.-M. Sinnhuber. Lower stratospheric organic and inorganic bromine budget for the Artic winter 1998/99. *Geophys. Res. Lett.*, 27(20):3305–3308, 2000.

U. Platt and J. Stutz. *Differential optical absorption spectroscopy*. Springer Verlag, 2008.

Ulrich Platt, Klaus Pfeilsticker, and Michael Vollmer. Radiation and optics in the atmosphere. In Frank Traeger, editor, *Springer Handbook of Lasers and Optics*, pages 1475–1517. Springer Berlin Heidelberg, 2012. ISBN 978-3-642-19408-5. doi: 10.1007/978-3-642-19409-2_23. URL http://dx.doi.org/10.1007/978-3-642-19409-2_23.

F. Ploeger, S. Fueglistaler, J.-U. Grooß, G. Günther, P. Konopka, Y.S. Liu, R. Müller, F. Ravegnani, C. Schiller, A. Ulanovski, and M. Riese. Insight from ozone and water vapour on transport in the tropical tropopause layer (ttl). *Atmospheric Chemistry and Physics*, 11(1):407–419, 2011. doi: 10.5194/acp-11-407-2011. URL http://www.atmos-chem-phys.net/11/407/2011/.

R. W. Portmann, J. S. Daniel, and A. R. Ravishankara. Stratospheric ozone depletion due to nitrous oxide: influences of other gases. *Philosophical Transactions of the Royal Society of London B: Biological Sciences*, 367(1593):1256–1264, 2012. ISSN 0962-8436. doi: 10.1098/rstb.2011.0377.

C. Prados-Roman, A. Butz, T. Deutschmann, M. Dorf, L. Kritten, A. Minikin, U. Platt, H. Schlager, H. Sihler, N. Theys, M. Van Roozendael, T. Wagner, and

K. Pfeilsticker. Airborne doas limb measurements of tropospheric trace gas profiles: case study on the profile retrieval of o_4 and bro. *Atmospheric Measurement Techniques*, 3(4):3925–3969, 2011. doi: 10.5194/amtd-3-3925-2010. URL http://www.atmos-meas-tech-discuss.net/3/3925/2010/.

J. Pukite, S. Kühl, T. Deutschmann, S. Dörner, P. Jöckel, U. Platt, and T. Wagner. The effect of horizontal gradients and spatial measurement resolution on the retrieval of global vertical no_2 distributions from sciamachy measurements in limb only mode. *Atmospheric Measurement Techniques*, 3(4):1155–1174, 2010. doi: 10.5194/amt-3-1155-2010. URL http://www.atmos-meas-tech.net/3/1155/2010/.

R. Raecke. Atmospheric spectroscopy of trace gases and water vapor in the tropical tropopause layer from the nasa global hawk. Master thesis, Institute of Environmental Physics, University of Heidelberg, Heidelberg, Germany, 2013.

William J. Randel and Eric J. Jensen. Physical processes in the tropical tropopause layer and their roles in a changing climate. *Nature Geoscience*, 6:169–176, 2013. doi: 10.1038/ngeo1733. URL http://dx.doi.org/10.1038/ngeo1733.

A. R. Ravishankara, J.S. , Daniel, and Portmann R. W. Nitrous oxide (n_2o): The dominant ozone-depleting substance emitted in the 21st century. *Science*, 326 (5949):123–125, 2009.

E. E. Remsberg. Methane as a diagnostic tracer of changes in the brewer–dobson circulation of the stratosphere. *Atmospheric Chemistry and Physics*, 15 (7):3739–3754, 2015. doi: 10.5194/acp-15-3739-2015. URL http://www.atmos-chem-phys.net/15/3739/2015/.

A. Richter, F. Wittrock, A. Ladstätter-Weißenmayer, and J.P. Burrows. Gome measurements of stratospheric and tropospheric bro. *Adv. Space Res.,*, 29(11): 1667–1672, 2002. doi: doi:10.1016/S0273-1177(02)00123-0.

C. D. Rodgers. *Inverse methods for atmospheric sounding, theory and practice*. Series on Atmospheric, Oceanic and Planetary Physics. World Scientific, 2000.

W. Roedel. *Physik unserer Umwelt: Die Atmosphäre*. Springer Verlag, Heidelberg, 2000.

A. Rozanov, S. Kühl, A. Doicu, C. McLinden, J. Pukite, H. Bovensmann, J. P. Burrows, T. Deutschmann, M. Dorf, F. Goutail, K. Grunow, F. Hendrick, M. von Hobe, S. Hrechanyy, G. Lichtenberg, K. Pfeilsticker, J. P. Pommereau, M. Van Roozendael, F. Stroh, and T. Wagner. Bro vertical distributions from sciamachy limb measurements: comparison of algorithms and retrieval results.

Atmospheric Measurement Techniques, 4(7):1319–1359, 2011. doi: 10.5194/amt-4-1319-2011. URL http://www.atmos-meas-tech.net/4/1319/2011/.

S. Sala, H. Bönisch, T. Keber, D. E. Oram, G. Mills, and A. Engel. Deriving an atmospheric budget of total organic bromine using airborne in situ measurements from the western pacific area during shiva. *Atmospheric Chemistry and Physics*, 14(13):6903–6923, 2014b. doi: 10.5194/acp-14-6903-2014. URL http://www.atmos-chem-phys.net/14/6903/2014/.

R. J. Salawitch, D. K. Weisenstein, L. J. Kovalenko, C. E. Sioris, P. O. Wennberg, K. Chance, M. K. W. Ko, and C. A. McLinden. Sensitivity of ozone to bromine in the lower stratosphere. *Geophysical Research Letters*, 32(5):n/a–n/a, 2005. ISSN 1944-8007. doi: 10.1029/2004GL021504. URL http://dx.doi.org/10.1029/2004GL021504. L05811.

R. J. Salawitch, T. Canty, T. Kurosu, K. Chance, Q. Liang, A. da Silva, S. Pawson, J. E. Nielsen, J. M. Rodriguez, P. K. Bhartia, X. Liu, L. G. Huey, J. Liao, R. E. Stickel, D. J. Tanner, J. E. Dibb, W. R. Simpson, D. Donohoue, A. Weinheimer, F. Flocke, D. Knapp, D. Montzka, J. A. Neuman, J. B. Nowak, T. B. Ryerson, S. Oltmans, D. R. Blake, E. L. Atlas, D. E. Kinnison, S. Tilmes, L. L. Pan, F. Hendrick, M. Van Roozendael, K. Kreher, P. V. Johnston, R. S. Gao, B. Johnson, T. P. Bui, G. Chen, R. B. Pierce, J. H. Crawford, and D. J. Jacob. A new interpretation of total column bro during arctic spring. *Geophysical Research Letters*, 37(21):n/a–n/a, 2010. ISSN 1944-8007. doi: 10.1029/2010GL043798. URL http://dx.doi.org/10.1029/2010GL043798. L21805.

RJ. Salawitch. Atmospheric chemistry: Biogenic bromine. *Nature*, 439:275 – 277, 2006.

S.P. Sander, R. R. Friedl, J. Barkern, D.M. Golden, M.J. Kurylo, P.H. Wine, J.P.D. Abbat, J.B. Burkholder, C.E. Kolb, G.K. Moortgat, R.E. Huie, and V.L. Orkin. Chemical kinetics and photochemical data for use in atmospheric studies, evaluation no. 17. *JPL Publication 10-6, Jet Propulsion Laboratory, Pasadena*, 2011. URL http://jpldataeval.jpl.nasa.gov/.

S. M. Schauffler, E. L. Atlas, F. Flocke, R. A. Lueb, V. Stroud, and W. Travnicek. Measurement of bromine-containing organic compounds at the tropical tropopause. *Geophys. Res. Lett.*, 25(3):317–320, 1998.

S.M. Schauffler, E.L. Atlas, D. Blake, F. Flocke, R.A. Lueb, J.M. Lee-Taylor, V. Stroud, , and W. Travnicek. Distribution of brominated organic compounds in the upper troposphere and lower stratosphere. *J. Geophys. Res.*, 104:21,513–21,535, 1999.

R. Schofield, S. Fueglistaler, I. Wohltmann, and M. Rex. Sensitivity of stratospheric br_y to uncertainties in very short lived substance emissions and atmospheric transport. *Atmospheric Chemistry and Physics*, 11(4):1379–1392, 2011. doi: 10.5194/acp-11-1379-2011. URL http://www.atmos-chem-phys.net/11/1379/2011/.

J. H. Seinfeld and S. N. Pandis. *Atmospheric Chemistry and Physics - From Air Pollution to Climate Change, 2nd Edition*. John Wiley and Sons, Inc., Hoboken, New Jersey, 2006. ISBN 978-0-471-72018-8.

A. Serdyuchenko, V. Gorshelev, M. Weber, W. Chehade, and J. P. Burrows. High spectral resolution ozone absorption cross-sections; part 2: Temperature dependence. *Atmospheric Measurement Techniques*, 7(2):625–636, 2014. doi: 10.5194/amt-7-625-2014. URL http://www.atmos-meas-tech.net/7/625/2014/.

H. Sihler, U. Platt, S. Beirle, T. Marbach, S. Kühl, S. Dörner, J. Verschaeve, U. Frieß, D. Pöhler, L. Vogel, R. Sander, and T. Wagner. Tropospheric bro column densities in the arctic derived from satellite: retrieval and comparison to ground-based measurements. *Atmospheric Measurement Techniques*, 5(11):2779–2807, 2012. doi: 10.5194/amt-5-2779-2012. URL http://www.atmos-meas-tech.net/5/2779/2012/.

B.-M. Sinnhuber and I. Folkins. Estimating the contribution of bromoform to stratospheric bromine and its relation to dehydration in the tropical tropopause layer. *Atmospheric Chemistry and Physics*, 6(12):4755–4761, 2006. doi: 10.5194/acp-6-4755-2006. URL http://www.atmos-chem-phys.net/6/4755/2006/.

B.-M. Sinnhuber, A. Rozanov, N. Sheode, O. T. Afe, A. Richter, M. Sinnhuber, F. Wittrock, J. P. Burrows, G. P. Stiller, T. von Clarmann, and A. Linden. Global observations of stratospheric bromine monoxide from sciamachy. *Geophysical Research Letters*, 32(20):n/a–n/a, 2005. ISSN 1944-8007. doi: 10.1029/2005GL023839. URL http://dx.doi.org/10.1029/2005GL023839. L20810.

B.-M. Sinnhuber, N. Sheode, M. Sinnhuber, M. P. Chipperfield, and W. Feng. The contribution of anthropogenic bromine emissions to past stratospheric ozone trends: a modelling study. *Atmospheric Chemistry and Physics*, 9(8):2863–2871, 2009. doi: 10.5194/acp-9-2863-2009. URL http://www.atmos-chem-phys.net/9/2863/2009/.

C.E. Sioris, L.J. Kovalenko, C.A. McLinden, R.J. Salawitch, M. Van Roozendael, F. Goutail, M. Dorf, K. Pfeilsticker, K. Chance, C. von Savigny, X. Liu, T.P. Kurosu, J.-P. Pommereau, H. Bösch, and J. Frerick. Latitudinal and vertical distribution of bromine monoxide and inorganic bromine in the lower stratosphere from sciamachy limb scatter measurements. *submitted to J. Geophys. Res.*, 2005.

Susan Solomon, Rolando R. Garcia, and A. R. Ravishankara. On the role of iodine in ozone depletion. *J. Geophys. Res.*, 99:20,491–20,499, 1994. doi: 10.1029/94JD02028.

R. A. Stachnik, L. Millán, R. Jarnot, R. Monroe, C. McLinden, S. Kühl, J. Pukite, M. Shiotani, M. Suzuki, Y. Kasai, F. Goutail, J. P. Pommereau, M. Dorf, and K. Pfeilsticker. Stratospheric bro abundance measured by a balloon-borne submillimeterwave radiometer. *Atmospheric Chemistry and Physics*, 13(6):3307–3319, 2013. doi: 10.5194/acp-13-3307-2013. URL http://www.atmos-chem-phys.net/13/3307/2013/.

J. Stutz, O. Pikelnaya, S. C. Hurlock, S. Trick, S. Pechtl, and R. von Glasow. Daytime oio in the gulf of maine. *Geophys. Res. Lett.*, 34:L22816, November 2007. doi: 10.1029/2007GL031332.

S. Tegtmeier, K. Krüger, B. Quack, E. L. Atlas, I. Pisso, A. Stohl, and X. Yang. Emission and transport of bromocarbons: from the west pacific ocean into the stratosphere. *Atmospheric Chemistry and Physics*, 12(22):10633–10648, 2012. doi: 10.5194/acp-12-10633-2012. URL http://www.atmos-chem-phys.net/12/10633/2012/.

L.P. Teisserenc de Bort. Variation de la temperature de l'air libre dans la zone comprise entre 8 km et 13 km d'altitude. *Comptes rendus de 'Academie Science Paris*, 134:987 – 989, 1902.

N. Theys, M. Van Roozendael, Q. Errera, F. Hendrick, F. Daerden, S. Chabrillat, M. Dorf, K. Pfeilsticker, A. Rozanov, W. Lotz, J. P. Burrows, J.-C. Lambert, F. Goutail, H. K. Roscoe, and M. De Mazière. A global stratospheric bromine monoxide climatology based on the bascoe chemical transport model. *Atmospheric Chemistry and Physics*, 9(3):831–848, 2009. doi: 10.5194/acp-9-831-2009. URL http://www.atmos-chem-phys.net/9/831/2009/.

N. Theys, M. Van Roozendael, F. Hendrick, X. Yang, I. De Smedt, A. Richter, M. Begoin, Q. Errera, P. V. Johnston, K. Kreher, and M. De Mazière. Global observations of tropospheric bro columns using gome-2 satellite data. *Atmospheric Chemistry and Physics*, 11(4):1791–1811, 2011. doi: 10.5194/acp-11-1791-2011. URL http://www.atmos-chem-phys.net/11/1791/2011/.

R. P. Thorn, E. P. Daykin, and P. H. Wine. Kinetics of the bro + no2 association reaction. temperature and pressure dependence in the falloff regime. *International Journal of Chemical Kinetics*, 25(7):521–537, 1993. ISSN 1097-4601. doi: 10.1002/kin.550250703. URL http://dx.doi.org/10.1002/kin.550250703.

G. Thuillier, M. Hersé, D. Labs, T. Foujols, W. Peetermans, D. Gillotay, P.C. Simon, and H. Mandel. The solar spectral irradiance from 200 to 2400 nm as measured

by the solspec spectrometer from the atlas and eureca missions. *Solar Physics*, 214(1):1–22, 2003. ISSN 0038-0938. doi: 10.1023/A:1024048429145. URL http://dx.doi.org/10.1023/A%3A1024048429145.

U. Tricoli, P. Vochezer, and K. Pfeilsticker. Transition operator calculation with green's dyadic technique for electromagnetic scattering: A numerical approach using the dyson equation. *Journal of Quantitative Spectroscopy and Radiative Transfer*, 162:77 – 88, 2015. ISSN 0022-4073. doi: http://dx.doi.org/10.1016/j.jqsrt.2015.04.006. URL http://www.sciencedirect.com/science/article/pii/S0022407315001570. Laser-light and Interactions with Particles 2014.

M. Van Roozendael, T. Wagner, A. Richter, I. Pundt, D.W. Arlander, J.P. Burrows, M. P. Chipperfield, C. Fayt, P.V. Johnston, J.C. Lambert, K. Kreher, K. Pfeilsticker, U. Platt, J. P. Pommereau, B.M. Sinnhuber, K.K. Tornkvist, and F. Wittrock. Intercomparison of bro measurements from ers-2 gome, ground-based and balloon platforms. *Adv. Space. Res.*, 29(22):1161 – 1666, 2002.

Guus J. M. Velders, David W. Fahey, John S. Daniel, Mack McFarland, and Stephen O. Andersen. The large contribution of projected hfc emissions to future climate forcing. *Proceedings of the National Academy of Sciences*, 106(27): 10949–10954, 2009. doi: 10.1073/pnas.0902817106. URL http://www.pnas.org/content/106/27/10949.abstract.

C. M. Volk, J. W. Elkins, D. W. Fahey, R. J. Salawitch, G. S. Dutton, J. M. Gilligan, M. H. Proffitt, M. Loewenstein, J. R. Podolske, K. Minschwaner, J. J. Margitan, and K. R. Chan. Quantifying transport between the tropical and mid-latitude lower stratosphere. *Science*, 272(5269):1763–1768, 1996. doi: 10.1126/science.272.5269.1763. URL http://www.sciencemag.org/content/272/5269/1763.abstract.

R. Volkamer, S. Baidar, T. L. Campos, S. Coburn, J. P. DiGangi, B. Dix, T. K. Koenig, I. Ortega, B. R. Pierce, M. Reeves, R. Sinreich, S. Wang, M. A. Zondlo, and P. A. Romashkin. Aircraft measurements of bromine monoxide, iodine monoxide, and glyoxal profiles in the tropics: comparison with ship-based and in situ measurements. *Atmospheric Measurement Techniques Discussions*, 8(1):623–687, 2015. doi: 10.5194/amtd-8-623-2015. URL http://www.atmos-meas-tech-discuss.net/8/623/2015/.

T. Wagner, B. Dix, C. von Friedeburg, U. Frieß, S. Sanghavi, R. Sinreich, and U. Platt. MAX-DOAS O_4 measurements: A new technique to derive information on atmospheric aerosols - principles and information content. *J. Geophys. Res.*, 109:D22205, 2004. doi: 10.1029/2004JD004904.

P. R. Wamsley, J. W. Elkins, D. W. Fahey, G. S. Dutton, R. C. Volk, C. M. Myers, S. A. Montzka, J. H. Butler, A. D. Clarke, P. J. Fraser, L. P. Steele, M. P. Lucarelli, E. L. Atlas, S. M. Schauffler, D. R. Blake, F. S. Rowland, W. T. Sturges, J. M. Lee, S. A. Penkett, A. Engel, R. M. Stimpfle, K. R. Chan, D. K. Weisenstein, M. K. W. Ko, and R. J. Salawitch. Distribution of halon-1211 in the upper troposphere and lower stratosphere and the 1994 total bromine budget. *J. Geophys. Res*, 103(D1): 1513–1526, 1998.

Siyuan Wang, Johan A. Schmidt, Sunil Baidar, Sean Coburn, Barbara Dix, Theodore K. Koenig, Eric Apel, Dene Bowdalo, Teresa L. Campos, Ed Eloranta, Mathew J. Evans, Joshua P. DiGangi, Mark A. Zondlo, Ru-Shan Gao, Julie A. Haggerty, Samuel R. Hall, Rebecca S. Hornbrook, Daniel Jacob, Bruce Morley, Bradley Pierce, Mike Reeves, Pavel Romashkin, Arnout ter Schure, and Rainer Volkamer. Active and widespread halogen chemistry in the tropical and subtropical free troposphere. *Proceedings of the National Academy of Sciences*, 112(30):9281–9286, 2015. doi: 10.1073/pnas.1505142112. URL http://www.pnas.org/content/112/30/9281.abstract.

Darryn Waugh and Timothy Hall. Age of stratospheric air: Theory, observations, and models. *Reviews of Geophysics*, 40(4):1–1–1–26, 2002. ISSN 1944-9208. doi: 10.1029/2000RG000101. URL http://dx.doi.org/10.1029/2000RG000101. 1010.

F. Weidner, H. Bösch, H. Bovensmann, J. P. Burrows, A. Butz, C. Camy-Peyret, M. Dorf, K. Gerilowski, W. Gurlit, U. Platt, C. von Friedeburg, T. Wagner, and K. Pfeilsticker. Balloon-borne limb profiling of uv/vis skylight radiances, o_3, no_2, and bro: technical set-up and validation of the method. *Atmospheric Chemistry and Physics*, 5(5):1409–1422, 2005. doi: 10.5194/acp-5-1409-2005. URL http://www.atmos-chem-phys.net/5/1409/2005/.

A. Wisher, D. E. Oram, J. C. Laube, G. P. Mills, P. van Velthoven, A. Zahn, and C. A. M. Brenninkmeijer. Very short-lived bromomethanes measured by the caribic observatory over the north atlantic, africa and southeast asia during 2009–2013. *Atmospheric Chemistry and Physics*, 14(7):3557–3570, 2014. doi: 10.5194/acp-14-3557-2014. URL http://www.atmos-chem-phys.net/14/3557/2014/.

WMO. *World Meteorological Organization, Scientific Assessment of Ozone Depletion: 2010, Global Ozone Research and Monitoring Project-Report No.52, 516 pp., Geneva, Switzerland*, 2011.

WMO. Scientific assesment of ozone depletion: 2014. *World Meteorological Organisation, Geneve, Switzerland*, Global Ozone Research and Monitoring Project—Report No. 55:416 pp., 2014.

Steven C. Wofsy, Michael B. McElroy, and Yuk Ling Yung. The chemistry of atmospheric bromine. *Geophysical Research Letters*, 2(6):215–218, 1975. ISSN 1944-8007. doi: 10.1029/GL002i006p00215. URL http://dx.doi.org/10.1029/GL002i006p00215.

X. Yang, N. L. Abraham, A. T. Archibald, P. Braesicke, J. Keeble, P. J. Telford, N. J. Warwick, and J. A. Pyle. How sensitive is the recovery of stratospheric ozone to changes in concentrations of very short-lived bromocarbons? *Atmospheric Chemistry and Physics*, 14(19):10431–10438, 2014. doi: 10.5194/acp-14-10431-2014. URL http://www.atmos-chem-phys.net/14/10431/2014/.

Selami Yilmaz. *Retrieval of Atmospheric Aerosol and Trace Gas Vertical Profiles using Multi-Axis Differential Optical Absorption Spectroscopy*. PhD thesis, Institute of Environmental Physics, University of Heidelberg, 2012.

Y. Yokouchi, H. Mukai, H. Yamamoto, A. Otsuki, C. Saitoh, and Y. Nojiri. Distribution of methyl iodide, ethyl iodide, bromoform, and dibromomethane over the ocean (east and southeast Asian seas and the western Pacific). *J. Geophys. Res.*, 102:8805–8809, 1997.

Y. Yokouchi, F. Hasebe, M. Fujiwara, H. Takashima, M. Shiotani, N. Nishi, Y. Kanaya, S. Hashimoto, P. Fraser, D. Toom-Sauntry, H. Mukai, and Y. Nojiri. Correlations and emission ratios among bromoform, dibromochloromethane, and dibromomethane in the atmosphere. *Journal of Geophysical Research: Atmospheres*, 110(D23):n/a–n/a, 2005. ISSN 2156-2202. doi: 10.1029/2005JD006303. URL http://dx.doi.org/10.1029/2005JD006303. D23309.

F. Ziska, B. Quack, K. Abrahamsson, S. D. Archer, E. Atlas, T. Bell, J. H. Butler, L. J. Carpenter, C. E. Jones, N. R. P. Harris, H. Hepach, K. G. Heumann, C. Hughes, J. Kuss, K. Krüger, P. Liss, R. M. Moore, A. Orlikowska, S. Raimund, C. E. Reeves, W. Reifenhäuser, A. D. Robinson, C. Schall, T. Tanhua, S. Tegtmeier, S. Turner, L. Wang, D. Wallace, J. Williams, H. Yamamoto, S. Yvon-Lewis, and Y. Yokouchi. Global sea-to-air flux climatology for bromoform, dibromomethane and methyl iodide. *Atmospheric Chemistry and Physics*, 13(17):8915–8934, 2013. doi: 10.5194/acp-13-8915-2013. URL http://www.atmos-chem-phys.net/13/8915/2013/.

D Lists

D.1 List of Frequently Used Abbreviations

AGAGE	Advanced Global Atmospheric Gases Experiment
ATTREX	Airborne Tropical Tropopause Experiment
CTM	Chemical transport model
DFRC	Dryden Flight Research Center
DOAS	Differential Optical Absorption Spectroscopy
(d)SCD	(differential) slant column density
ECMWF	European Centre for Medium-Range Weather Forecasts
GH	Global Hawk
LS	Lower stratosphere
LZRH	Level of zero radiative heating
MBL	Marine boundary layer
mSc	Marine stratocumulus cloud
MaRS	Master Retrieval Software
McArtim	Monte Carlo atmospheric radiative transfer inversion model
NASA	National Aeronautics and Space Administration
NOAA	National Oceanic and Atmospheric Administration
OD	Optical depth
PG	Product gas
RRS	Rotational Raman Scattering
RT	Radiative transfer
RTE	Radiative transfer equation
RTM	Radiative transfer model
SF	Science flight
SG	Source gas
TTL	Tropical tropopause layer
UAV	Unmanned aerial vehicle
UT	Upper troposphere
UV	Ultra-violet
vmr	Volume mixing ratio
VSLS	Very short-lived species
WMO	World Meteorological Organization

D.2 List of Figures

D.3 List of Tables

E Acknowledgements

I want to express my gratitude to many people supporting me in different ways in the course of this thesis:

- First of all I like to start out by thanking Prof. Dr. Klaus Pfeilsticker who opened up the possibility to work on this interesting research field. The many fruitful conversations, whether of private or scientific nature, created a lot of helpful ideas and advises.
- Prof. Dr. Thomas Leisner who agreed to serve as a referee on this thesis.
- Thanks to Prof. Dr. Jochen Stutz who shares a major contribution of giving me the opportunity to work on the NASA ATTREX project. It was a great pleasure to work together during the Global Hawk deployments in Dryden, 2011 and 2013. Thanks for helping with the logistics at UCLA and Dryden. I also appreciate all the very helpful discussions regarding the data analysis.
- I am extremely grateful to all the people who were proof-reading different parts of the thesis: Lisa, Tina, Tilman, Peter, Dominique, Johannes, Sebastian, Stefan, Alex, Dave.
- Of course I want to thank the whole research group for the great atmosphere (what a word pun) and company in- and outside the office: Tina, Lisa, Tilman, Alex, Ugo, Stefan, Jannik and Dominique. Also including of course the "past generations": Katja, Cris, Lena, Sabrina, Isabella, Mareike, Jenny, Tim, Sebastian, Marcel, Marcel, Rasmus, Jannis, ...
- I also would like to mention the colleagues I worked directly together with in Dryden and during the data analysis: Rasmus, Max, Lisa, Ugo. Not to forget Tim for providing McArtim and helpful tips.
- Thanks to everybody from NASA and ESPO leading the project, to the people managing the logistics in Dryden, and to all the other instrument teams. A special thanks to Dave Jordan who made the stay in Dryden even more fun.
- Thanks to Martyn and Ryan for their quick and excellent support with the SLIMCAT/TOMCAT model data.
- I thank Elliot and Maria for the support regarding the GWAS data, and also for the nice company during the field campaign at Dryden.

- Ralph Pfeifer and the whole workshop crew who did a great job in building the instrument in a very short time frame.
- Last but definitively not least, I want to thank my family and friends for supporting me not only during this thesis but also for the unconditional support in private. There are special people who mean incredibly much to me but who I don't want to list here. I am sure that they feel addressed.